NASA/CR—2012-217451 21–12567

Quiet High Speed Fan II (QHSF II): Final Report

Karen Kontos, Don Weir, and Dave Ross
Honeywell, Phoenix, Arizona

August 2012

NASA STI Program . . . in Profile

Since its founding, NASA has been dedicated to the advancement of aeronautics and space science. The NASA Scientific and Technical Information (STI) program plays a key part in helping NASA maintain this important role.

The NASA STI Program operates under the auspices of the Agency Chief Information Officer. It collects, organizes, provides for archiving, and disseminates NASA's STI. The NASA STI program provides access to the NASA Aeronautics and Space Database and its public interface, the NASA Technical Reports Server, thus providing one of the largest collections of aeronautical and space science STI in the world. Results are published in both non-NASA channels and by NASA in the NASA STI Report Series, which includes the following report types:

- TECHNICAL PUBLICATION. Reports of completed research or a major significant phase of research that present the results of NASA programs and include extensive data or theoretical analysis. Includes compilations of significant scientific and technical data and information deemed to be of continuing reference value. NASA counterpart of peer-reviewed formal professional papers but has less stringent limitations on manuscript length and extent of graphic presentations.

- TECHNICAL MEMORANDUM. Scientific and technical findings that are preliminary or of specialized interest, e.g., quick release reports, working papers, and bibliographies that contain minimal annotation. Does not contain extensive analysis.

- CONTRACTOR REPORT. Scientific and technical findings by NASA-sponsored contractors and grantees.

- CONFERENCE PUBLICATION. Collected papers from scientific and technical conferences, symposia, seminars, or other meetings sponsored or cosponsored by NASA.

- SPECIAL PUBLICATION. Scientific, technical, or historical information from NASA programs, projects, and missions, often concerned with subjects having substantial public interest.

- TECHNICAL TRANSLATION. English-language translations of foreign scientific and technical material pertinent to NASA's mission.

Specialized services also include creating custom thesauri, building customized databases, organizing and publishing research results.

For more information about the NASA STI program, see the following:

- Access the NASA STI program home page at *http://www.sti.nasa.gov*

- E-mail your question to *help@sti.nasa.gov*

- Fax your question to the NASA STI Information Desk at 443–757–5803

- Phone the NASA STI Information Desk at 443–757–5802

- Write to:
  STI Information Desk
  NASA Center for AeroSpace Information
  7115 Standard Drive
  Hanover, MD 21076–1320

NASA/CR—2012-217451 21–12567

Quiet High Speed Fan II (QHSF II): Final Report

Karen Kontos, Don Weir, and Dave Ross
Honeywell, Phoenix, Arizona

Prepared under Contract NAS3–01136, Task number 2

National Aeronautics and
Space Administration

Glenn Research Center
Cleveland, Ohio 44135

August 2012

Acknowledgments

This work was funded under NASA Contract NAS3-01136 from the NASA Glenn Research Center. The author would like to express thanks for the many useful contributions of the staff at the NASA Glenn Research Center. Special thanks go to John Gazzaniga who served as the Technical Monitor, and to Joe Grady who provided support from the Quiet Aircraft Technology program office. Significant contributions to this report were made by many individuals, but the author would like to specifically recognize the contributions of those who have served as focal points in key technical areas throughout the QHSF II program: Joe Panovsky for aeroelastic tool development and design, Nick Nolcheff and Dave Hanson for aerodynamics, Srinivas Chunduru for mechanical design, Lysbeth Lieber for rotor-strut interaction analyses, Glen Schroering for rig hardware fabrication and instrumentation, Bill Schuster for acoustic analyses, and Bruce Bouldin for aerodynamic installation analyses.

This work was sponsored by the Fundamental Aeronautics Program at the NASA Glenn Research Center.

Level of Review: This material has been technically reviewed by NASA technical management OR expert reviewer(s).

Available from

NASA Center for Aerospace Information
7115 Standard Drive
Hanover, MD 21076–1320

National Technical Information Service
5301 Shawnee Road
Alexandria, VA 22312

Available electronically at http://www.sti.nasa.gov

TABLE OF CONTENTS

TABLE OF CONTENTS (Cont)

TABLE OF CONTENTS (Cont)

LIST OF FIGURES

LIST OF FIGURES (Cont)

LIST OF FIGURES (Cont)

LIST OF FIGURES (Cont)

LIST OF FIGURES (Cont)

LIST OF FIGURES (Cont)

LIST OF FIGURES (Cont)

LIST OF FIGURES (Cont)

LIST OF TABLES

REVOLUTIONARY AERO-SPACE ENGINE RESEARCH (RASER) TASK ORDER NO. 2 QUIET HIGH SPEED FAN II (QHSF II) FINAL REPORT

1. ACKNOWLEDGEMENTS

This work was funded under NASA Contract NAS3-01136 from the NASA Glenn Research Center. The author would like to express thanks for the many useful contributions of the staff at the NASA Glenn Research Center. Special thanks go to John Gazzaniga who served as the Technical Monitor, and to Joe Grady who provided support from the Quiet Aircraft Technology program office. Significant contributions to this report were made by many individuals, but the author would like to specifically recognize the contributions of those who have served as focal points in key technical areas throughout the QHSF II program: Joe Panovsky for aeroelastic tool development & design, Nick Nolcheff and Dave Hanson for aerodynamics, Srinivas Chunduru for mechanical design, Lysbeth Lieber for rotor-strut interaction analyses, Glen Schroering for rig hardware fabrication and instrumentation, Bill Schuster for acoustic analyses, and Bruce Bouldin for aerodynamic installation analyses.

2. INTRODUCTION

2.1 Motivation

Honeywell Engines, Systems & Services (Honeywell), building on the technology developed under the Quiet High Speed Fan contract (AOI 14, NAS3-27752) (Reference 1), has designed and fabricated an advanced forward swept fan with the following characteristics:

1. Reduced noise at supersonic tip speeds, in comparison to current state-of-the-art fan technology

2. Improved aeroelastic stability within the anticipated operating envelope

3. Aerodynamic performance consistent with current state-of-the-art fan technology

2.2 Description of Work

2.2.1 Aerodynamic and Mechanical Design

Honeywell has completed a new design for the QHSF II (lower hub/tip ratio and higher specific flow than the Baseline I fan). Aerodynamic and mechanical design studies were conducted to allow for study of alternative fan blade and vane geometry.

Honeywell conducted an analytical Design of Experiments (DOE) of potential blade and vane modifications with the goal of identifying a design that provides improved vibration response while maintaining or improving aerodynamic and acoustic performance. The DOE included: modifying the incidence of the forward-swept fan blades to improve aeroelastic response, examining the sensitivity in performance with reduced levels of forward sweep at the rotor LE tip, and modifying the geometry of 3-D aft-swept vanes including removal of scallop to improve performance and reduce noise. A design was selected based on the results of the DOE study.

Detailed aerodynamic analysis was performed at design and off-design speeds, using 2-D axisymmetric streamline curvature analysis of the overall fan stage (rotor, stator, front frame), and 3-D viscous flow analyses for both isolated rotor and stator airfoils as well as combined stage designs. Mechanical analyses of the redesigned fan blade attached to the existing disk and stator vane was performed. An analysis of the rotor-stator-strut interaction was performed to assess the risk of strut-induced fan rotor forced vibration. A comparison of the predicted aerodynamic performance of the Quiet High Speed Fan II (QHSF II) to the original Quiet High Speed Fan (QHSF I) and the corresponding baseline fans was performed.

Honeywell performed CFD analysis of the Baseline II and QHSF II stator & strut configurations at different stator clocking angles to determine the influence of stator configuration on the rotor flow field. The aerodynamic design of the Baseline II stator was modified as necessary to efficiently run with the QHSF II rotor.

2.2.2 Aeroelastic Analysis

Prior to the initiation of the QHSF II design and in collaboration with NASA, an aeroelastic tool calibration study was conducted using the QHSF I result, which established the best practices for flutter prediction using the TURBO aeroelastic analysis code. A baseline aerodynamic solution for the QHSF I using the Average Passage / NASA (APNASA) CFD code was prepared. A tip clearance sensitivity study was conducted. In collaboration with NASA, Honeywell conducted a mode shape sensitivity study. NASA conducted a grid sensitivity study and an inlet/exit boundary condition sensitivity study. Honeywell defined the part speed geometry for the QHSF I, and NASA performed 3-D unsteady aerodynamic analyses of the QHSF I along two speed lines (part speed and near design speed) using TURBO. NASA assessed the impact of rig size differences on the aeroelastic response. In collaboration with NASA, Honeywell prepared a summary of the tool calibration study results.

In collaboration with NASA, Honeywell conducted an aeroelastic evaluation of the DOE design modifications and an aeroelastic analysis of the final redesigned configuration, and provided a comparison of the predicted aerodynamic damping and flutter boundary with the QHSF I and with the Baseline I.

2.2.3 Acoustic Analysis

Honeywell evaluated the effect of the DOE blade design modifications on the rotor-stator interaction tone duct mode noise levels at several part speed conditions using SOURCE3D. Predictions of the interaction tone noise levels of the final design using SOURCE3D/TfaNS, as well as comparisons to the QHSF I and the Baseline I at the same operating conditions, were also prepared.

2.2.4 Blade and Vane Fabrication

Honeywell generated solid models and detail drawings of the QHSF II fan, stator, and stator housing rings. Twenty-seven fan blades (22 + 5 spares) were machined from bar stock. Acoustic ring signature and holography data on the blades to determine natural frequencies and strain gage locations were produced. Honeywell installed strain gages on the blades using traditional type strain gages. The wiring was run to dog-bone connectors on the front of the blades. NASA mated the instrumented blades with the rotor and completed the strain gage wiring into the existing hub and rotor.

Honeywell fabricated a set of 55 (50 plus 5 spares) stator vanes each for both the QHSF II and the Baseline II designs. Honeywell also fabricated the stator hub and tip mounting rings and assembled the stators.

2.2.5 Rig Modifications

Honeywell designed and procured additional 22” rig hardware as required by the new Baseline II fan design. This hardware included the fan disk, spinner, front frame, and additional stator assembly hardware. Honeywell made all modifications to existing rig hardware as necessary to accommodate the new flow path. The front frame of the rig was modified to accommodate hot wire/film probes to make flow measurements downstream of the vanes. NASA provided the hot wire/film probes and supporting instrumentation.

3. AEROELASTIC TOOL VALIDATION

3.1 TURBO Modeling for QHSF I

The QHSF I design consists of 22 forward-swept inserted blades with a moderate aspect ratio and state-of-the-art aerodynamic performance and operability (Reference 1 and 2). During rig testing in a high-speed wind tunnel, the fan performed well at design speed (100 percent speed), and was successfully throttled to the stall line. However, large vibratory responses due to flutter were encountered just above the sea level static (SLS) operating line at several part-speed conditions. The flutter mode was identified as the fundamental bending mode of the airfoil, in a 2 nodal diameter (ND) forward-traveling wave (FTW) pattern. The experimentally determined flutter boundary is depicted in Figure 1.

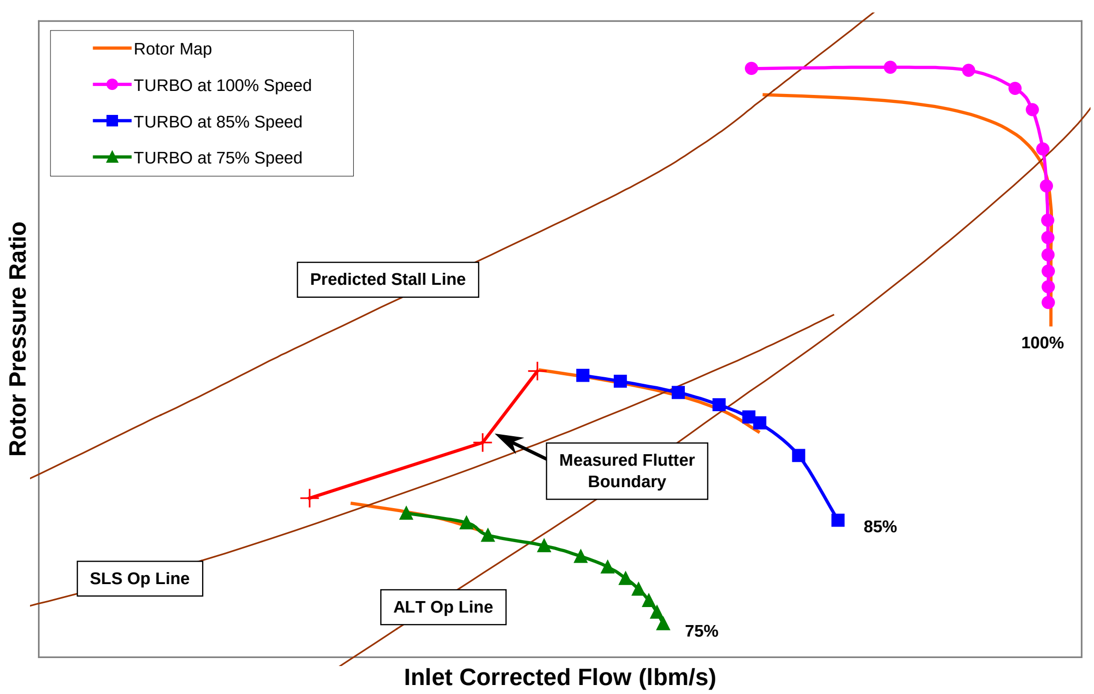

Figure 1. Flutter Boundary Based on Rig Testing and the Predicted Speed Lines From TURBO.

To help understand the reasons for the occurrence of flutter in this design, a detailed computational assessment was undertaken using the TURBO code developed by Mississippi State University (Reference 3 and 4) and NASA Glenn Research Center (Reference 5). TURBO is a 3D, time-accurate unsteady, Reynolds-Averaged Navier-Stokes code with the ability to model rotating or stationary blade rows, rotor-stator interaction, and blade motion. The approach followed for the flutter analysis in TURBO consists of introducing the blade motion by physically deforming the surfaces of the blade as defined by the mode shape at the prescribed vibratory frequency (Reference 5). Phase lag boundary conditions (Reference 6) are used, which allow any desired nodal diameter to be calculated with a single passage. The resulting aerodynamic work per cycle is converted into a more meaningful damping value to determine stability of the blade motion. If the damping is positive, the motion is stable. If the damping is negative, the motion is unstable and flutter can occur. In this paper, damping values are reported in terms of critical damping ratio, ζ. All structural analyses were conducted using the commercial finite element program ANSYS (Reference 7).

An aeroelastic tool calibration study was conducted using the QHSF I rotor geometry. The test conditions were at an inlet total pressure of 14.3 psi and an inlet total temperature of 73°F. Steady and unsteady flow computations were conducted for a total of three speed lines. The correlation effort included 100 percent, 85 percent, and 75 percent speed lines. Recall that no flutter was encountered during any testing at design speed, while the rig tests indicated significant flutter response just slightly toward the stall side of the operating line at the two lower speeds. Choosing these three speeds allows predictions along both stable and unstable speed lines to be evaluated. Table 1 summarizes speeds of interest.

Table 1. Speeds of Interest for NASA Rig.

% Speed	Corrected RPM	Physical RPM
100	15357	15572
85	13053	13236
75	11518	11679

3.1.1 TURBO Grid

The baseline grid for TURBO was generated by MMESH and then smoothed using a Poisson algorithm in CURVE2. The geometry used for this grid was based on the fully hot (100 percent speed) airfoil shape. Later the grid was refined to be consistent with the actual speed line analyzed.

MMESH is a grid-generation code developed at NASA Glenn. It takes the airfoil geometry and generates the three-dimensional computational grids for APNASA code (Reference 8). CURVE2 is a Honeywell developed code. It takes the shear-H grid from MMESH and creates a smooth and nearly orthogonal computational grid by solving Poisson equation for TURBO code.

Values for the tip clearance are based on measurements taken during the NASA 22” rig testing. NASA provided the results, and values of interest are summarized in Table 2. There is significant skew in the clearance, and modifications were made to the grid generator to allow the actual gap to be modeled. However, the initial model uses the average of the leading and trailing edge gaps. Note that the full physical clearance is modeled. Four cells (radially) are used for the tip gap.

Table 2. Tip Clearances at Speeds of Interest for NASA Rig.

Location	85% Speed	75% Speed
Lead Edge	0.046	0.053
Mid Chord	0.033	0.040
Trail Edge	0.015	0.021
Average	0.031	0.037

The grid size was limited to the maximum size that would run on Honeywell workstations. Parameters that describe the resulting grid are:

- # axial cells (*ni*)= 121
- # radial cells (*nj*) = 51
- # tangential cells (*nk*) = 39
- leading edge (*ile*) = 32
- trailing edge (*ite*) = 86
- blade tip (*jtip*) = 47.

Following the practice recommended by Chen et al. (Reference 9), a utility program was used to initialize the TURBO solutions by mapping an existing APNASA solution on a fine grid. This initial solution is for a different speed, and actually for the 18" rig size. But this solution is still a much better starting point than uniform flow, and so the convergence of the TURBO steady solution should be much faster. Note that the original aerodynamic grid files and solutions are flipped relative to the hardware (i.e., direction of rotation is opposite). To ensure consistency between the CFD grid and the FEM mesh, the TURBO grid and initial solution were flipped after the mapping procedure using a second utility program. This consistency of orientation (or rotation direction) is required to allow mapping of mode shapes and other quantities between the aerodynamic and mechanical domains. This final grid is shown in Figure 2.

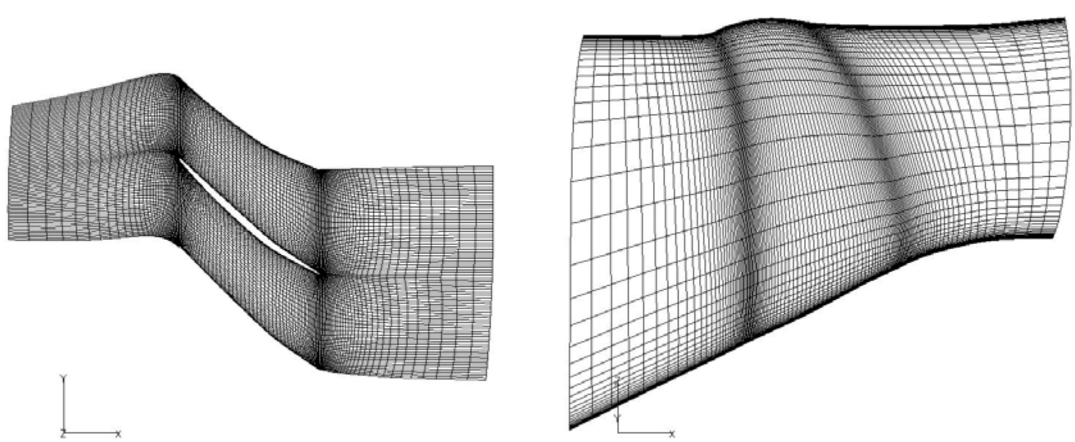

Figure 2. Grid of the QHSF I Used for the TURBO Analyses.

3.1.2 Inlet and Exit Profiles

The inlet and exit profiles of pressure, temperature, and flow angles which define the boundary conditions for the steady CFD analyses are based on a combination of NASA rig measurements, Honeywell rig measurements, and calculations from APNASA. The stations for the inlet profile are a combination of spans from the NASA measurements and spans in the APNASA input. The NASA data provides stations near the tip to specify the total pressure losses, while APNASA provides those near the hub to account primarily for changes in radial flow angle. The transition occurs just above 80 percent span.

The results from measurements in the NASA rig provided the inlet total pressure profile near the tip, accounting for losses due to the inlet (bellmouth, etc). At the hub, no measurements were available, so a computational estimate of the boundary layer as calculated by APNASA for the analysis of the 18” rig is used. This hub boundary layer extends 1 percent into the flow field. Two additional stations, at 0.5 percent and 1 percent span, were added to the APNASA stations to permit this profile to be specified. At other spans, a constant value for total pressure was assumed.

The inlet total temperature and tangential flow angle were assumed to be constant. The radial flow angle was obtained from APNASA input. All the stations from the APNASA input were used up to about 80 percent span, since the angle is nonzero up to this span. A value of 0.5 degrees was specified at 86.61 percent span to act as a transition. Beyond this span, the radial angle was specified to be zero, and the span locations correspond to the NASA measurements.

The exit profile for the static pressure was based on work done earlier for the 18” rig. Ideally, there would be measurements from the NASA tests, but no data was available between the rotor and the stator. Data at the hub and case was available from the 18” rig tests. It was assumed that this profile would be the same for both rigs. The work conducted previously determined that the ratio of the tip static pressure to the hub static pressure was 1.1635. This was found to be in reasonably good agreement with a TURBO analysis run using the assumption of radial equilibrium. However, the experimental value was used for all TURBO analyses of the NASA rig. These data are summarized in Table 3 and Figure 5.

3.1.3 QHSF I TURBO Solution

Most of the background information for the TURBO analysis has been specified previously. However, key features are noted here. The initial TURBO steady analysis was set up following Honeywell current best practices. This case provided a baseline for determining sensitivities to alternative modeling approaches.

This first set of analyses focused on the 85 percent speed line, or 13236 RPM (physical). A constant tip clearance of 0.031” was used, corresponding to 85 percent speed. Exit conditions for the first analysis were arbitrarily selected to have the hub static pressure equal to the average inlet total pressure. The tip static pressure was then determined by multiplying this value by 1.1635, to provide a profile consistent with experimental measurements. The initial flow field was specified from a mapping of an existing APNASA solution. The TURBO grid and initial flow field were then flipped to align the CFD grid with the hardware and the FEM mesh.

Table 3. Inlet Profiles for Total Pressure and Radial Flow Angle at 85% Speed.

Inlet Radius	Span	85% Speed Pt (norm)	Pt (psi)	Pt (Pa)	Radial Angle
1.900	0.0000	0.9434	13.491	93014.6	25.9995
	0.0050	0.9853	14.090	97145.7	25.5192
	0.0100	1.0000	14.300	98595.0	25.0388
	0.0837	1.0000	14.300	98595.0	17.9586
	0.1480	1.0000	14.300	98595.0	14.4816
	0.1963	1.0000	14.300	98595.0	12.5103
	0.2447	1.0000	14.300	98595.0	10.8811
	0.2803	1.0000	14.300	98595.0	9.8474
	0.3095	1.0000	14.300	98595.0	9.0772
	0.3353	1.0000	14.300	98595.0	8.4482
	0.3613	1.0000	14.300	98595.0	7.8559
	0.4564	1.0000	14.300	98595.0	5.9715
	0.5181	1.0000	14.300	98595.0	4.9274
	0.5745	1.0000	14.300	98595.0	4.0614
	0.6267	1.0000	14.300	98595.0	3.3188
	0.6754	1.0000	14.300	98595.0	2.6660
	0.7215	1.0000	14.300	98595.0	2.0797
	0.7652	1.0000	14.300	98595.0	1.5506
	0.8070	1.0000	14.300	98595.0	1.0716
9.666	0.8661	1.0000	14.300	98595.0	0.5000
9.804	0.8815	0.9999	14.299	98585.2	0.0000
9.946	0.8973	0.9998	14.297	98575.3	0.0000
10.099	0.9144	0.9996	14.294	98555.6	0.0000
10.257	0.9320	0.9993	14.290	98526.0	0.0000
10.398	0.9477	0.9990	14.286	98496.5	0.0000
10.552	0.9649	0.9834	14.063	96958.4	0.0000
10.710	0.9825	0.9461	13.529	93280.8	0.0000
10.788	0.9912	0.9302	13.302	91713.1	0.0000
10.828	0.9957	0.9140	13.070	90115.9	0.0000
10.867	1.0000	0.8800	12.584	86763.6	0.0000

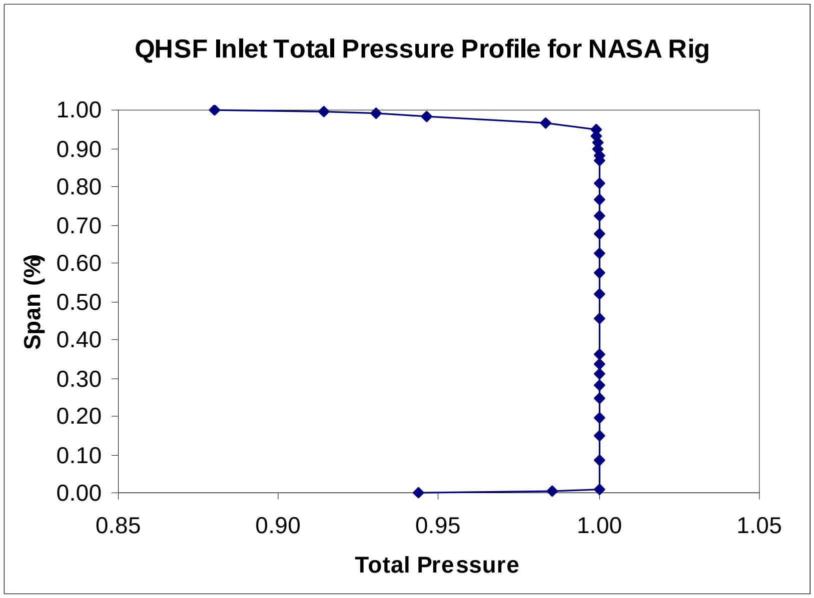

Figure 3. Inlet Profile for Total Pressure at 85% Speed.

TURBO in the steady mode was then used to converge the flow field to the new boundary conditions. This solution used 1000 iterations at a CFL number of 1000, utilizing the k-ε turbulence model. The solution converged well, but there were some (very) minor oscillations in the mass flow versus iteration that was damped out. The overall results from the solution are:

$$
\begin{aligned}
\dot{m}_{corr} &= \left(\frac{38.1869 + 38.1749}{2}\right)(2.2)(1.042) = 87.53 \text{ lbm/s} \\
p_R &= 1.457 / 0.9707 = 1.501 \\
\eta &= 0.9156
\end{aligned}
\tag{1}
$$

3.1.4 Static Deflections

The tip deflections at speeds of interest were calculated for the QHSF I in NASA rig size (22” diameter). These deflections were determined using nonlinear, large deflection static analysis in ANSYS. The model, shown in Figure 4, includes pressure loads and temperatures based on earlier CFD analysis at the Aerodynamic Design Point (ADP), or 100 percent speed. Note that the gas loads were determined for an inlet total pressure of 12.5 psi, corresponding to the Honeywell rig test, while the inlet total pressure in the NASA rig was 14.3 psi. These calculations may be repeated with gas loads that reflect the true inlet pressure and the actual speed, and perhaps even the position along the speed line. The results presented here are best taken as an indication of the importance of each of these influences.

The deflections at the blade tip are summarized in Table 4, with the coordinate systems shown Figure 5. The values tabulated are averages for the tip section of deflections along the chord (u_ξ), normal to the chord (u_η), and rotation (ϕ). These average values are based on the displacement of the nodes at the leading and trailing edges. For reference, the tip true chord is 4.586 inches, and the tip stagger (as measured from the axial direction) is -58.9°.

A total of 5 cases were run. First, the effect of the gas loads was isolated. Then, analyses at 100 percent and 85 percent speed were conducted, both with and without gas loads. From the results, note that the stagger increases with speed. The effect of the gas loads is fairly small, only about +0.2° (at either speed), and acts to reduce the amount of change in the stagger. Relative to the fully hot shape at 100 percent, the blade rotates +0.4° at the 85 percent speed condition, and this is in the direction of reducing stagger.

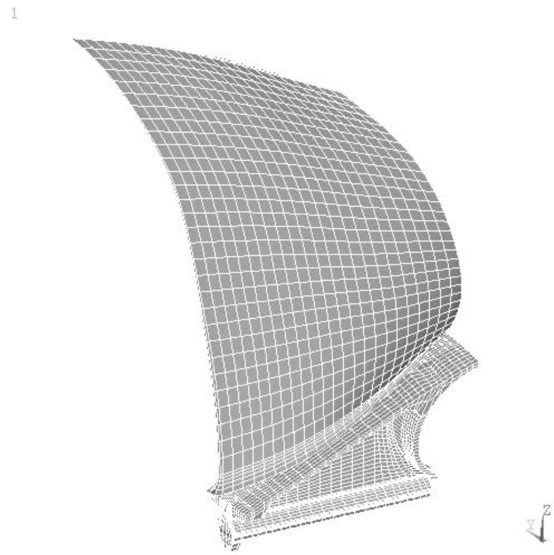

Figure 4. ANSYS Model of Full Blade.

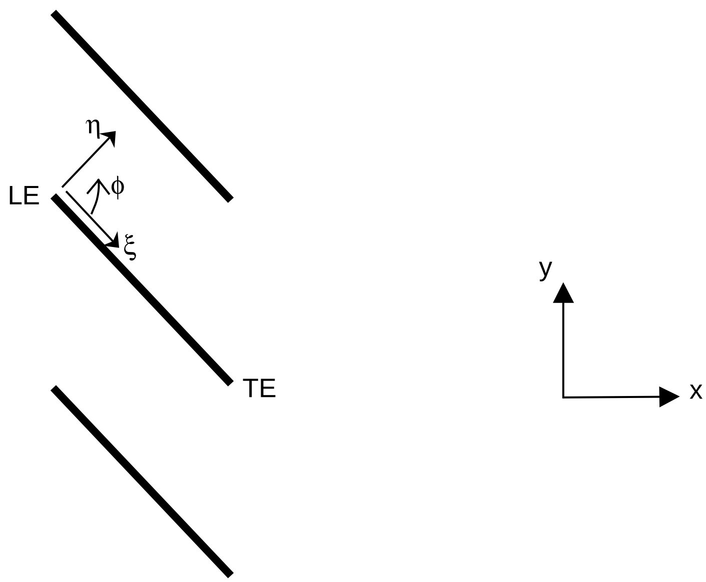

Figure 5. Coordinate Systems for Static Blade Deflections - the View Is Radially Inward.

A new steady TURBO solution for the 22” rotor blade for part speed analysis was developed. The solution grid is for the actual blade-shape at 85 percent speed (rather than fully hot) and includes the skewed tip gap based on the NASA measurements. A grid file, steady TURBO solutions for fac=1.00, steady input files, unsteady input files, and mode shape files for several nodal diameter patterns were provided to NASA. Figure 6 shows a comparison of the calculated 85 percent speed line performance as compared to the measured performance in the 18” rig.

Table 4. Static Tip Deflections as a Function of Speed and Gas Loads.

Phys Speed	% Speed	Gas Loads	u_ξ (in)	u_η (in)	ϕ (deg)
0	0	ADP	0.068	-0.177	1.166
15572	100	no	-0.090	0.325	-2.720
15572	100	ADP	-0.073	0.290	-2.573
13236	85	no	-0.084	0.296	-2.390
13236	85	ADP	-0.062	0.251	-2.182

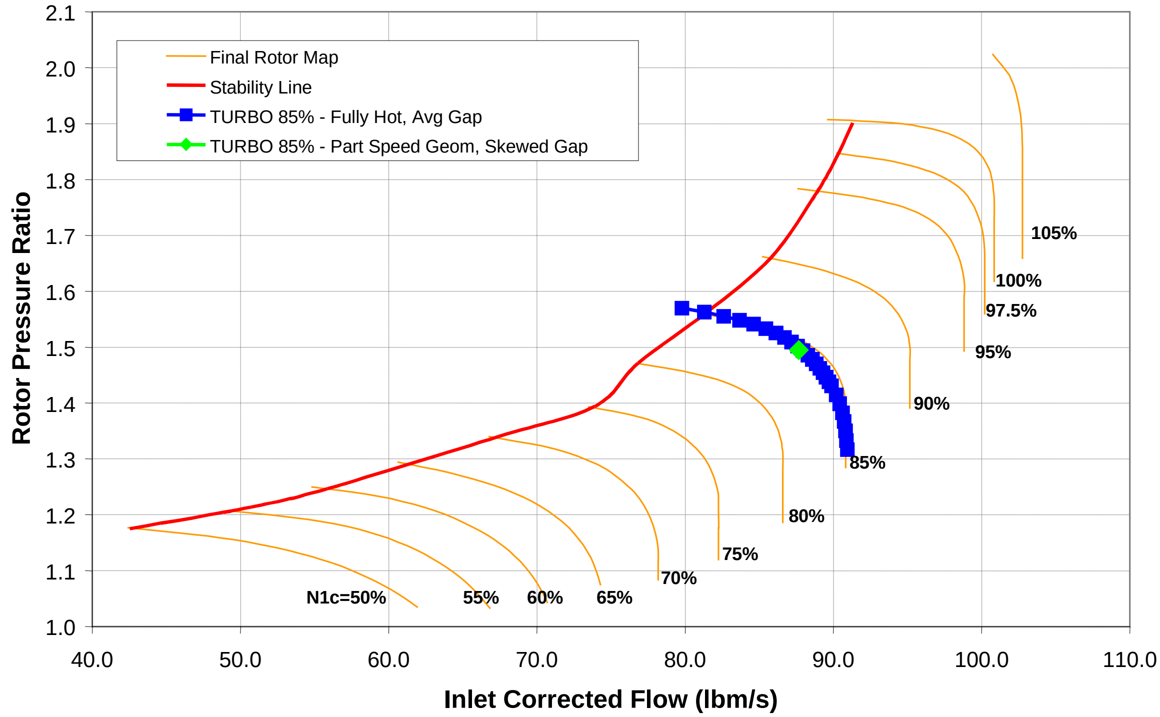

Figure 6. The Steady TURBO Analysis of the QHSF I in NASA 22" Rig Size for the 85% Speed Line Using Actual Blade Shape and Tip Clearance Is Compared to the Fan Map Extrapolated From 18" Rig Data.

3.2 Tip Clearance Sensitivity

The importance of tip clearance effects on the predicted stability boundary was quantified for the QHSF I correlation effort. Related studies on the Baseline I fan indicated a significant effect of tip clearance on aerodynamic damping, and so it was initially thought to be crucial to model the gap accurately for the present correlation effort.

During the initial analysis of the QHSF I in the 18” rig size, a detailed parametric study of the effects of the tip clearance was performed. While the study was conducted at the 18” rig size rather than the 22” size, the chosen 85 percent speed line is consistent with the analysis for the 22” rig. Three different tip gaps were used: the nominal physical value of 0.039”, a tighter gap of 0.010”, and a nearly limiting case of 0.002”. Note that the latter two values were chosen arbitrarily to span the tip gaps of interest. Unexpectedly, this study indicated little effect of the tip gap on either the steady flow field or the aerodynamic damping. The damping at two steady conditions along the 85 percent speed line is presented in Figure 7. The drop in damping as the tip gap is tightened is fairly significant for the peak efficiency condition. There is still a noticeable drop at near stall conditions, but the change in damping is only slightly more than 0.1 percent. The range of gaps considered is considerably larger than would actually need to be considered.

A second result is obtained indirectly from the work done to date on the 22” rig. On the original “100 percent Geometry” analyses, the average tip clearance calculated from experimental measurements was used. For the subsequent “85 percent Geometry” analyses, the skewed tip gap as actually measured in the rig was accurately modeled. Results from these sets of analyses show only minor differences, as has been previously documented. The conclusion is that the skew in the tip gap has little influence. While this conclusion is somewhat contaminated by the fact that both the blade geometry as well as the tip gap were changed at the same time, the chance that each is a significant influence and just happen to cancel each other out is remote.

The conclusion is that the tip gap must be modeled with reasonable accuracy for the QHSF I, but it is not a strong driver on the blade’s stability. Note that this conclusion does not agree with the stability trends of other fan blades analyzed recently at Honeywell, such as the Baseline I fan. The root cause for the difference may lie in the basic geometry of the QHSF I design. Figure 8 compares the static pressure field for the Baseline I fan and the QHSF I. Both of these plots are for a radial station near the tip (but below the tip gap) at near stall conditions. As the plots indicate, the pressure across the blade tip is significantly less in the QHSF I design due to the shock still being captured in the passage due to the forward sweep. It is this pressure difference that will be the driving mechanism for tip leakage flows, and determine the importance of the tip gap. With less of a pressure difference, the QHSF I has a lower sensitivity to clearance effects.

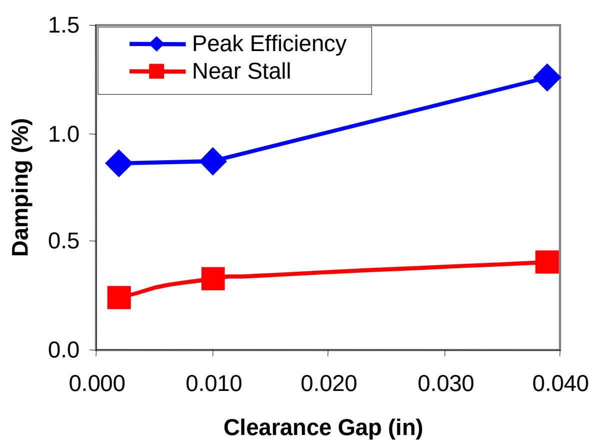

Figure 7. **Change in Aerodynamic Damping as a Function of Tip Clearance. These Results Were Obtained From the Analysis of the 18” Rig at 85% Speed for the 2 Nodal Diameter Forward Traveling Wave.**

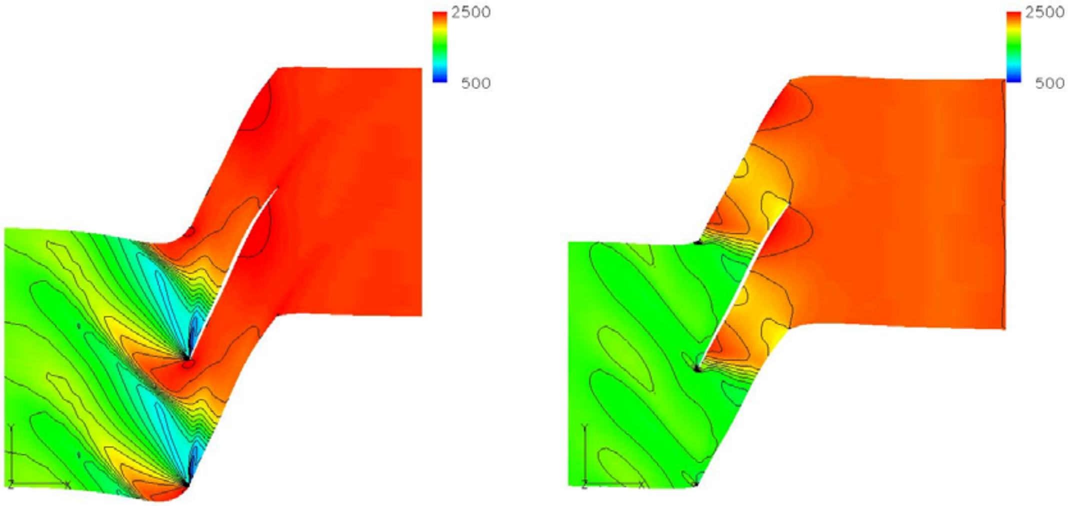

Baseline I QHSF I

Figure 8. Comparison of the Static Pressure Fields of the Baseline I Fan and the QHSF I. The Difference in Pressure Across the Blade Tip Is Significantly Larger for the Baseline I Fan and, as a Result, This Design Is More Sensitive to Changes in Tip Clearance. These Sections Are Slightly Below the Blade Tip, at 85% Speed, Near Stall Conditions.

3.3 Mode Shape Sensitivity

The sensitivity of the TURBO results to the assumptions used is the mode shape calculations was evaluated. The first mode vibration shapes with the following hub boundary conditions were calculated with ANSYS:

- Root fixed in all directions
- Dovetail fixed in all directions
- Dovetail fixed in local normal direction
- Disk cyclic symmetry

The results of each of the analyses are presented in Figure 9 to Figure 12.

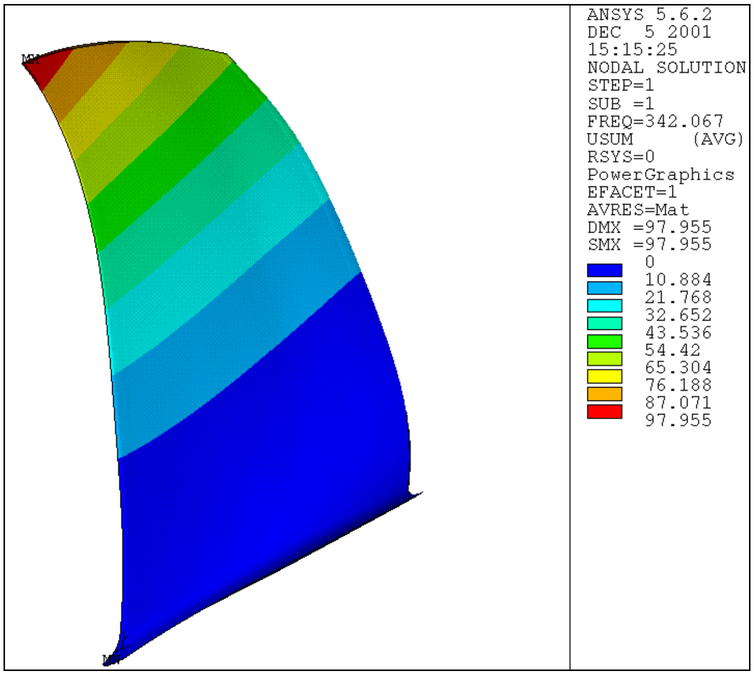

Figure 9. The QHSF I ANSYS Airfoil Only Analysis With Root Fixed in All Directions Calculated a First Mode Frequency of 342 Hz.

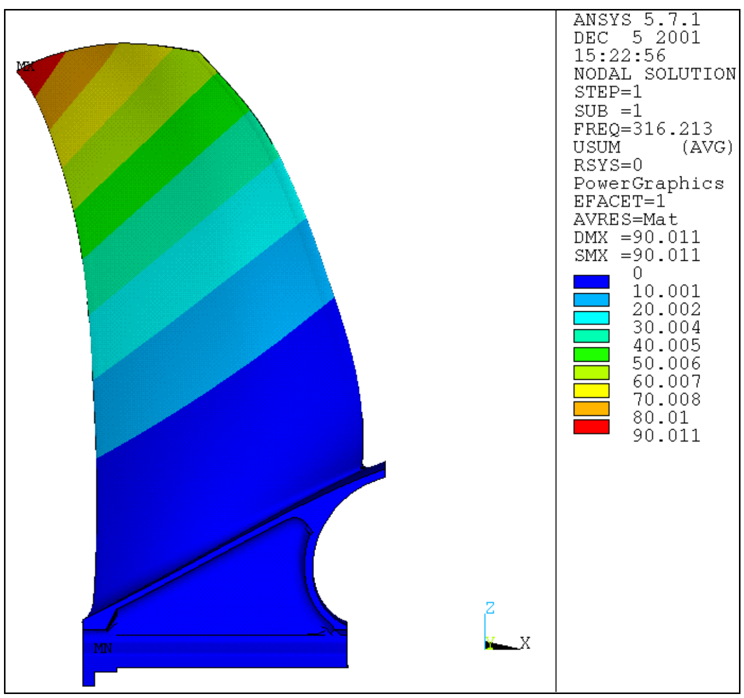

Figure 10. The QHSF I ANSYS Airfoil and Platform Analysis With the Dovetail Fixed in All Directions Calculated a First Mode Frequency of 316 Hz.

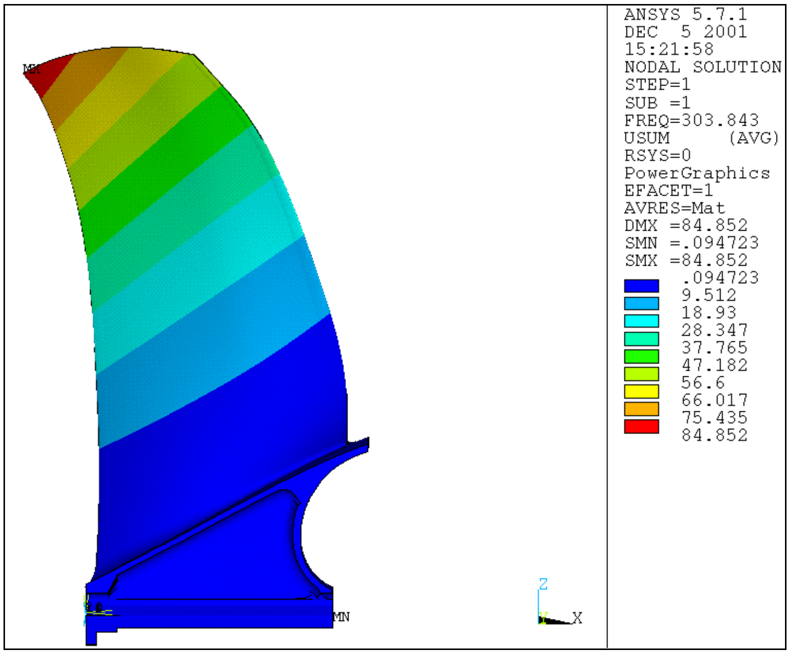

Figure 11. The QHSF I ANSYS Airfoil and Platform Analysis With the Dovetail Fixed in Local Normal Direction Calculated a First Mode Frequency of 304 Hz.

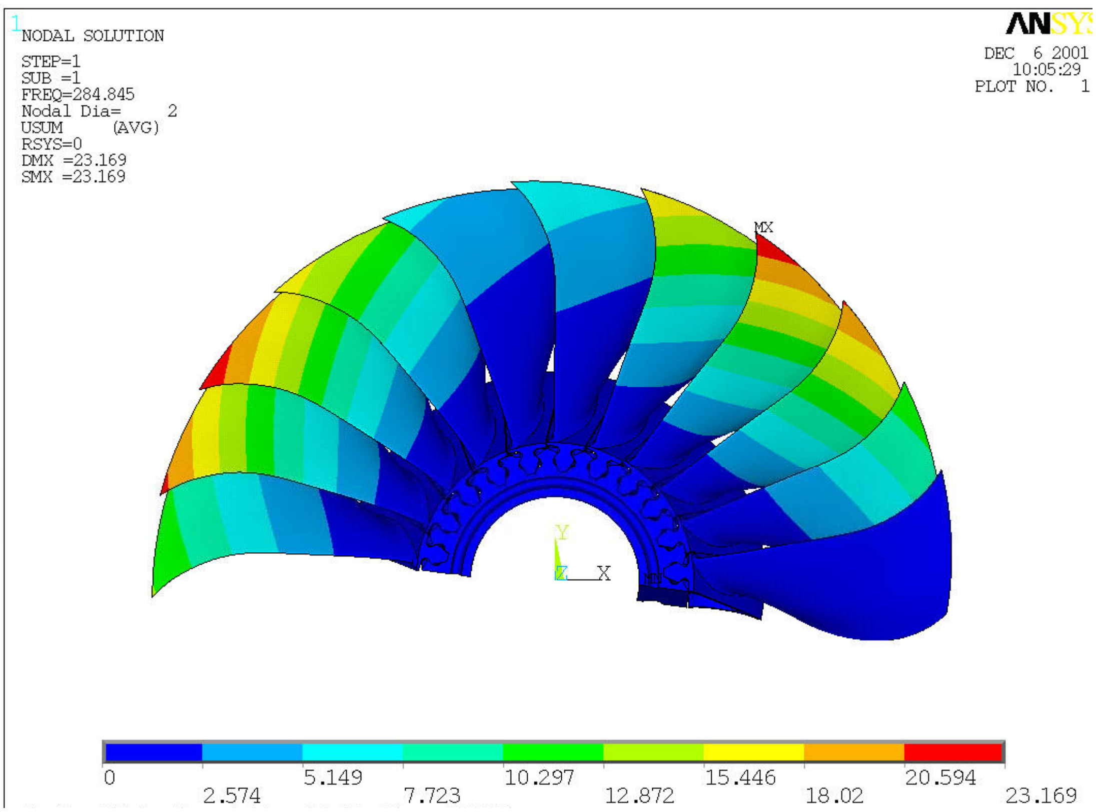

Figure 12. The QHSF I ANSYS Airfoil, Platform & Disk Analysis With Disk Cyclic Symmetry for the Nodal Diameter = 2 Case Calculated a First Mode Frequency of 285 Hz.

The effects of changes in mode shape on TURBO aerodynamic damping was examined. Figure 13 shows the results for the viscous, 85 percent speed, near-stall, 2 nodal diameter forward travelling wave case using 5 different mode shape models from ANSYS. Very small differences in the calculated aerodynamic damping are seen. Figure 14 shows that a similar trend can be seen for calculations at all inter-blade phase angles. During design iterations, it will be possible to use the simpler airfoil-alone model to calculate mode shapes for TURBO aeroelastic analysis.

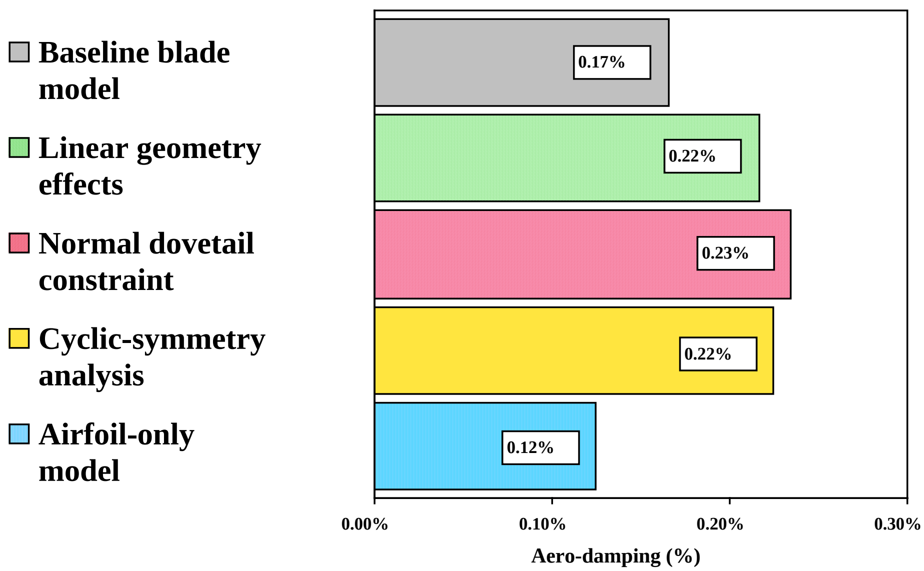

Figure 13. Results of the TURBO Mode Shape Study Show Little Sensitivity to the Assumptions Used for Calculation of the Mode Shapes.

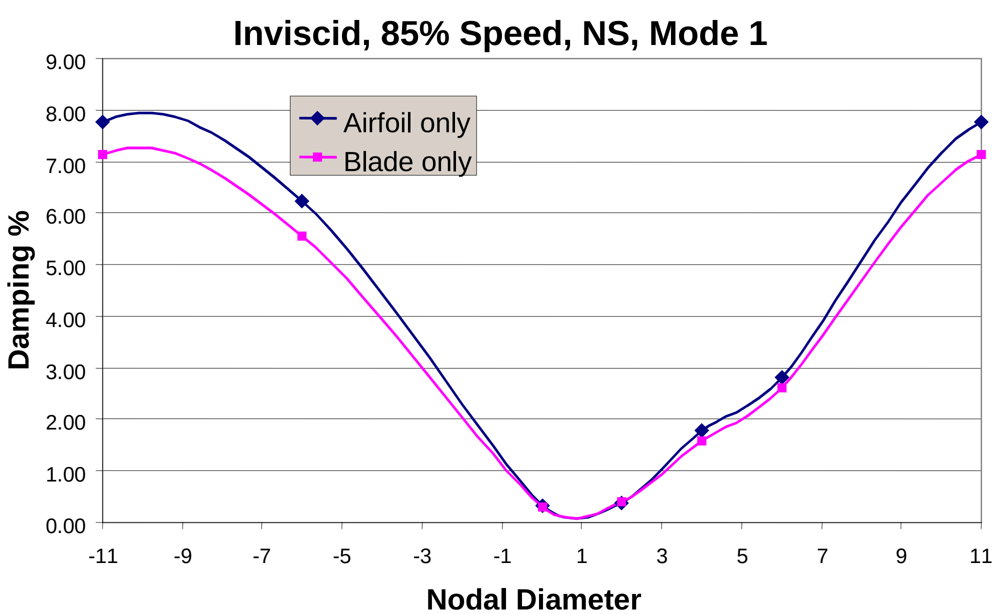

Figure 14. The Full Blade Model Showed Little Difference in Aerodynamic Damping as Compared to the Airfoil Only Model.

3.4 Boundary Condition Sensitivity

Because previous studies have shown a high sensitivity to inlet total pressure profile effects and especially the shroud inlet boundary layer (Reference 10), care was taken in the analysis to accurately capture this profile and account for changes with speed. To determine the significance for the present fan design, the analysis was re-run with a uniform inlet profile and also by specifying radial equilibrium at the exit rather than the experimentally-obtained exit profile of static pressure. In Figure 15, the dashed line indicates the damping at different positions along the 85 percent speed line using the experimental profiles. The triangles denote solutions with other assumptions for the inlet and exit profiles, and are seen to lie very near the dashed line. These results indicate that the profile changes do affect the damping to a small degree, but are attributed primarily to the change in position on the fan map.

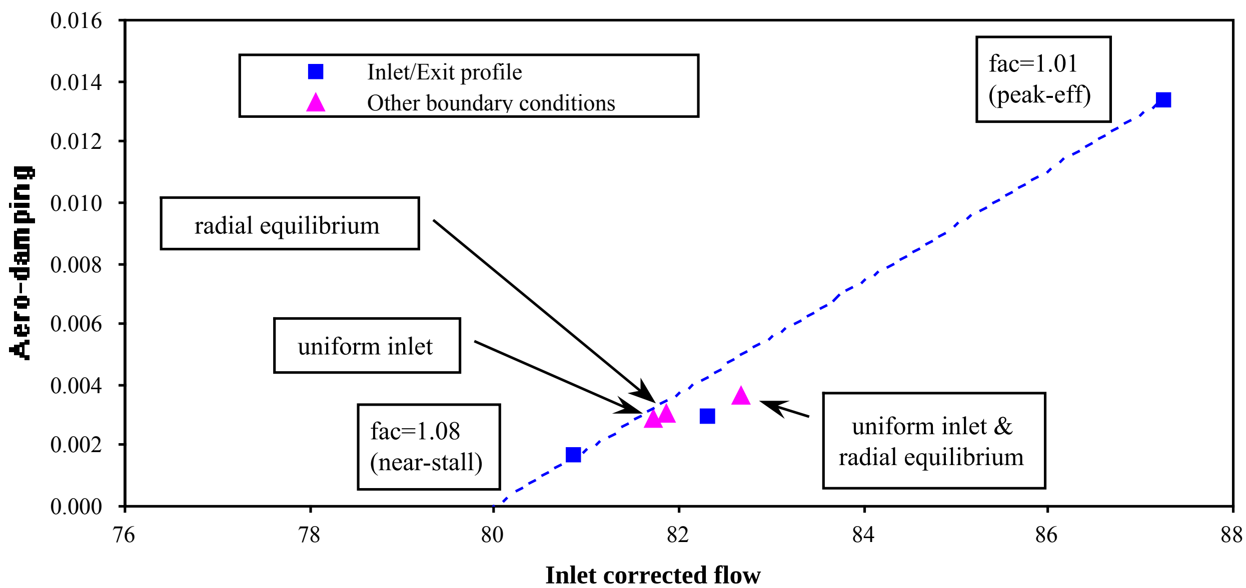

Figure 15. Changes to the Inlet and Exit Pressure Profiles Have Only a Minor Effect on the Predicted Damping.

3.5 Part Speed Geometry Sensitivity

One detail of the analysis that was initially thought to be crucial for accurate predictions of the flutter boundary was the use of part speed geometry. The airfoil geometry was updated at each speed to reflect the actual deflections due to the speed and other loads. This refinement is in contrast to simply using the fully hot design shape for all speeds. To evaluate whether this refinement is necessary, the analysis at 85 percent speed was repeated using the fully hot (100 percent speed) geometry. Results demonstrate that the effect on the damping calculation is small over the entire ND range. The fan map shown in Figure 16 indicates that the change in steady solutions is also fairly minor, while the resulting extrapolation of the flutter boundary is slightly affected but not substantially. The impact of using part-speed geometry is minimal and is of importance only in cases that require the very highest accuracy in the prediction of the flutter boundary, such as a final design verification or a correlation effort.

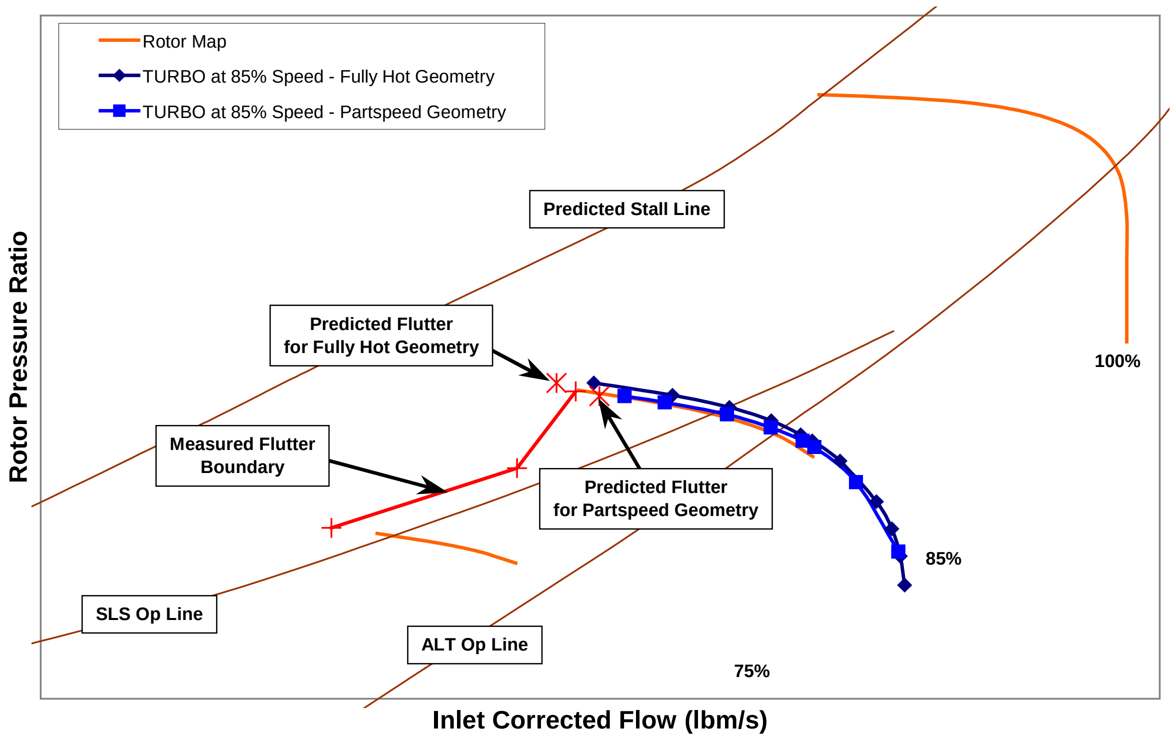

Figure 16. Effect of Part-Speed Geometry on Steady Solutions and Flutter Boundary.

3.6 Comparison With QHSF I Data

A TURBO part-speed geometry analysis, with the 85 percent speed geometry and skewed tip gap, was completed for 85 percent speed line for the QHSF I rotor. Figure 17 shows the convergence of aerodynamic damping with cycle count for the near-stall condition for various nodal-diameter modes. It can be seen from the picture that all modes were adequately converged.

Figure 18 shows a plot of the aerodynamic damping as a function of the nodal diameter number of the traveling wave. It can be seen that the location of the minimum damping is consistent with the measured results and the use of the 85 percent vs. 100 percent hot shape geometry had little effect on the results.

Figure 19 shows the 18”-fan operating map scaled to 22” size, the predicted steady speed line from TURBO at 85 percent, and the projected location of aeroelastic instability from TURBO. The predicted instability agrees well with the measured instability line.

To help understand the reasons for the change in damping when approaching stall, the distribution of damping on the surface of the blade was considered. Figure 20 shows the damping distribution at the least stable nodal diameter, ND (+2) at 85 percent speed. Correlating this plot with that for Mach number distribution, we find that regions of significant damping are strongly tied to shock location. At peak efficiency (PE) conditions, the passage shock runs roughly from mid-chord of the pressure surface to near the trailing edge of the suction surface of the adjacent blade. This is demonstrated in Figure 20a by the Mach number contours in the blade-to-blade view at 90 percent span. (The shock locations have been highlighted in this plot.) From Figure 20b, a significant region of positive damping is associated with the shock on the pressure surface, while Figure 20c shows a region of negative damping associated with the shock on the suction surface. For near-stall (NS) conditions, Figure 20d gives the shock location at 90 percent span. Figure 20e shows that as the shock moves forward the positive damping region follows it and is now at the blade leading edge. The suction surface plot in Figure 20f indicates that the de-stabilizing region has moved forward from the trailing edge to mid-chord, and has grown in strength relative to PE conditions. It is interesting to note that the loss of stability in throttling from PE to NS is due to nearly equal changes in damping on each surface. Similar plots for the most stable ND (11), not included here for brevity, indicate the de-stabilizing regions of Figure 20 become stable, while stable regions become more stable and larger in extent.

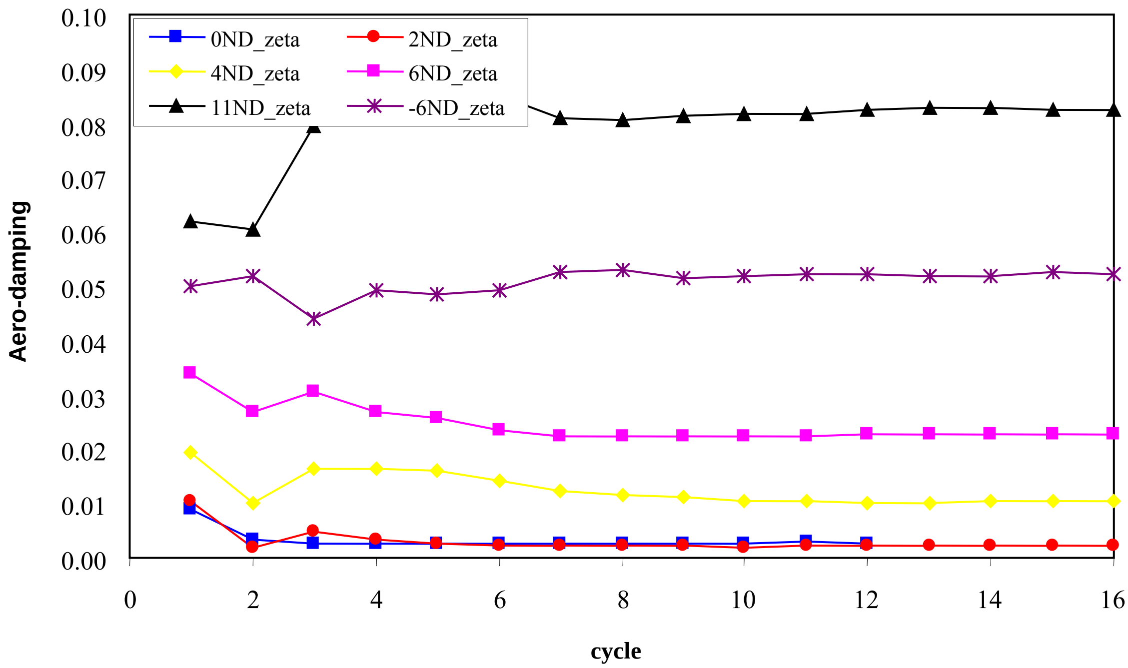

Figure 17. The TURBO Calculation Near Stall for the 100% Speed Line Shows Good Convergence on the Aerodynamic Damping.

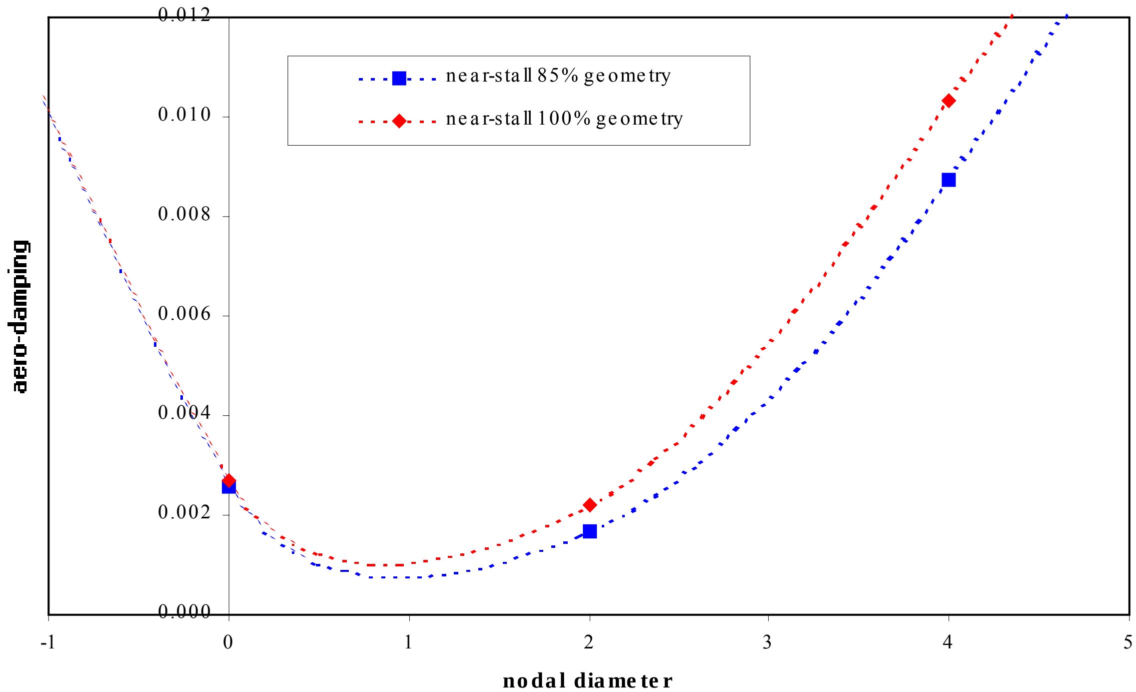

Figure 18. The TURBO Analysis Identified the Nodal Diameter Wave With Minimum Damping.

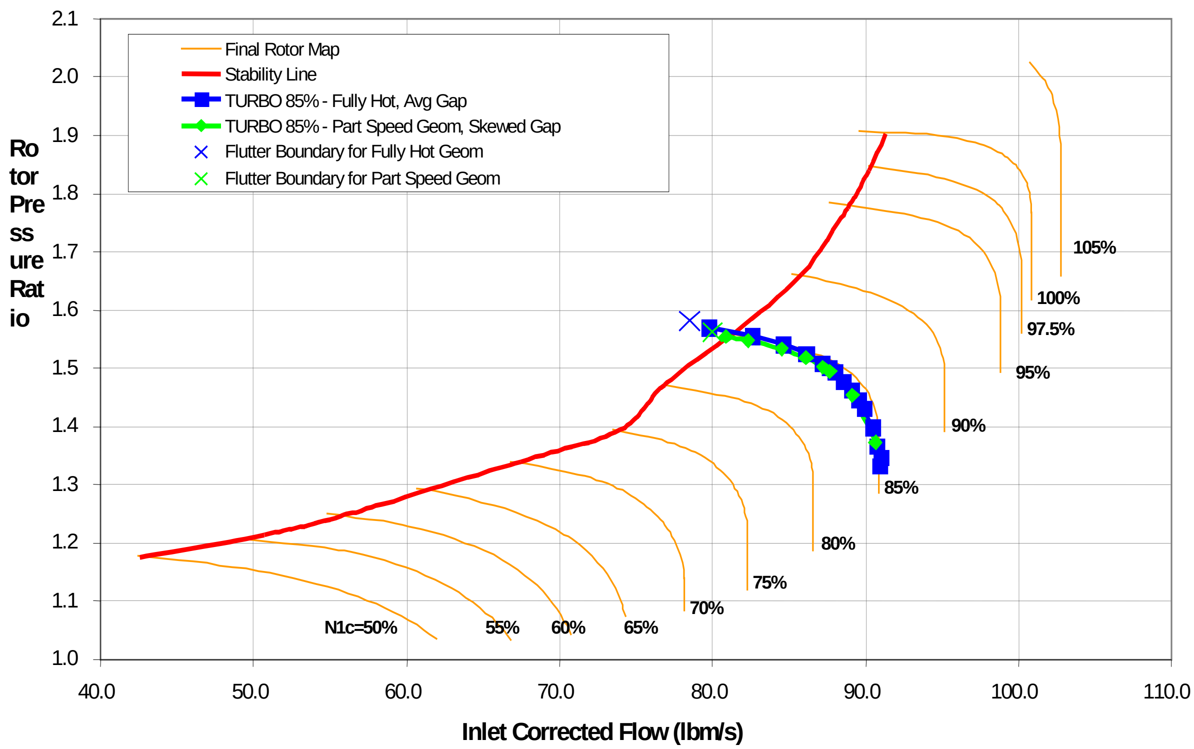

Figure 19. TURBO Predicted the 85% Speed Line Instability Point With Reasonable Accuracy.

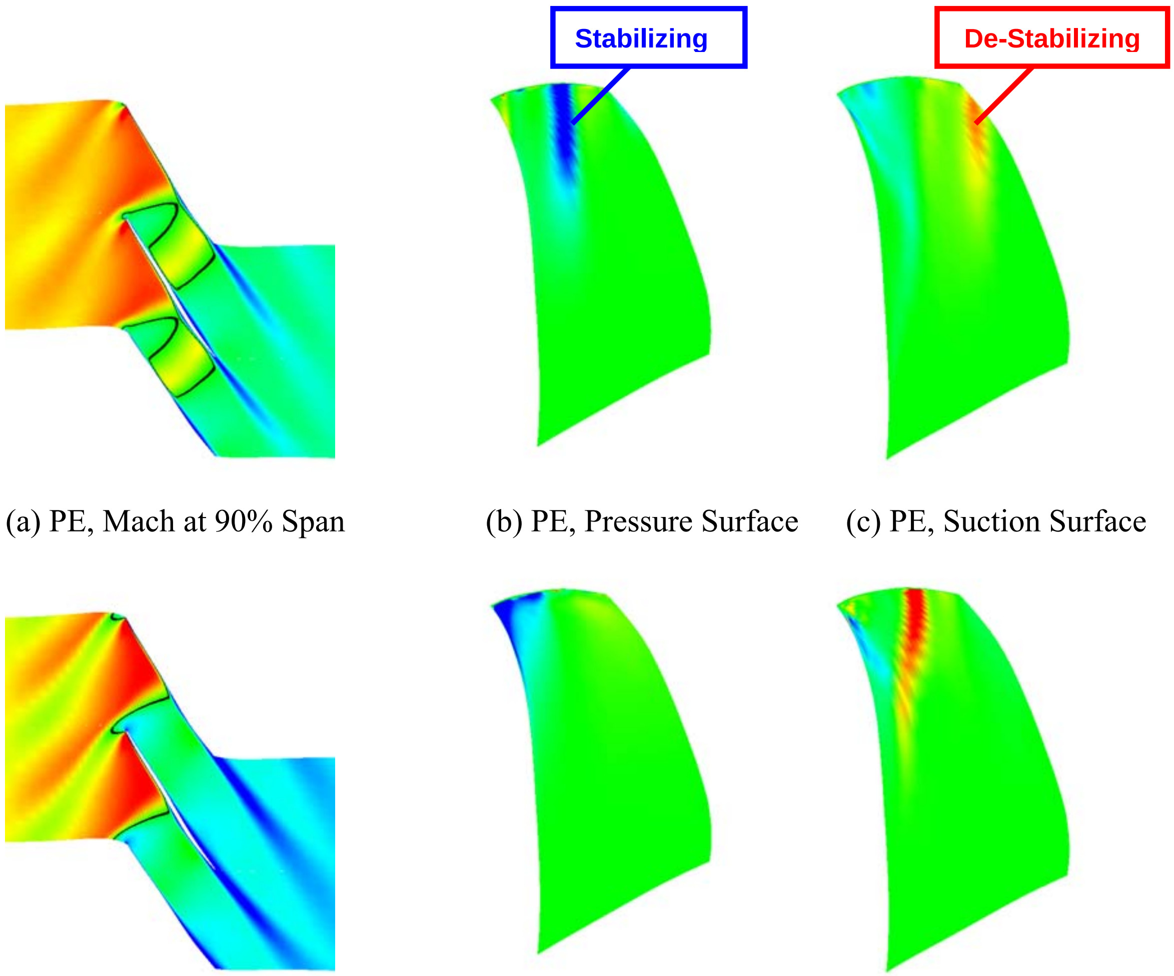

(a) PE, Mach at 90% Span (b) PE, Pressure Surface (c) PE, Suction Surface

(d) NS, Mach at 90% Span (e) NS, Pressure Surface (f) NS, Suction Surface

Figure 20. Distribution of Aerodynamic Damping on Blade Surfaces.

The QHSF I rotor aeroelastic behavior at 75 percent speed was calculated with TURBO. Inviscid analysis was used to screen the important inter blade phase angles (IBPA) and modes. Viscous analyses were performed at the IBPAs where the damping was low in the inviscid analysis. Results are shown in Figure 21 for both the peak efficiency (PE) and near stall (NS) points. A reasonable prediction of flutter boundary was obtained, though not as good as 85 percent speed. Mode 1 was predicted as critical, but mode 3 damping was always extremely low.

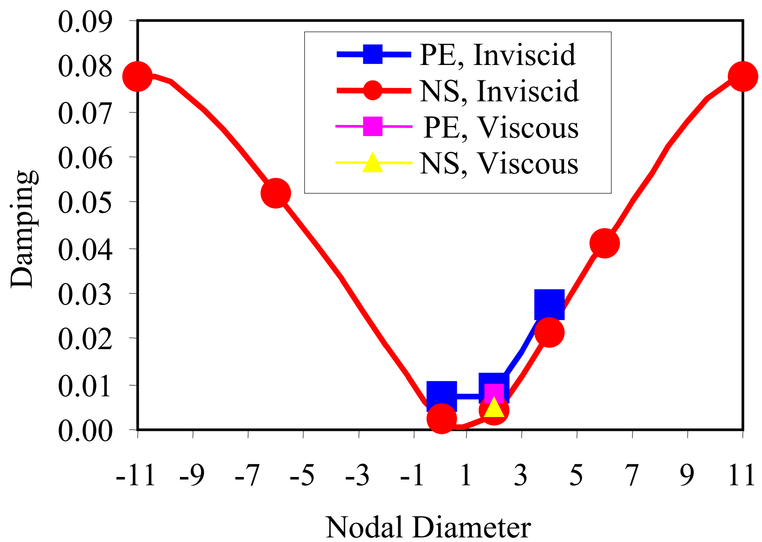

(a) Mode 1 (first bending)

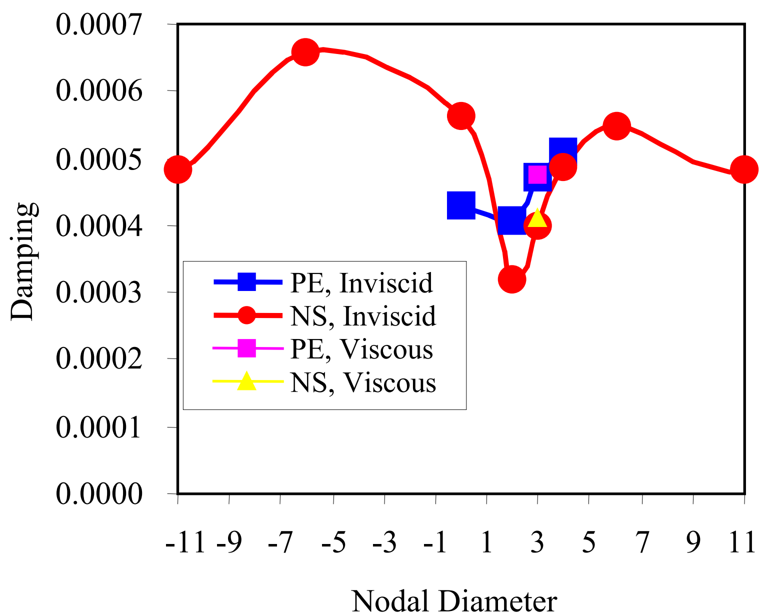

(b) Mode 3 (first torsion)

Figure 21. TURBO Damping Results for the QHSF I on the 75% Speed Line.

Figure 22 provides a summary of the stability line calculations for the two part speed cases.

The 100 percent speed line performance map was generated with TURBO-AE by the NASA Glenn staff. The calculated map differences are consistent with differences observed for stage data between the 22-inch and 18-inch scale rigs as shown in Figure 23. These results are consistent with the previous analysis from the 75 percent and 85 percent speed lines and Honeywell's experience. This difference in not considered an issue considering the analysis accuracy.

The flutter prediction for 100 percent speed line was completed with TURBO-AE by the NASA Glenn staff. Mode 1 analyzed for several nodal diameter patterns. It was determined that the 2 nodal diameter pattern was least stable near stall, whereas the 0 nodal diameter was least stable near the peak efficiency point as shown in Figure 24. Extrapolation of the data showed that the predicted flutter boundary was beyond the stall line, consistent with the measured data. To determine if the difference in the predicted vs. measured flow made a difference in the flutter prediction, the speed line calculated by TURBO-AE at 100 percent speed was shifted to match at the peak efficiency point (see Figure 25). Even after accounting for the shift in performance map, the predicted flutter boundary lies beyond stall line.

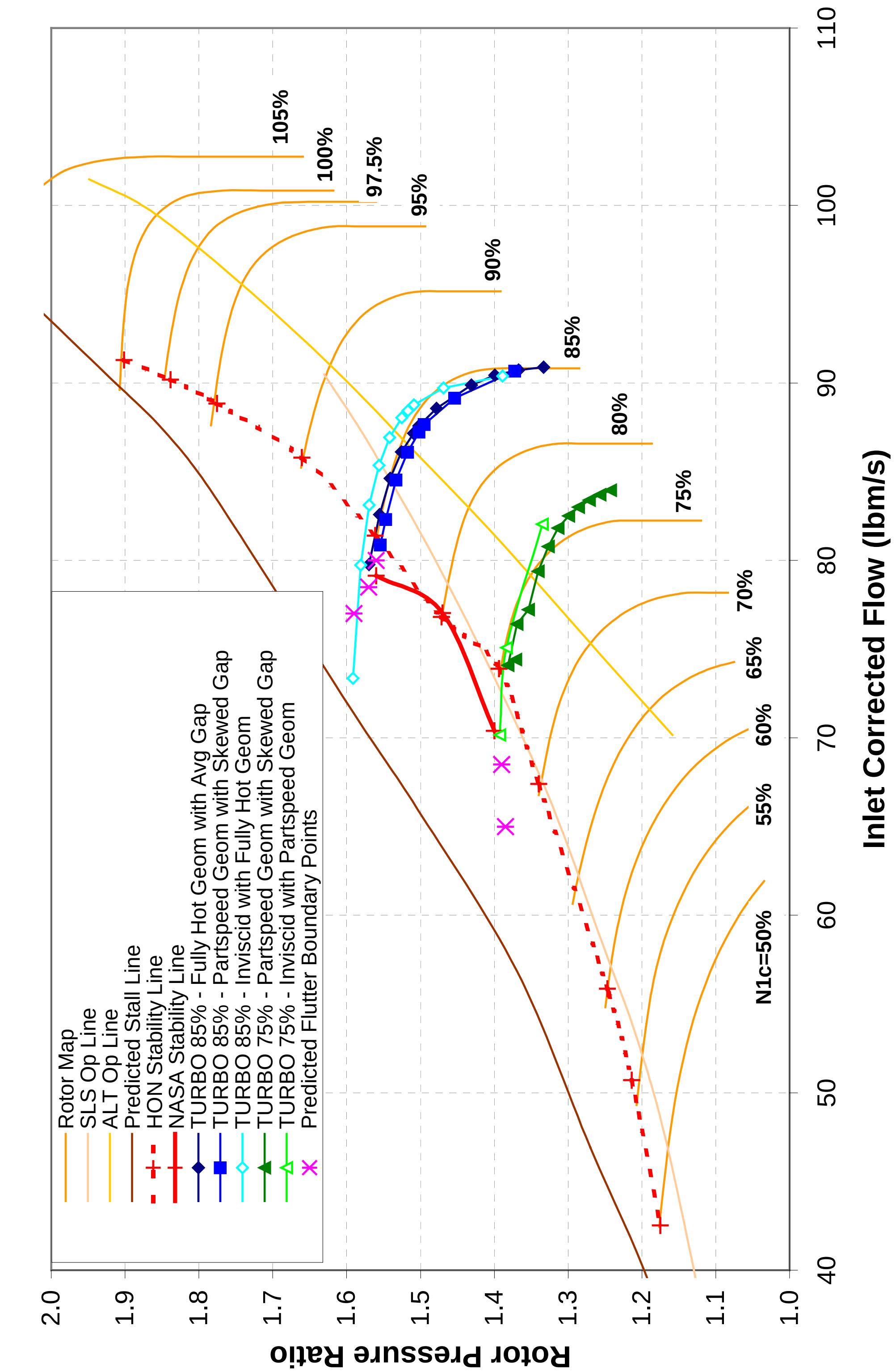

Figure 22. Summary of Stability Predictions for the 85% and 75% Speed Lines.

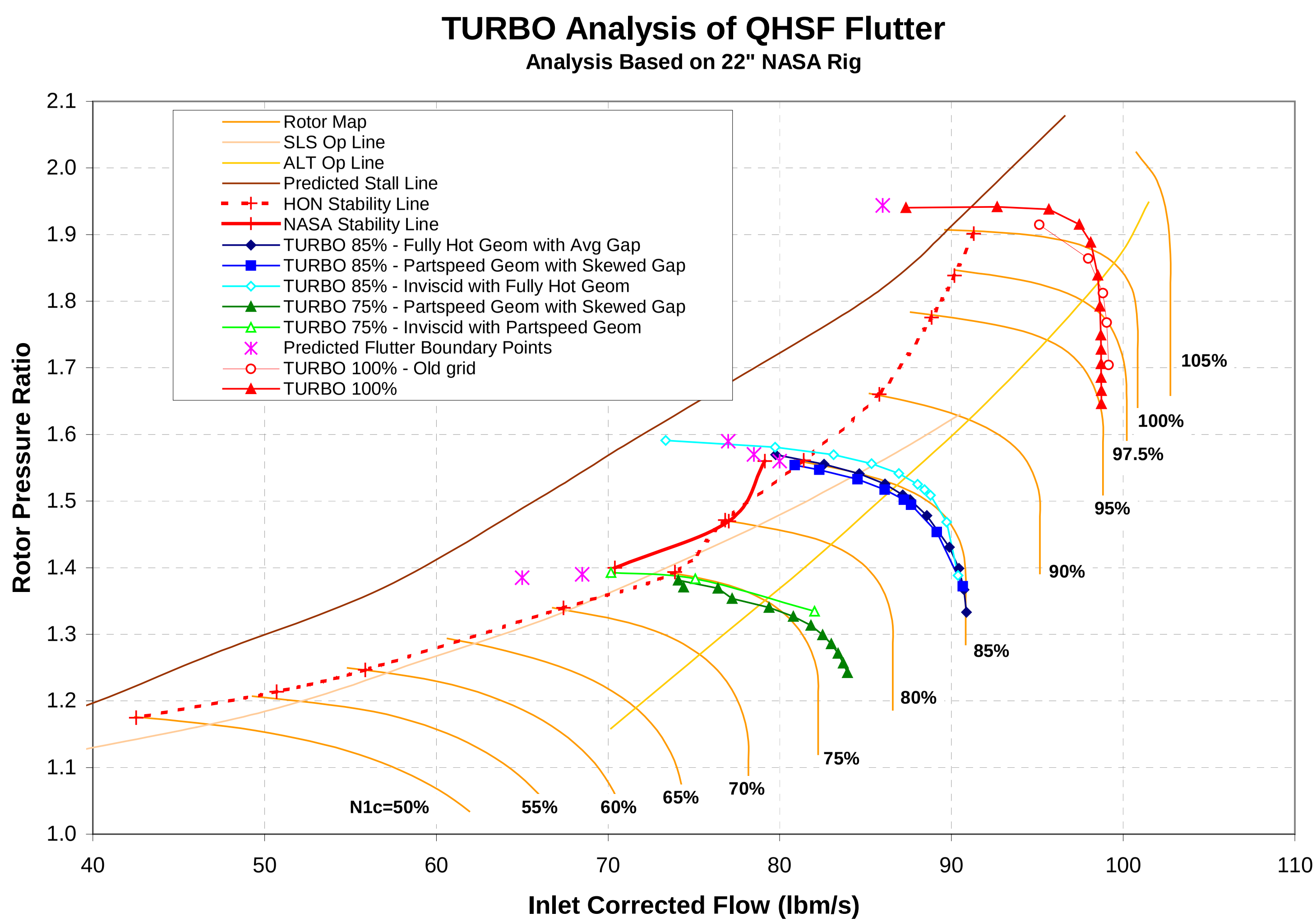

Figure 23. The TURBO-AE Steady Calculation at 100% Speed Has Been Added to the Performance Summary Map.

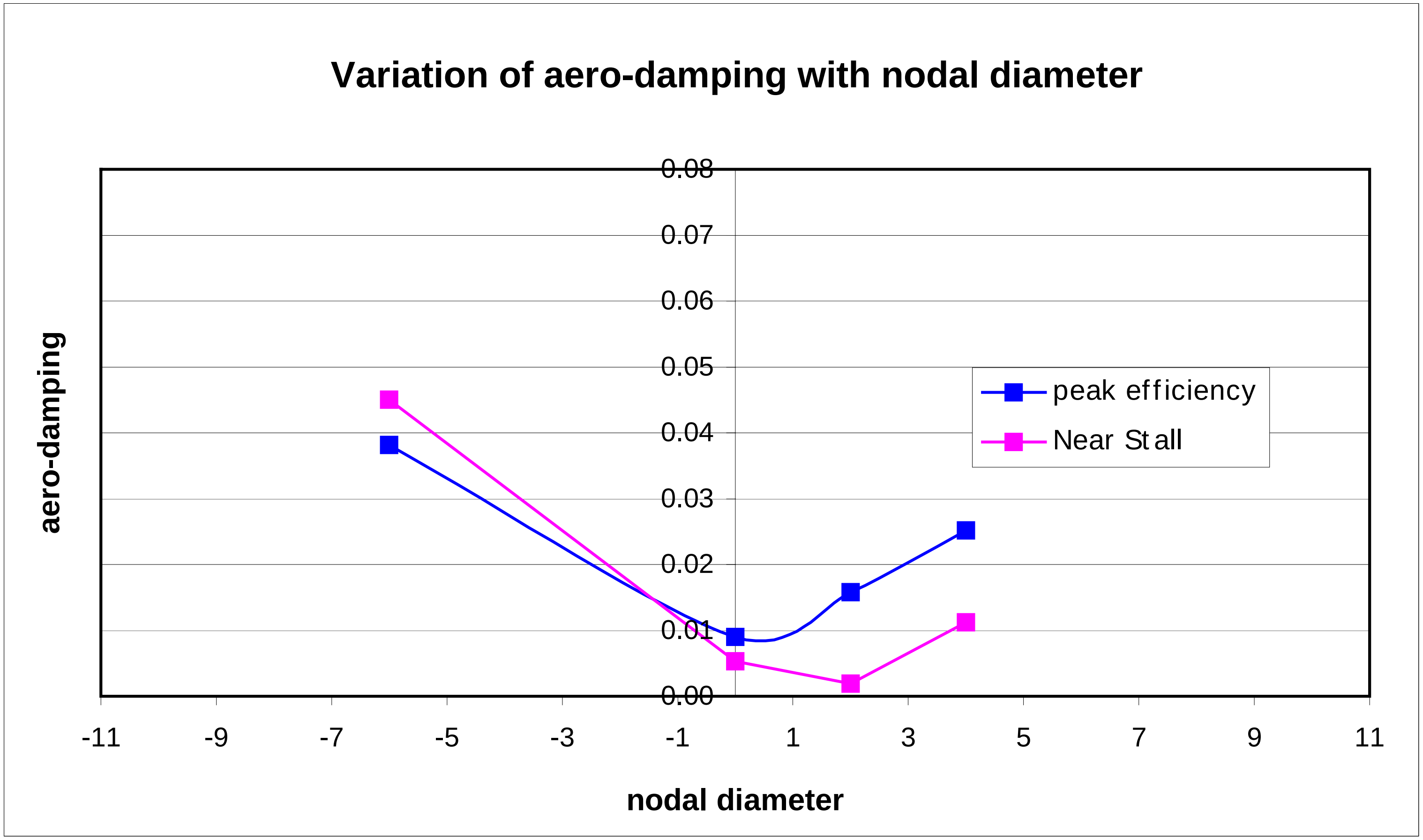

Figure 24. The TURBO-AE Analysis Shows That the Minimum Damping Occurs for the 2 Nodal Diameter Pattern Near Stall at 100% Speed.

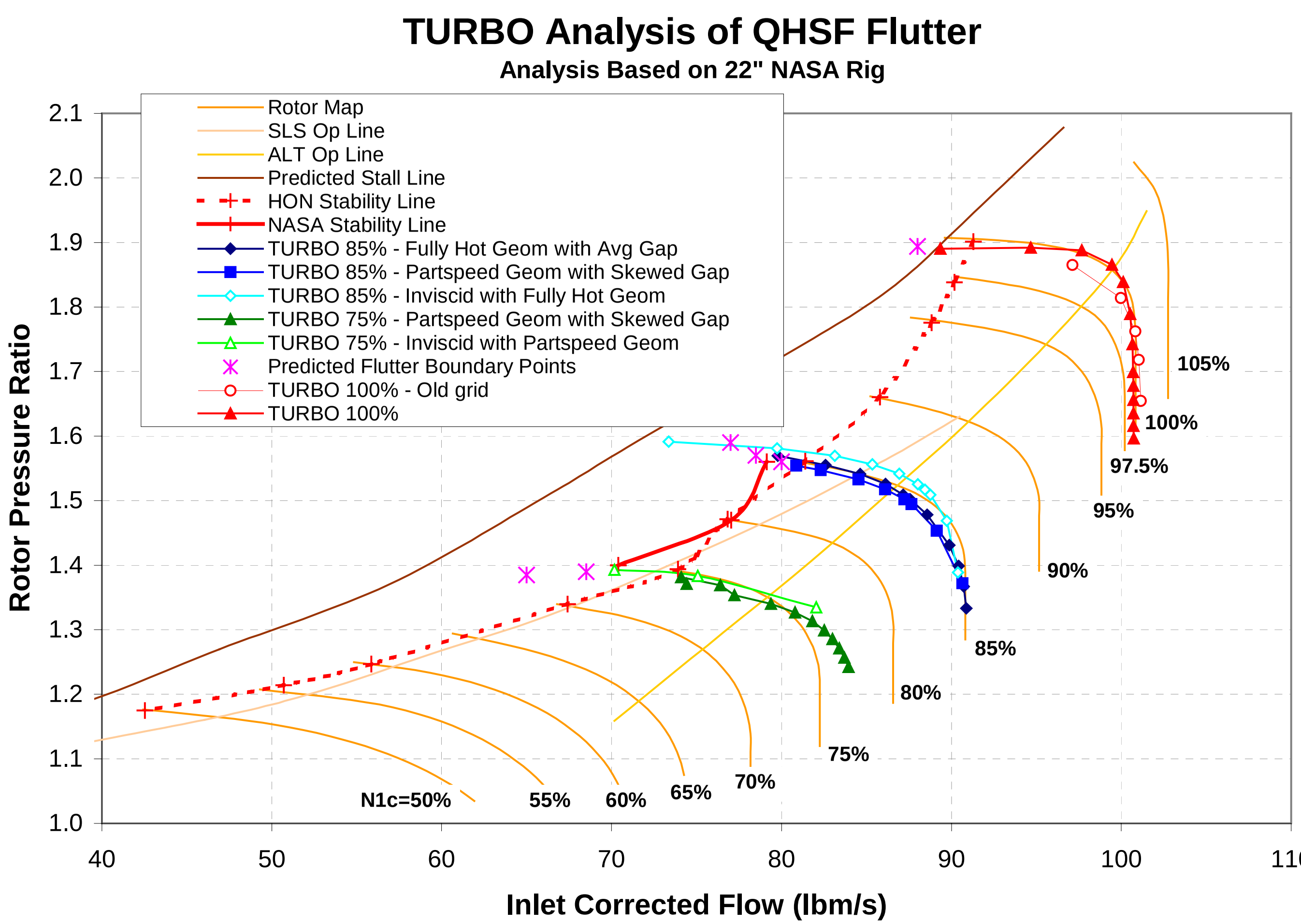

Figure 25. Adjusting of the TURBO-AE Calculated 100% Speed Line to Match the Measured Speed Line at Peak Efficiency Shows That the Correct Flutter Prediction Is Maintained.

4. EVALUATION OF QHSF I TEST DATA

4.1 Evaluation of Performance Differences Between the 18” and 22” Rig Tests of the QHSF I

An attempt was made to derive a rotor-only performance map of the 22” QHSF I rig, since the rotor performance was not directly measured in the test. It was thought that data from the 18” rig could be used to estimate the rotor-only performance from the 22” test. An assessment of the differences between the QHSF I aerodynamic performance in the Honeywell 18” rig (Reference 1) and the NASA 22” rig (Reference 11) tests was conducted. This assessment was motivated by the differences in aeroelastic performance of the 18” and 22” rig tests of the QHSF I as summarized in Table 5.

Table 5. The Summary of Aeroelastic Results Identify the Differences Between the 18" and 22" Rigs.

Speed	HON (18" diam)	NASA (22" diam)
50%	Mode at 860 Hz (system umbrella mode?) response >1000 ue. Occurs near stall.	Reached predicted stall line.
55%	Mode at 860 Hz (system umbrella mode?) response >600 ue. Occurs above op line.	Reached stress limits before hitting predicted stall line. No component of flutter (all forced response / SFV).
60%	Responses in 125-350 ue range in Modes 2 & 3.	Reached stress limits before hitting predicted stall line. No component of flutter (all forced response / SFV).
65%	Mode 2 NSV predominates.	Reached stress limits before hitting predicted stall line. No component of flutter (all forced response / SFV).
70%	Mode 2 NSV up to 900 ue near op line at 737 Hz. Increase to 72% speed resulted in rapid onset of flutter in Mode 1, with amplitudes exceeding 2000 ue at 350 Hz.	Reached stress limits before hitting predicted stall line. No component of flutter (all forced response / SFV).
75%	Mode 1 flutter up to 2000 ue on op line in 2 ND FTW. At lower pressure ratio, modes 1, 2 and 3 all exhibit moderate levels of NSV (125-450 ue).	Mode 3 (926 Hz) NSV identified during data reduction, 3 ND FTW. Levels are low, up to 130 ue-SA. Forced response from 1/rev up to 200 ue.
80%	Mode 1 flutter just above op line, in 2 ND FTW. Levels are in 500 ue range at steady state data point, higher transiently.	Mode 1 flutter identified during data reduction, 2ND FTW. Levels are low, up to 70 ue-SA. Overall signal dominated by forced response from 1/rev, up to 180 ue.
85%	Mode 1 flutter above op line. 2 ND FTW. Levels reach 700 ue at 385 Hz at steady state data point, higher transiently.	Mode 1 flutter observed at 308 Hz, up to 497 ue-SA. 2 ND FTW. Forced response from 1/rev up to 240 ue.
90%	Mode 1 flutter above op line. 2 ND FTW.	Reached stress limits before hitting predicted stall line. No component of flutter (all forced response / SFV).
95%	Mode 1 flutter above op line. 2 ND FTW.	Reached predicted stall line.
100%	Reached predicted stall line.	Reached predicted stall line.

Figure 26 is the full map of the work characteristics of the 18" and 22" QHSF I fan rigs and Figure 27 is a detail of the 100 percent speed line. The work characteristics are different between the two fans, which verifies the rotor is setting the choke flow. It is possible that as the back-pressure was lowered, the rotor work, efficiency, and pressure ratio became low enough to send the stator enough corrected flow that it choked as well. Unfortunately, the stator choke behavior cannot be proven from the data.

The performance differences are consistent with aeroelastic differences, which may suggest a different hot running shape between the 18” and 22” blades. Also, it is noted that for the two rigs to operate at the same operating line, the 18" rig is running further from choke and most likely at higher incidence levels. This difference in incidence levels may explain the changes in aeroelastic behavior.

There does not appear to be an effective way to get to the 22" rotor-only performance by extracting the stator performance from the overall stage performance. Stator loss buckets are typically defined based on incidence or inlet corrected flow. Stator loss data is not available for the 22" rig, and it would be questionable to assume that the 18” and 22” vanes are the same and back out the rotor from the stage. It would have to be assumed that the loss buckets are a function of exit corrected flow (instead of inlet conditions) and there is no way to quantify this error. Also, the stator performance is a function of the span-wise distribution of loss. It is likely that since the rotor performance is different, the stator inflow was not the same. It would be a significant effort, using several non-quantified assumptions, to derive a 22" rotor-only performance map.

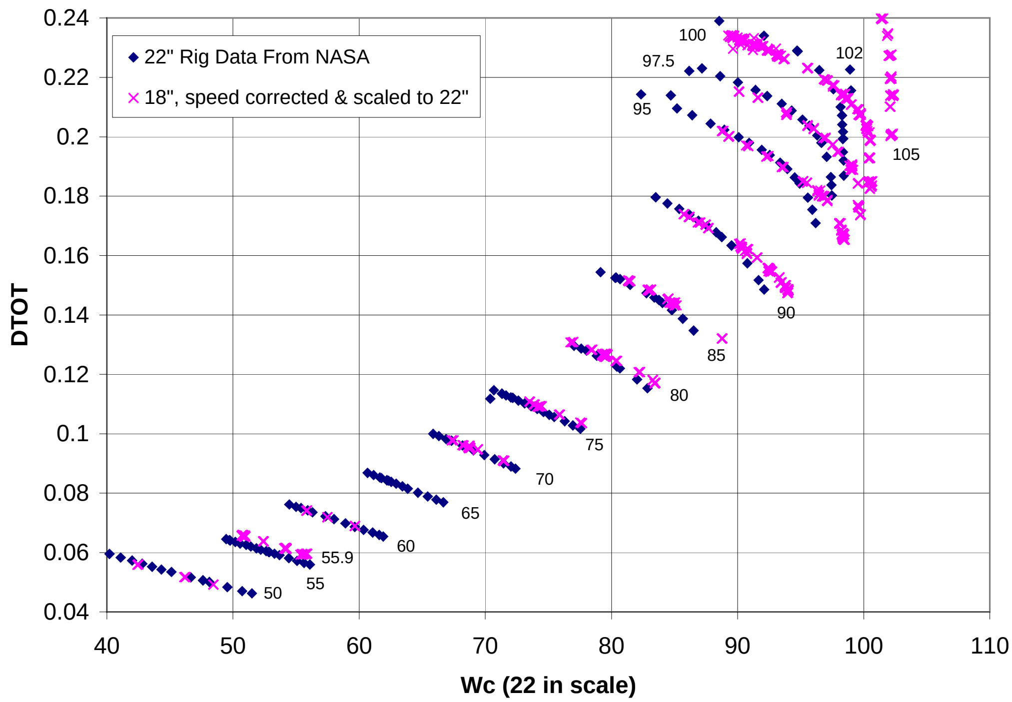

Figure 26. A Comparison of the 18” and 22” Rig Data Shows Differences in the Fan Stage Work Performed.

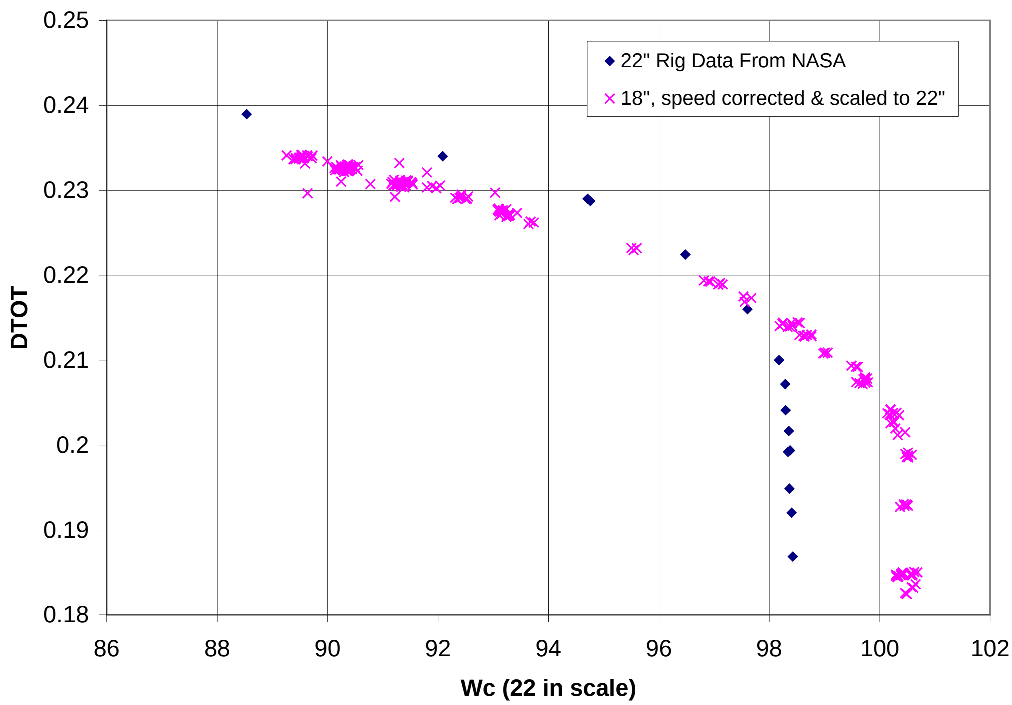

Figure 27. Detailed Examination of the 100% Speed Line Shows That the 18” QHSF I Reached a Higher Choked Mass Flow Than the 22” QHSF I.

In order to resolve the question of geometric scaling and potential “non-linear” effects on the hot shape deflection pattern of the blade, a full blade ANSYS model was run. Both the 22” and 18” rig sizes were assessed, with the geometry scaled using an available command in ANSYS. All analyses were at 100 percent speed, with the speed for the two rig sizes adjusted by the inverse of the geometric scale factor. Both linear and nonlinear analyses were conducted, as well as cases with and without gas loads and temperatures (i.e., speed only). The linear cases were run primarily as a check on the scaling operation, since these results must scale by definition. Cases without gas loads were run with uniform room temperature. Cases with gas loads were run with the aerodynamic design point (ADP) pressure distribution and a radial temperature profile corresponding to these conditions. Note that the identical pressure distribution and temperature profile was applied to both rig sizes.

The results for six analyses are tabulated in Table 6. The physical displacements (the magnitude of the displacement, in inches) at the tip leading edge (LE) and trailing edges (TE) are provided for each run, and then these are normalized by the tip radius of each rig size. The resulting normalized values for corresponding loadings are identical. While only the tip displacements are summarized here, other locations on the airfoils also exhibit the same behavior.

Table 6. **Effect of Geometric Scaling on Hot Blade Shape. Table Lists Displacements at LE and TE of Tip for Several Loading Alternatives. The Displacements for Each Rig Size, When Normalized by Tip Radius Are Identical for Corresponding Cases.**

Rig Size	Gas Loads	Temps	Solution	Disp at Tip LE, in	Disp at Tip TE, in	Norm Disp LE	Norm Disp TE
22	no	RT	linear	2.1233	1.2328	.1930	.1121
22	no	RT	nonlinear	0.4428	0.2410	.0403	.0219
22	ADP	ADP	nonlinear	0.4004	0.2068	.0364	.0188
18	no	RT	linear	1.7131	0.9946	.1930	.1121
18	no	RT	nonlinear	0.3573	0.1944	.0403	.0219
18	ADP	ADP	nonlinear	0.3230	0.1669	.0364	.0188

The conclusion from this study is that the identical hot shape will result from identical cold shapes if the only change is a geometric scaling. This result is true even when pressure and temperature loading is included.

Note that the relationships between physical and corrected conditions change under different ambient conditions. The deflection of the blade is driven by the physical conditions. So if the two rigs were run to the same corrected conditions at different ambient conditions, there would be a difference in the loads. This difference in ambient conditions, though, would have to be quite large to significantly affect the hot shape.

Also note that this study did not attempt to address the issue of whether the actual hardware used in each rig deflects as intended. The deflection of each size could be affected significantly by the conformance of those blades to the intended (and analyzed) nominal shape. In order to conduct such a study, detailed geometric measurements of representative sample blades in each scale would be needed, and then new ANSYS models constructed.

4.2 Evaluation of the Acoustic Results of the 22” Rig Test of the QHSF I

An assessment of the noise data from the QHSF 22” rig wind tunnel test was conducted. The purpose of this assessment was to identify the acoustic benefits (and problems) of the QHSF I design and to validate the design process for the QHSF II design. Figure 28 shows the summary of the results of the QHSF I far field noise measurements (Reference 12). Also shown on the figure are the Baseline I results and the later measurements of the Baseline I fan rotor and the QHSF I stator.

The QHSF I successfully reduced interaction tone noise for both rotor-stator and rotor-strut interaction. This tone reduction is responsible for up to 6 EPNdB reduction at higher fan tip speeds. Figure 29 presents a spectrum comparison showing the effect.

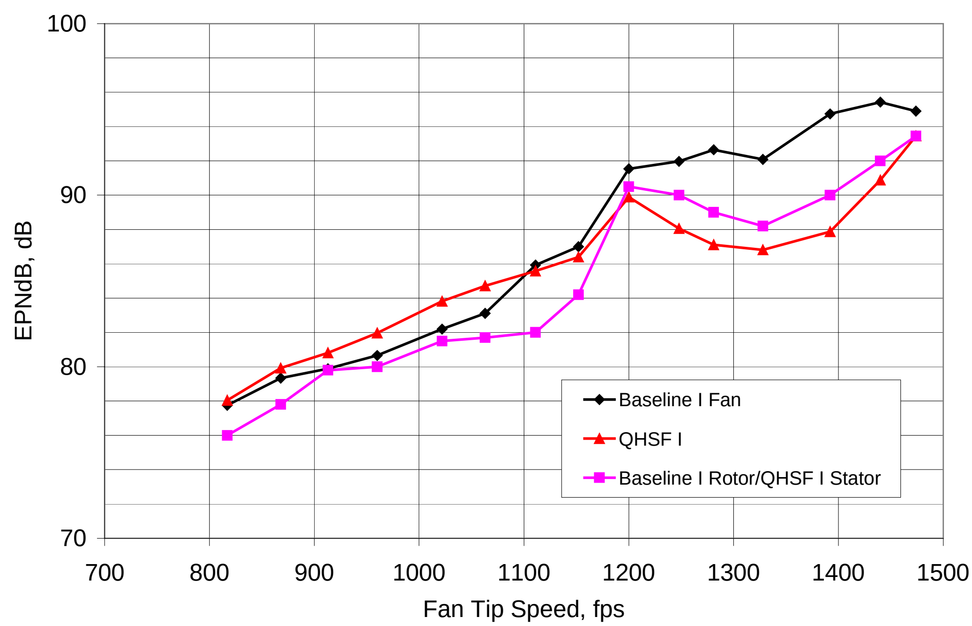

Figure 28. Results of the 22" Rig Testing Showing Dramatic Differences in Noise Levels for a 1500 ft Fly Over at Matched Thrust Conditions From the Three Fan Configurations.

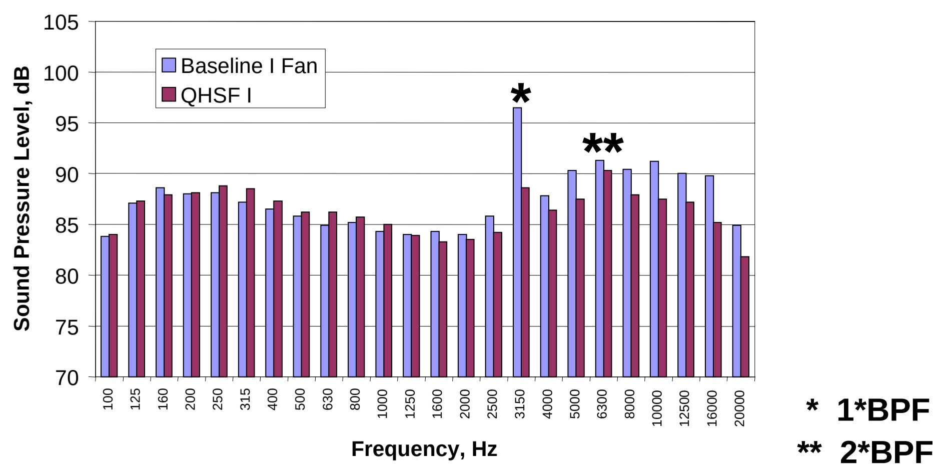

Figure 29. At Supersonic Tip Speeds, the Primary Noise Reduction Was in the Blade Passage Tone (13831 Rig RPM, 131 Degrees From the Inlet).

4.2.1 V072 Validation

A check was performed to see if V072 is a reliable prediction tool. The V072 predictions were assumed to be conservative for the original design because of the inaccurate loss profile of the Baseline I fan. Actual reductions in tones were greater than those predicted, and the general trends predicted by V072 were confirmed by test data. Figure 30 shows the results for the forward arc and Figure 31 shows the results for the aft arc.

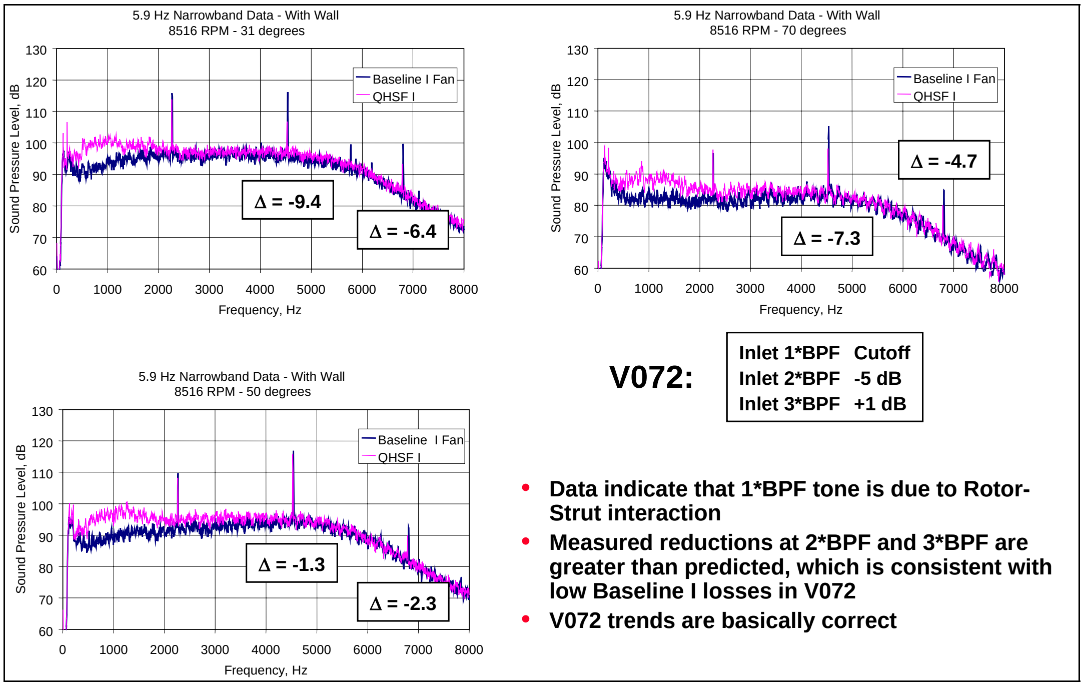

Figure 30. Comparison With Measured Narrow Band Data Shows That V072 Underestimated the Tone Noise Reduction at 2x and 3x the Blade Passage Tone at 55.5% Speed in the Forward Arc.

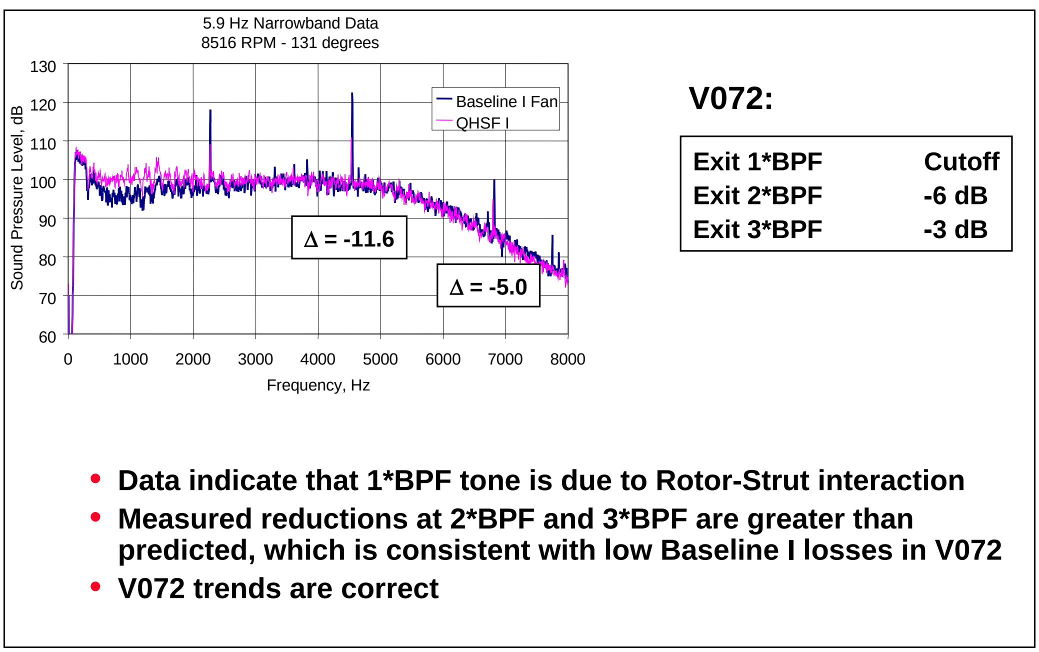

Figure 31. Comparison With Measured Narrow Band Data Shows That V072 Underestimated the Tone Noise Reduction at 2x and 3x the Blade Passage Tone at 55.5% Speed in the Aft Arc.

4.2.2 Broadband Noise Source

An unknown broadband noise source was identified in the QHSF I data that must be identified and eliminated for the redesign as shown in Figure 32. The LDV data in Figure 33 was taken during the test and shows a flow separation on the QHSF I rotor blades at 9510 RPM. The data at higher rotor speeds show little separation.

4.2.3 Comparison With CFD

The first study performed was a comparison of the measured wake structures of the Baseline I and QHSF I rotors at the LDV plane, at 81.4 percent and 90.1 percent corrected fan speed. The position of the LDV plane downstream from the rotor trailing edge is shown for both rotors in Figure 34.

The wake structure in the flow path cross-section was compared graphically, using the FIELDVIEW program. As shown in Figure 35, at both speeds, the wakes from the Baseline I and the QHSF I rotors have a similar slope throughout the inner span region. However, in the outer span region, the QHSF I wake displays more tangential lean. This increase in lean is a result of the increased distance between the rotor trailing edge and the LDV plane in the outer span region, due to the forward sweep of the QHSF I rotor. The wake rotates further tangentially through this additional axial distance, in effect having more lean than the wake in the inner span region, at the LDV plane. The aft sweep and lean of the stator leading edge further enhance this effective "lean" of the rotor wake. As a result, the QHSF I rotor wake traverses the stator leading edge much more slowly than does the Baseline I rotor wake. This behavior serves to reduce the rotor-stator interaction tone noise.

In addition to examining the graphical representation of the wake structure using the LDV data, a more detailed study of the wake profiles was conducted with the LDV measurements. Wake width and depth were compared for the Baseline I and QHSF I rotors at 81.4 percent and 90.1 percent corrected fan speed, for three selected span-wise positions (38 percent, 57.4 percent, and 78.8 percent of the rotor trailing edge span). The wake profiles were normalized by the free stream resultant velocity, and were shifted tangentially, to overlap for comparison purposes. The wakes at 81.4 percent and 90.1 percent corrected fan speed are shown in Figure 36 and Figure 37, respectively. At 38.0 percent span, the Baseline I and QHSF I wakes display very similar profiles, because the distance from the trailing edge to the LDV plane is essentially identical. Moving out to 57.4 percent span, the depth of the wake is greatly reduced for the QHSF I rotor and the width is increased, due to the increased distance from the rotor trailing edge. This trend continues at 78.8 percent span; however, while the wake is only slightly evident at 81.4 percent speed, it maintains more strength at 90.1 percent speed.

Clearly, the QHSF I rotor wake exhibits less strength over the outer portion of the span at the LDV plane, due to the increased distance from the rotor trailing edge. This behavior is further enhanced at the stator leading edge, and serves to reduce the impact of the rotor-stator interaction tone noise.

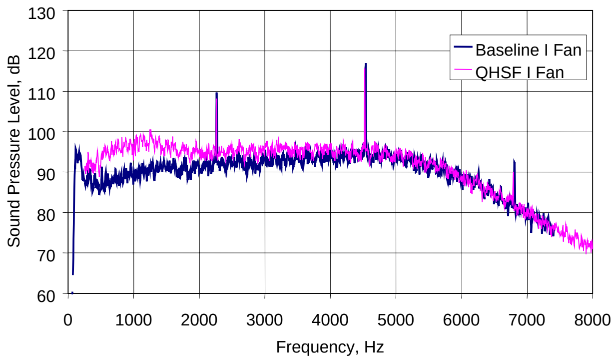

(a) 8516 RPM

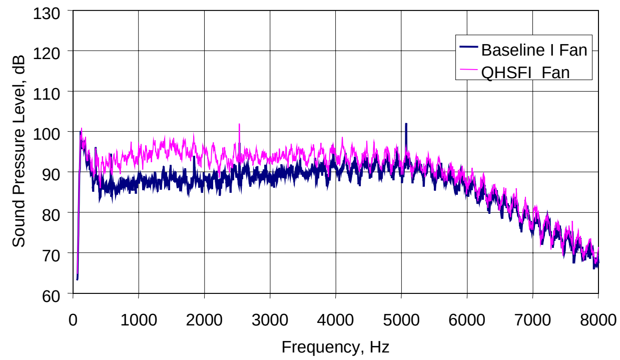

(b) 9510 RPM

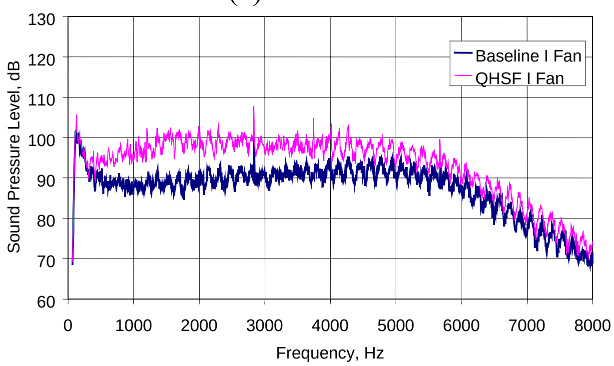

(a) 10,646 RPM

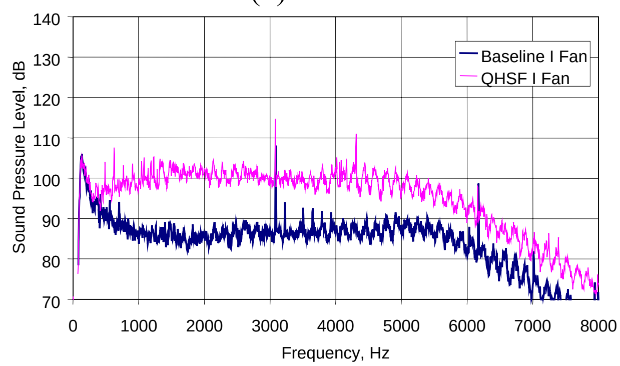

(b) 11,572 RPM

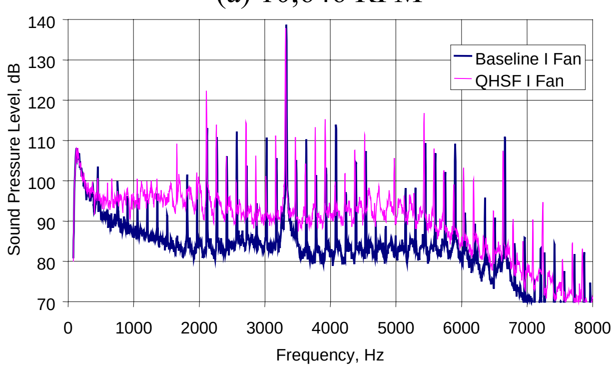

(a) 12,500 RPM

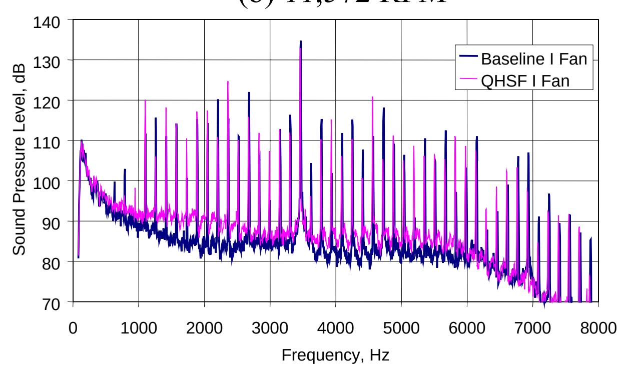

(b) 13,000 RPM

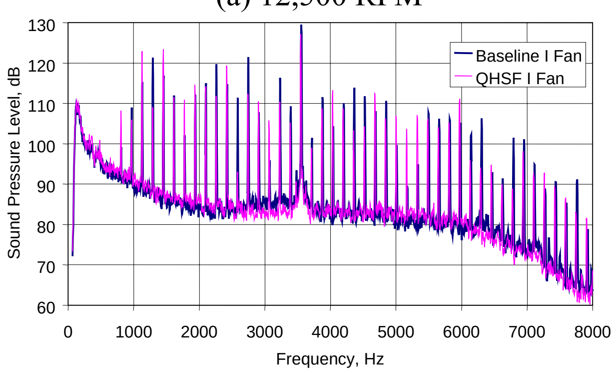

(a) 13,342 RPM

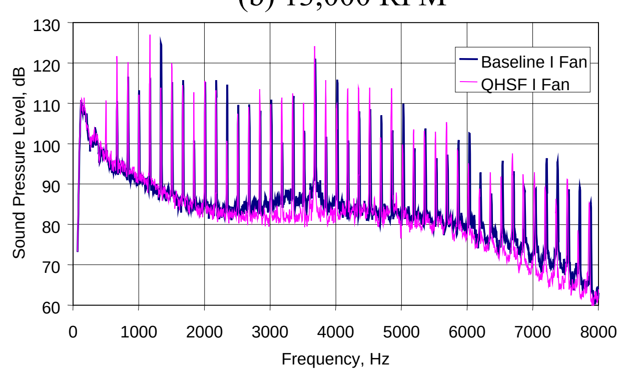

(b) 13,831 RPM

Figure 32. Unknown Broadband Noise Source Must Be Identified and Eliminated for Redesign of the QHSF (Data at 61 Degrees With Barrier).

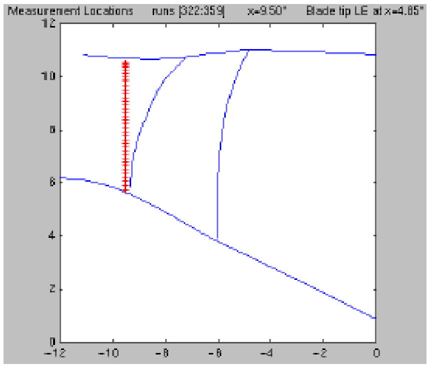

(a) axial position of LDV survey

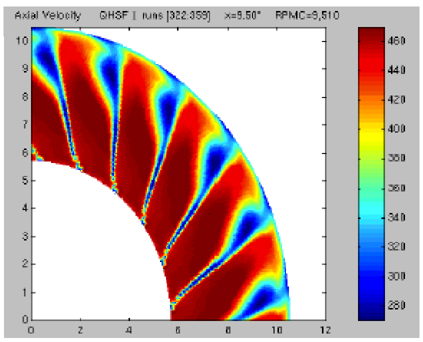

(b) 9510 RPM

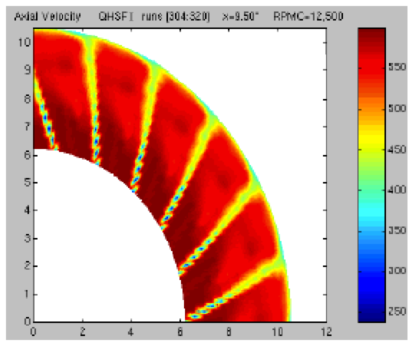

(c) 12,500 RPM

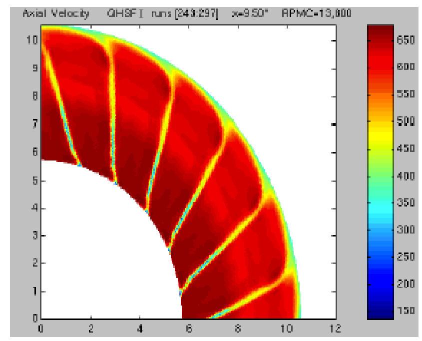

(d) 13,831 RPM

Figure 33. LDV Axial Velocity Data Taken Downstream of the QHSF I Show Flow Separation at Low RPM That Is Reduced at Higher Values of RPM.

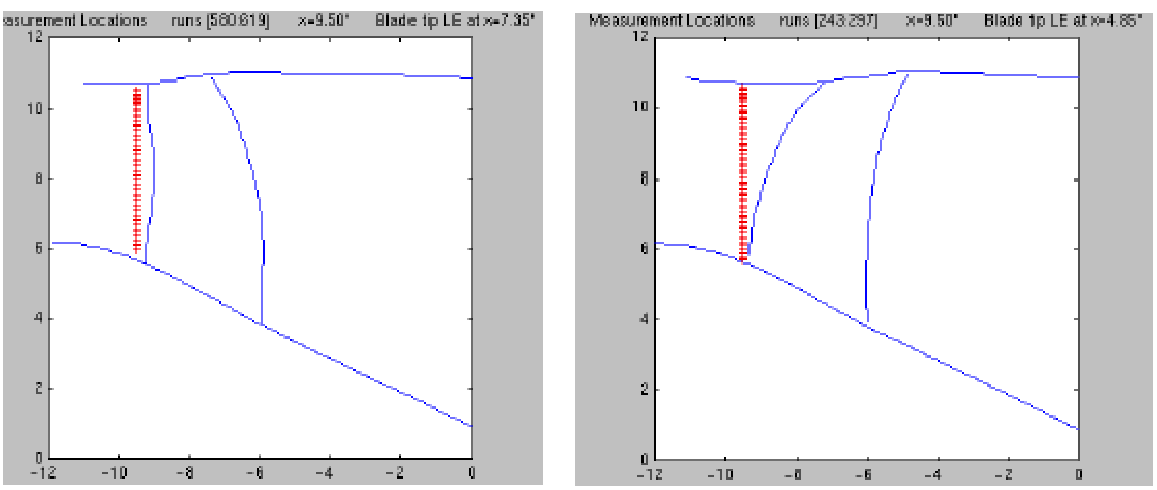

Figure 34. Location of the LDV Planes Relative to the Trailing Edges of the Baseline I and QHSF I Rotors.

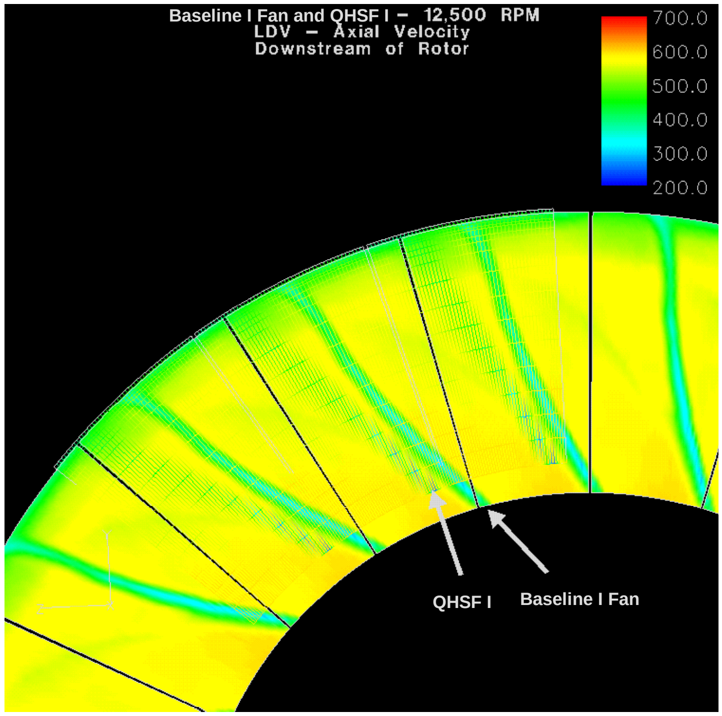

(a) 12500 RPM

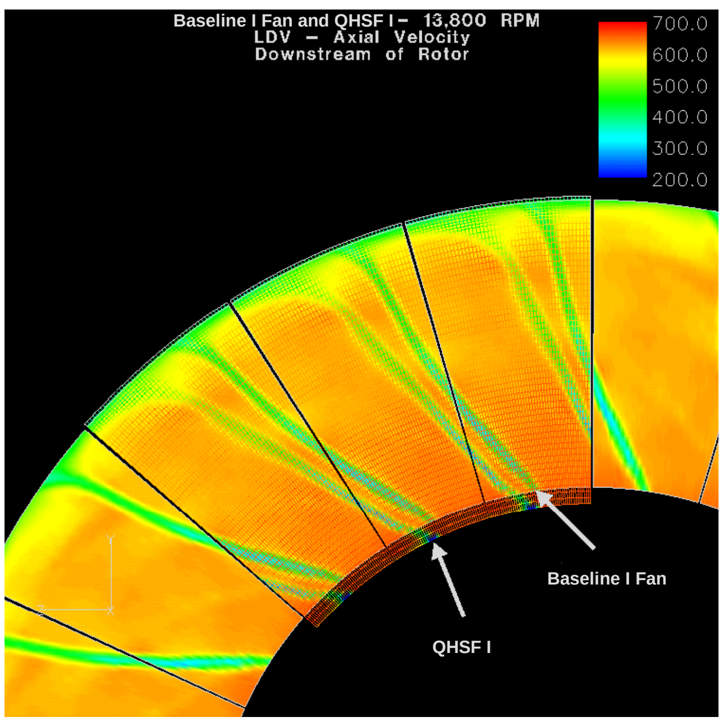

(b) 13831 RPM

Figure 35. The Wake Structure at the LDV Plane for the Baseline I and QHSF I Rotors, at 81.4% and 90.1% Corrected Fan Speed.

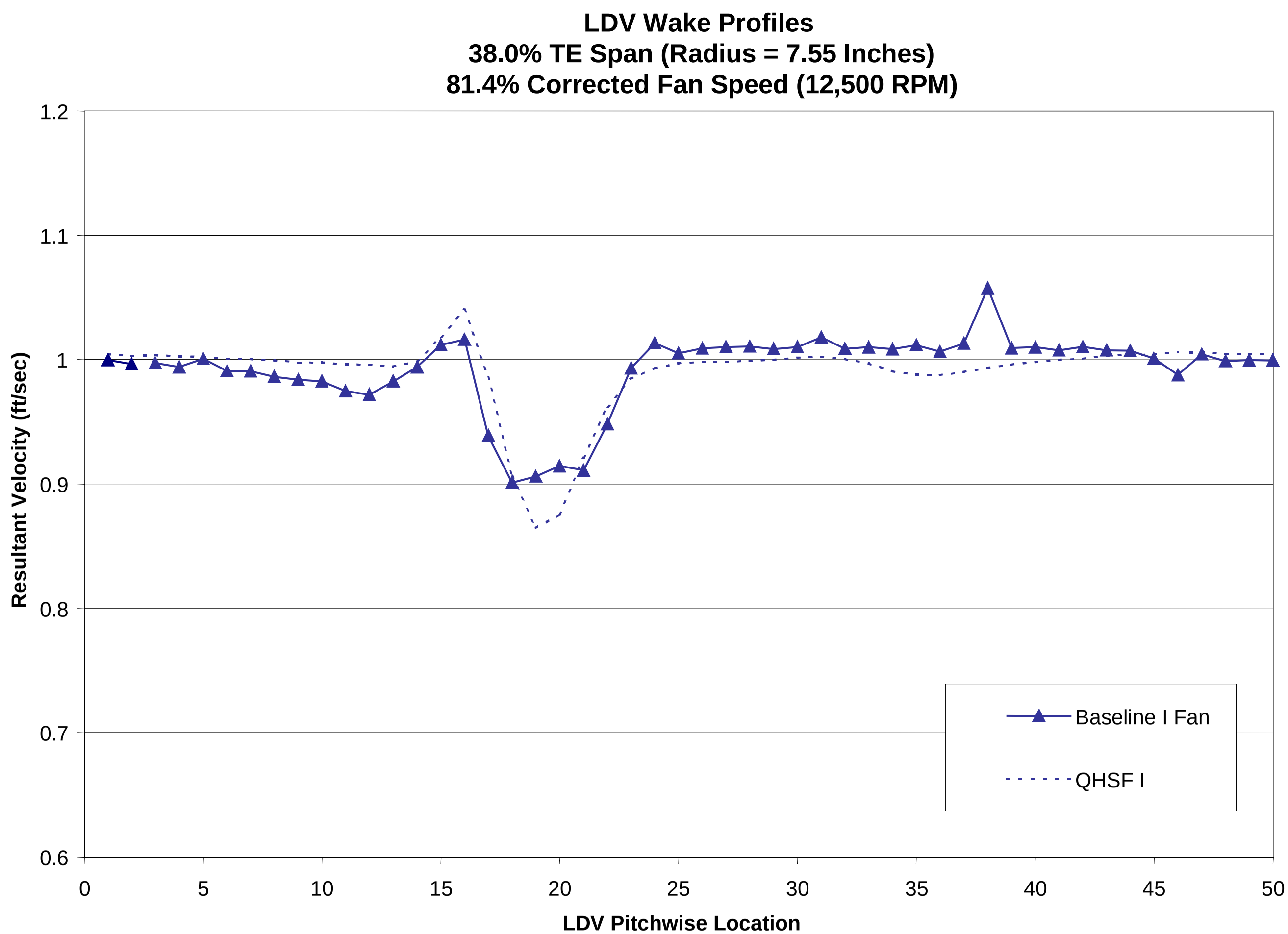

Figure 36. Comparison of Baseline I and QHSF I Rotor Wake Profiles at 81.4% Corrected Fan Speed.

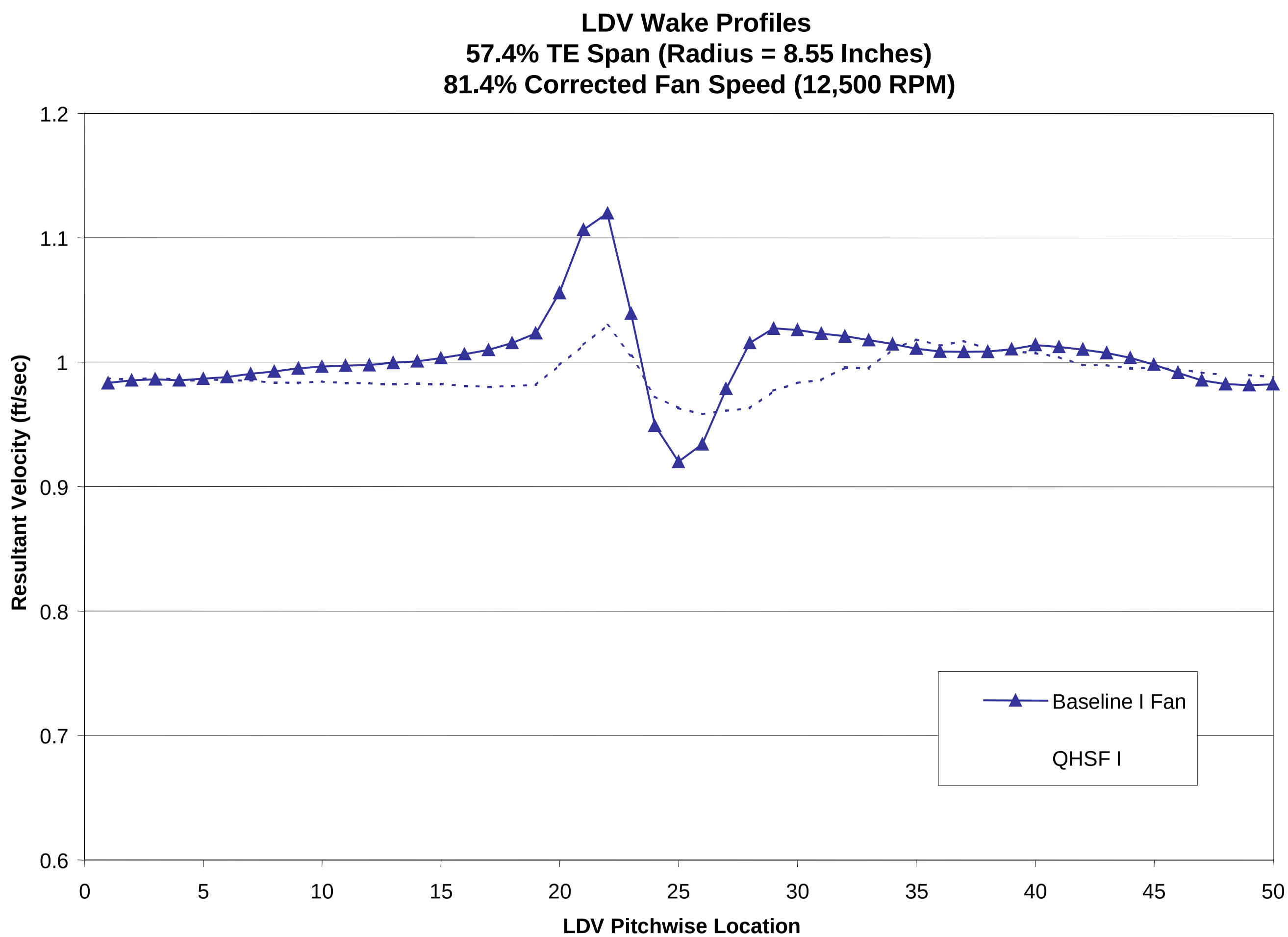

Figure 36. Comparison of Baseline I and QHSF I Rotor Wake Profiles at 81.4% Corrected Fan Speed (Cont).

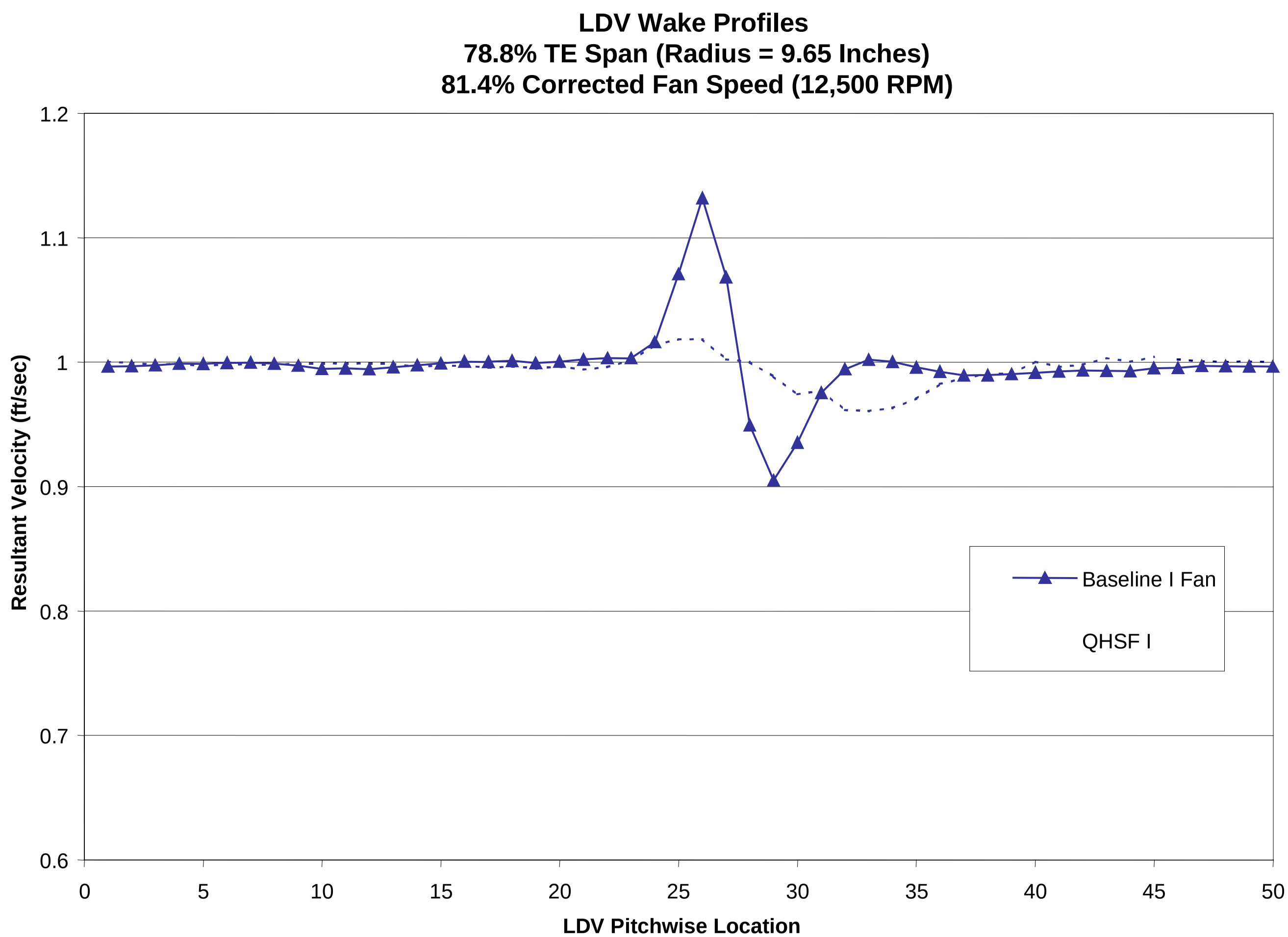

Figure 36. Comparison of Baseline I and QHSF I Rotor Wake Profiles at 81.4% Corrected Fan Speed (Cont).

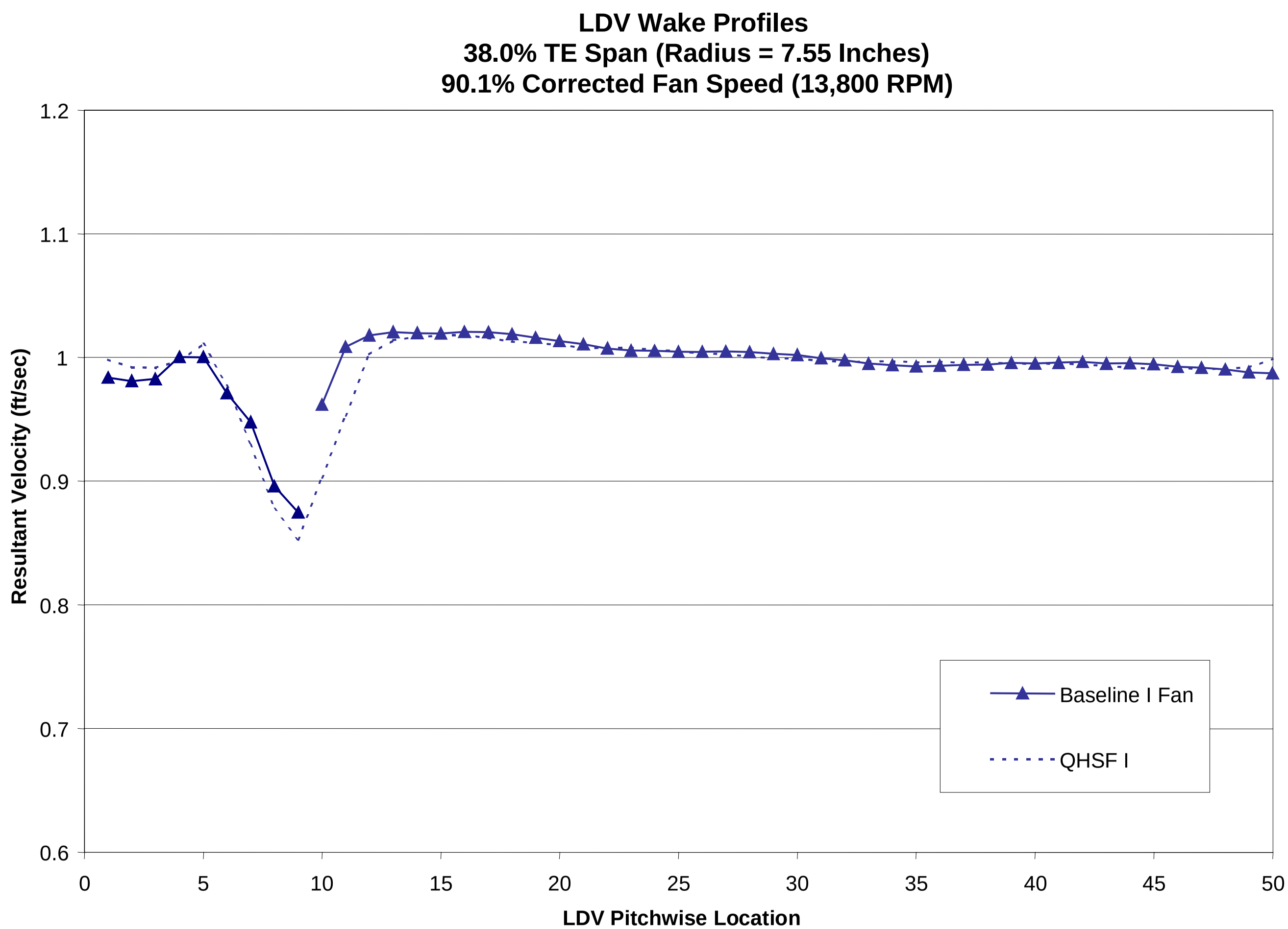

Figure 37. Comparison of Baseline I and QHSF I Rotor Wake Profiles at 90.1% Corrected Fan Speed.

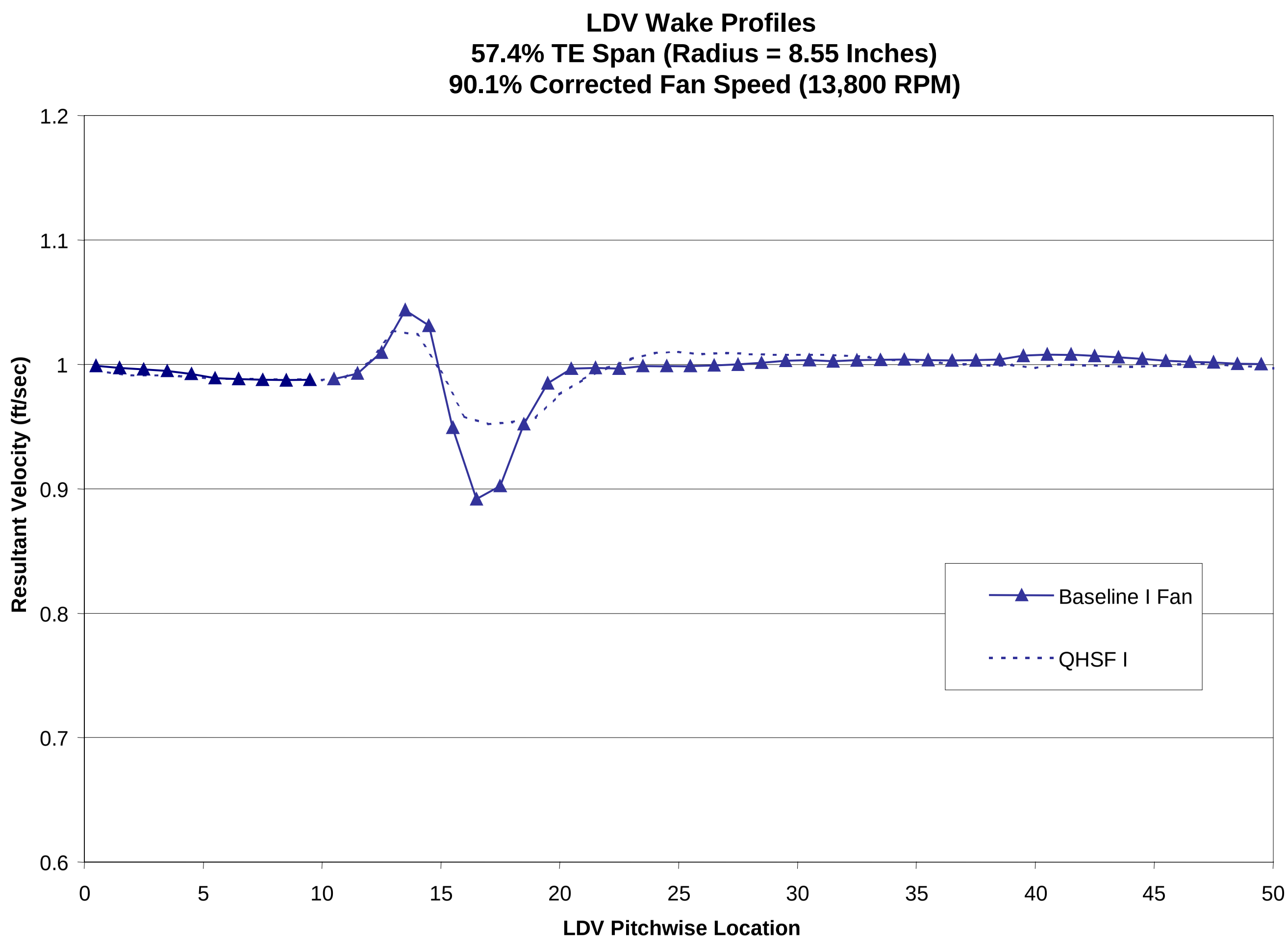

Figure 37. Comparison of Baseline I and QHSF I Rotor Wake Profiles at 90.1% Corrected Fan Speed (Cont).

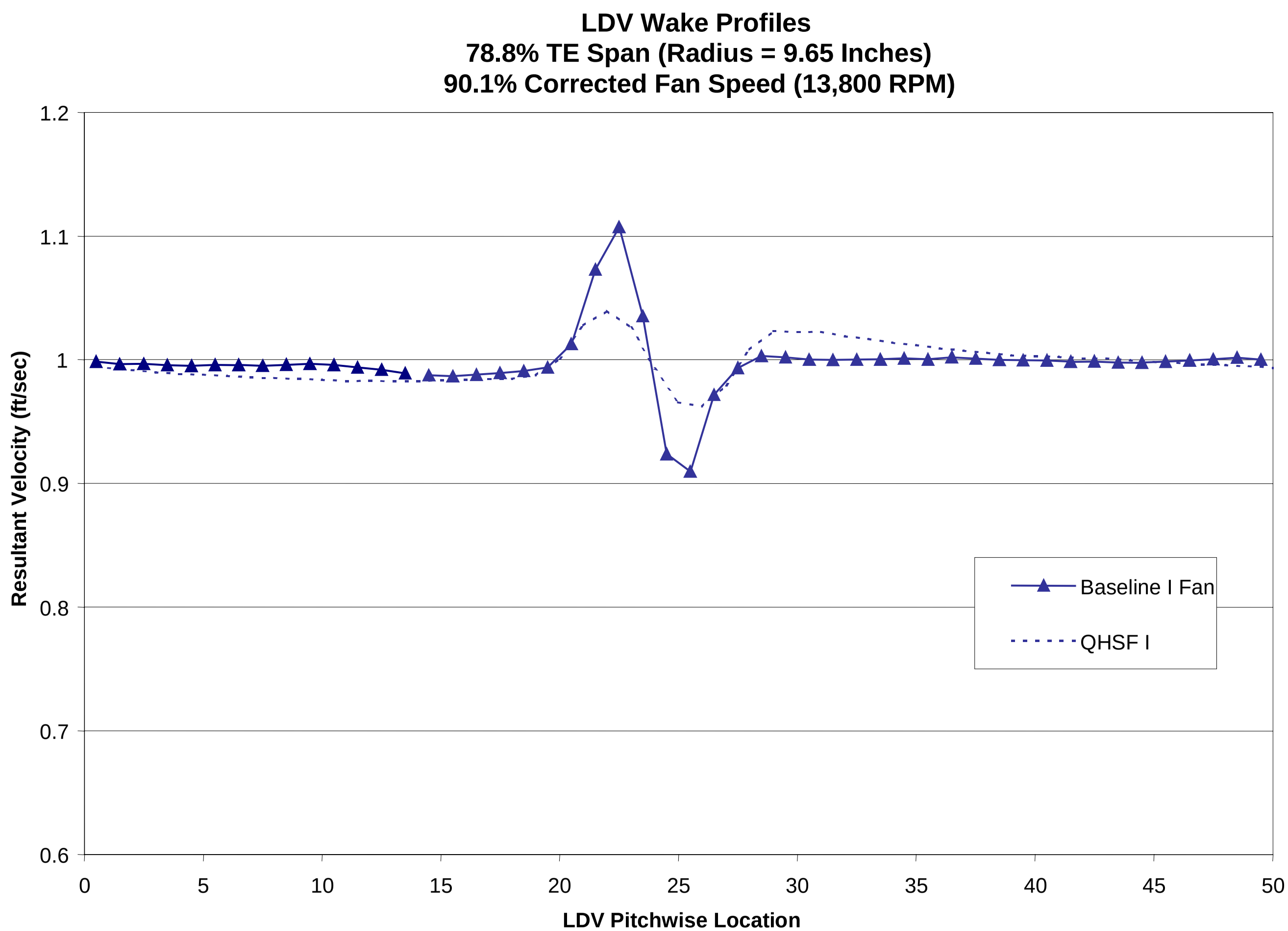

Figure 37. Comparison of Baseline I and QHSF I Rotor Wake Profiles at 90.1% Corrected Fan Speed (Cont).

The LDV data were also compared to the CFD data. Comparisons of the overall wake structure at same downstream plane were made for both the QHSF I and Baseline I rotors. The operating line points were analyzed at the corrected fan speeds shown in Table 7. The CFD predictions were taken from the DAWES analyses performed as part of QHSF I design activity. In the inner span region at the LDV measurement plane, the slopes of the wakes of the QHSF I and Baseline I rotors are similar. In the outer span region, the QHSF I wakes display more tangential lean at LDV plane. This difference is due to the increased distance between rotor trailing edge and the LDV plane resulting from the forward sweep of the QHSF I rotor. The wakes rotate further tangentially through the additional axial distance, producing more lean than the wakes in the inner span region. The CFD predictions of the rotor wake structure at the LDV plane appear to be in good qualitative agreement with the LDV data as shown in Figure 38 to Figure 41.

Table 7. The Available Corrected Fan Speeds for the LDV Measurements and CFD Analyses Were Matched as Closely as Possible.

Baseline I Fan		QHSF I	
LDV Data	**CFD Analyses**	**LDV Data**	**CFD Analyses**
81.4%		81.4%	80%
	85%		
90.1% (Sideline)		90.1% (Sideline)	90%

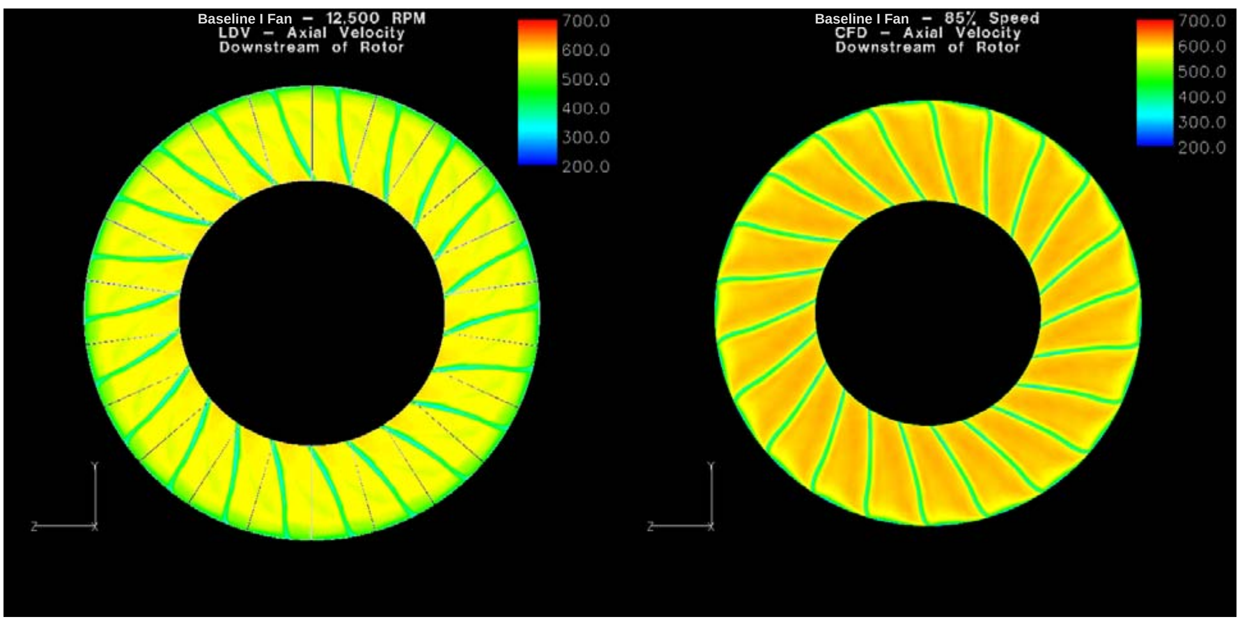

(a) LDV - 81.4% Speed (b) CFD – 85.0% Speed

Figure 38. A Good Comparison Is Seen Between the Measured and Calculated Rotor Wakes for the Baseline I Fan at a Typical Cutback Takeoff Condition.

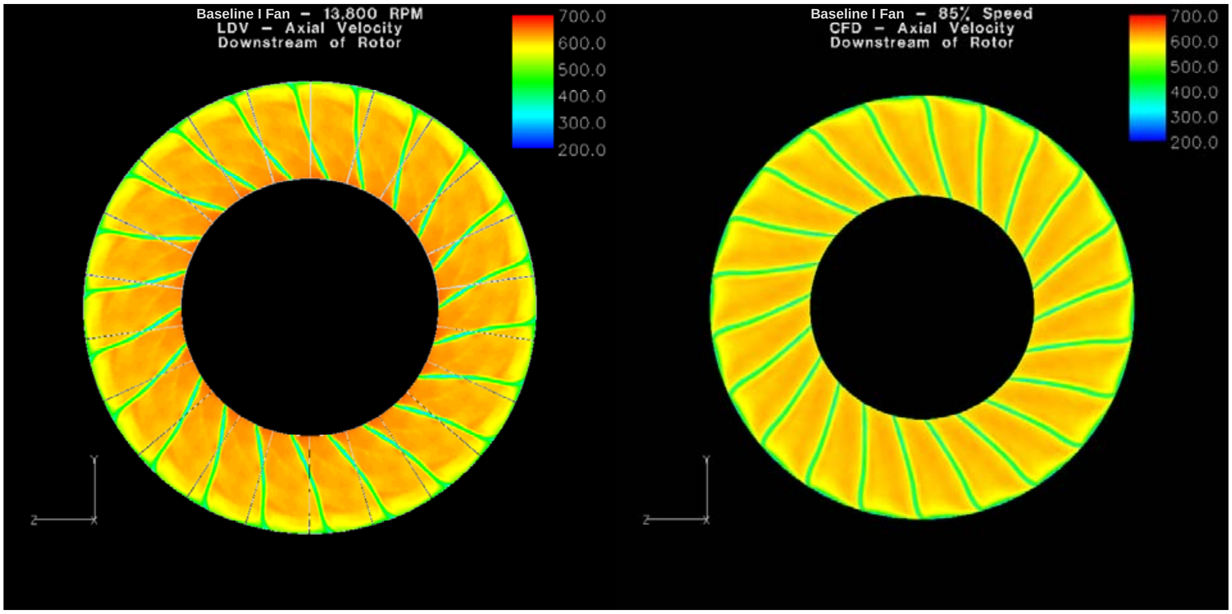

(a) LDV – 90.1% Speed (b) CFD – 85.0% Speed

Figure 39. A Good Comparison Is Seen Between the Measured and Calculated Rotor Wakes for the Baseline I Fan at a Typical Full Power Takeoff Condition.

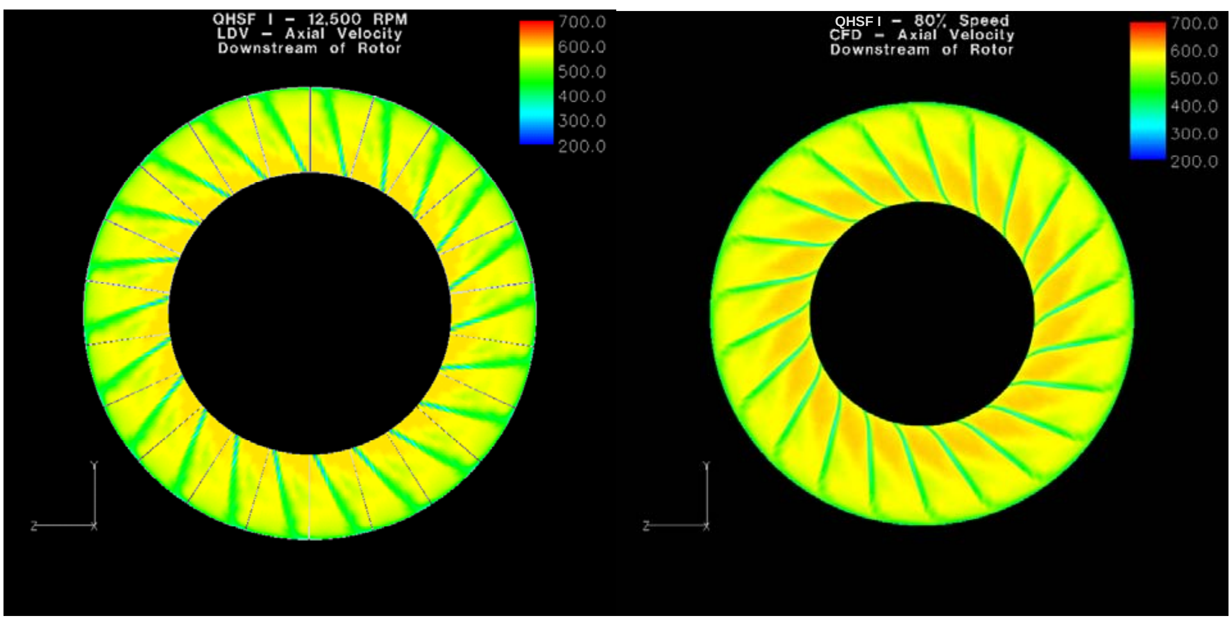

(a) LDV – 81.4% Speed (b) CFD – 80.0% Speed

Figure 40. A Good Comparison Is Seen Between the Measured and Calculated Rotor Wakes for the QHSF I at a Typical Cutback Takeoff Condition.

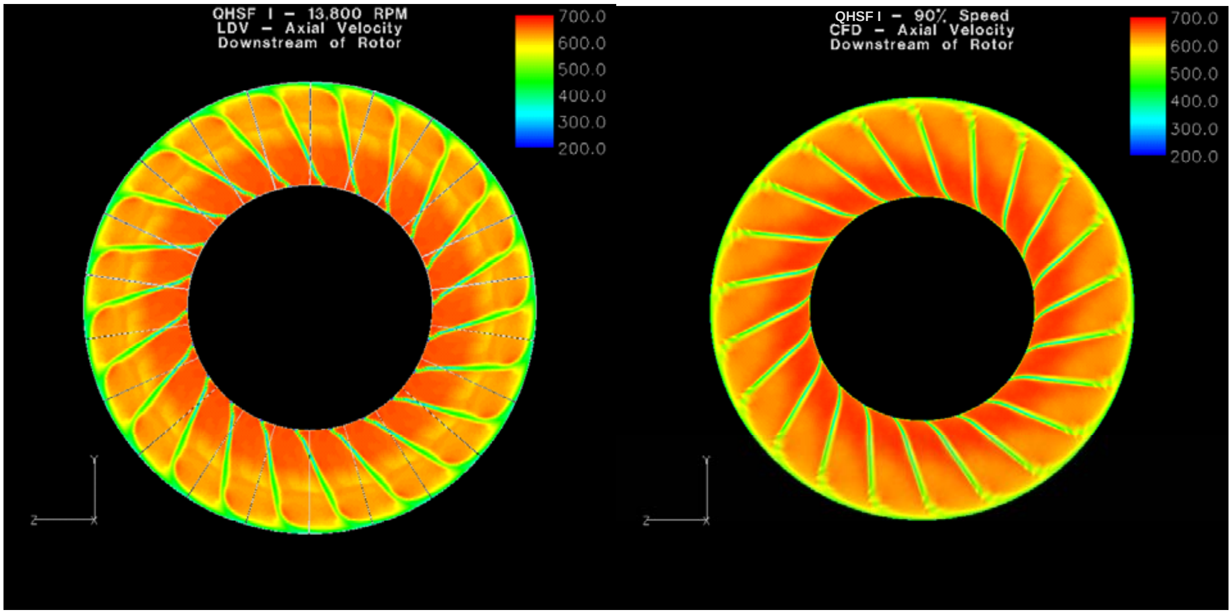

(a) LDV – 90.1% Speed

(b) CFD – 90.0% Speed

Figure 41. A Good Comparison Is Seen Between the Measured and Calculated Rotor Wakes for the QHSF I at a Typical Full Power Takeoff Condition.

4.3 Evaluation of the Rotor/Strut Interaction

During QHSF I testing, rotor-strut interaction tones were observed at 90 percent speed for the Baseline I fan, but were not present for the QHSF I fan (Reference 13). Figure 42 shows typical circumferential mode results from those measurements. Both the Baseline I fan and the QHSF I have 22 fan blades and 10 struts. Therefore, the expected rotor/strut circumferential modes are

(… -18, -8, 2, 12, 22, …)

It was proposed that the difference in stators might have impacted strut-induced pressure disturbances at the rotor exit. A rotor-stator-strut interaction study was conducted to

- identify pressure disturbances upstream of the stator that could be produced by the strut
- identify any differences in pressure distribution from one strut passage to the next, due to the differing relative position of stators vs. struts for each strut passage over 180 degrees
- qualitatively assess any differences between the pressure distributions upstream of the Baseline I and QHSF I stators

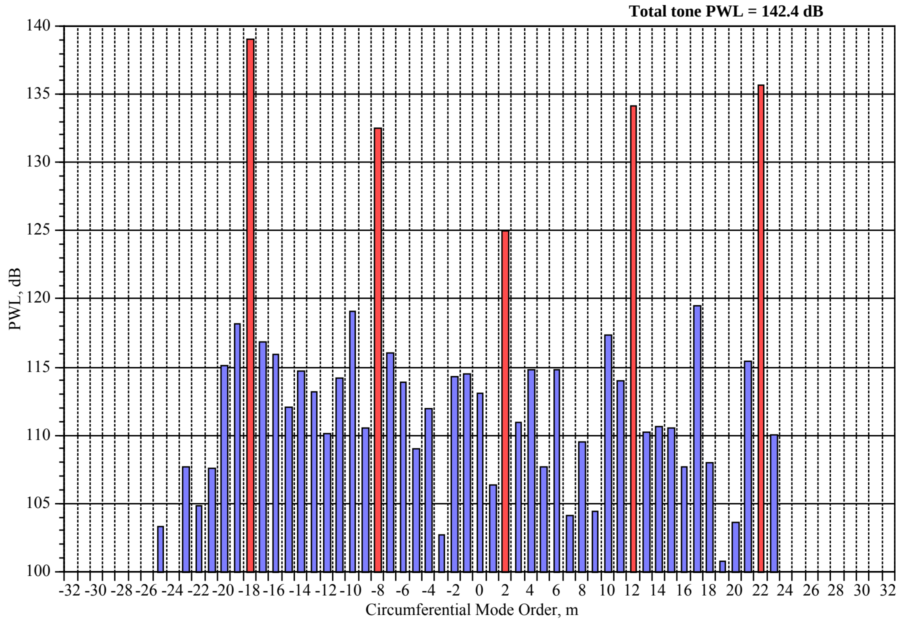

(a) Baseline I Fan

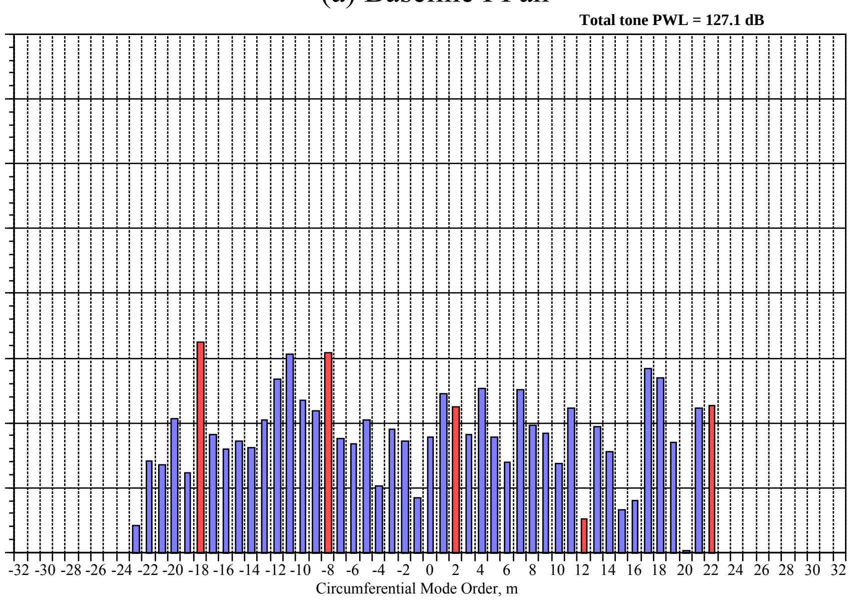

(b) QHSF I

Figure 42. Acoustic Modal Measurements in the Aft Fan Duct With a Rotating Rake Show Significant Rotor Strut Tones for the Baseline I Fan.

CFD analyses were performed with the Fluent® CFD code for the two fan configurations:

- Baseline I Stator + Strut
- QHSF I Stator + Strut

The strut geometry was identical for both studies. The upstream boundary conditions were taken to be the QHSF I rotor exit conditions from 18” rig test data at 90 percent corrected speed on the standard sea level operating line. Predicted static pressure fields were examined upstream of stators. The actual configuration of both fans was 52 stator vanes and 10 struts; therefore, by applying periodic boundary conditions on a 26 vane and 5 strut model, a full flow field was evaluated. Diagnostic runs were also made with an approximate model consisting of 5 vanes and 1 strut. Table 8 provides a summary of the analysis runs performed.

Table 8. Summary of CFD Models Run in the Rotor/Strut Potential Interaction Study.

Model	Cell count	Comment
Baseline I	1.5 M	26 stator, 5 strut
	3.3 M	26 stator, 5 strut
	4.9M	26 stator, 5 strut, 1 adaptation on Ps gradient
	1.9 M	5 stator, 1 strut
QHSF I	1.9 M	26 stator, 5 strut
	3.3 M	26 stator, 5 strut
	5.4M	26 stator, 5 strut, 1 adaptation on Ps gradient
	2.2 M	5 stator, 1 strut

Figure 43 shows the CFD geometries that were used for the 5 strut models. Periodic boundary conditions were applied to be consistent with the full 360-degree fan configuration as shown in Figure 44. The unstructured grid used to perform the analysis is shown in Figure 45.

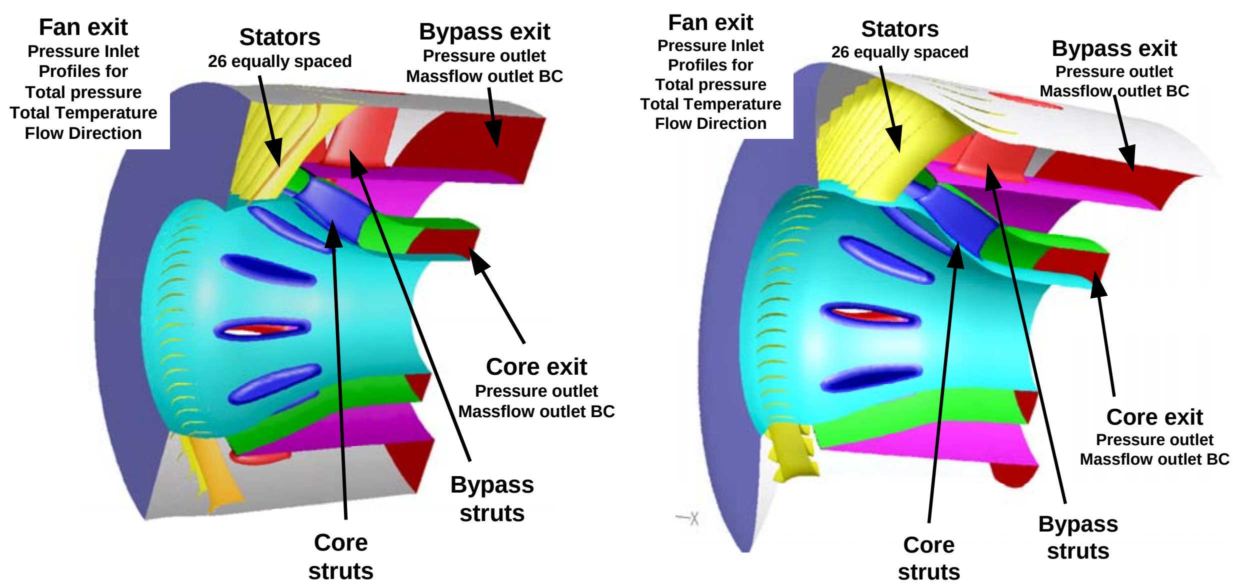

(a) Baseline I Fan (b) QHSF I

Figure 43. CFD Models for the Rotor/Strut Interaction Study Modeled 26 Vanes, 5 Struts, and the Split Flow Path.

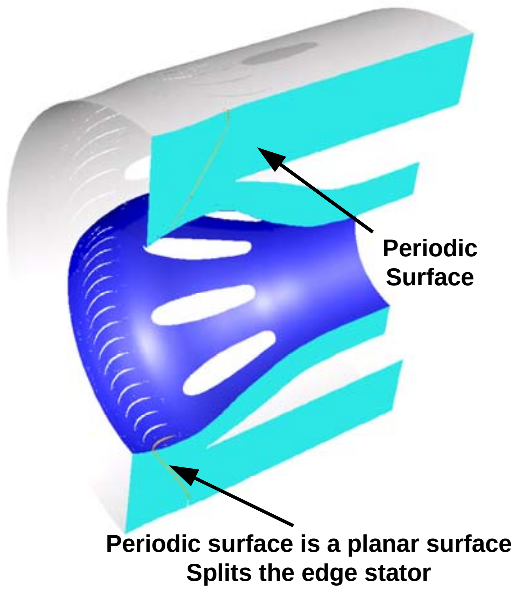

Figure 44. A Periodic Boundary Condition Was Used to Model the Total 360 Degree Flowfield.

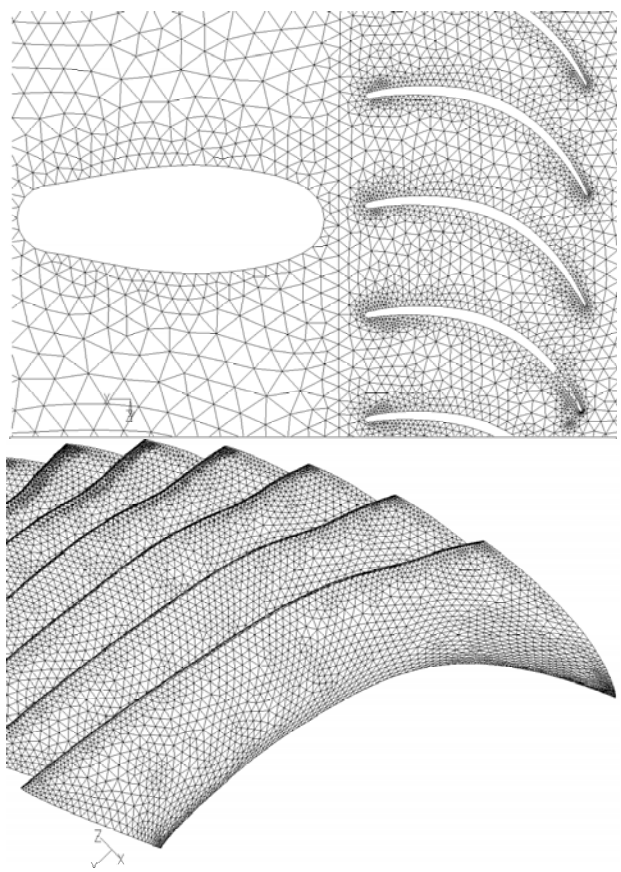

Figure 45. An Unstructured Grid Was Used to Model the Rotor/Strut Interaction Flowfield (QHSF I).

The contour plots in Figure 46 and Figure 47 show that there is more static pressure variation at the rotor exit and in the mid-region between the rotor and stator for the Baseline I fan than the QHSF I. To further visualize the variation in static pressure between the two fans, the static pressure results were plotted at several data planes. Figure 48 and Figure 49 show the location of the data planes for the two fans. Figure 50 show overlays of circumferential cuts of the two-stator systems to demonstrate the difference in the stator configurations for the two fans.

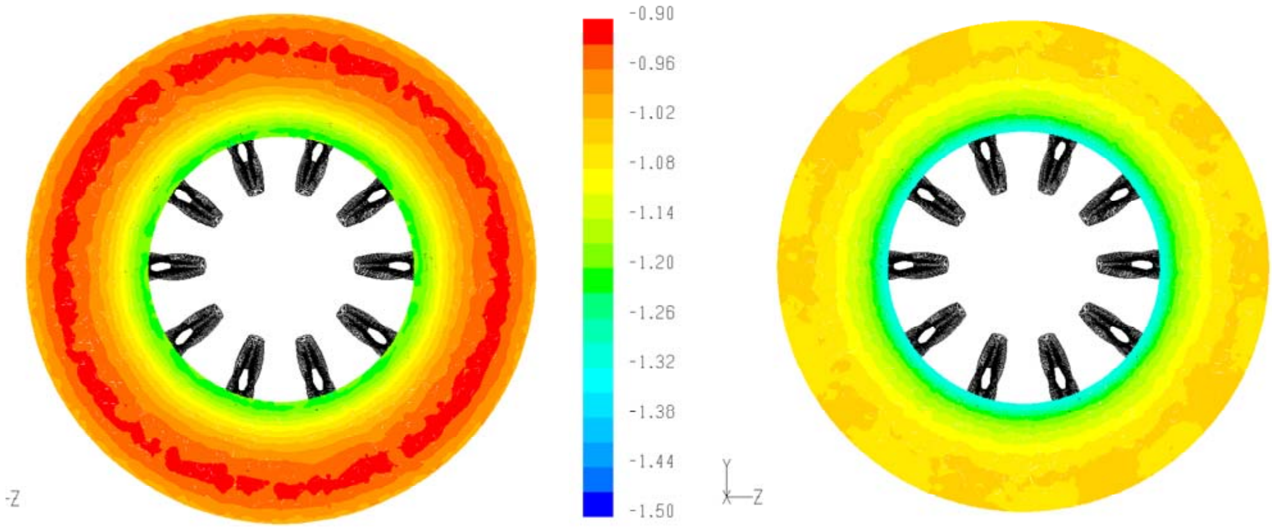

$$Cp = \frac{(P_s - \overline{P}_{t\cdot fan-exit})}{\overline{P}_{t\cdot fan-exit} - \overline{P}_{s\cdot fan-exit}}$$

(a) Rotor Exit (b) Mid Region

Figure 46. Pressure Coefficient Contours Between the Rotor and Stator Have Been Produced From the Fluent® CFD Analysis for the Baseline I Fan.

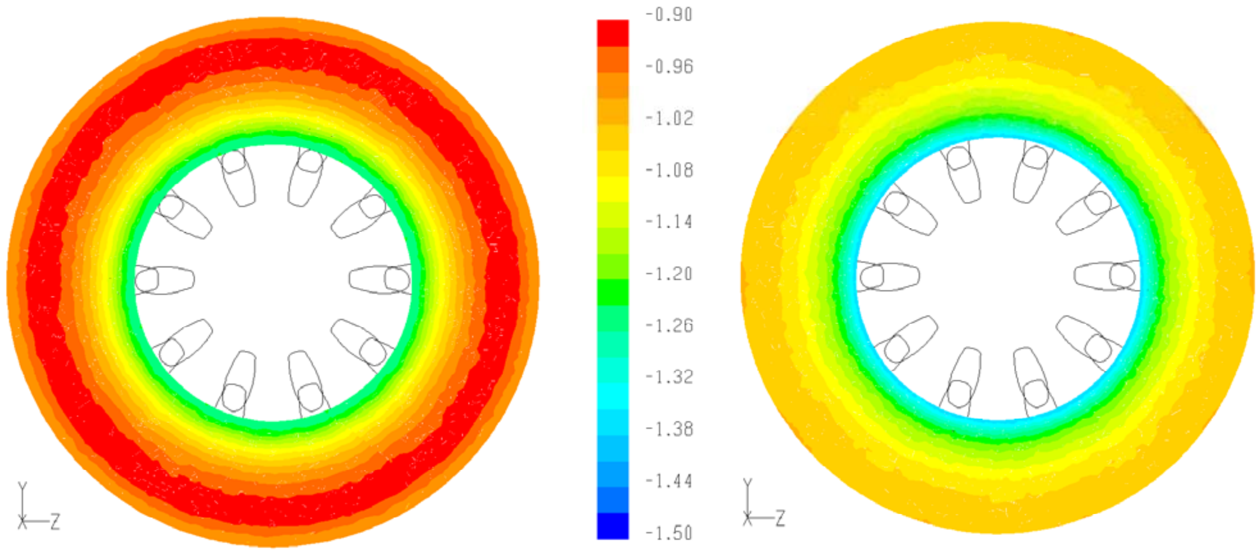

$$Cp = \frac{(P_s - \overline{P}_{t\cdot fan-exit})}{\overline{P}_{t\cdot fan-exit} - \overline{P}_{s\cdot fan-exit}}$$

(a) Fan Exit (b) Mid Region

Figure 47. Pressure Coefficient Contours Between the Rotor and Stator Have Been Produced From the Fluent® CFD Analysis for the QHSF I.

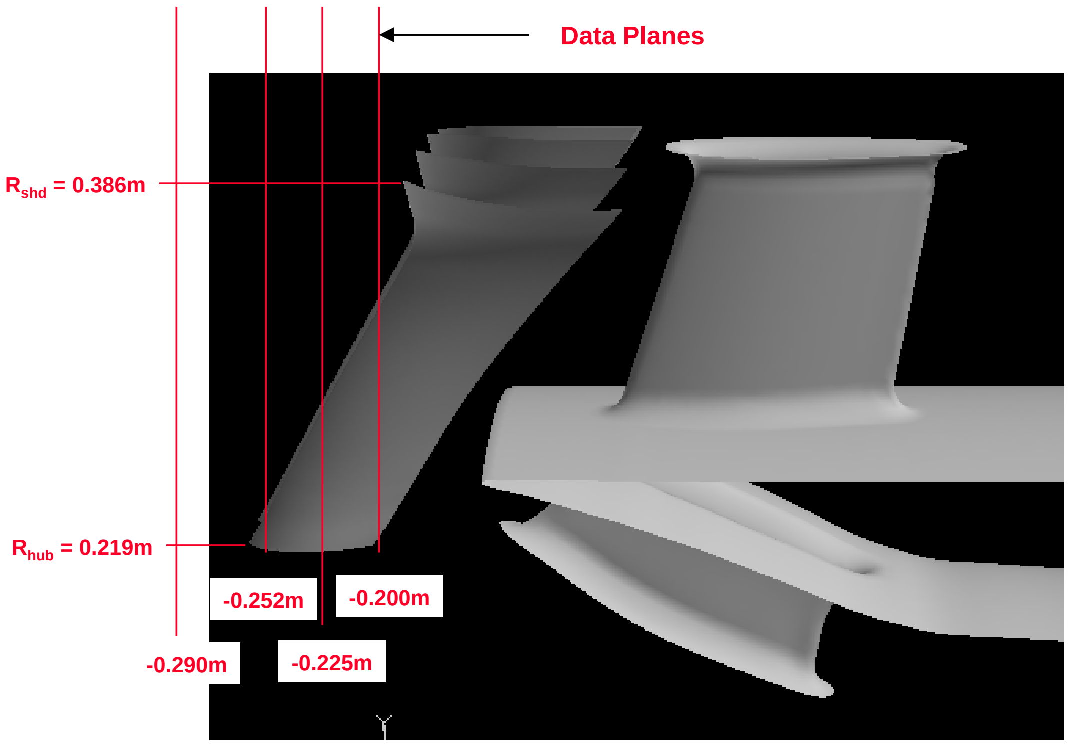

Figure 48. Data Planes Were Selected for Comparison of Circumferential Static Pressure Profiles (Baseline I Fan).

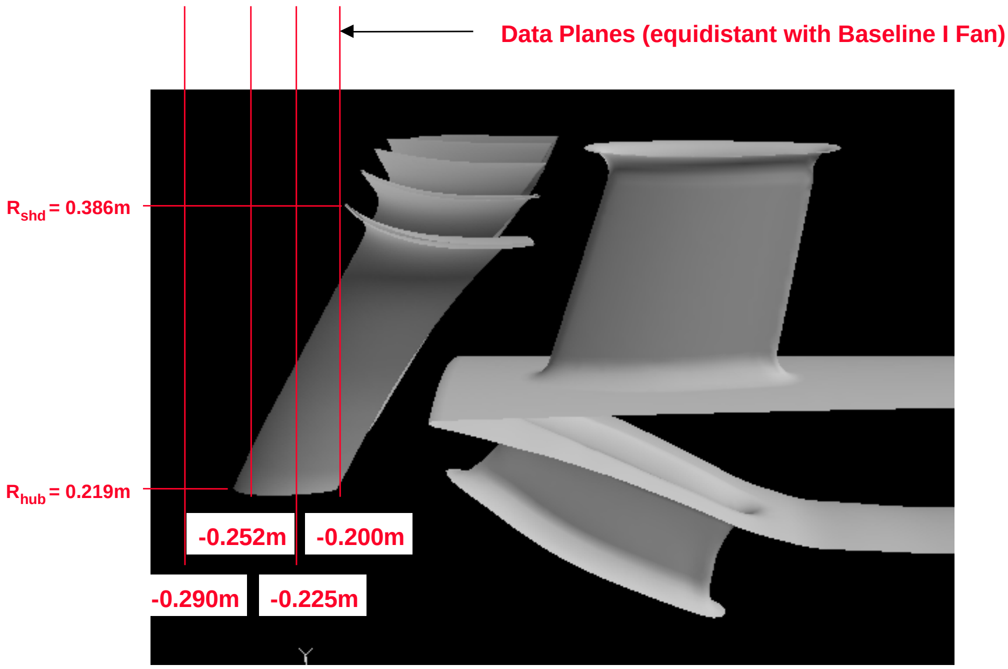

Figure 49. Data Planes Were Selected for Comparison of Circumferential Static Pressure Profiles (QHSF I).

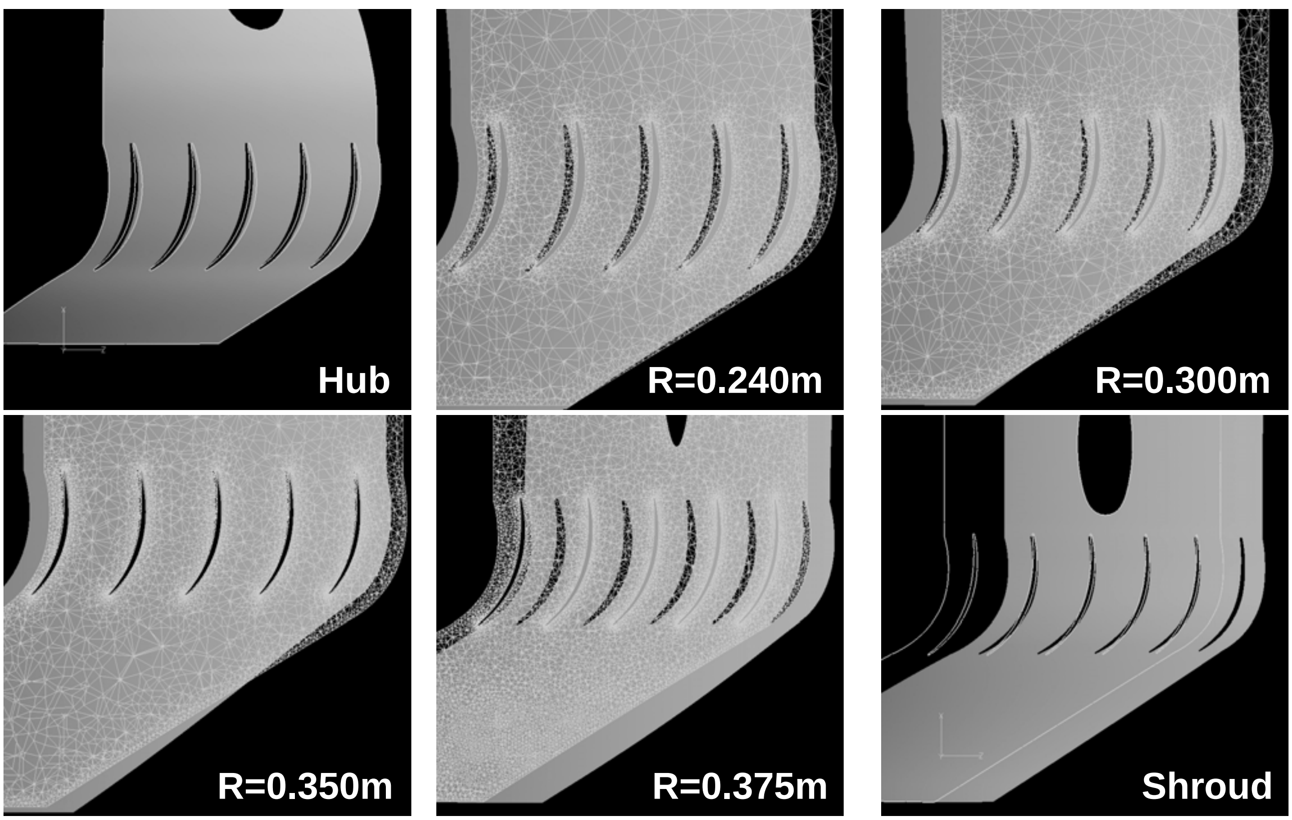

Figure 50. Circumferential Cuts Show the Relative Positions of the Baseline I and QHSF I Vanes at Various Radii (QHSF I Shown in Black).

Significant differences in the stator geometries occur out near the tip. Data comparisons were performed at the radii shown in Figure 51. Figure 52 and Figure 53 show the circumferential variation of the static pressure for the QHSF I and Baseline I fans at 3 different axial positions for the two radii. It is clear from the data that the Baseline I fan has more static pressure variation than the QHSF I. This evidence suggests that the cause of the rotor strut interaction tones is the rotor responding to the variation of the potential pressure field of the struts.

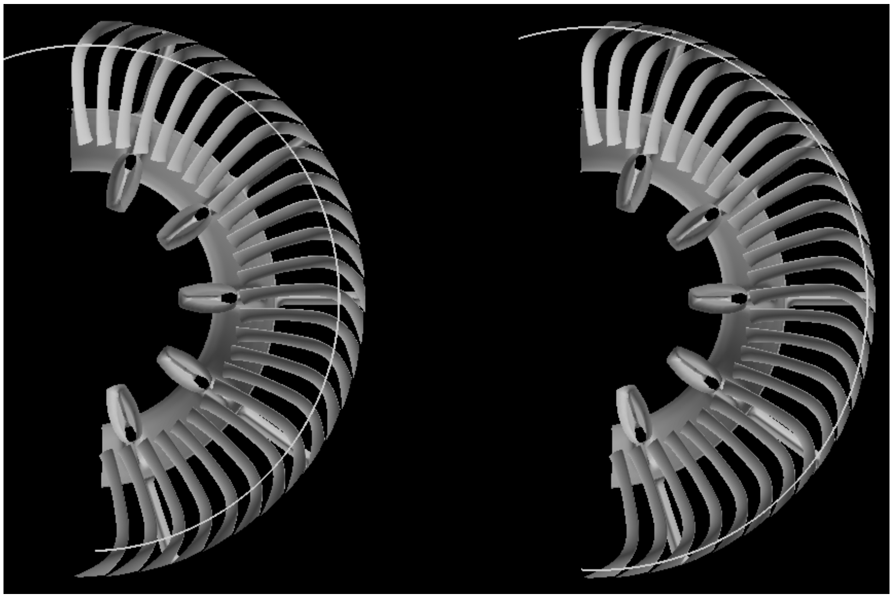

(a) R=0.350m (b) R=0.375m

Figure 51. Data Comparisons Emphasize Two Radii Near the Vane Shroud (QHSF I Shown).

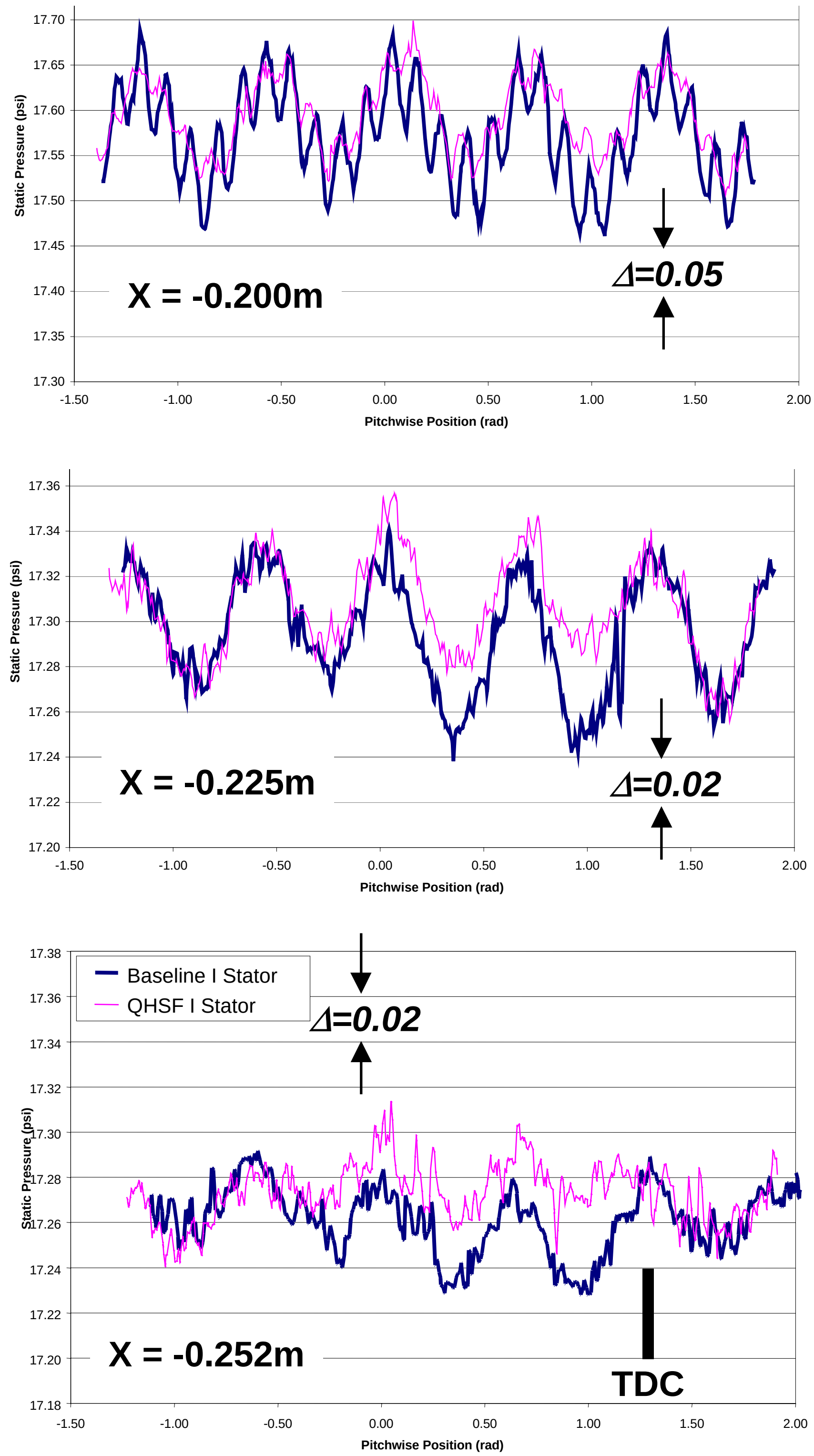

Figure 52. Comparison of Circumferential Pressure Distributions at R-0.375m (QHSF I Data Shifted in Angle and Level to Align With Baseline I Data).

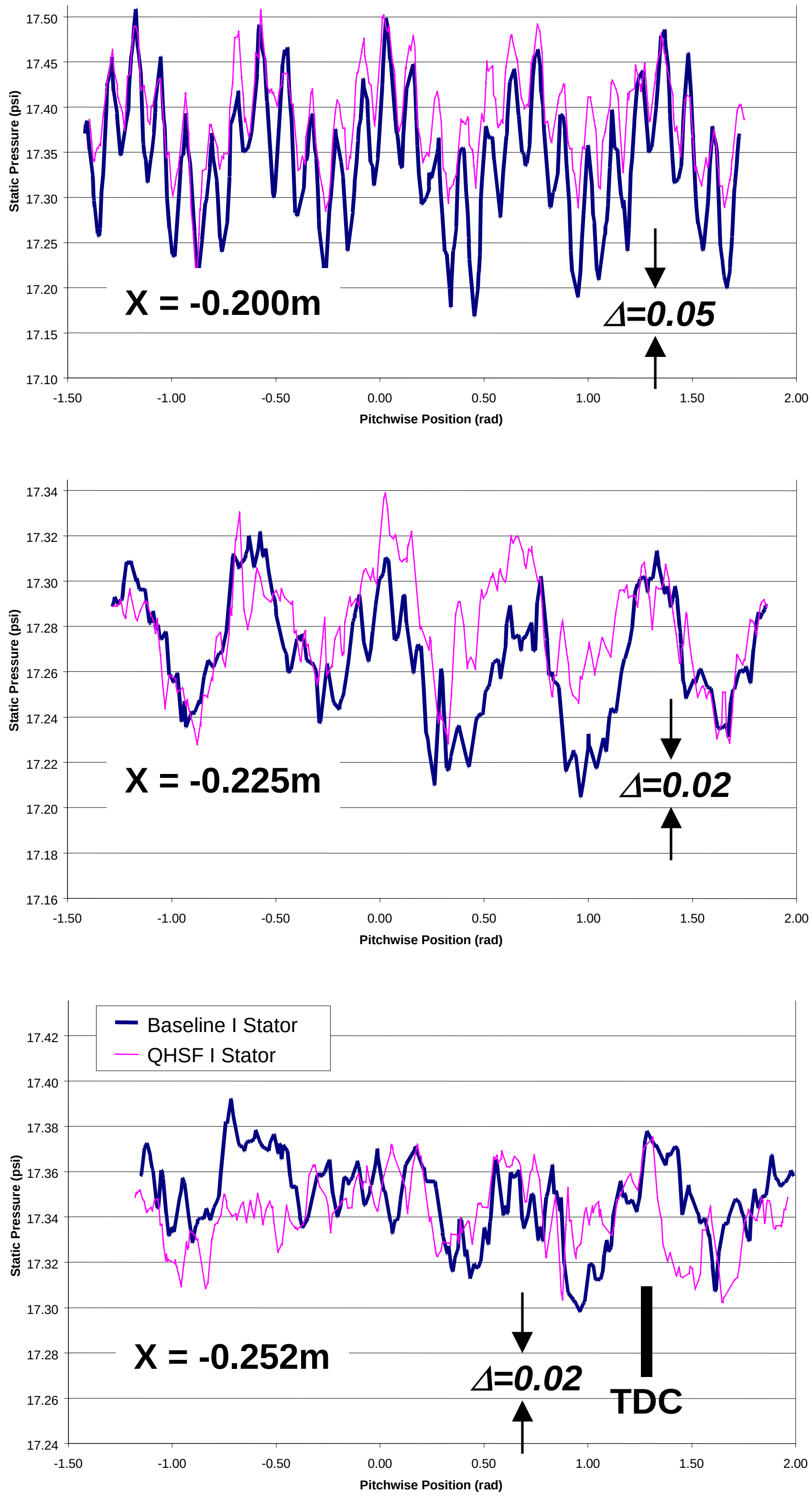

Figure 53. Comparison of Circumferential Pressure Distributions at R=0.350m (QHSF I Data Shifted in Angle and Level to Align With Baseline I Data).

5. QHSF II DESIGN

5.1 Approach for the QHSF II Design

The QHSF II design will be developed using an analytical Design of Experiments (DOE) to define an optimum rotor and stator system. The interdisciplinary process being used is described in Figure 54. The DOE outline is:

- Blade Forward Sweep
  - Axial and tangential sweep components coupled
  - Key outputs: Acoustics, Aeroelastics, Aerodynamics
- Blade Tangential Lean
  - Optimized independent of selected axial sweep
  - Key outputs: Acoustics, Aeroelastics, Mechanical
- Blade Thickness Distribution
  - Key outputs: Aeroelastics, Mechanical, Aerodynamics
- Stator Optimization
  - Sweep & Lean
  - Key outputs: Acoustics, Aerodynamics, Mechanical
- Rotor Incidence
  - Key outputs: Aerodynamics, Aeroelastics

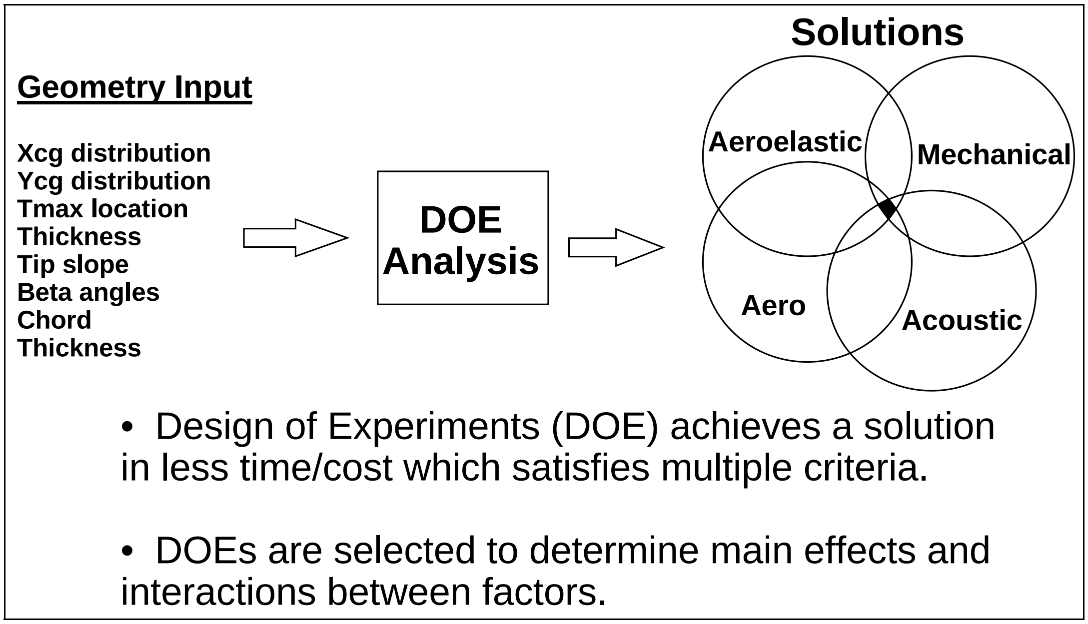

Figure 54. An Interdisciplinary Process Has Been Defined for the Design of the QHSF II.

5.2 Rotor Stacking Design of Experiments

The first DOE for the QHSF II fan rotor determined the blade forward sweep stacking. The configurations are assumed to have equal axial and radial center of gravity (Xcg and Ycg) offsets to facilitate evaluating multiple configurations. Four parameters are used to define the blade stacking as shown in Figure 55. Table 9 summaries the 25 cases for DOE 1.

A number of dependent variables (Y-factors) have been defined for DOE 1. These quantities will be used to evaluate the merits of the various configurations in the DOE and point to the possible go-forward designs for the DOE 2. Table 10 to Table 13 summaries the factors for DOE 1.

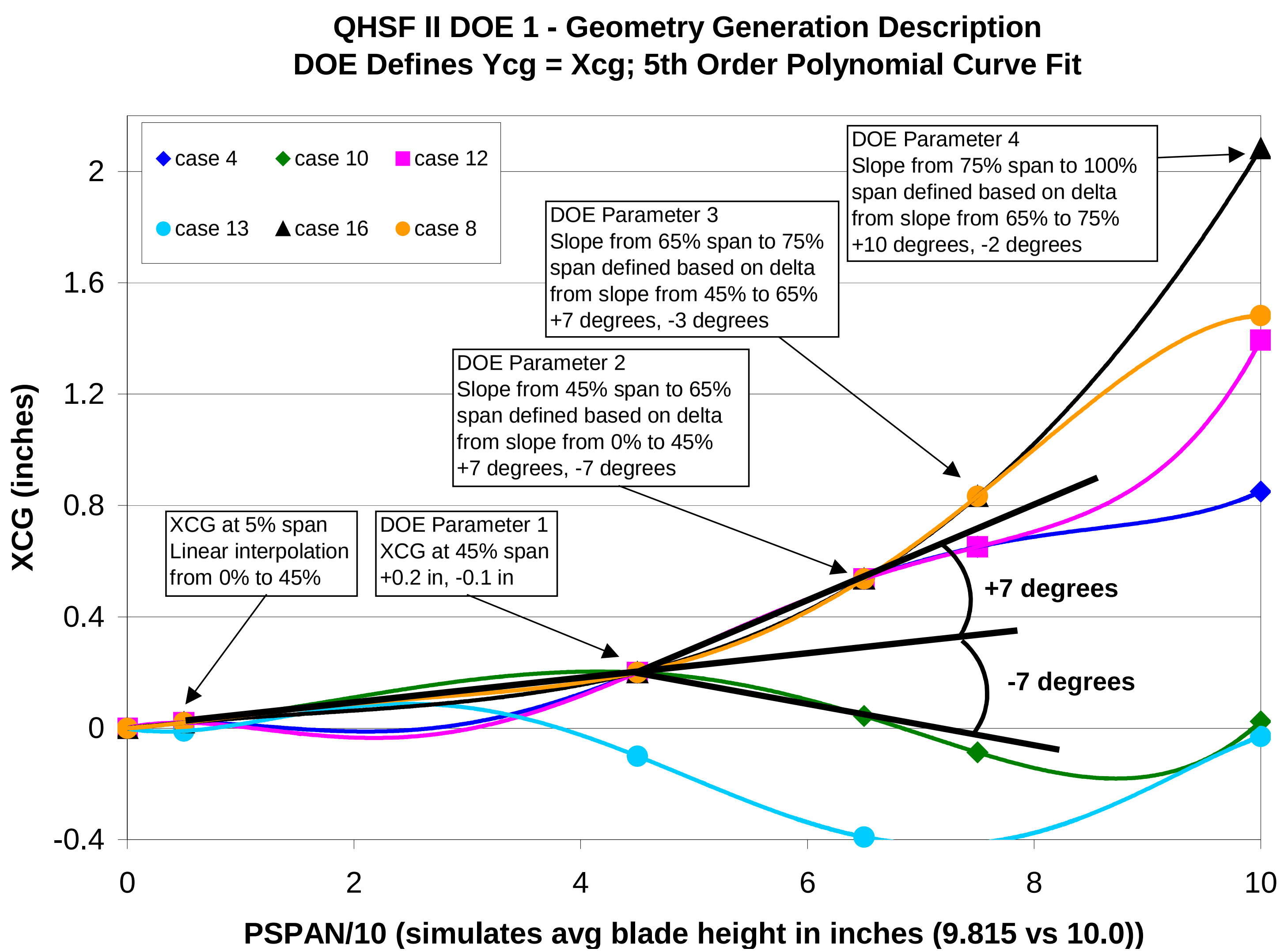

Figure 55. Four Parameters Define the Rotor Blade Stacking for DOE 1.

Table 9. Summary of the Cases for DOE 1.

HIGHLIGHTED CASES ARE PART OF THE PARTIAL FACTORIAL RUN FIRST

StdOrder	RunOrder	CenterPt	Blocks	xcg45	delslope65	delslope75	delslope100	
1	1	1	1	-0.1	-7	-3	-2	
2	2	1	1	0.2	-7	-3	-2	
3	3	1	1	-0.1	7	-3	-2	
4	4	1	1	0.2	7	-3	-2	
5	5	1	1	-0.1	-7	7	-2	
6	6	1	1	0.2	-7	7	-2	
7	7	1	1	-0.1	7	7	-2	
8	8	1	1	0.2	7	7	-2	
9	9	1	1	-0.1	-7	-3	10	
10	10	1	1	0.2	-7	-3	10	
11	11	1	1	-0.1	7	-3	10	
12	12	1	1	0.2	7	-3	10	
13	13	1	1	-0.1	-7	7	10	
14	14	1	1	0.2	-7	7	10	
15	15	1	1	-0.1	7	7	10	
16	16	1	1	0.2	7	7	10	
17	17	0	1	0.05	0	2	4	CENTER POINT
18	18		2	-0.1	0	2	4	AXIAL POINTS
19	19		2	0.2	0	2	4	
20	20		2	0.05	-7	2	4	
21	21		2	0.05	7	2	4	
22	22		2	0.05	0	-3	4	
23	23		2	0.05	0	7	4	
24	24		2	0.05	0	2	-2	
25	25		2	0.05	0	2	10	

Table 10. Acoustic Y-Factors for DOE 1.

Y-factor	Data type
delz 50	Axial distance RTE – VLE midspan
delz 100	Axial distance RTE – VLE tip
dB des	Interaction noise sound power level
eff swp des	Rotor LE effective sweep
% c 50 des	Passage shock loc. Design Nc, 50% span
% c 60 des	Passage shock loc. Design Nc, 60% span
% c 70 des	Passage shock loc. Design Nc, 70% span
% c 80 des	Passage shock loc. Design Nc, 80% span
% c 90 des	Passage shock loc. Design Nc, 90% span
% c 95 des	Passage shock loc. Design Nc, 95% span
dB 89	Interaction noise sound power level
eff swp 89	Rotor LE effective sweep
% c 50 89	Passage shock loc. 89% Nc, 50% span
% c 60 89	Passage shock loc. 89% Nc, 60% span
% c 70 89	Passage shock loc. 89% Nc, 70% span
% c 80 89	Passage shock loc. 89% Nc, 80% span
% c 90 89	Passage shock loc. 89% Nc, 90% span
% c 95 89	Passage shock loc. 89% Nc, 95% span

Table 11. Aeroelastic Y-Factors for DOE 1.

Y-factor	Data type
Damping - extrapolated to stall line	scalar for each speedline
Damping - massflow at flutter boundary	scalar for each speedline
Damping - flutter margin relative to PE	scalar for each speedline
Damping - critical nodal diameter	scalar for each speedline
Reduced frequency, mode 1	spanwise distrib for each steady condition
Reduced frequency, mode 2	spanwise distrib for each steady condition
Reduced frequency, mode 3	spanwise distrib for each st eady condition
Twist/flex ratio	spanwise distrib for each steady condition
Incidence	spanwise distrib for each steady condition
Relative Mach	spanwise distrib for each steady condition
Optional:	
Shock location (as % chord)	spanwise distrib for each steady condition
Shock strength (as delta p)	spanwise distrib for each steady condition
Separations (location, size)	spanwise distrib for each steady condition

Table 12. Aerodynamic Y-Factors for DOE 1.

Y-factor	Data type
Wc	Inlet Wc at Peak Effy
Eff	Rotor Peak Effy
PR	Rotor PR at Peak Effy
Ws50	Wennerstrom shock loss @ 50% span
Ws70	Wennerstrom shock loss @ 70% span
Ws80	Wennerstrom shock loss @ 80% span
Ws90	Wennerstrom shock loss @ 90% span
Ws100	Wennerstrom shock loss @ 100% span

Table 13. Mechanical Y-Factors for DOE 1.

Y-factor	Data type
psmax	max pressure surface stress
ssmax	max suction surface stress
plemax	max leading edge PS stress 4-100% span
slemax	max leading edge SS stress 4-100% span
umax tip	max tip deflection
u tiple	tip leading edge deflection
freq 1	frequency margin mode 1
freq 2	frequency margin mode 2
freq 3	frequency margin mode 3
fec 1	placement of 2/rev crossing mode 1
fec 2	placement of 4/rev crossing mode 2
fo dam	fold-over damage

An extensive evaluation of the acoustic, aerodynamic, mechanical and aeroelastic properties of the 25 configurations was performed. The data were all collected into the MINITAB® software to perform regression, analysis of variance, and sensitivity studies. The rotor blade stacking was particularly sensitive to five key parameters:

- Total sound power in the first two harmonics of the rotor/stator interaction noise at 89 percent speed as calculated by SOURCE3D (RSI_89_T)
- Maximum Mach Number relative to the blade leading edge at 89 percent speed as calculated from the mean streamline method (max mrn)
- Fold over damage to the blade from a bird impact at 100 percent speed as calculated by the NOSAPM program (FO Damag)
- Total fan weight flow at the design point as calculated by the inviscid TURBO-AE (Wc)
- Maximum leading edge stress at 100 percent speed as calculated with ANSYS

Maximum leading edge stress was later dropped from the analysis when it was determined that it could be easily controlled with small changes in Ycg. Table 14 shows a summary of the sensitivity study from MINITAB®. The results show that the optimum acoustic, mechanical, aerodynamic, and aeroelastic design is one that has the stacking initially aft for the inboard part of the blade, and then curving forward at the tip, corresponding to Case 14. Figure 56 shows the blade stacking profile as compared to the most aft swept (Case 1), the most forward swept (Case 16), the QHSF I, and the Baseline I sweep distribution. It can be seen from the figure that the slope of the blade near the tip approaches the original QHSF1 design, but the blade as less forward sweep inboard to meet mechanical requirements. Figure 57 shows how the fold over damage criterion had a significant impact on the optimum design selection. Figure 58 shows the decrease in the leading edge shock strength as the forward sweep is increased.

The go-forward design of the rotor was selected to be Case 14a. Case 14a is the optimum configuration from DOE I that was subsequently optimized for Ycg offset in ANSYS to minimize leading edge stress and blade normal Mach number. Figure 59 shows an overlay of the QHSF I fan and the Case 14a fan.

Table 14. Summary of the Sensitivity of the Four Key Parameters to the Rotor Blade Stacking.

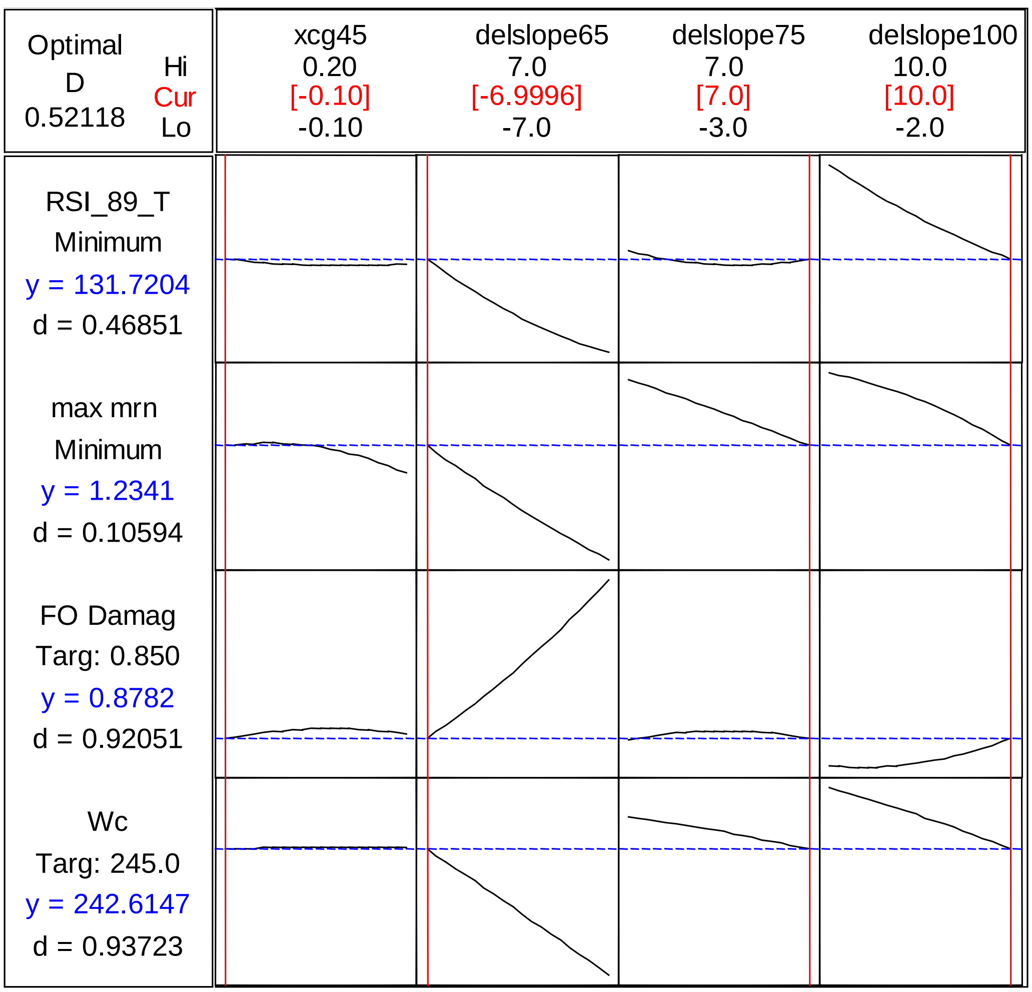

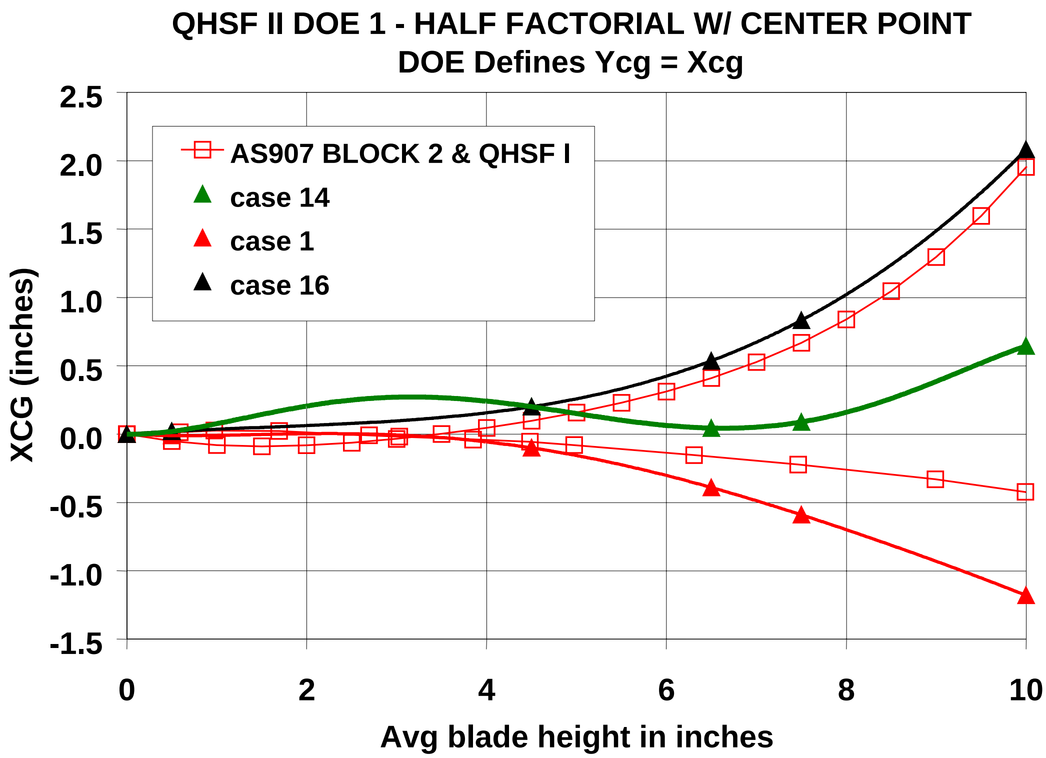

Figure 56. A Go-Forward Blade Stacking Has Been Defined to Meet All Acoustic, Mechanical, Aerodynamic, and Aeroelastic Requirements.

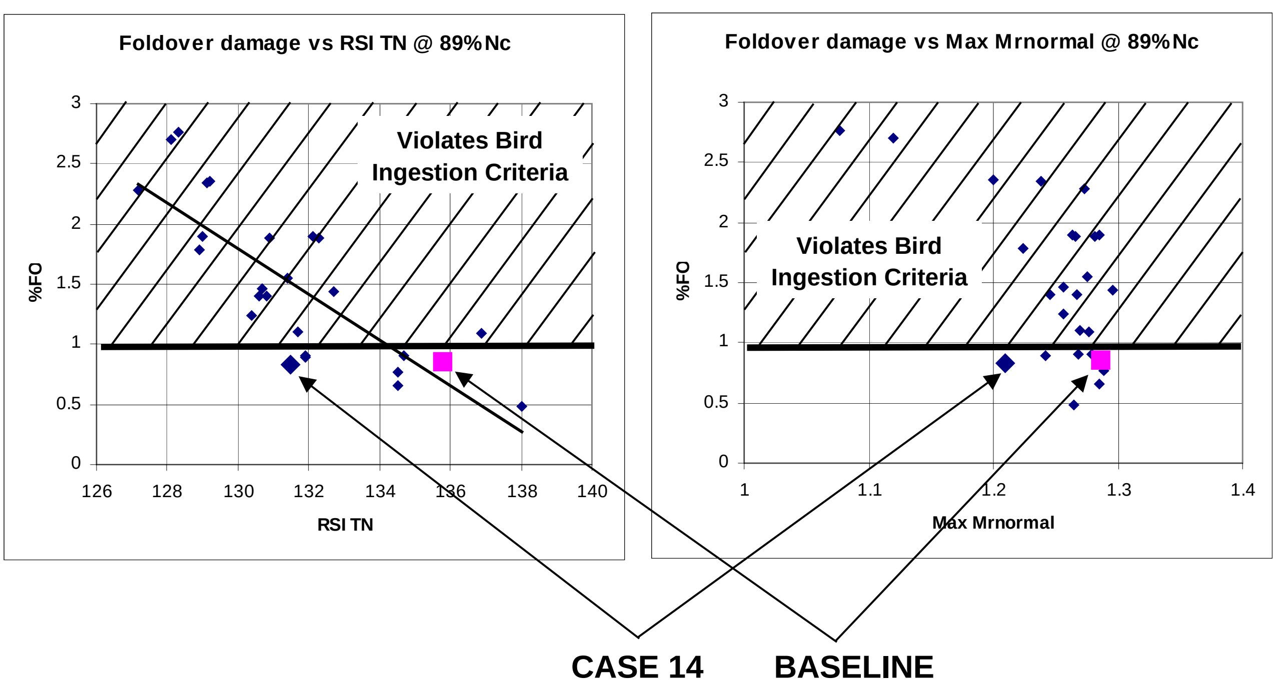

Figure 57. The Bird Strike Criterion Put a Restriction on the Design Space for Rotor DOE 1.

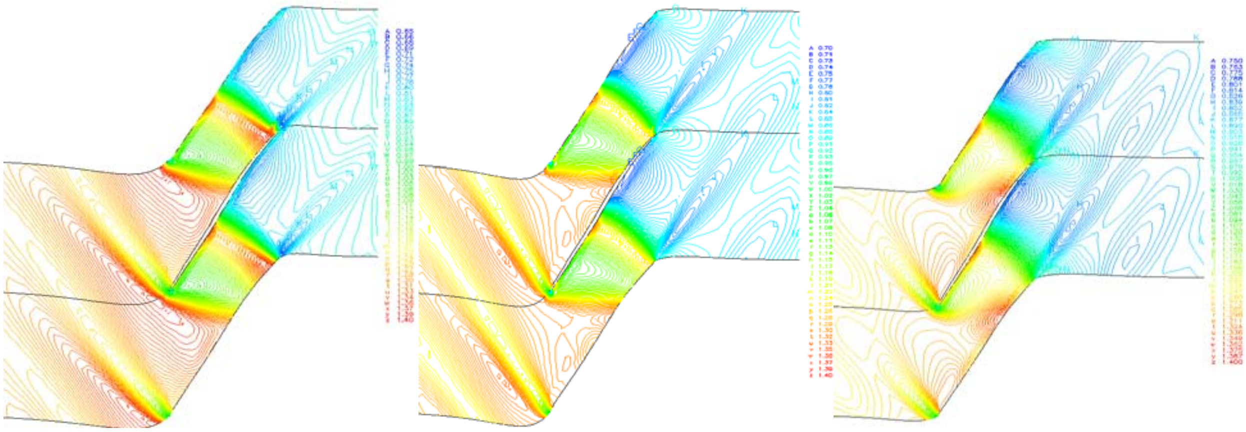

(a) Case 1 (b) Case 14 (c) Case 16

Figure 58. The Strength of the Shock in Front of the Blade Leading Edge at 90% Span Was Shown to Decreased With Increasing Forward Sweep.

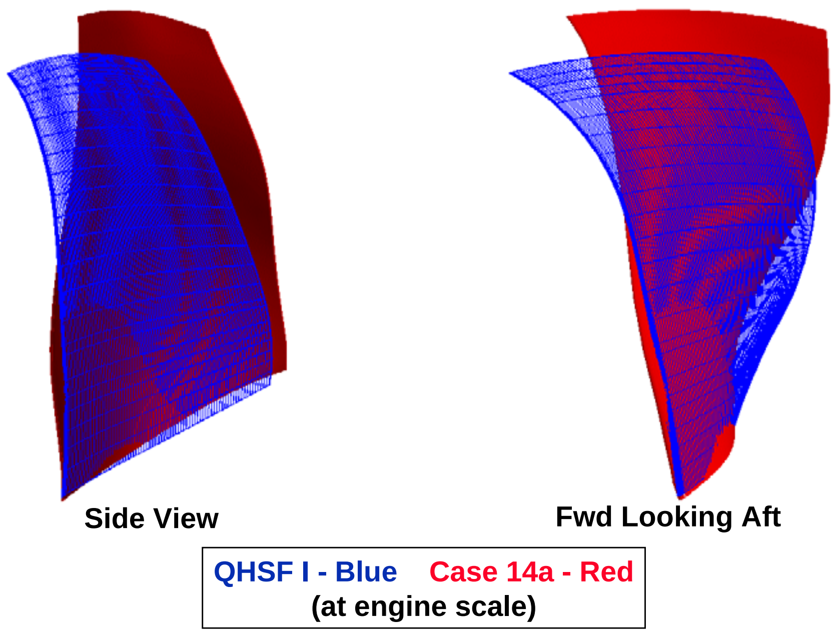

Figure 59. Comparison of the Go-Forward Rotor Blade Design to the QHSF I.

The TURBO code in the inviscid mode was used to evaluate the aeroelastic stability of the 25 configurations for DOE 1. The surprising result was that the instability point was relatively insensitive to the blade rotor blade stacking. Figure 60 shows the variation in the calculated instability point for the 25 configurations.

To assess the acoustic impact of changes in rotor stacking, SOURCE3D predictions were generated for the 25 DOE configurations at 89 percent and 100 percent speed. Figure 61 shows the overall sound power at the blade pass and twice blade pass tone for each of the configurations at 89 percent speed.

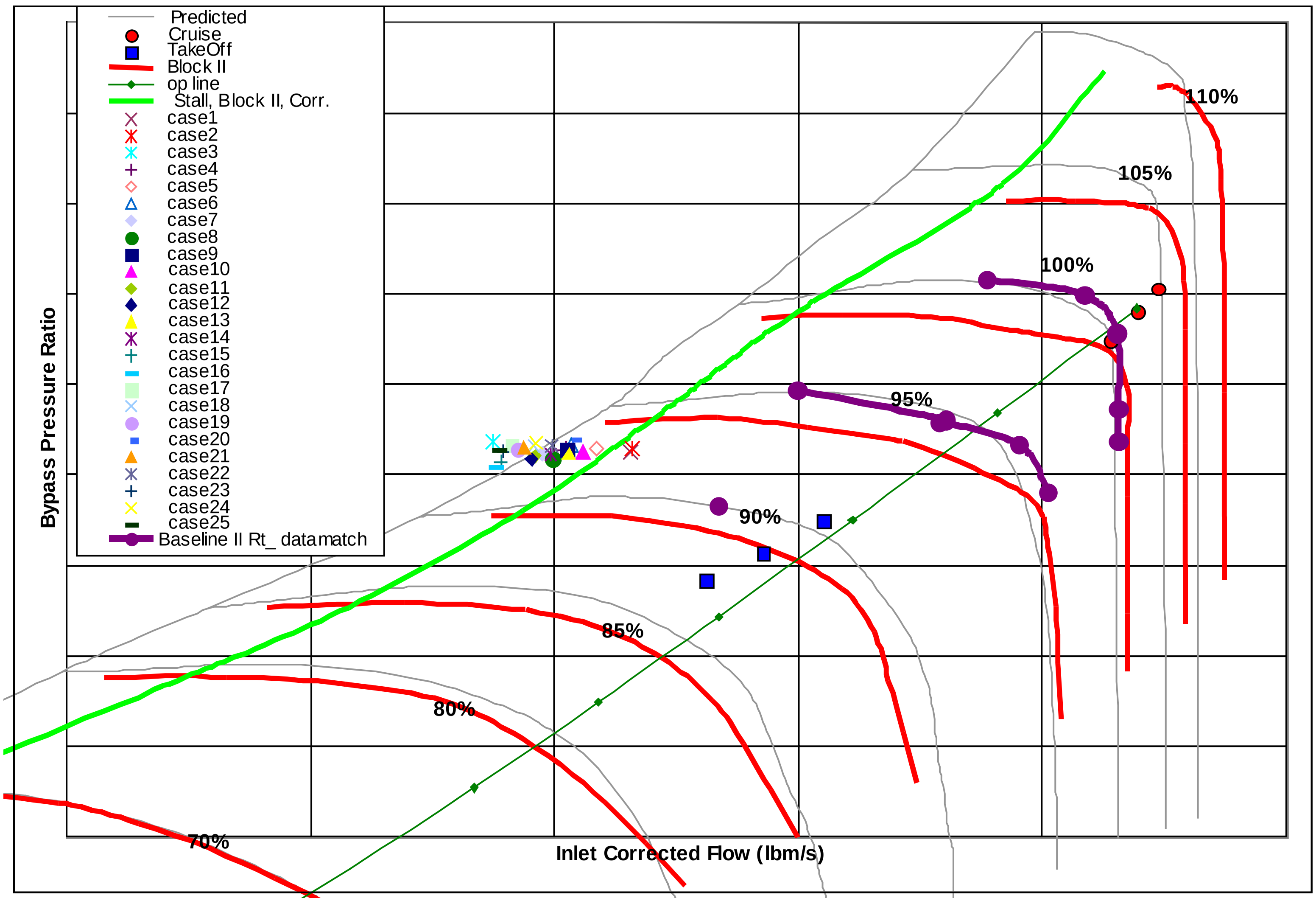

Figure 60. QHSF II, Flutter Boundaries for DOE 1 Cases in Baseline II Tested Map.

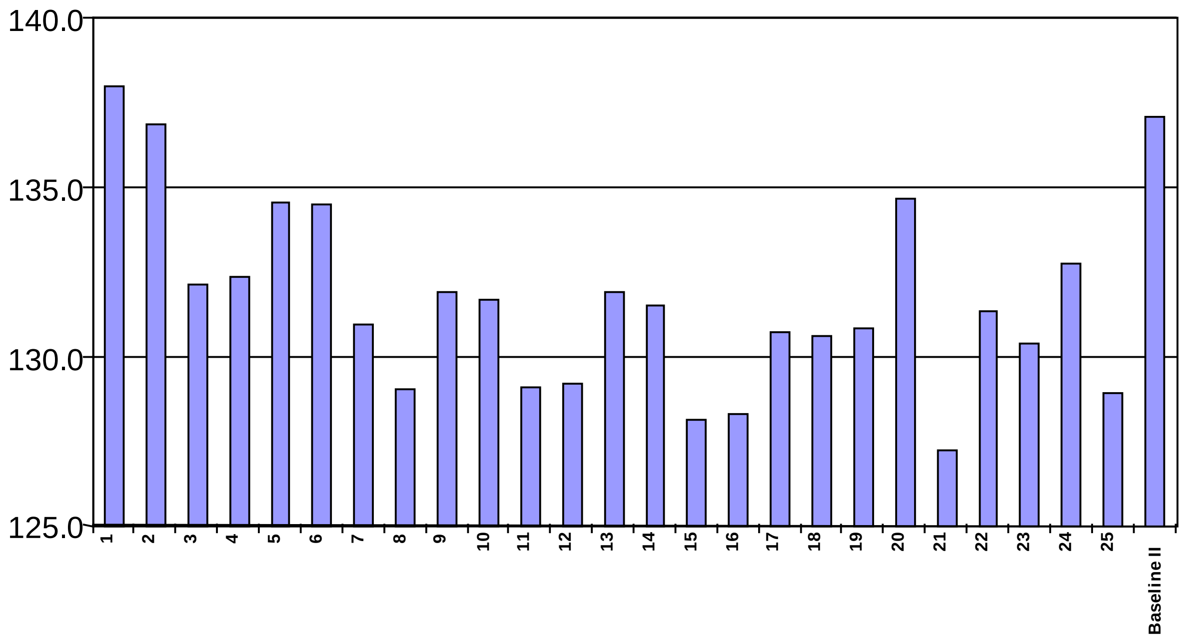

Figure 61. The Logarithmic Sum of the Sound Power Levels for the Rotor-Stator Interaction Noise at 89% Speed Shows Significant Variation for Range of DOE Parameters.

5.3 Aeroelastic Verification of the Case 14a Rotor Design

Confirmation runs for the Case 14a rotor with TURBO in the viscous mode. The aeroelastic behavior of the rotor at 60 percent, 70 percent, 89 percent, and 100 percent was determined to verify the stability of the design throughout the fan operating range.

The steadystate solutions, including the results from both NASA and Honeywell, are shown in Figure 62. All NASA and Honeywell runs are TURBO viscous results at 89 percent speed. There are 3 points on the map based on Honeywell's results: Pexit=14.0, 14.7, and 14.9. The points at Pexit=14.0 and 14.9 are fully converged, but Pexit=14.7 was only run 500 iterations. Both Honeywell and NASA results show a consistent trend along the speed line.

For the unsteady analyses, Honeywell used values of Pexit of 14.7 and 14.9 while NASA used Pexit of 14.28 and 14.84. NASA ran 12 vibratory cycles and Honeywell ran 20 cycles starting from the steady state solutions. All NASA and Honeywell unsteady runs are fully converged according to the convergence history of damping. The extrapolation to obtain the mass flow at zero damping, given in Figure 63, shows some difference between Honeywell and NASA results. In the large part, this is because the damping is relatively high (all above 0.5), so that the extrapolation to zero damping is quite sensitive. If the damping is small (below 0.2), the extrapolation will not be this sensitive. Figure 64 shows the damping extrapolation with pressure ratio. The pressure ratio is not as sensitive as the mass flow because at near stall conditions the speed line is almost flat on the mass flow vs. pressure ratio map (Figure 62).

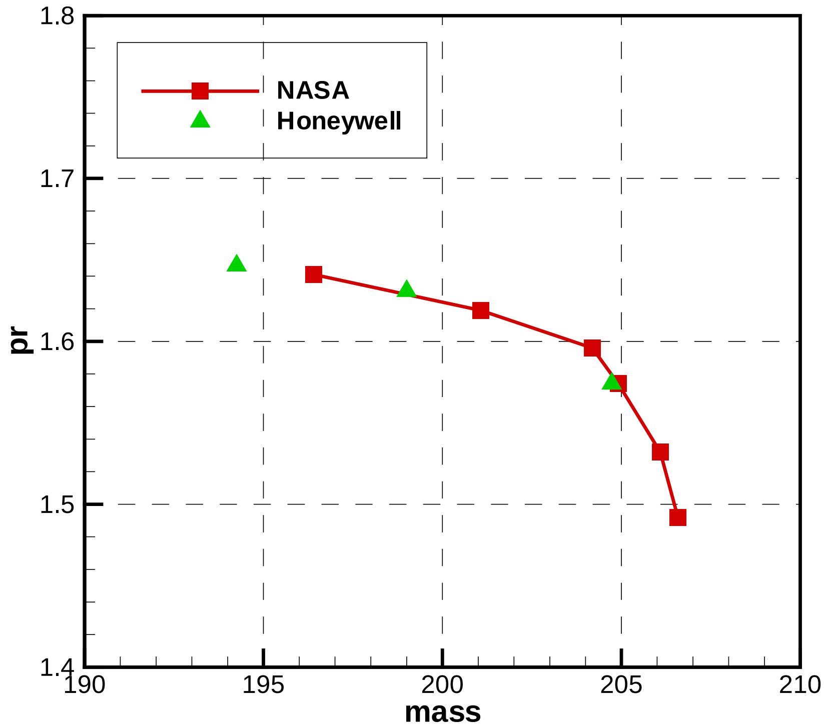

Figure 62. Steady-State Solutions for Pressure Ratio (pr) and Mass Flow Rate (m) at 89% Speed for the Case 14a Rotor Show a Consistent Trend.

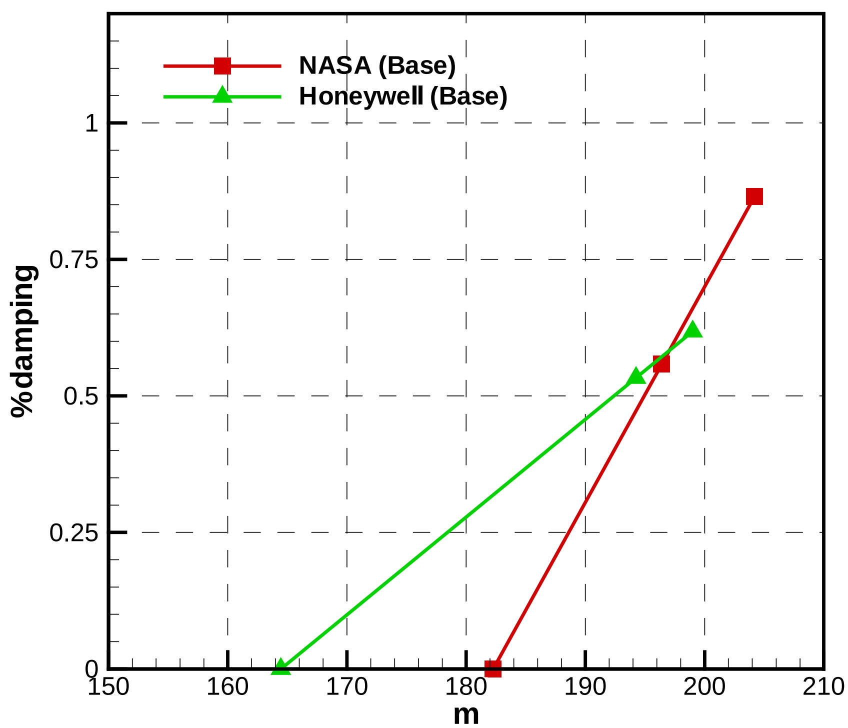

Figure 63. Damping Extrapolation as a Function of Mass Flow Rate (m) Is Shown at 89% Speed for the Case 14a Rotor.

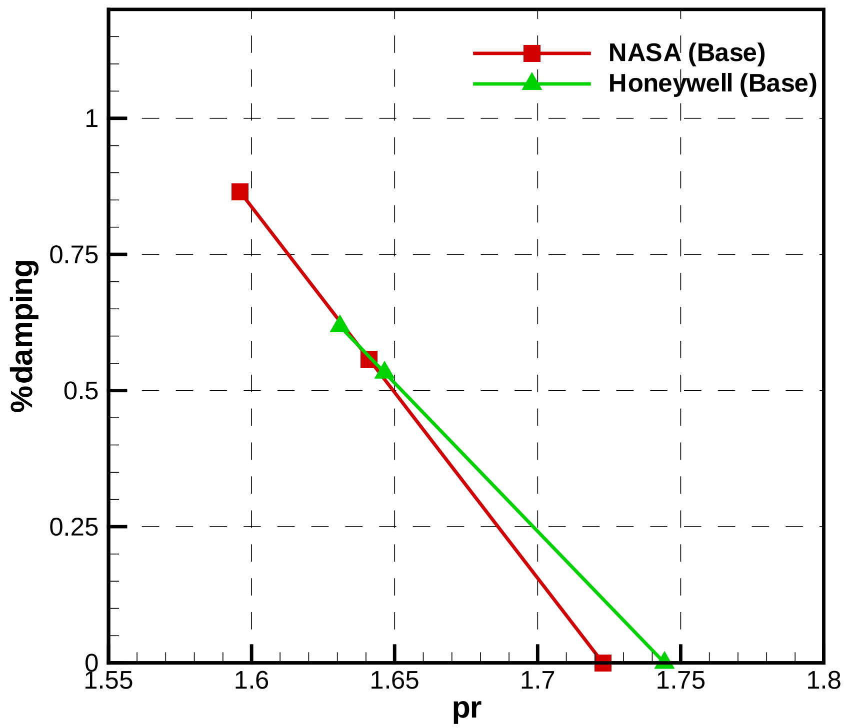

Figure 64. Damping Extrapolation With Pressure Ratio (pr) Is Shown at 89% Speed for the Case 14a Rotor.

Sensitivity studies were conducted with TURBO to determine the influence of reduced frequency and twist to flex ratio on the flutter boundary. The geometry of Case 14a at 89 percent speed was used as the test case. Two operating points, Pexit=14.7 and Pexit=14.9 (fac=1.05 and 1.0643), were used to predict the flutter boundary. Six nodal diameters (0, 2, 4, 6, -2, and –4) were run for each operating point to obtain the least stable nodal diameter.

The reduced frequency of the Case 14a rotor at 87.5 percent span is 0.3423 and 0.3442 for Pexit values of 14.7 and 14.9, respectively. For frequency sensitivity analyses, two reduced frequency cases are run: half and double Case 14a. All other parameters including pressure ratio and mode shape remain the same. The damping plotted in Figure 65 indicates that it is more stable when the reduced frequency is increased. The extrapolation of the damping with pressure ratio given in Figure 66 shows a similar situation.

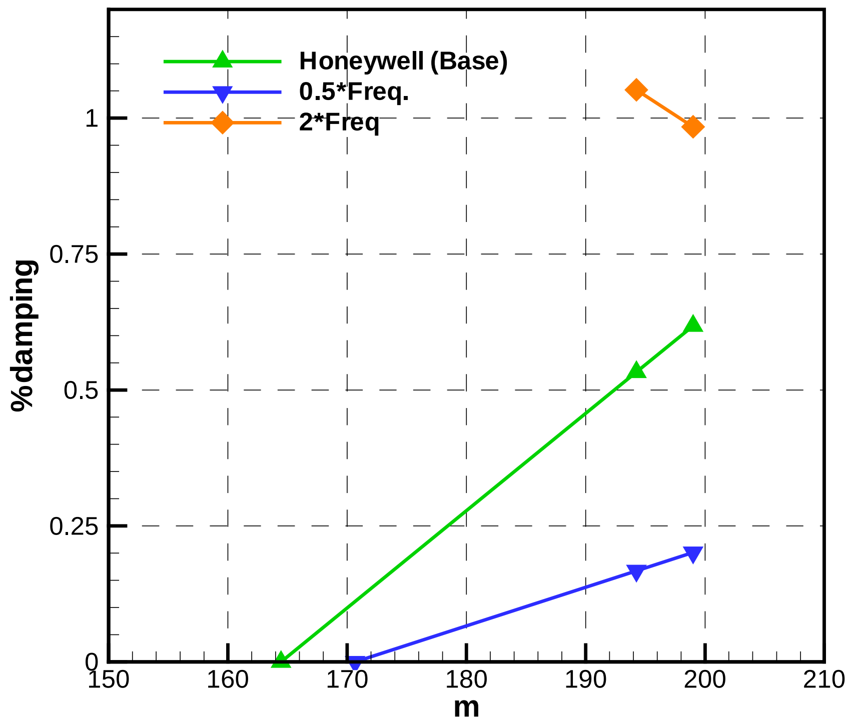

Figure 65. Frequency Sensitivity: Damping Extrapolation With Mass Flow Rate (m) Is Shown at 89% Speed for the Case 14a Rotor.

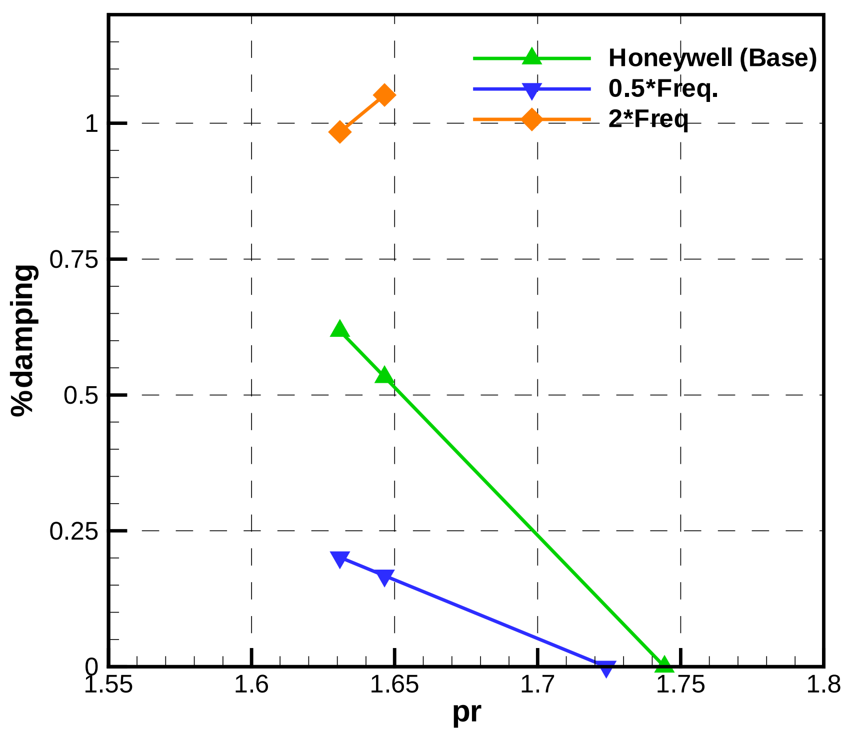

Figure 66. Frequency Sensitivity: Damping Extrapolation With Pressure Ratio (pr) Is Shown at 89% Speed for the Case 14a Rotor.

Two new mode shape files were created for the twist-to-flex ratio sensitivity analyses. The twist-to-flex ratio of zero is pure bending at 87 percent span while the twist-to-flex ratio of infinity is pure torsion. The amplitude of the movement of airfoil at each span-wise location is similar to the Case 14a, which has a twist-to-flex ratio of approximately 0.4. With reduced frequency fixed, Figure 67 and Figure 68 show that it is more stable when twist-to-flex ratio is small. This aeroelastic sensitivity study has quantified the sensitivity of aerodynamic damping to changes in the frequency and the mode shape, which will be useful in assessing the design trade-off during the QHSF II design effort.

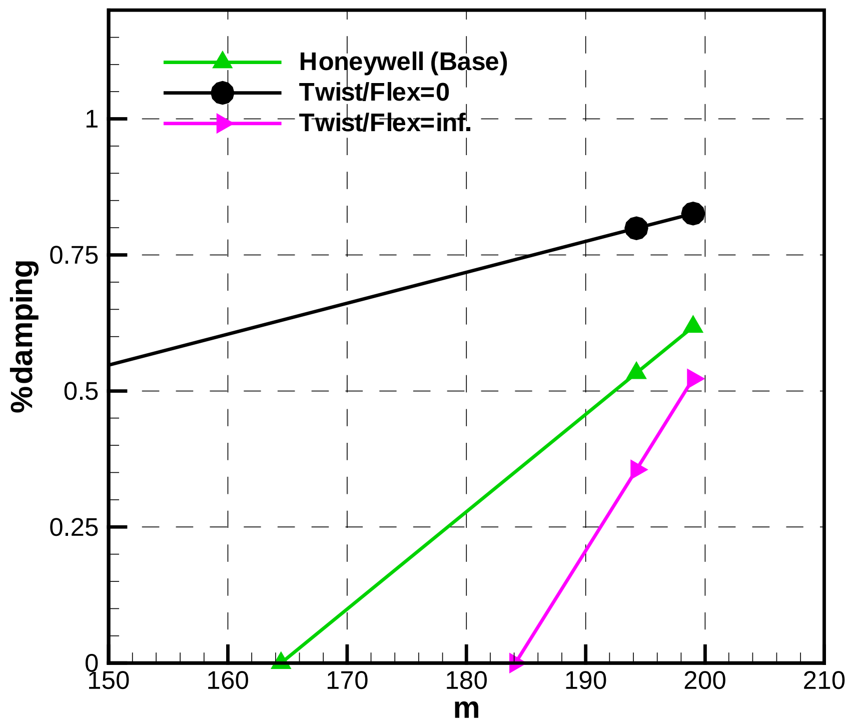

Figure 67. Twist-to-Flex Ratio Sensitivity: Damping Extrapolation With Mass Flow Rate (m) Is Shown at 89% Speed for the Case 14a Rotor.

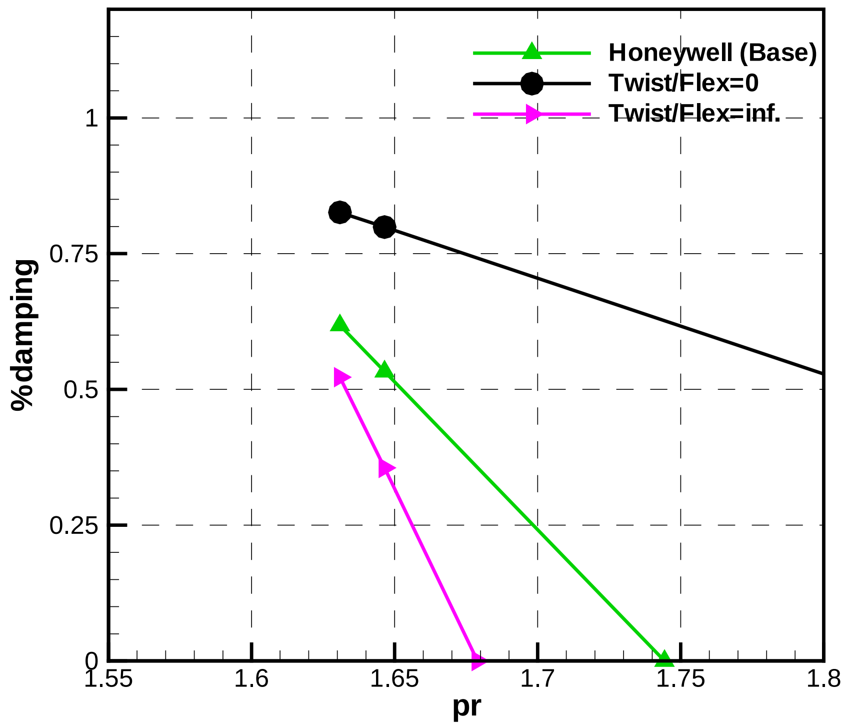

Figure 68. Twist-to-Flex Ratio Sensitivity: Damping Extrapolation With Pressure Ratio (pr) Is Shown at 89% Speed for the Case 14a Rotor.

Figure 69 shows a summary of the aeroelastic analysis of the Case 14a rotor. A qualitative assessment of the predicted instability points produced the stability line on the figure.

The viscous TURBO analysis indicates that the fan will have a potential stability problem at 70 percent speed. The near stall steady-flow results at 70 percent speed show flow separation on the suction surface at about 75 percent span. The Case 14a fan was rerun using TURBO in the inviscid mode to compare to viscous solution obtained from NASA. It was first verified that the steady inviscid solution did not show any flow separation. Figure 70 shows the mass flow rate versus pressure ratio map from the TURBO steady solutions for the 70 percent speed line. As expected, the inviscid TURBO solution predicts higher flow with the same pressure ratio (or higher pressure-ratio with the same flow) than the viscous solution. For each operating point, TURBO unsteady flutter solutions were run for nodal diameters of 0, 2, 4, 6, and –2. Typical unsteady convergence histories of the damping are shown in Figure 71. The unsteady runs are fully converged for a total of 20 vibratory cycles from the steady state solutions. The resulting damping versus nodal diameter comparison is given in Figure 72. The minimum damping occurs between nodal diameters 0 and 2. The damping versus mass flow rate comparison of the inviscid results with the viscous results is given in Figure 73. The inviscid results show that instability point occur at a slightly lower mass flow rate than viscous results, but the design still becomes unstable in the operating rage below stall. This small shift in the stability point is probably due to the viscous solution showing a separation which inviscid solution did not capture.

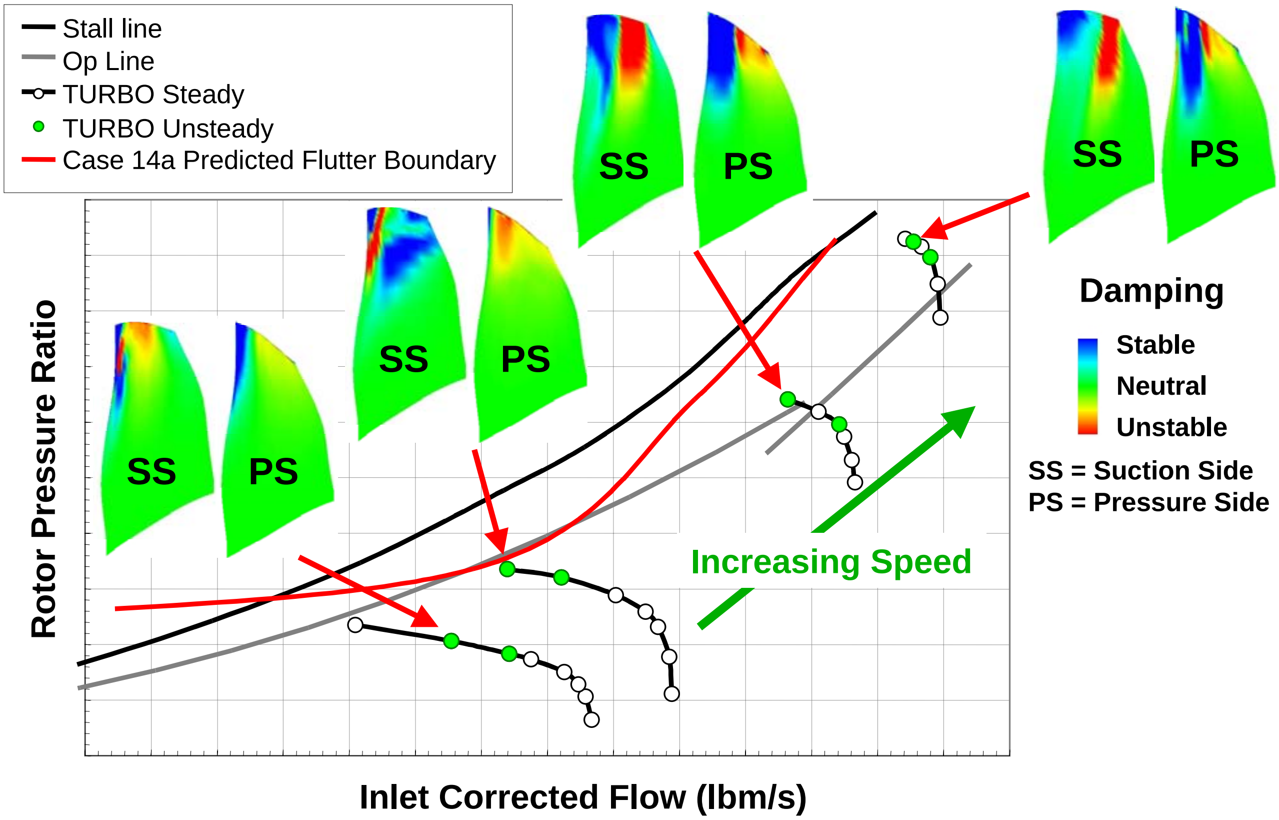

Figure 69. Analysis of the Case 14a Rotor Blade With TURBO Shows That the Blade Is Unstable Near the Operating Line at an Intermediate Speed Condition.

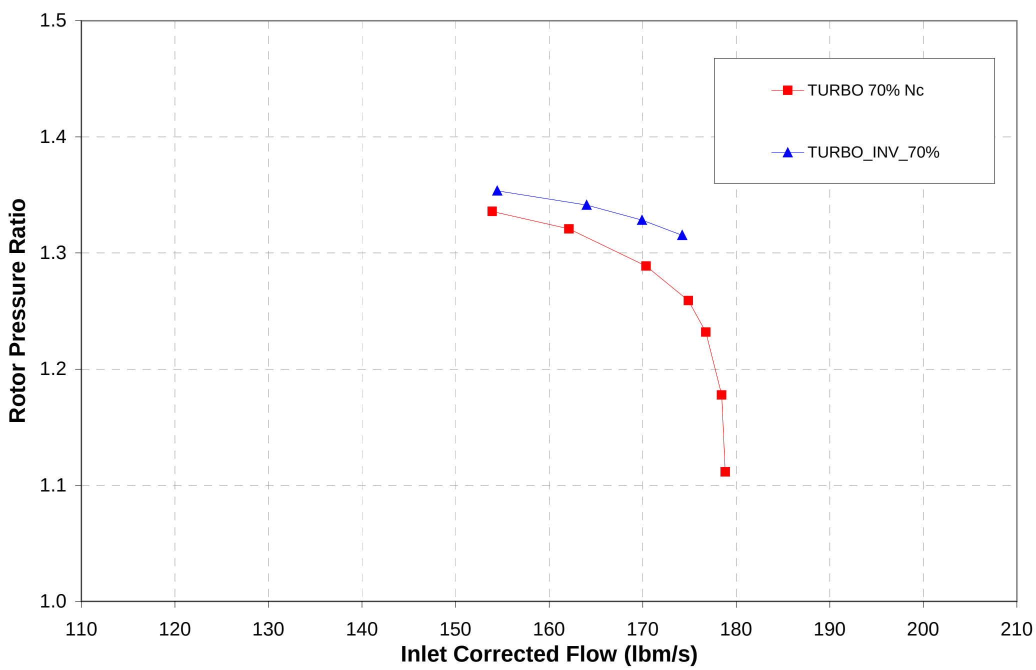

Figure 70. The Steady Flow Results From Inviscid TURBO Show the Expected Change in Pressure Ratio and Flow Characteristics From the Viscous TURBO Results.

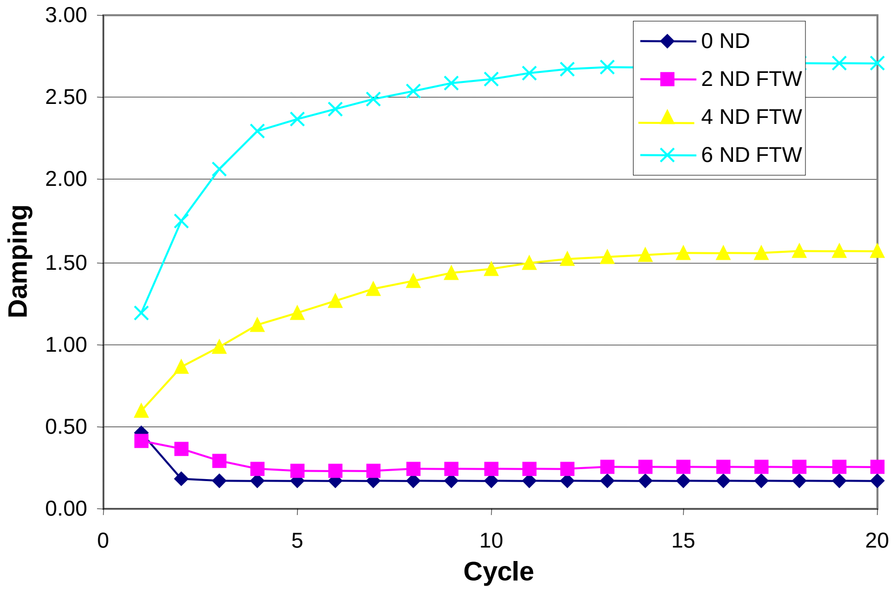

Figure 71. A Satisfactory Convergence History Was Obtained With the Viscous TURBO Analysis.

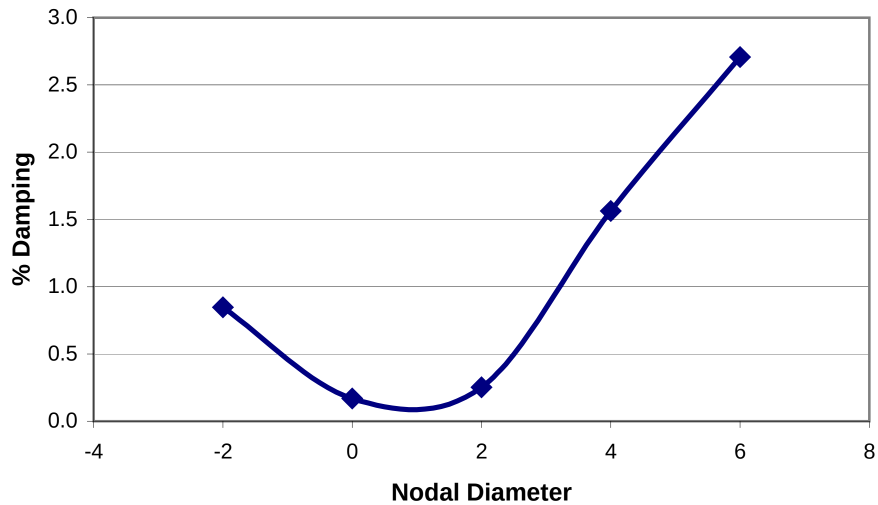

Figure 72. The Minimum Damping for the Inviscid Analysis of the 70% Speed Line Occurs Between 0 and 2 Nodal Diameters.

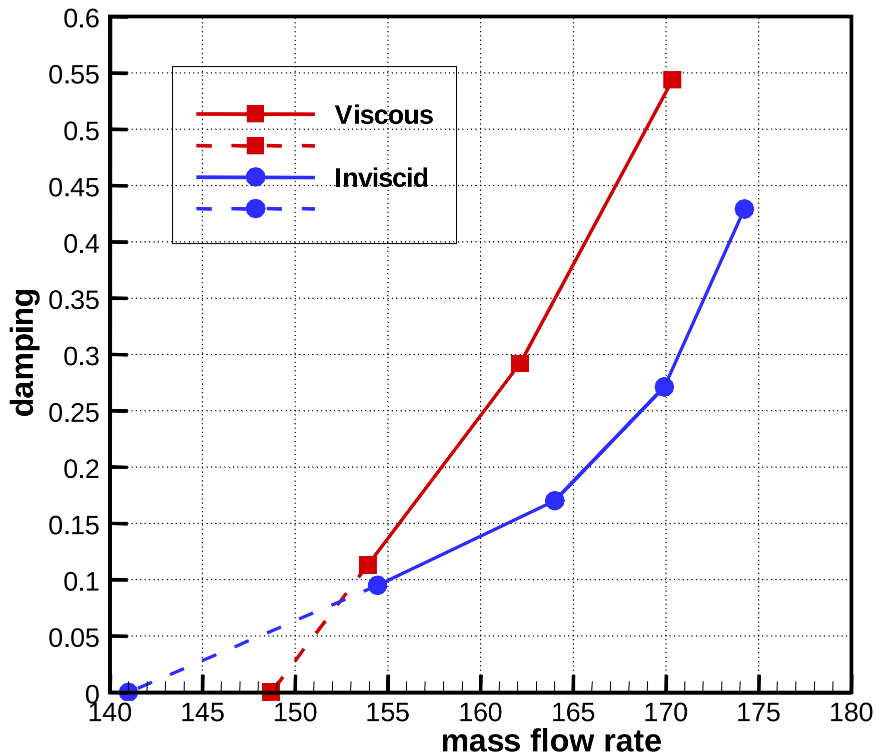

Figure 73. The Inviscid TURBO Results Show a Slight Improvement in Stability Over the Viscous Results.

The TURBO results for Case 14a showed a small region of flow separation (Figure 74 and Figure 75). It was decided to continue the analysis with rotor ITER07, on which the rotor performance was closer to design intent and no separation was seen (Figure 76). The previous Case 14a TURBO analyses were conducted with mode shapes from an airfoil-only ANSYS model. It was discovered that there was a significant change in the mode shapes and frequencies for Case 14a with the attachment (unlike the results for QHSF I). It appears that rotor blade ITER07, with blade/attachment mode shapes and frequencies, is a stable configuration.

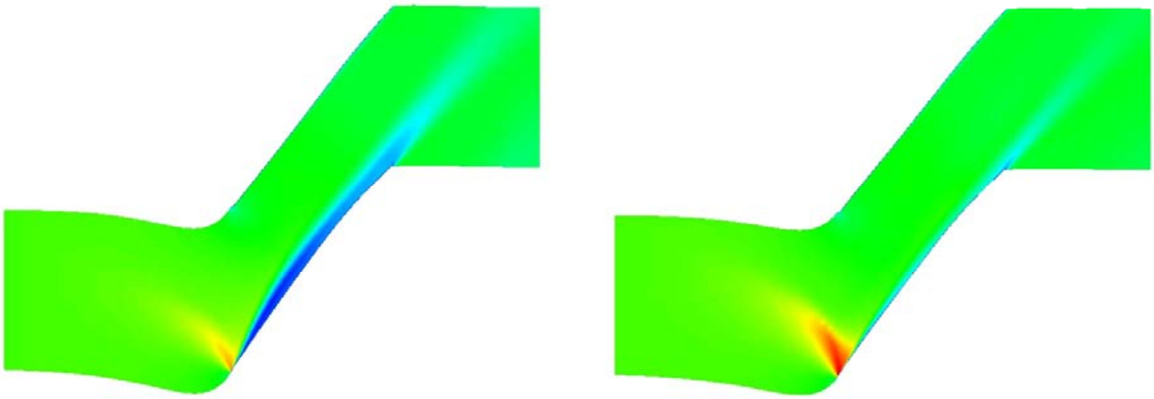

(a) Case 14a (b) ITER07

Figure 74. Mach Number Contours in the Blade Passage Show a Region of Flow Separation in the Case 14a Rotor Design.

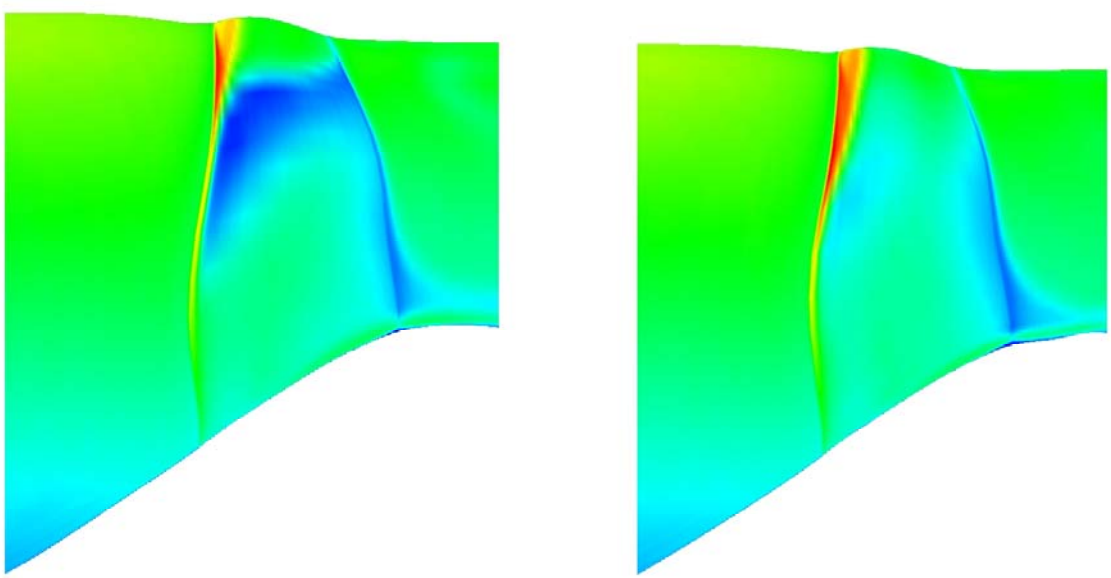

(a) Case 14a (b) ITER07

Figure 75. Mach Number Contours Near the Blade Suction Surface Show a Region of Flow Separation in the Case 14a Rotor Design.

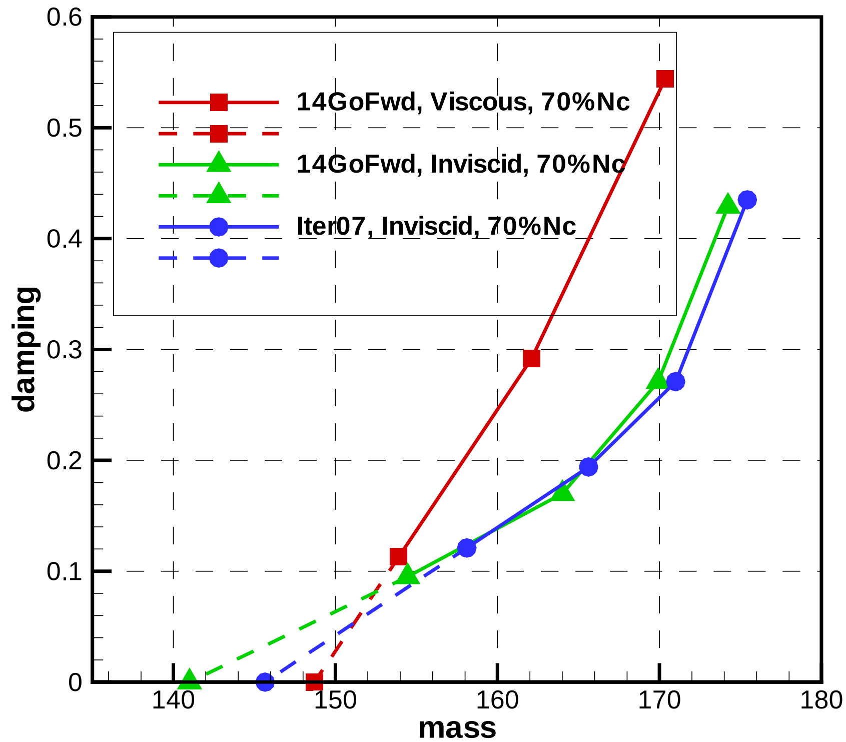

Figure 76. The Aerodynamic Damping as a Function of Mass Flow Rate (Mass) Shows the Small Effect of the Separation Region on the Blade Stability.

5.4 Justification for the Use of the TURBO Evaluation of the Case 14a Rotor

The TURBO code was a key element in the design of QHSF II. The QHSF I design relied on the empirical guidelines available at that time to determine the acceptability of the fan blade design from a stability standpoint. The stability assessment was based on the consideration of reduced frequency, defined as

$$k = \frac{b\omega}{V}$$

where
k = reduced frequency
b = half-chord (true chord/2)
ω = circular frequency
V = reference velocity

Honeywell has defined critical reduced frequency values based on experience to assure a stable design; the reduced frequency must be above the critical values of

$k > 0.165$ for pure bending
$k > 0.80$ for pure torsion

For these calculations, the parameters are based on values at 75 percent span for design point conditions. (In the QHSF I final report, an equivalent parameter called the "flutter parameter" was used. Honeywell has since adopted the industry standard "reduced frequency" and the criteria have been updated accordingly.)

For the QHSF I, the reduced frequency was calculated for each mode. Then each mode was classified as either a bending mode or a torsion mode so that the reduced frequency could be compared to the appropriate criterion. This classification was based on a calculation of the twist-to-flex ratio, which quantifies the amount of torsion in a particular mode and is defined by

$$\psi = \frac{b\alpha}{h}$$

where
ψ = twist-to-flex ratio
b = half-chord (true chord / 2)
α = angular deflection in mode shape (pitching motion)
h = translational deflection in mode shape (plunging motion).

The value of the twist-to-flex ratio at the 75 percent and 95 percent spans was determined. For modes with small values of twist-to-flex ratio, the bending criterion was applied; for larger values, the torsion criterion was used. For example, mode 1 had a twist-to-flex value at each span of approximately 0.4, and the mode was classified as a bending mode. The reduced frequency was about 0.3, which is above the criterion of 0.165 for pure bending modes, and so the blade should be stable based on this empirical guideline. Other modes similarly met the appropriate guidelines.

Obviously, this approach was not successful in QHSF I, as flutter was encountered for mode 1 at part speed conditions near the stall line. There were a number of contributors to the breakdown of the design criteria. Note that in the empirical approach outlined above, there is no consideration of engine speed, operating condition along a speed line, incidence, shock location, contribution from tip effects, etc. All of these are known from experimental data and previous computational studies to be important contributors to the actual flutter behavior. Flutter is also known to be very sensitive to mode shape. The mode shape was considered only to calculate twist-to-flex to determine the criterion to be used, and the classification was based on judgement. (Note that if mode 1 had been classified as a torsion mode, flutter would have been expected.) At the time, there was no criterion for modes with intermediate values of twist-to-flex ratio.

The QHSF I experience is an example that highlights the need for advanced computational tools such as TURBO-AE, and demonstrates that the use of the tool is crucial to have a successful redesign effort in the QHSF II program. With these advanced tools, the effects that are known to be important can be addressed directly. The entire blade is included, rather than just a single representative span. The actual mode shape calculated by finite element analyses is used. And the steady flow field is based on the actual speed and operating conditions.

The potential benefits of using TURBO-AE are clear, given that it successfully predicts the QHSF I design to be unstable. If the tool had been available during the original design, the flutter would have been predicted and changes could have been incorporated during the design phase to eliminate the problem. A second benefit has already occurred during the QHSF II design work. We had assumed up to this time that the forward sweep of the QHSF I was a significant de-stabilizing influence. However, our results have clearly shown that this is not true, and forward sweep actually has a small benefit for flutter. This insight has had a significant effect on our design approach.

TURBO-AE was applied to predict the aeroelastic stability of the Case 14a rotor and determined that it was not stable on the 75 percent speed line near stall. This result would not have been determined from analysis of reduced frequency and twist-to-flex ratio. Figure 77 shows a plot of the reduced frequency as a function of incidence. Two points are shown on the figure for each speed: one at peak efficiency and one near the stall line. There is nothing in this data that signals that the 70 percent speed line should be unstable as compared to the other speed lines. A similar conclusion is reached from the reduced frequency vs. twist-to-flex ratio plot shown in Figure 78.

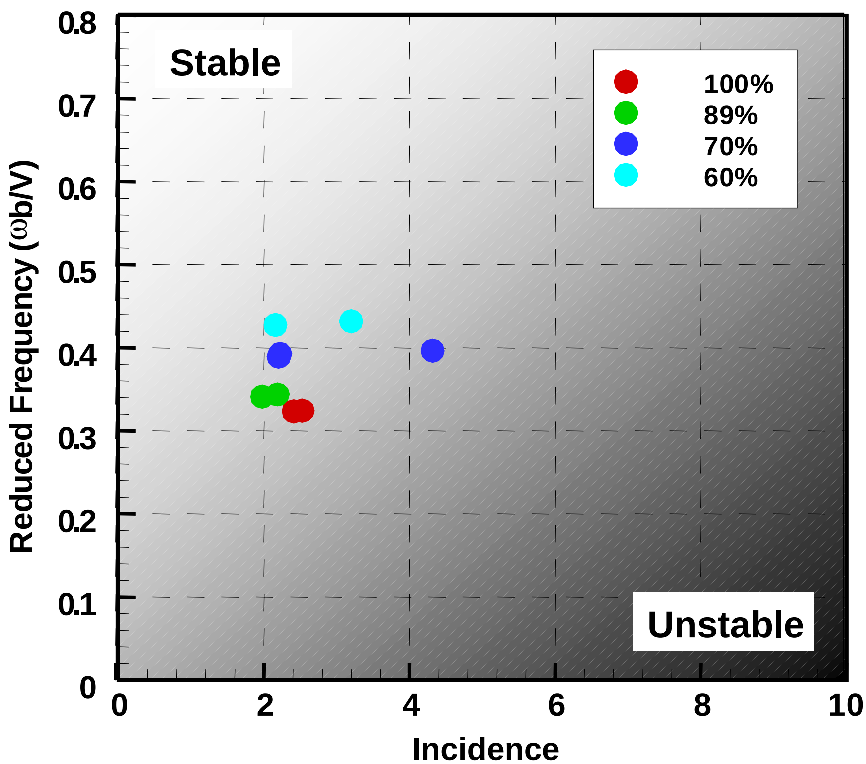

Figure 77. Evaluation of the Reduced Frequency of the Case 14a Rotor Blade Does Not Identify the Instability at 70% Speed.

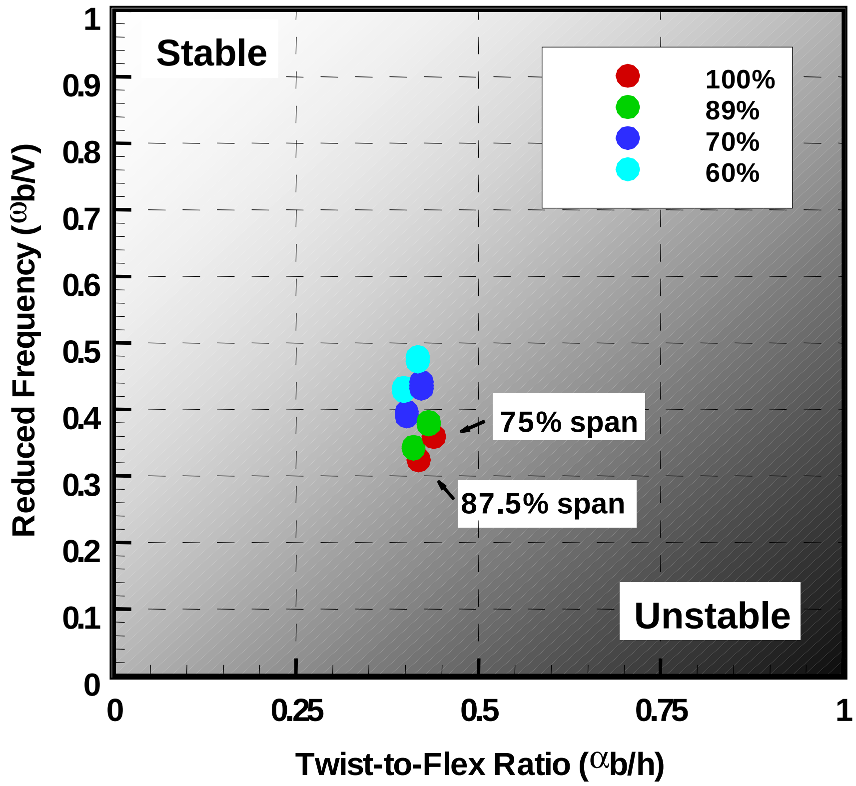

Figure 78. Evaluation of the Reduced Frequency of the Case 14a Rotor Blade Does Not Identify the Instability at 70% Speed.

In summary, the reduced frequency limit is a useful guideline to distinguish blade designs and/or modes that are either very stable (so that further detailed analysis is not necessary) or very unstable (so that a significant design change is needed to eliminate flutter) from marginally stable designs. As such, it can be a very effective screening tool. Recent experience indicates that modern fan designs result in blades where factors such as mode shape and operating conditions must be taken into account. In these cases, the use of an advanced computational tool such as TURBO-AE is crucial in properly determining the stability of the design. In the QHSF II, we are using TURBO-AE as part of a Design of Experiments approach to help identify the factors that are de-stabilizing the blade. TURBO-AE is needed in the detailed blade design process to define an aeroelastically stable fan design.

5.5 Final Rotor Optimization

An ADPAC 3-D viscous CFD model of the Case 14a rotor and the Baseline II stator was developed to do detailed analyses of the fan stage. This model was used to optimize the rotor blade thickness and incidence distribution.

The ADPAC full-stage model is comprised of two rotor blocks, one core stator block, one core duct/strut block, one bypass stator block and one bypass duct/strut block. This split-flow modeling technique, using separate core and bypass stream throttle pressures, has been shown to be necessary to properly establish the prescribed fan bypass ratio using current CFD codes. Otherwise, the rotor passage shock in the tip region will not be properly located for the aerodynamic design reference conditions. The complex grid structure for the full-stage ADPAC model introduced a new complication to the post-processing analysis due to the highly skewed grid surfaces in the rotor (see Figure 79). Grid surfaces could no longer be assumed to approximate streamline surfaces through the rotor passage, prompting a modification to the post-processing code that provides flow properties along quasi-streamlines.

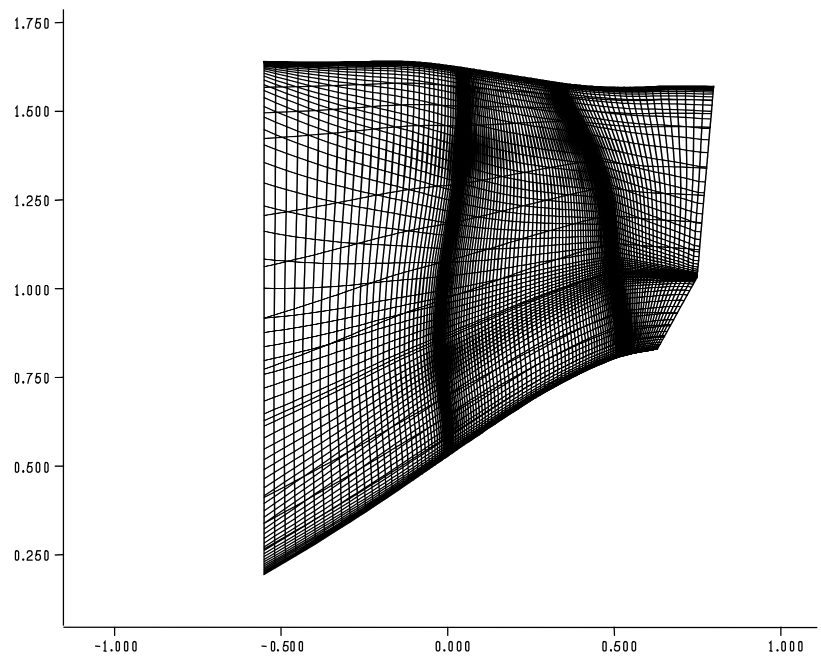

Figure 79. Comparison of the ADPAC Computational Grid for the Split-Stator Configuration With the Streamline Pattern.

Since the CFD analysis of the rotor for DOE 1 was performed in TURBO, it was desirable to compare the TURBO and ADPAC analysis results for Case 14a to ensure that the transition to a different software tool did not change the performance of Case 14a. Figure 80 shows a comparison of the Mach number contours at two different radial positions for the two codes. Figure 81 shows a comparison of the Mach number contours near the suction and pressure surfaces for the two codes. Little difference is seen for the two models.

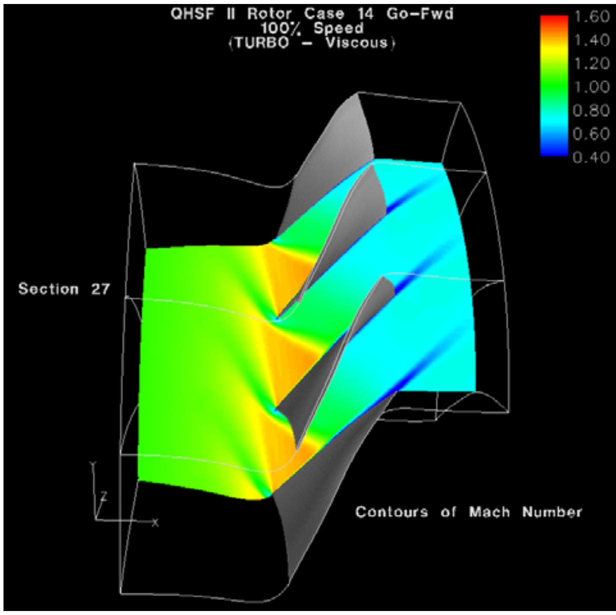

(a) TURBO – 60.1% span

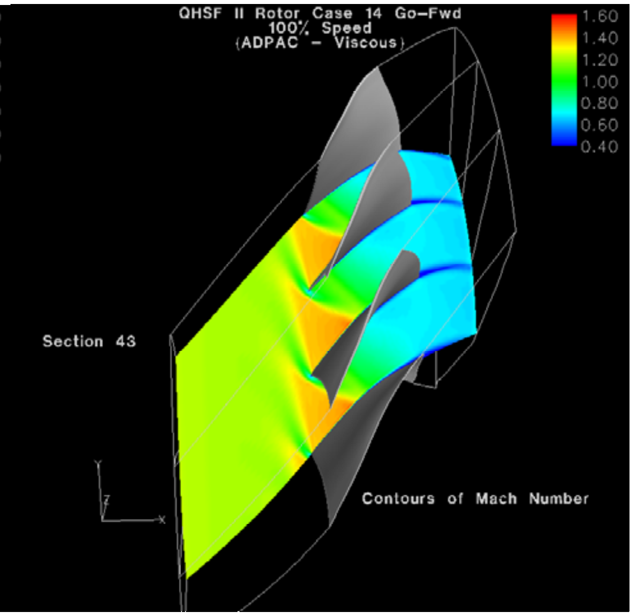

(b) ADPAC – 60.1% span

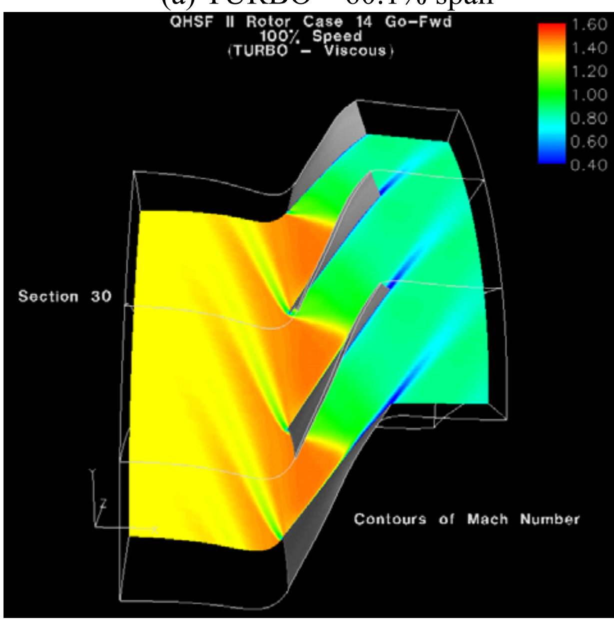

(a) TURBO – 80.0% span

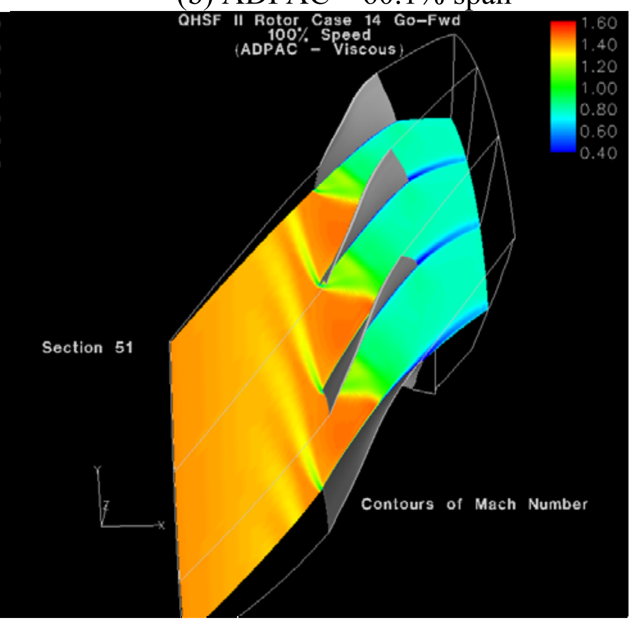

(b) ADPAC – 80.0% span

Figure 80. A Comparison of the TURBO and ADPAC Mach Number Contours Shows No Significant Flowfield Differences.

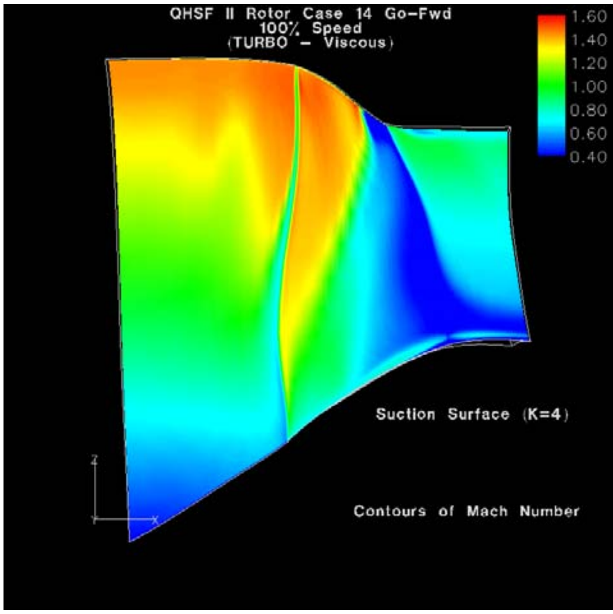

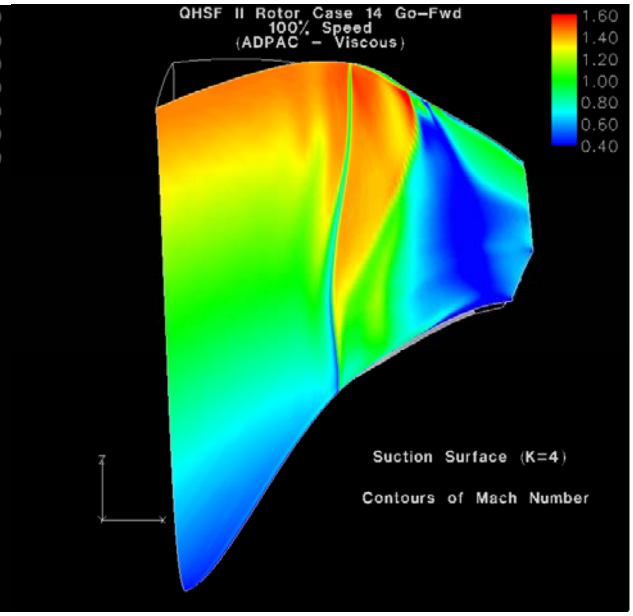

(a) TURBO – Suction Surface (b) ADPAC – Suction Surface

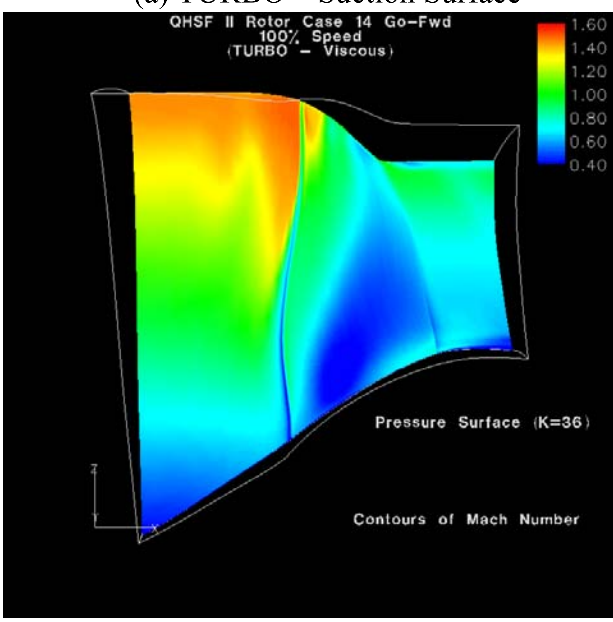

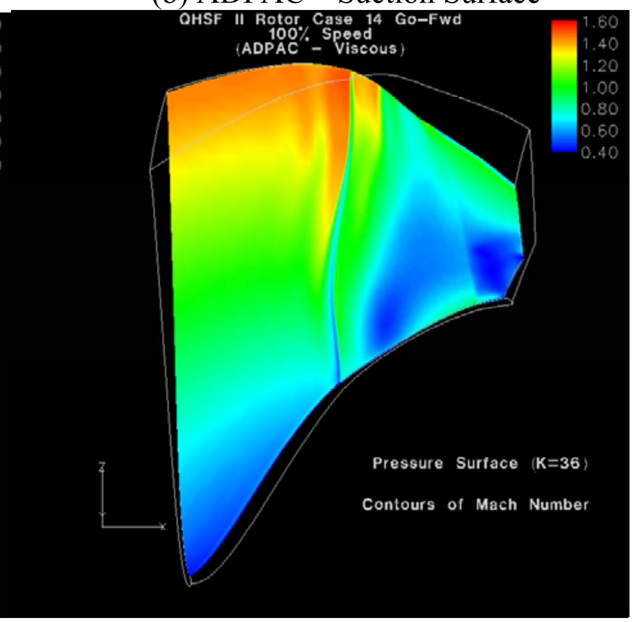

(a) TURBO – Pressure Surface (b) ADPAC – Pressure Surface

Figure 81. A Comparison of the TURBO and ADPAC Mach Number Contours Shows No Significant Flowfield Differences.

To begin the process of optimizing the Case 14a rotor aerodynamic design, several rotor airfoil models with different mean line angle distributions were constructed using the streamline curvature/airfoil generator code. Vibration characteristics of the resultant blades (i.e., airfoil plus attachment) were analyzed. CFD analyses of the airfoils were performed on the candidate mean line distributions.

In response to the decision to return to the full-span stator design of QHSF I, the ADPAC model was then modified to include the full span stator design. After completion of the revision, the rotor evaluations were resumed.

For the Case 14a rotor aerodynamic design, several rotor airfoil models with different mean line angle distributions were analyzed with the ADPAC code to optimize rotor performance. Airfoil changes include modifications to incidence, angle passage area distribution, and turning, such that rotor performance was brought closer to design point objectives. These initial ADPAC analyses show that design flow can be achieved as shown in Figure 82.

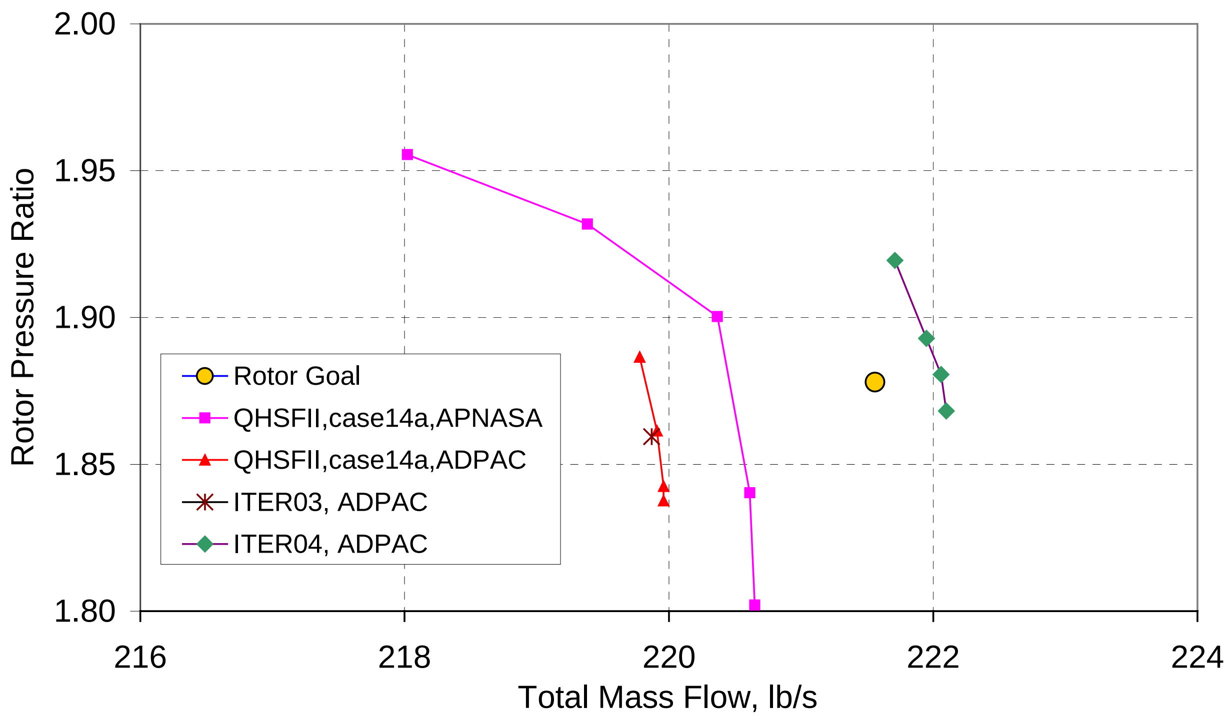

Figure 82. Preliminary ADPAC Results Show That the Case 14a Rotor Has the Potential to Meet the Design Point Flow and Pressure Ratio by Adjusting the Mean Line Angle Distribution.

A total of 25 configurations were analyzed with ADPAC (referred to as ITER01 to ITER25).

A Campbell diagram (shown in Figure 83) of design iteration ITER07 indicated a mode 2/3E crossing at 100 percent RPM. A study was completed to assess tradeoffs between blade and attachment weight for optimum mechanical performance. Figure 84 illustrates the ITER07 status relative to the mechanical design goal. Based on the results of this study, a sloped attachment was selected, which results in adequate frequency margin with minimal aeroelastic risk. Figure 85 confirms that the design goals have been achieved with the sloped attachment.

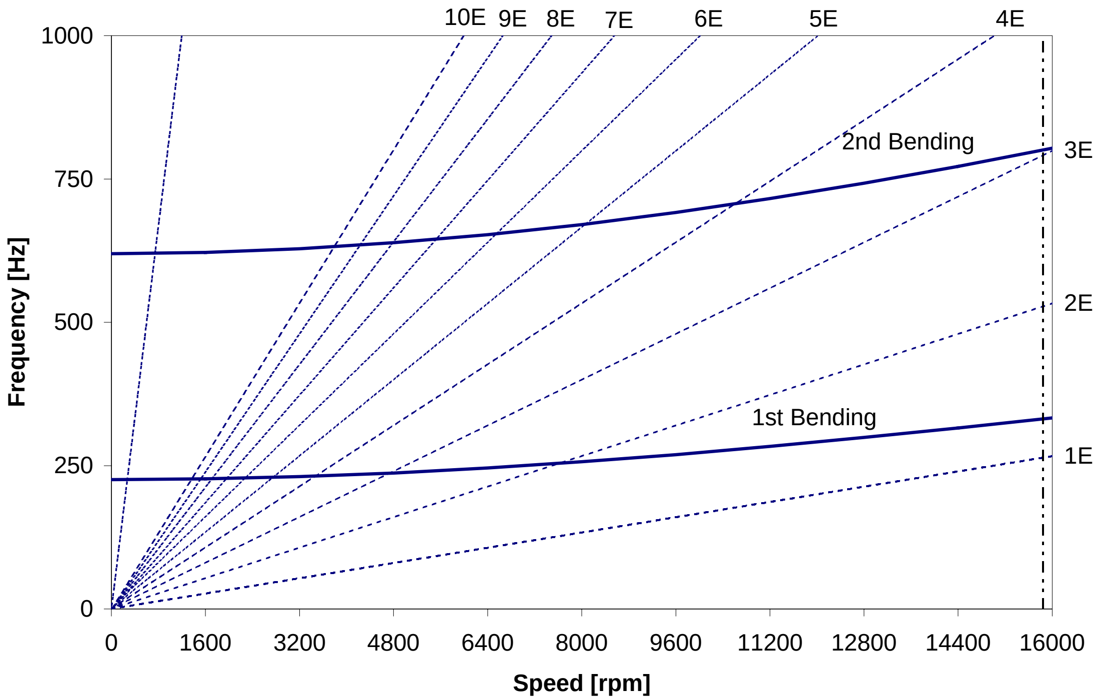

Figure 83. The ITER07 Case Shows Mode 2/3E Crossing at 100% RPM.

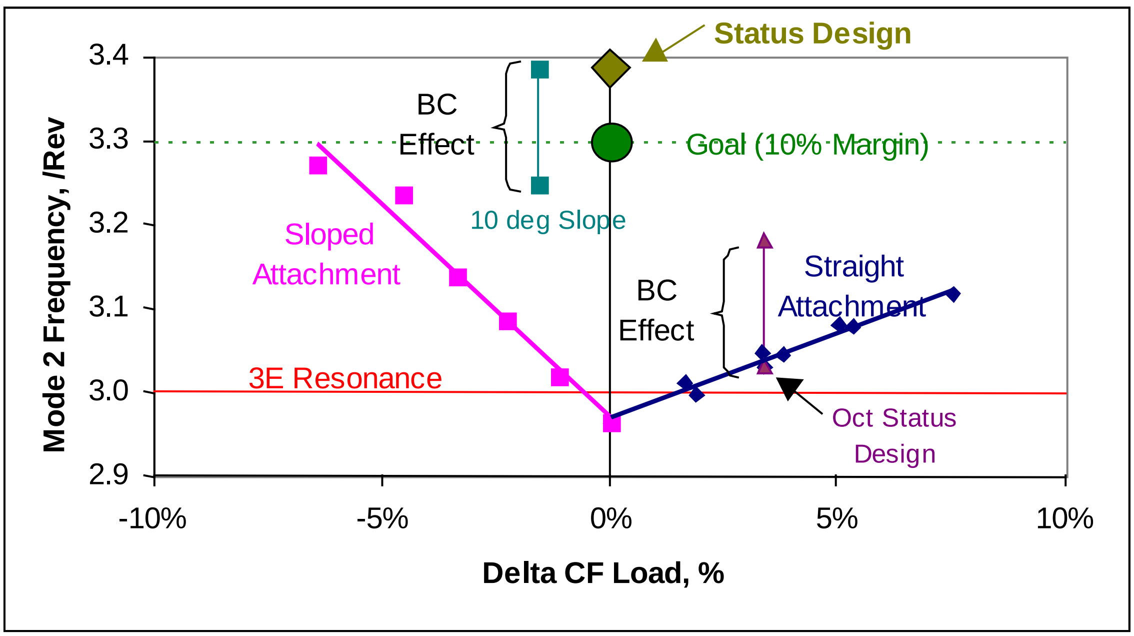

Figure 84. A Design Study Completed to Restore Adequate Frequency Margin Suggested Sloped Attachment Solution.

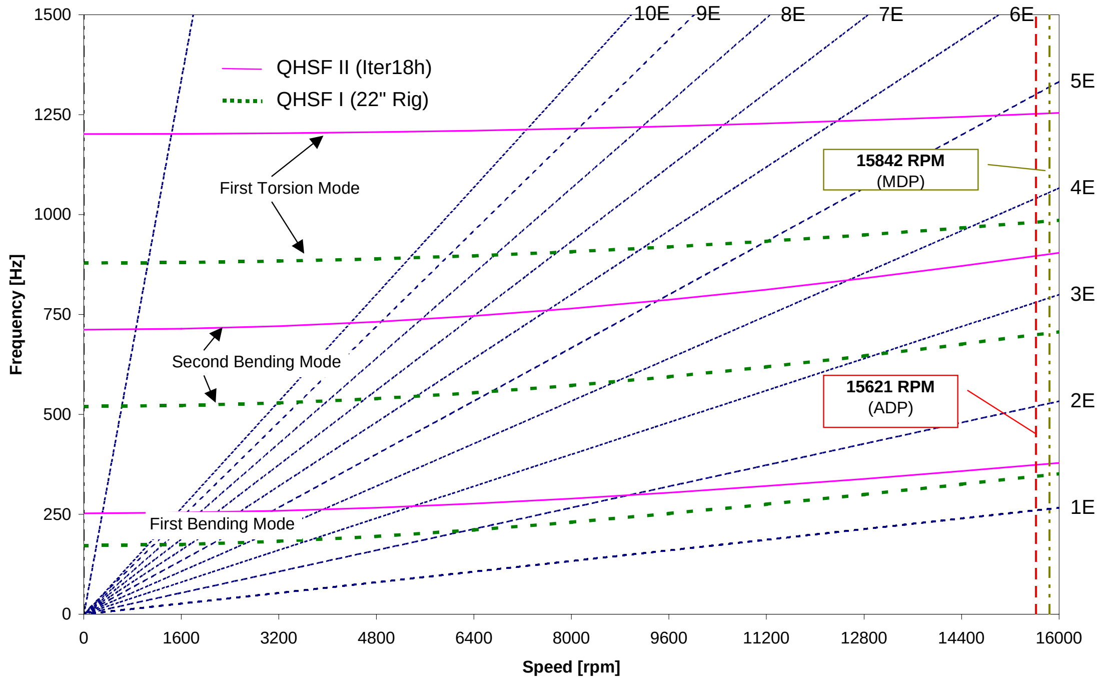

Figure 85. The Campbell Diagram for the ITER07 Rotor Blade With Sloped Attachment Shows Adequate Design Margin.

5.6 Stator Design

15 split-span stator vane configurations were defined for the first stator DOE as shown in Figure 86. The axial sweep was kept constant for this evaluation. The acoustic and mechanical evaluations were completed to determine the optimum stator for the Case 14a rotor. However, after extensive evaluation of the SOURCE3D and ANSYS results, it was determined that the conservative design at the hub (leaning against the direction of fan rotation) to prevent suction side flow separation was a significant negative influence on the acoustic results. Three of the DOE 1 cases (1, 5, and 7) that had significant tip sweep in the direction of rotation were carried forward into stator DOE 2 (see Figure 87). The lean distribution labeled “Case 1 Mod” is the Case 1 profile that has been adjusted to have zero lean at the hub. This profile was added to access the impact of the suction side lean on the tone noise reduction. It was also decided to perform DOE 2 with a 50 vane stator instead of the 70 vane stator of DOE 1 to reduce the broadband noise levels and have a stator count similar to the QHSF I (52 vanes).

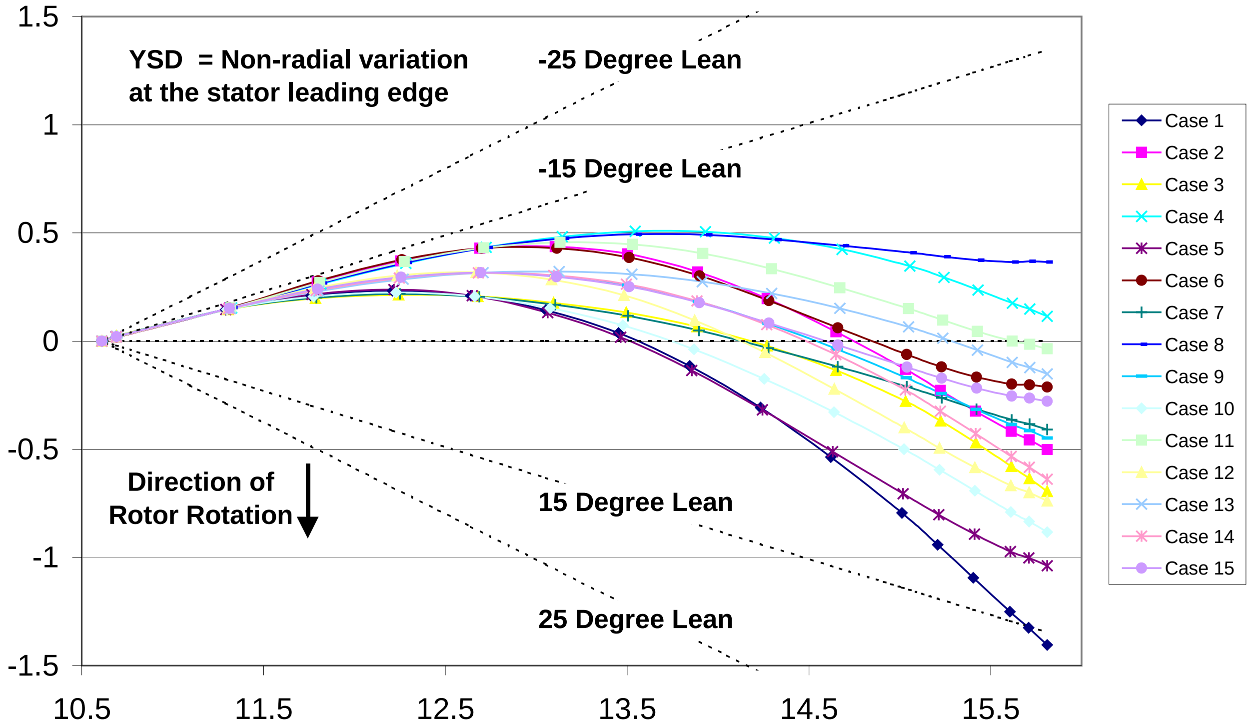

Figure 86. Comparison of the Stator Lean Profiles (YSD Parameter) for the 15 Cases of Stator DOE 1.

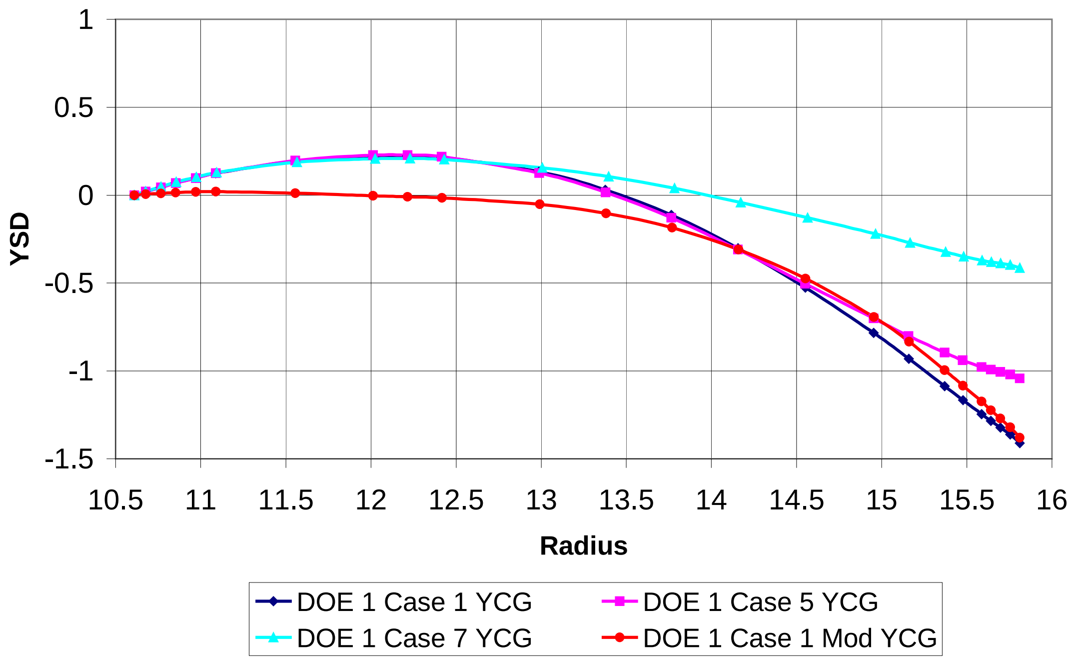

Figure 87. These Four Circumferential Lean Distributions Were Used for Stator DOE 2.

To overcome the negative impact on noise of the vane suction side lean at the hub, both non-linear sweep in the axial direction and non-linear lean on the tangential direction were explored in DOE 2. The design concept is to apply sweep where the vane cannot be leaned and apply lean where the vane cannot be swept. The concept is shown in Figure 88.

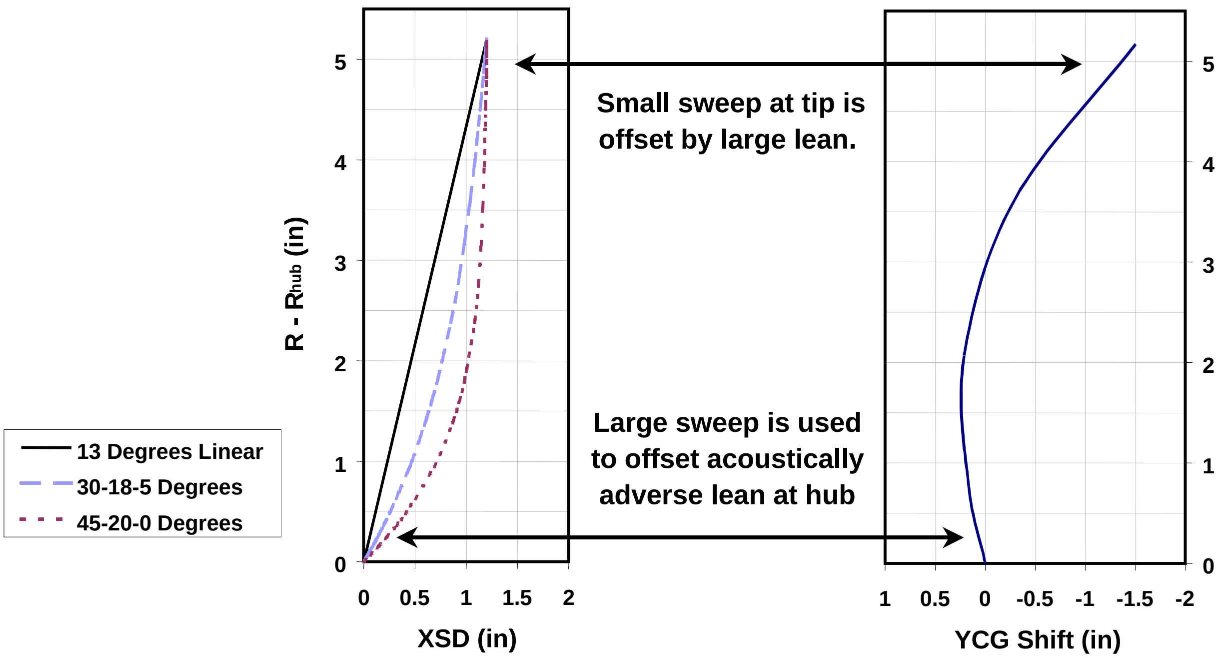

Figure 88. The Design Approach for Stator DOE 2 Is to Apply Non-Linear Sweep to Take Maximum Advantage of the Optimum Lean.

Two nonlinear axial sweeps were defined for stator vane DOE 2 in addition to the nominal linear sweep as shown in Figure 89. Constraints on the vane position at the hub and shroud for the 50-vane configuration limited the linear sweep to 13 degrees.

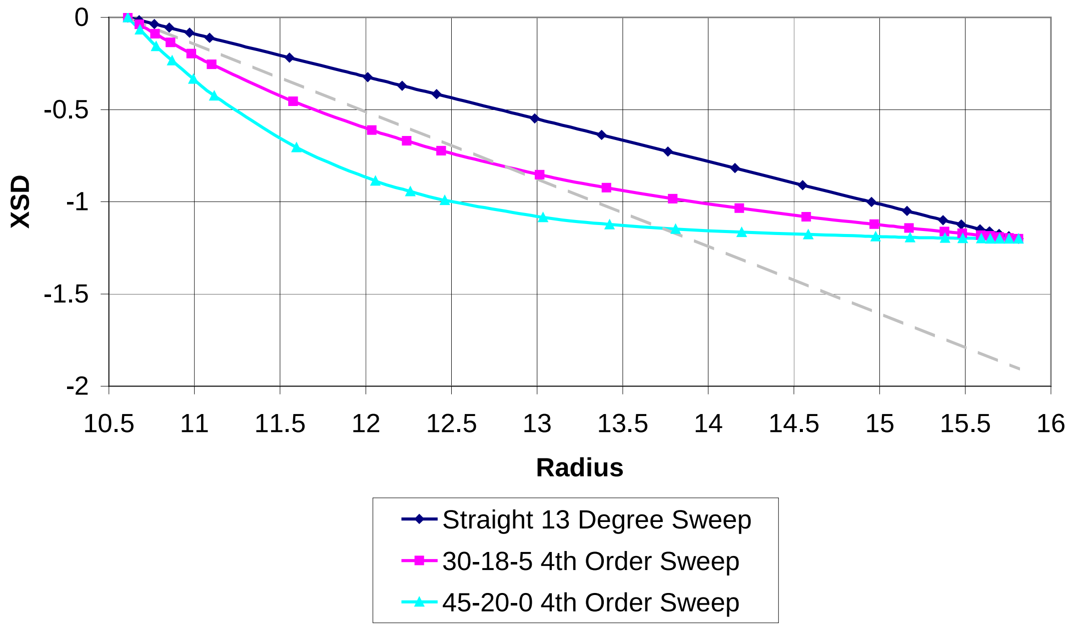

Figure 89. These Three Axial Sweep Distributions Were Used for Stator DOE 2.

Based on the acoustic results, Case 109 (see Table 15) was chosen as the go-forward design. Case 109 has the 45-20-0 4th order sweep profile and the Case 1 tangential lean profile from DOE 1.

Table 15. Tone Sound Power Results of Stator DOE 2 From SOURCE3D at 61.7% Corrected Fan Speed.

	Sweep 1 = Straight	Sweep 1 = 30-18-5	Sweep 1 = 45-20-0
YCG = Bypass Stator DOE 1 Case 1m	Case 104 -2.0	Case 108 -2.6	Case 112 -2.6
YCG = Bypass Stator DOE 1 Case 1	Case 101 -1.3	Case 105 -1.9	Case 109 -2.2
YCG = Bypass Stator DOE 1 Case 5	Case 102 -0.1	Case 106 0.1	Case 110 0.4
YCG = Bypass Stator DOE 1 Case 7	Case 103 0.5	Case 107 1.5	Case 111 1.9

The decision was made for the QHSF II to return to the full span stator configuration since the optimum core and bypass stator counts were both 50. Confirmation runs were performed to ensure that the full span stator preserved the tone noise reduction benefit obtained with the split span stator design of DOE II. Figure 90 shows the summary of the analysis. SOURCE3D predicts a 3 dB reduction in tone sound power for the QHSF II go forward design as compared to the Baseline II rotor at 61.7 percent speed. Figure 91 shows a two view drawing of the go-forward vane design.

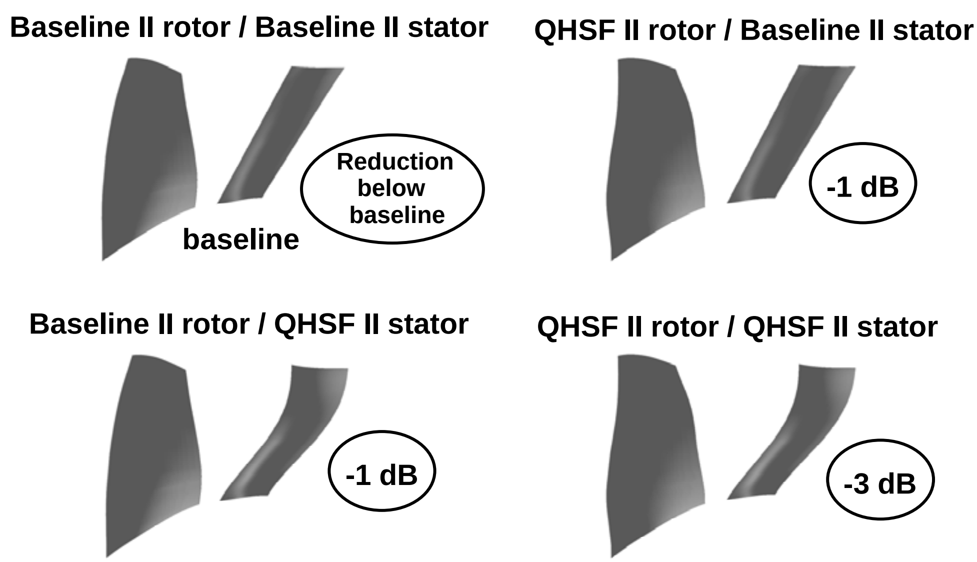

Figure 90. Summary of the Total Rotor/Stator Interaction Tone Sound Power Reduction at a Typical Aircraft Approach Condition Due to the Elements of the QHSF II.

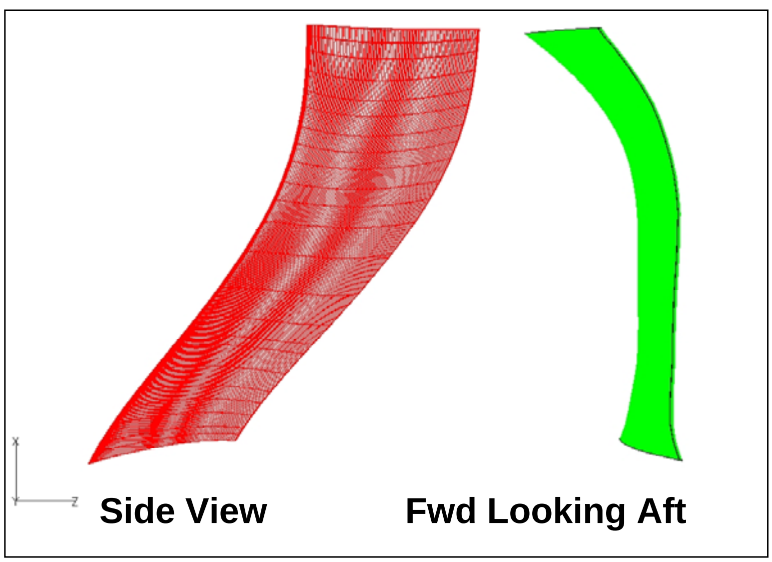

Figure 91. The Go-Forward Design for the QHSF II Stator Is a Full Span Vane With Nonlinear Axial Sweep and Tangential Lean.

A confirmation analysis of the go-forward stator mechanical design was conducted with ANSYS. As expected, the vane has atypical vibration mode shapes and the flutter parameters are not all within the Honeywell design experience (see Figure 92).

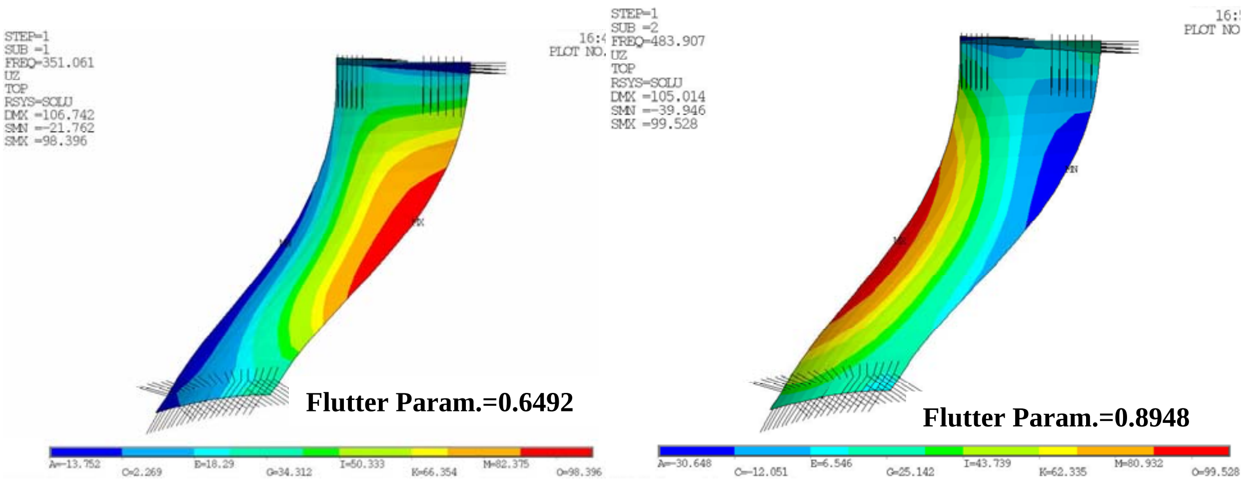

(a) Mode 1 (b) Mode 2

Figure 92. Preliminary Mode Shapes for the QHSF II Stator Vane Show a Potential Mode 2 Flutter Problem.

5.7 SOURCE3D and V072 Studies for QHSF II Stator DOE I

The fan tone noise calculations for the first stator DOE were performed using an engine scale fan flowpath as shown in Figure 93. The fan had a forward-swept rotor and a split-span stator. The tone noise predictions were performed using the SOURCE3D program, which is part of NASA's TFaNS fan tone noise prediction tool, and the V072 program, an earlier tool upon which the SOURCE3D program is based.

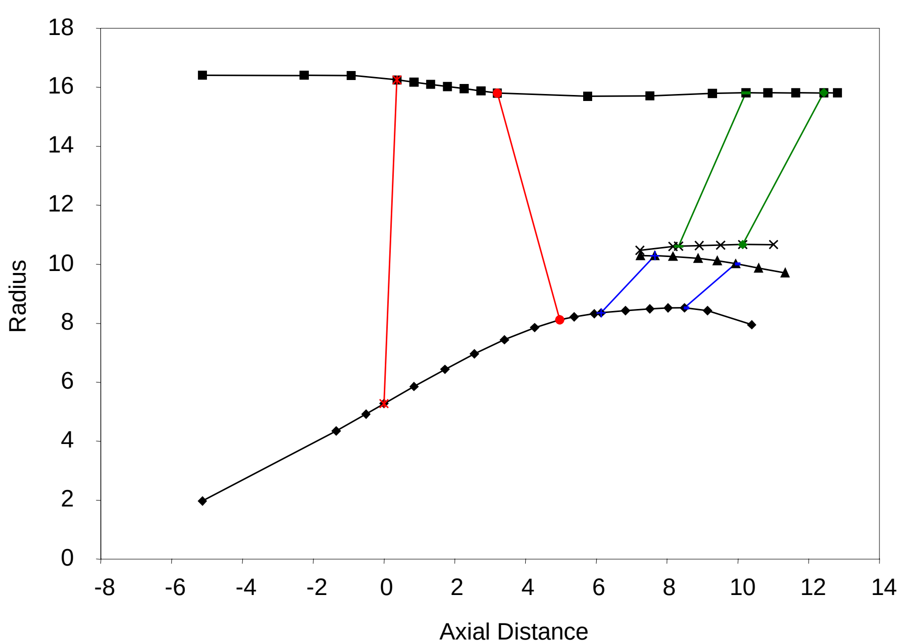

Figure 93. A Split-Stator Fan Flow Path Was Used for the Initial Stator DOE Tone Noise Calculations.

5.7.1 Calibration of SOURCE3D With Straight-Lean Stators

To calibrate the results of the SOURCE3D program, tone noise predictions for the bypass-portion of the QHSF II fan were examined at three speeds (62 percent, 77 percent, and 89 percent). The stators of DOE I were replaced by a set of 5 stators with straight lean of +25 degrees, +15 degrees, 0 degrees - straight radial, -15 degrees, and –25 degrees. Positive lean angles were defined as lean in the direction of rotor rotation. (Note that the SOURCE3D/V072 variable YSD is negative, for vane lean in the direction of rotor rotation.) The behavior of these cases was expected to follow the trend of increased tone noise as the stator was leaned against rotation.

The SOURCE3D results showed different trends at each speed, as presented in Figure 94 to Figure 96. Depending on which circumferential modes dominated, the sound power level was either nonlinear (62 percent speed), constant (77 percent speed), or linear (89 percent speed) with stator lean. At 77 percent and 89 percent speed, the 1*BPF (m = 22) and 2*BPF (m = 44) rotor-locked modes had constant PWL for all stator leans. At all speeds, the 2*BPF (m = -26) circumferential mode showed nonlinear behavior with lean. Also, the 3*BPF (m = -4) mode was nonlinear with lean, at 62 percent speed.

All radial modes were constant for the rotor-locked circumferential modes. All other radial modes demonstrated non-linear variation with stator lean. It was the combination of these radial modes that determined the overall behavior of the PWL trend with stator lean.

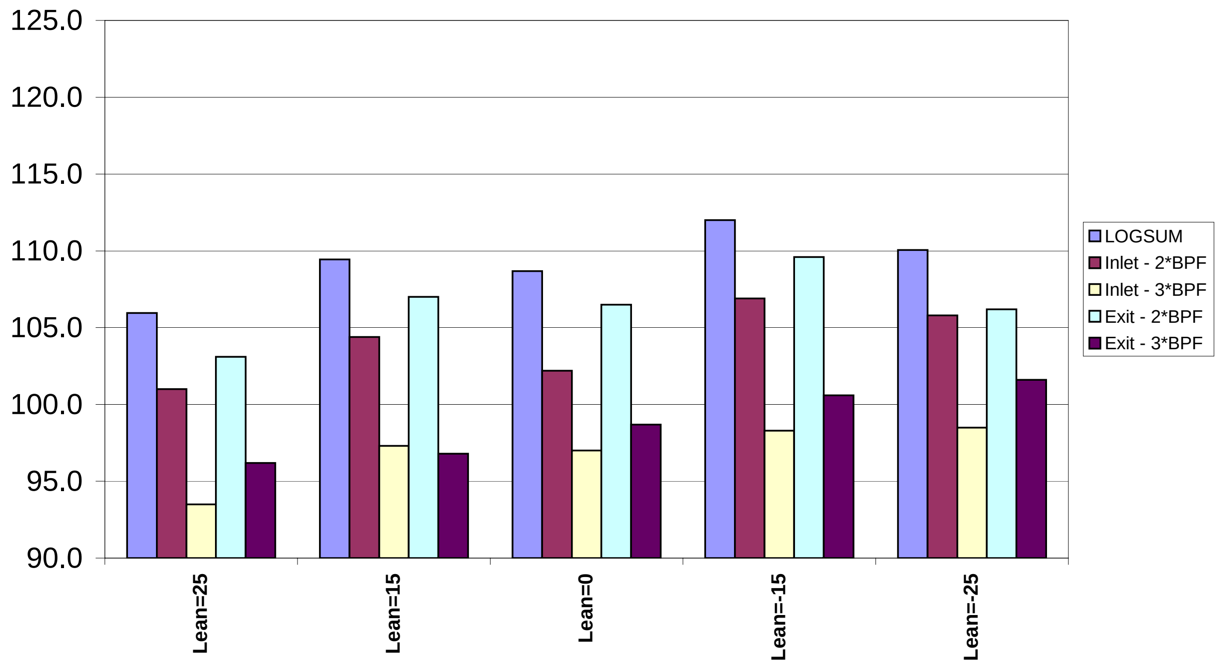

Figure 94. SOURCE3D Results for QHSF II at 62% Speed, With Straight-Leaned Stators.

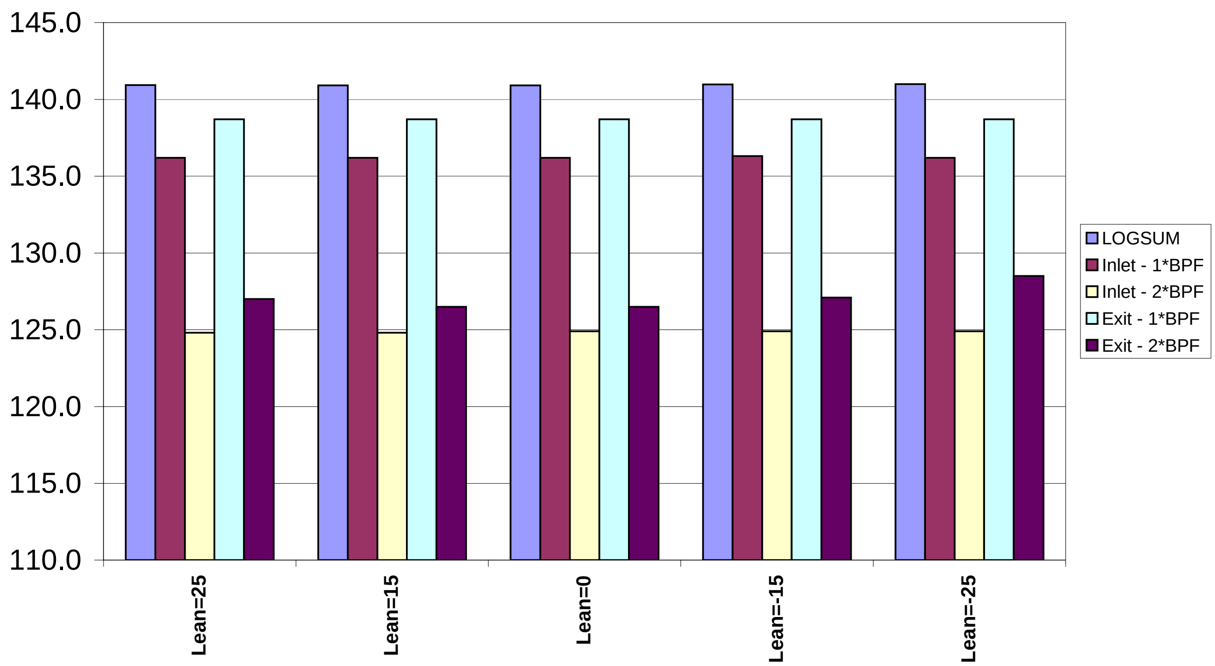

Figure 95. SOURCE3D Results for QHSF II at 77% Speed, With Straight-Leaned Stators.

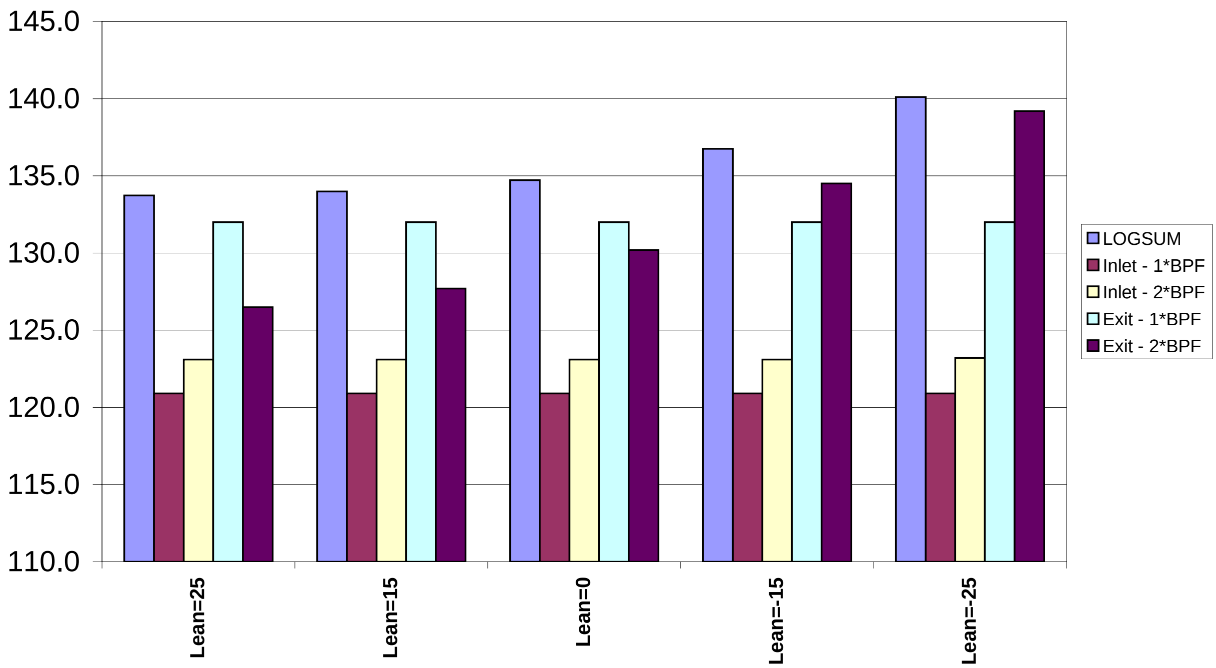

Figure 96. SOURCE3D Results for QHSF II at 89% Speed, With Straight-Leaned Stators.

5.7.2 Comparison of SOURCE3D and V072 at 62 Percent Speed

Review of the QHSF I Design Report showed that the V072 analyses performed for the QHSF I stator at 55.9 percent speed predicted a fairly linear variation of PWL with stator lean, unlike the 62 percent speed SOURCE3D predictions. To determine if V072 was consistent with the predictions from SOURCE3D for the QHSF II, the set of straight-lean stators was studied at 62 percent speed, using V072 with input files generated by PREV072 (a preprocessor to V072 developed at Honeywell).

The V072 input files were generated with all 24 streamlines from AXCAPS, in contrast to the SOURCE3D input files, which used a subset of 17 streamlines. The straight-lean stator geometry was copied from the SOURCE3D input files, and additional data was added to account for the additional streamlines. One difference between the input files concerned the representation of YRD, the circumferential offset of the rotor trailing edge, relative to the radial direction. The scheme for calculating YRD for a split-span stator in PREV072 resulted in bypass YRD values that were not zero-based at the flow splitter radius. It was not clear that this was necessary within the SOURCE3D/V072 algorithms; however, the SOURCE3D input had used zero-based YRD distributions.

Comparison of the SOURCE3D and V072 results at 62 percent speed (Figure 94 and Figure 97, respectively) showed that the V072 overall PWL values were higher. Also, the V072 results showed less non-linearity with stator lean compared to SOURCE3D. This behavior was even more apparent when the differences in PWL for the leaned stators relative to the unleaned stators were compared for SOURCE3D and V072. As shown in Figure 98 and Figure 99, the behavior of the V072 case was more consistent with the expected trends. In general, the variation in results between SOURCE3D and V072 was of a similar magnitude to the variations due to stator lean.

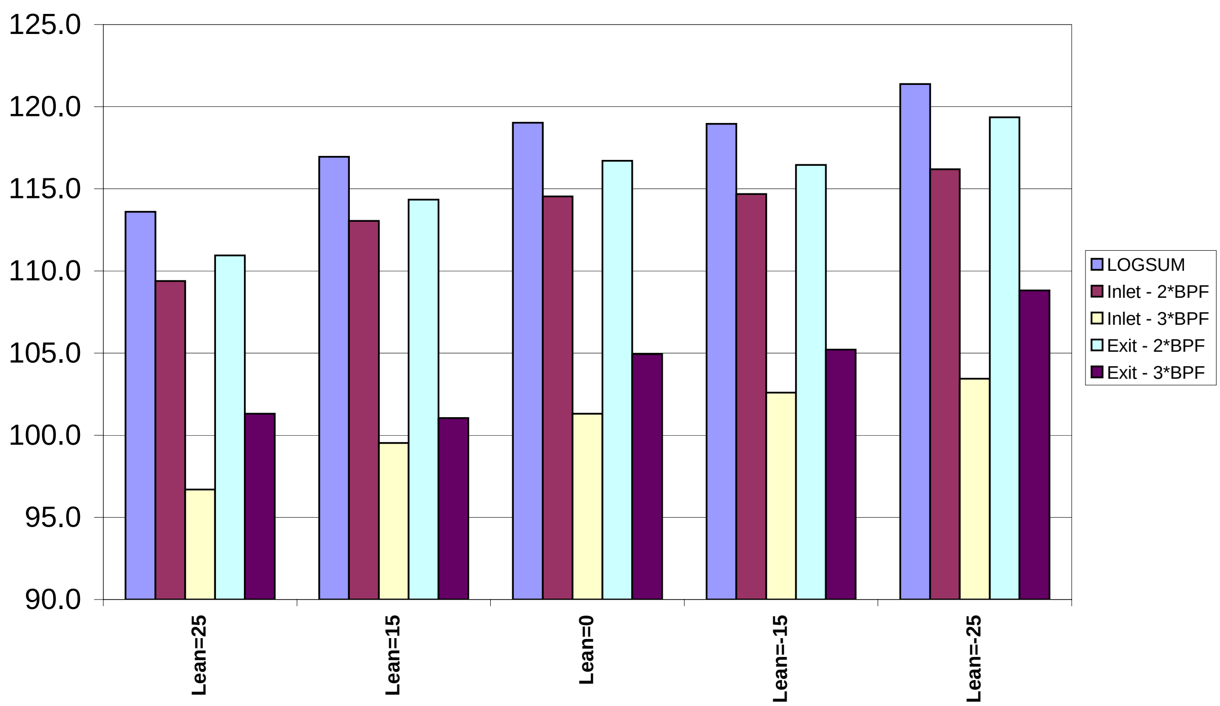

Figure 97. V072 Results for QHSF II at 62% Speed, With Straight-Leaned Stators.

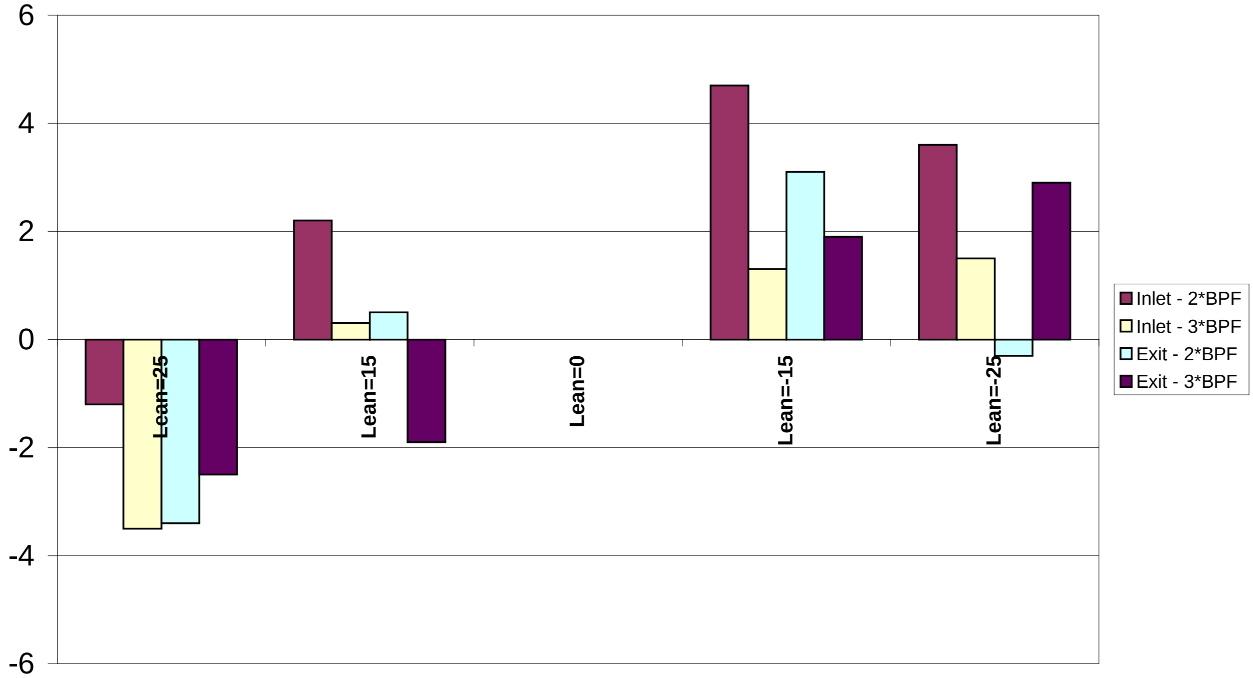

Figure 98. Comparison of the SOURCE3D Results Relative to Unleaned Stator.

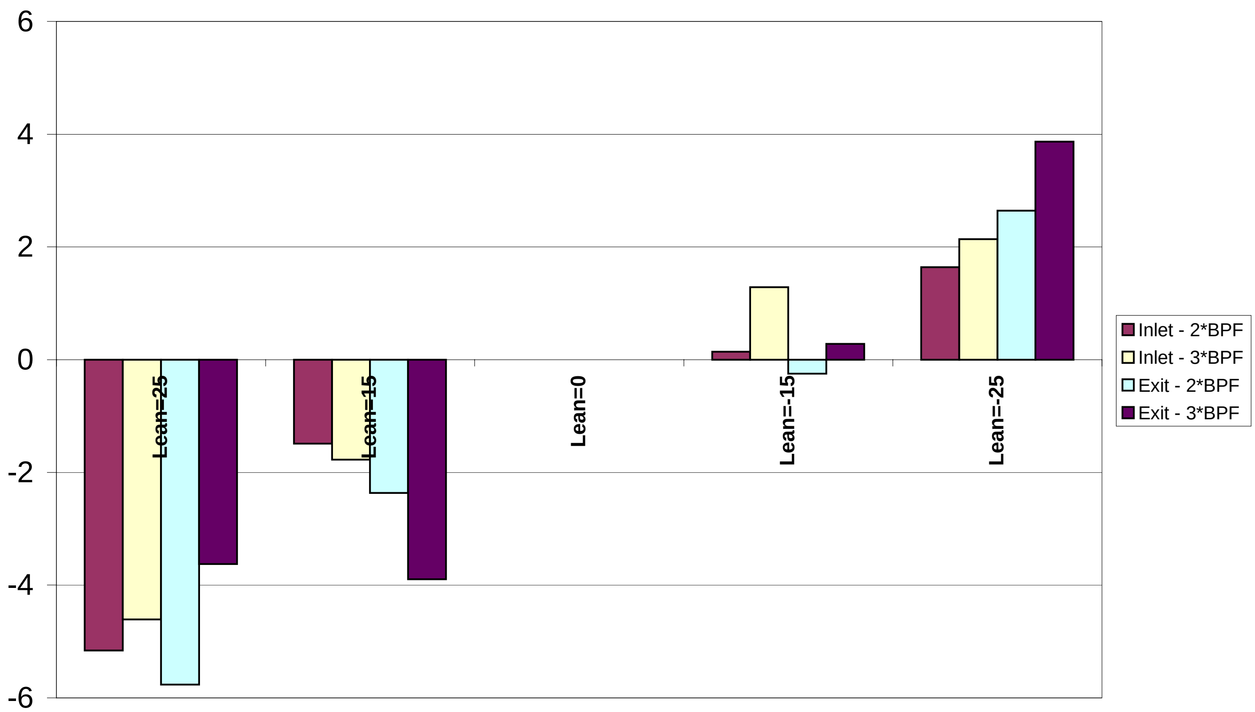

Figure 99. Comparison of V072 Results Relative to Unleaned Stator.

5.7.3 Modification of PREV072 Calculation of YRD

The circumferential offset of the rotor trailing edge, relative to the radial direction (YRD) was being computed in PREV072 inconsistently with its usage in V072. YRD was computed in PREV072 using the offset angle relative to the hub and the local radius at the rotor trailing edge. Although this produced an accurate circumferential offset, the V072 program did not use YRD in the same way. In V072, the offset angles that were obtained from YRD were computed using the reference radii (i.e., the RADIUS array specified in the input file), which in this case was at the bypass stator leading edge.

PREV072 was modified to compute YRD based on the reference radius. In addition, for bypass-only analyses, the offset was recomputed to have a zero-base at the flow splitter. Results of this modification are shown in Figure 100. Only a minimal change in PWL was seen for the modification to YRD. This was even more apparent in Figure 100, where trends for the differences in PWL relative to the unleaned stator remained similar, with the revised input files. This would seem to indicate that the zero- and non-zero-based YRD distributions result in essentially the same rotor wake behavior at the stator leading edge.

As a check of the validity of the original SOURCE3D input, the new correctly computed YRD distribution for the V072 input was compared with the YRD distribution used in SOURCE3D. There was a significant difference in the two distributions. Although this discrepancy in rotor trailing edge circumferential offset was constant across all cases examined, it may have contributed to the disparity in the SOURCE3D and V072 results.

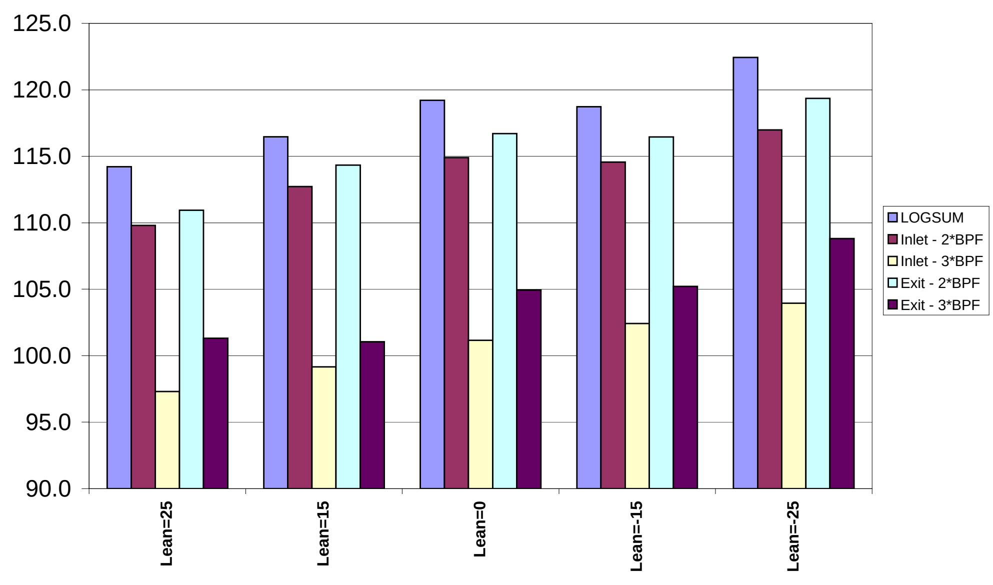

Figure 100. V072 Results Based on the Revised Specification of YRD.

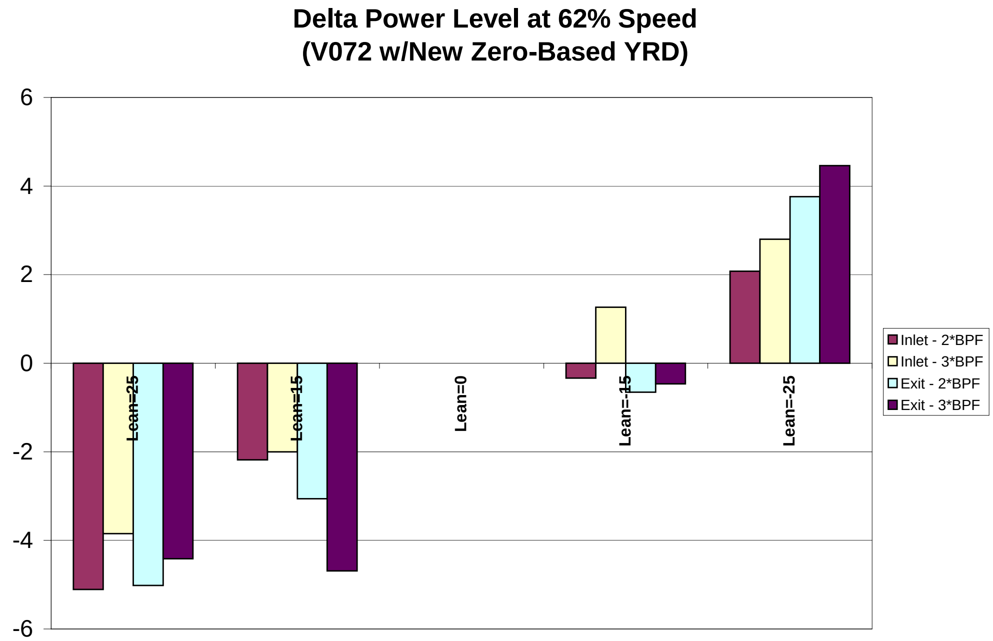

Figure 101. Comparison of V072 Results Relative to Unleaned Stator, With Revised Specification of YRD.

5.7.4 Comparison of QHSF I Cases With QHSF II

After modifying PREV072, new V072 analyses were performed for the Baseline I fan and QHSF I, along with the Baseline II straight stator and a QHSF II leaned stator case. Speeds were not directly comparable; however, all cases were near Approach. The Baseline I and QHSF I cases were at 55.9 percent Speed, the Baseline II case was at Approach, and the QHSF II fan with the +15 Degree leaned stator was at 62 percent Speed. Results are shown in Figure 102.

General sound power level trends of the Baseline I, QHSF I, Baseline II, and QHSF II fans indicated that the QHSF II was comparable to the Baseline II fan, and Baseline II fan had louder tones than the old baseline and QHSF I.

Comparison of the QHSF I case relative to the Baseline I fan showed somewhat different trends (varying by several dB) than those presented in the QHSF I Design Report (Reference 1). In the final report, the differences were generally reported to be much greater. A contributing factor may be the underestimate of the radial loss distribution specified for the Baseline I rotor in the original QHSF I evaluations. This original loss model was replaced by the QHSF I loss distribution for the current V072 analysis of the Baseline I fan.

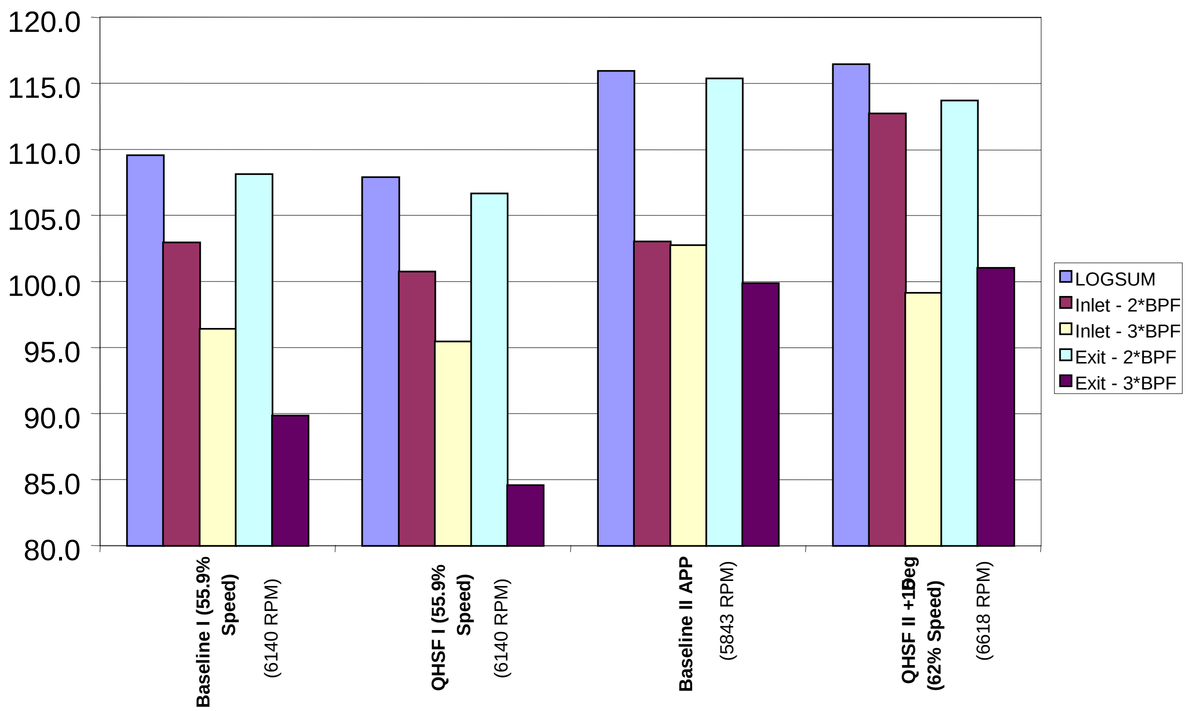

Figure 102. Comparison of the QHSF I and QHSF II Cases With the Baseline I and Baseline II Cases.

5.7.5 Adjustment for Low Cutoff Ratio

It was noted that some of the radial modes had cutoff ratios very close to 1.0, along with very large predicted sound power levels. Because the accuracy of the cutoff ratio calculation in V072 was not well established, there remained some question as to the validity of the sound power levels for these modes. To determine the impact of the modes with low cutoff ratio, the V072 results were adjusted by computing the sound power levels after discarding any modes having cutoff ratios less than or equal to 1.1. The primary impact of this adjustment was on the QHSF II case, which was reduced significantly in overall sound power level, as shown in Figure 103. Compared to the unfiltered results shown in Figure 102, this sound power level indicates a substantial decrease in fan tone noise for the QHSF II stator with +15 degrees of straight lean.

To determine the impact on sound power level with stator lean, results for the 5 straight-lean stator cases at 62 percent speed were filtered to remove any mode with a cutoff ratio less than or equal to 1.1. The results of this analysis are shown in Figure 104. The cutoff ratio filtering impacted only the 2*BPF modes, reducing them significantly, relative to the unfiltered modes shown in Figure 100. As a result, the overall sound power levels were also substantially reduced for the filtered predictions.

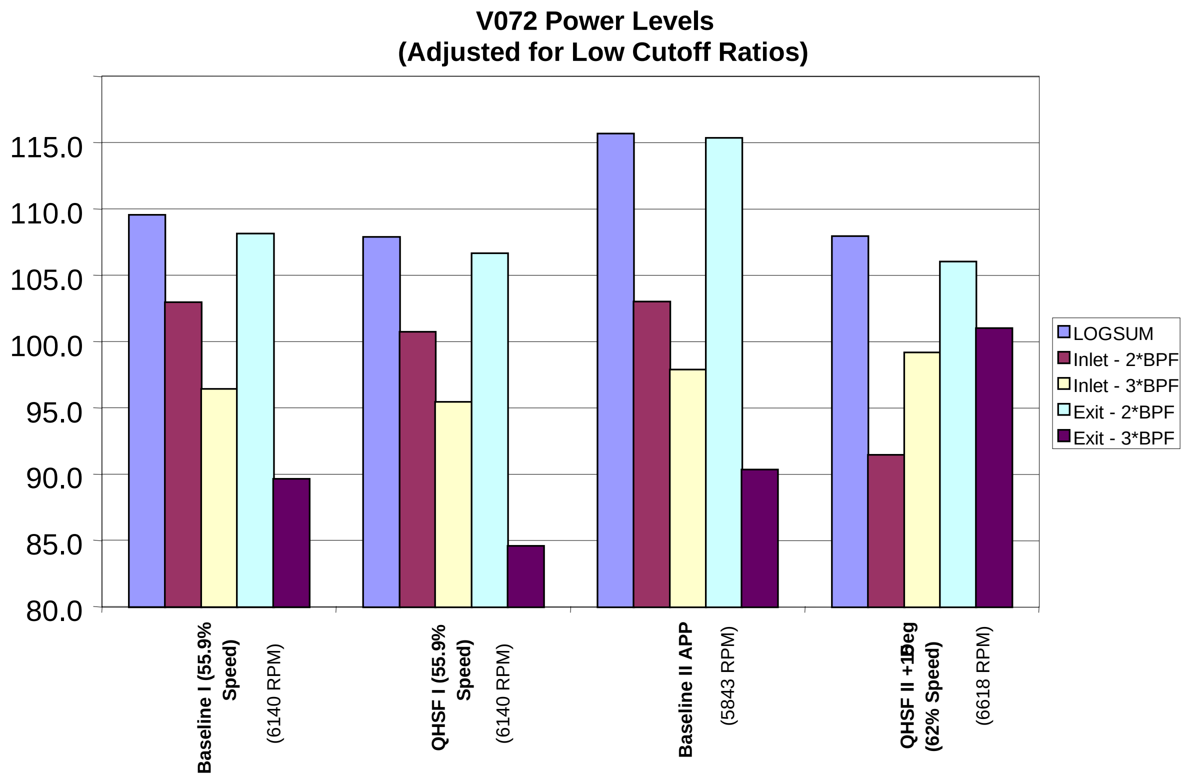

Figure 103. Comparison of QHSF I and QHSF II Cases Adjusted for Low Cutoff Ratio.

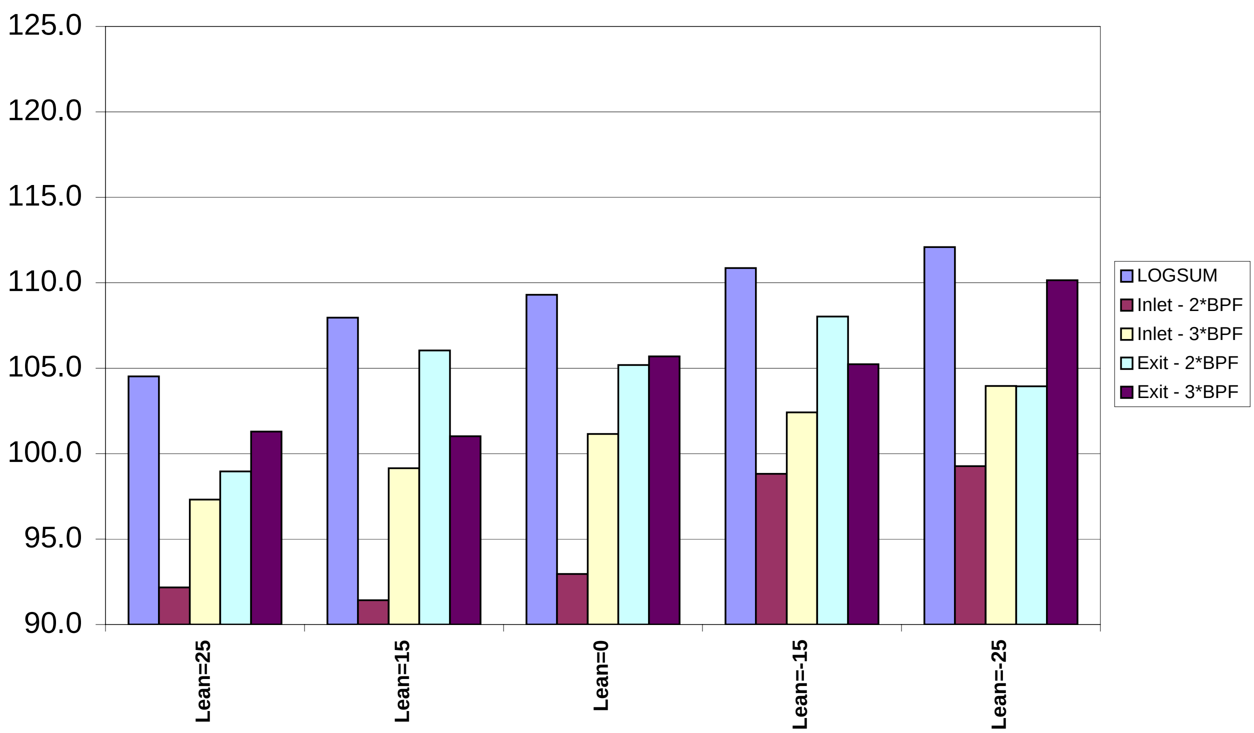

Figure 104. Variation in PWL for QHSF II With Stator Lean at 62% Speed, Adjusted for Low Cutoff Ratio.

5.7.6 Comparison of Rotor Loss Profiles

Before reaching any conclusions concerning the QHSF II stator V072 analyses, additional issues were considered. One area of concern was the rotor loss distribution for the QHSF II. Rotor loss distributions for the QHSF I at 55.9 percent speed, the Baseline II fan at Approach, and QHSF II at 62 percent speed were compared, as shown in Figure 105. The QHSF I and Baseline II profiles appeared to be similar; however, the QHSF II distribution was quite low in the outer span region.

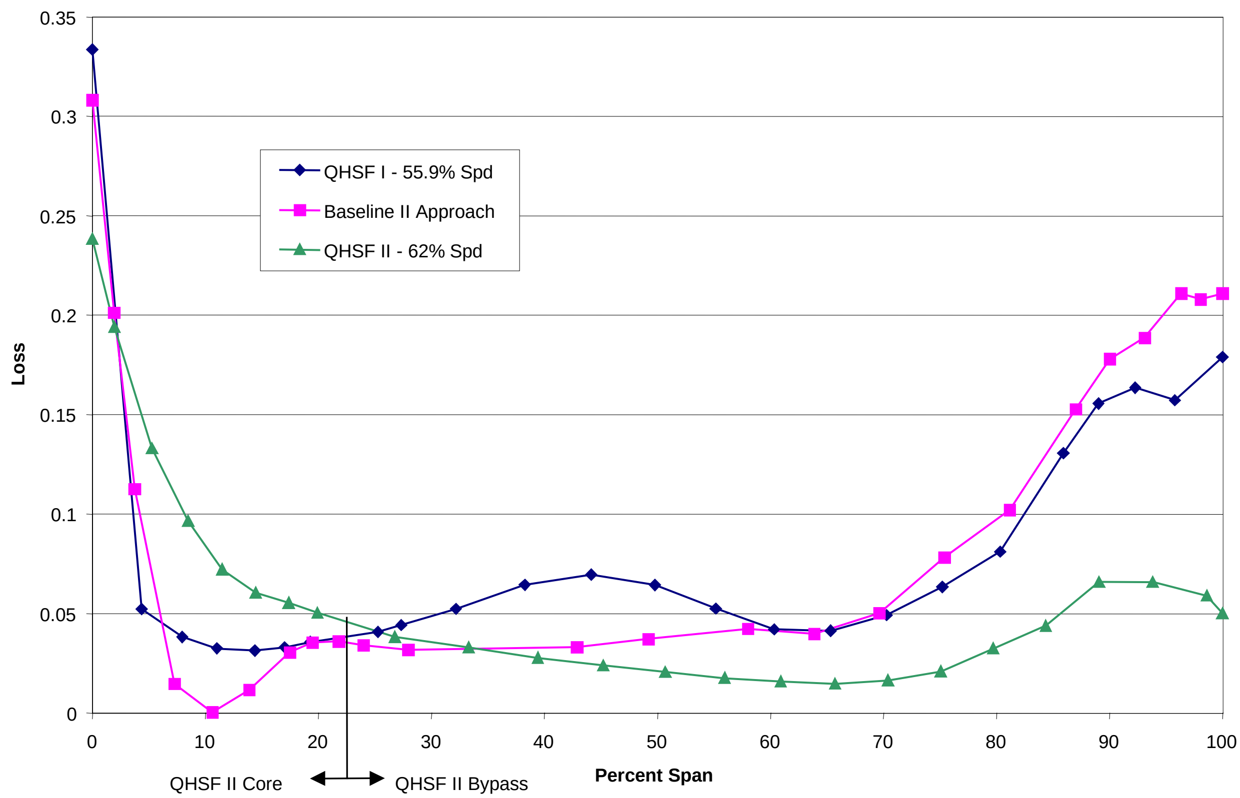

Figure 105. Radial Loss Distributions From AXCAPS.

5.8 Final QHSF II Design

The final aerodynamic design of the rotor and stator for the QHSF II was selected to be Case 18h (which was derived from Rotor ITER18 and Stator Case 109). Case 18h is the optimum configuration resulting from a series of analytical DOEs that were subsequently further optimized for reduced mechanical stress and improved aerodynamic performance. Figure 106 depicts the geometry of the final QHSF II design relative to the baseline engine.

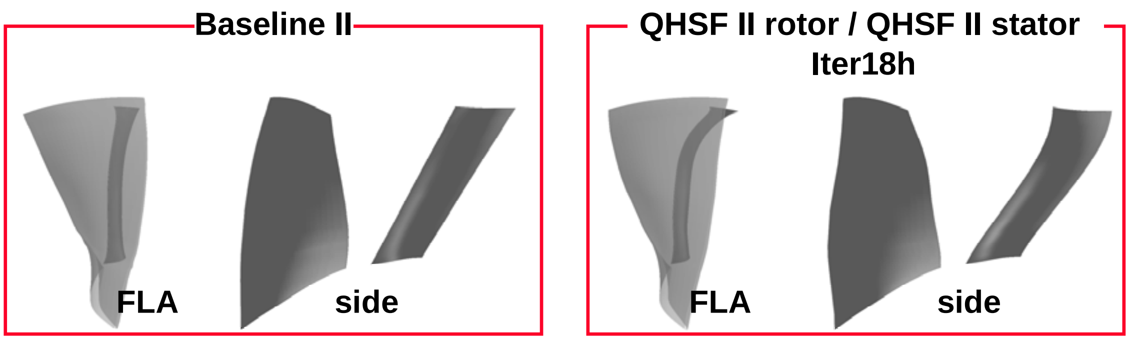

Figure 106. QHSF II Reduces Noise Through Rotor Sweep and Stator Sweep and Lean.

5.8.1 Aerodynamic Performance

Figure 107 shows the aerodynamic performance of the QHSF II rotor at 100 percent corrected fan speed. Figure 108 shows the aerodynamic performance of the QHSF II stage at 100 percent corrected fan speed. The QHSF II stage meets pressure ratio and efficiency goals. Suction-side Mach number contours are shown in Figure 109 for the QHSF II and Baseline II rotors. Figure 110 shows the Mach number contours at the rotor exit. The rotors show very similar aerodynamic performance.

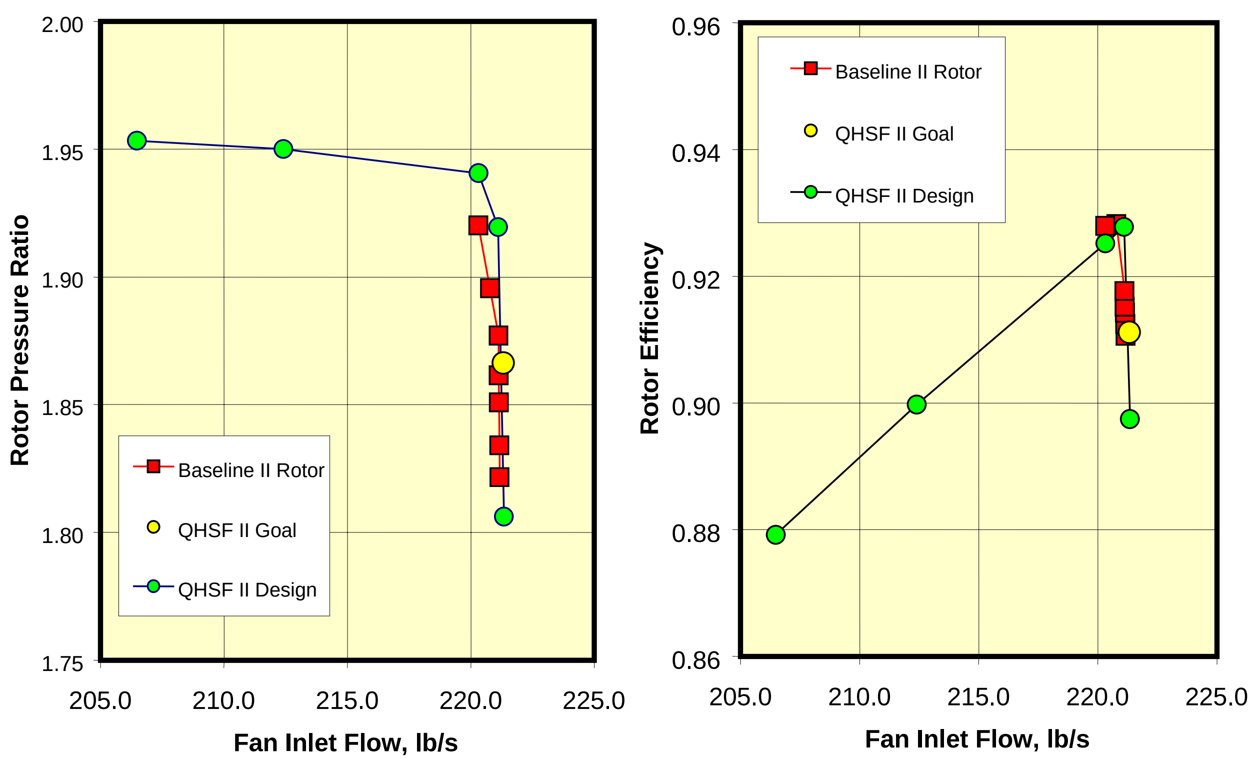

Figure 107. The QHSF II Rotor Meets Pressure Ratio and Efficiency Goals Set for the Program.

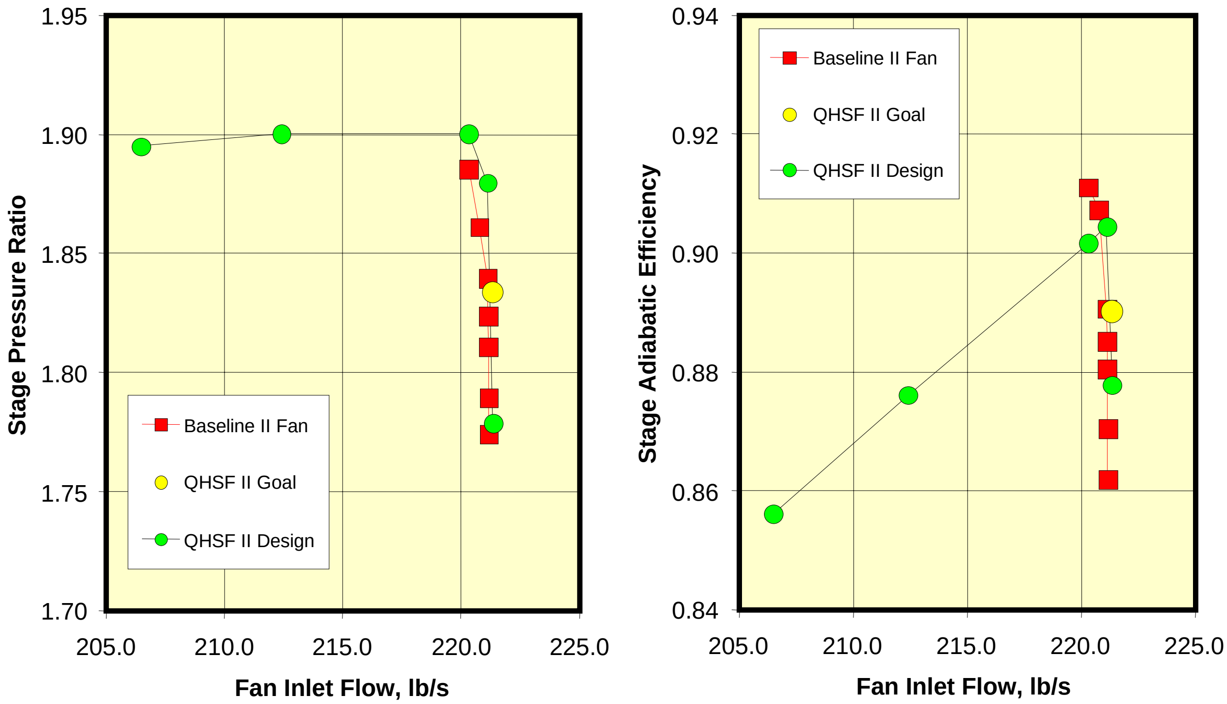

Figure 108. The QHSF II Stage Meets Pressure Ratio and Efficiency Goals Set for the Program.

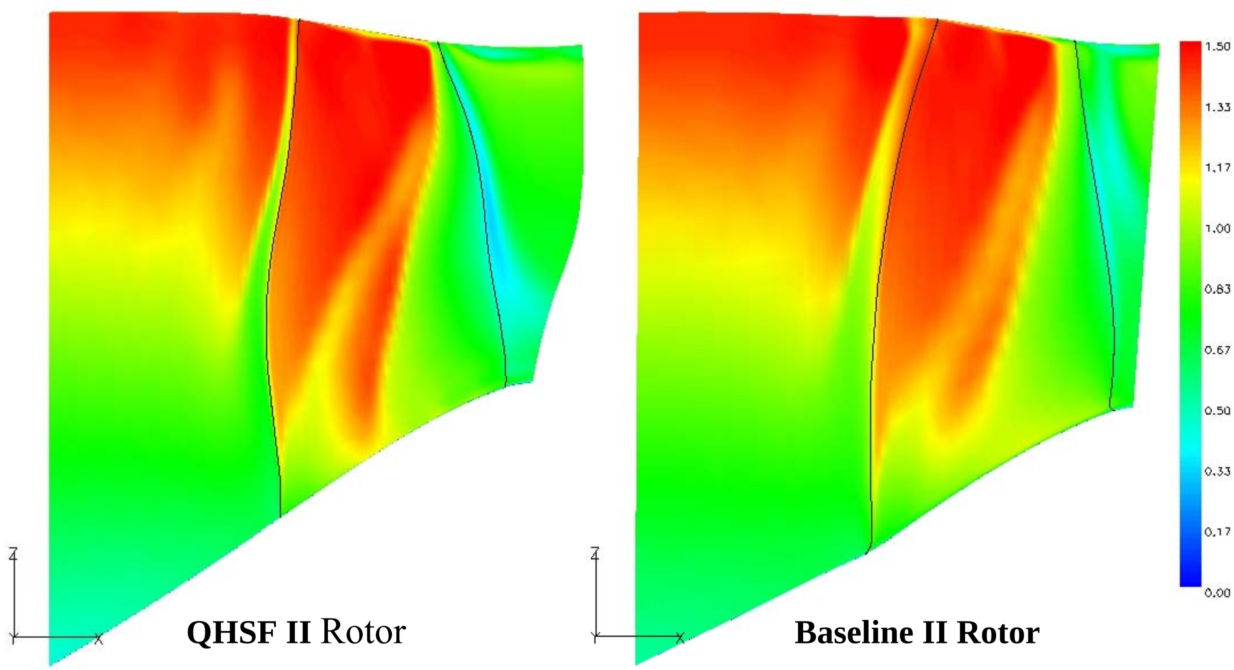

Figure 109. The Results of the ADPAC Analyses Show the Differences in Mach Number Contours on the Suction Side of the Blade Between the Baseline II and QHSF II Rotor.

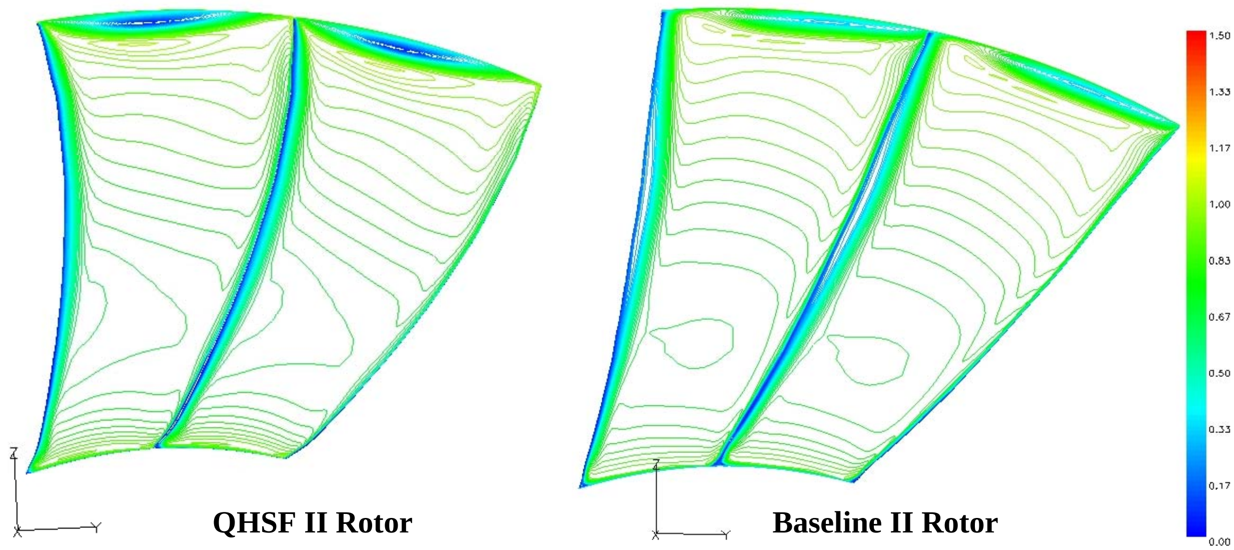

Figure 110. The Results of the ADPAC Analyses Show the Differences in Mach Number Contours at the Rotor Exit Between the Baseline II and QHSF II Rotor.

Figure 111 shows the suction side Mach number contours for the QHSF II and Baseline II stators. Figure 112 shows the Mach number contours at the vane exit. There is a small amount of flow separation introduced in the QHSF II stator design relative to the Baseline II design. The separation was estimated to be worth approximately 0.5 point in efficiency as shown in Figure 113 and has an undetermined noise impact judged to be of low risk.

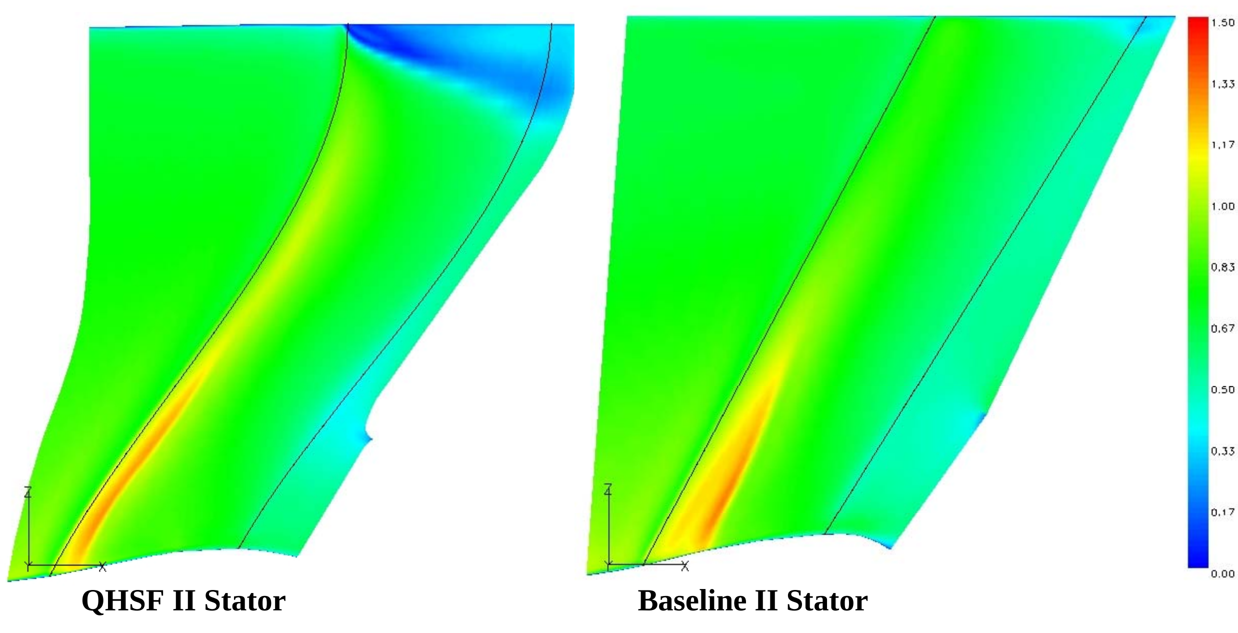

Figure 111. The Results of the ADPAC Analyses Show the Differences in Mach Number Contours on the Suction Side of the Vane Between the Baseline II and QHSF II Stator.

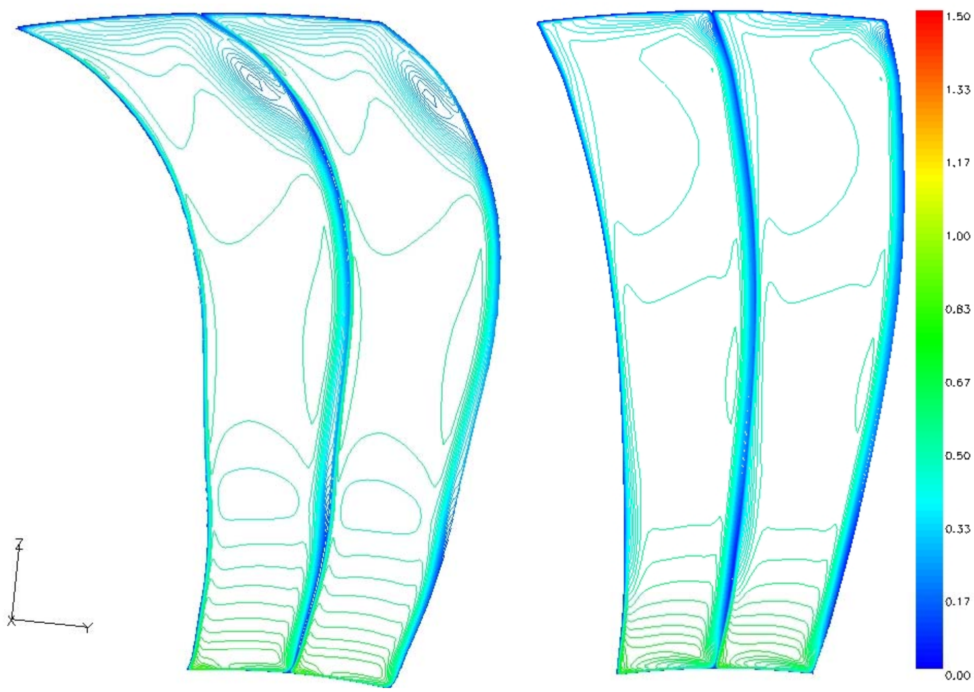

Figure 112. The Results of the ADPAC Analyses Show the Differences in Mach Number Contours at the Vane Exit Between the Baseline II and QHSF II Stator.

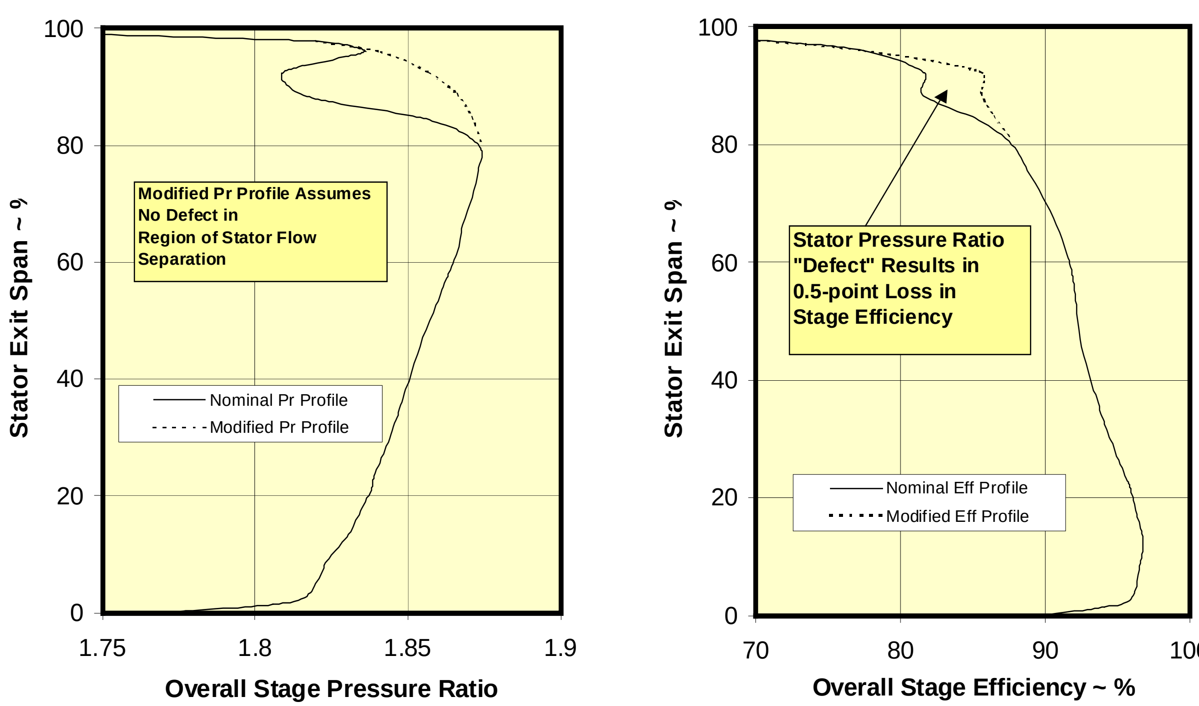

Figure 113. A Quick Analysis of the Stator Separation Indicated a Small Reduction in Efficiency for the QHSF II Stator.

As part of the original design goals for the QHSF I program, an attempt was made to adjust the rotor shock position at the critical takeoff condition so that the shock would be totally captured in the blade passage. Unfortunately, the multidiscipline optimization process of DOE 1 led to a design that did not achieve shock capture. Figure 114 shows Mach number contours for a typical take-off condition at four spanwise radii on the blade. It can be seen from the figure that the shocks are not contained in the blade passage. Figure 115 shows the Mach number contours near the pressure and suction side of the blade surface. The spanwise variation in shock position is clearly shown.

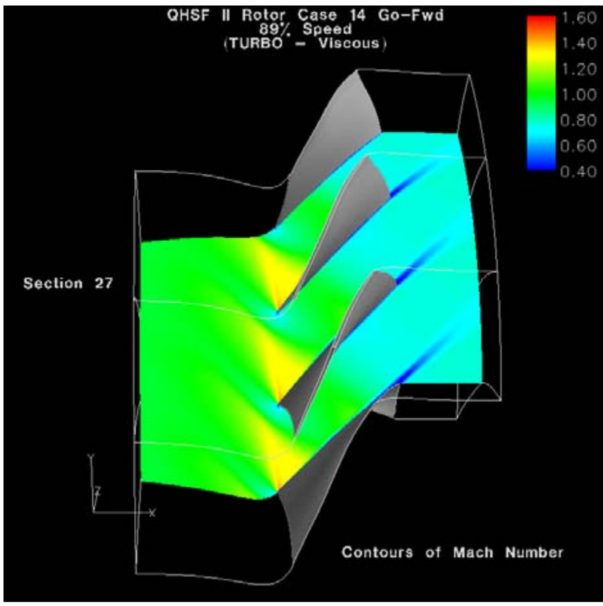

(a) 60.1% span

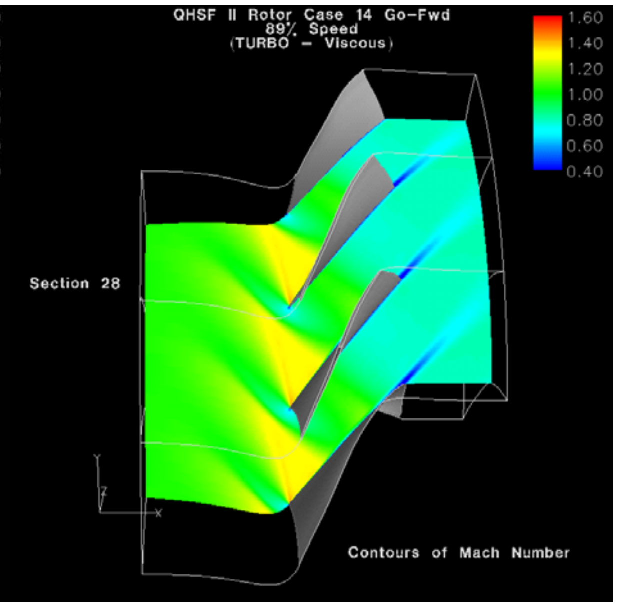

(b) 68.3% span

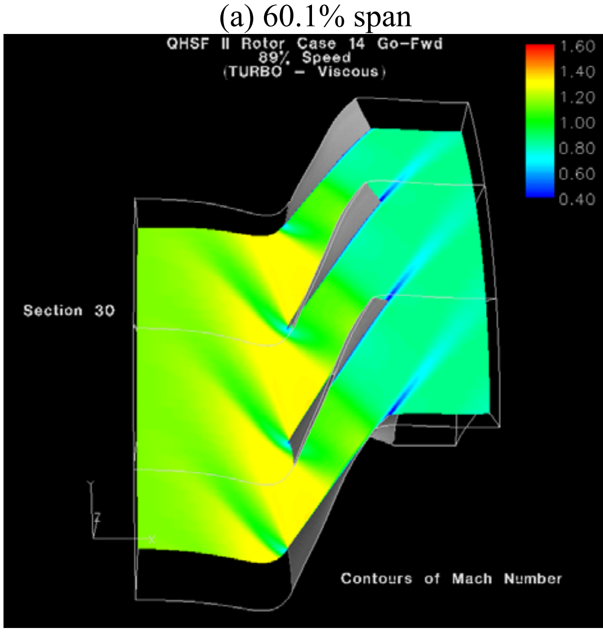

(c) 80.0% span

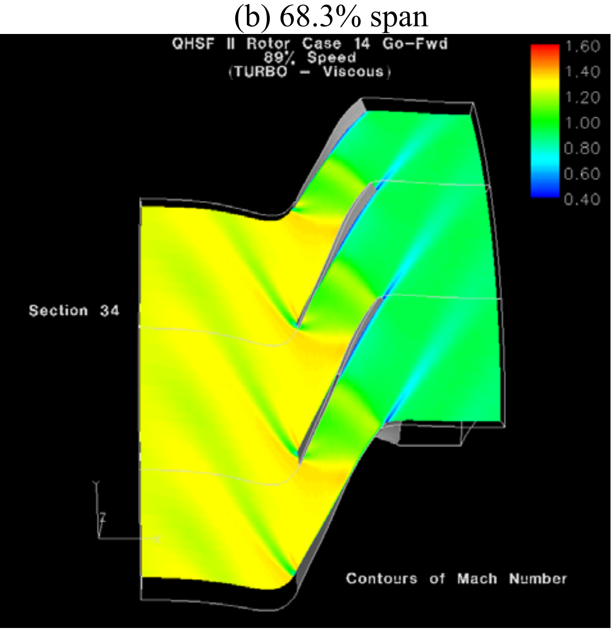

(d) 92.1% span

Figure 114. Mach Number Contours From the TURBO Viscous Analysis at 89% Speed Show That Shock Capture Was Not Achieved for the QHSF II Fan.

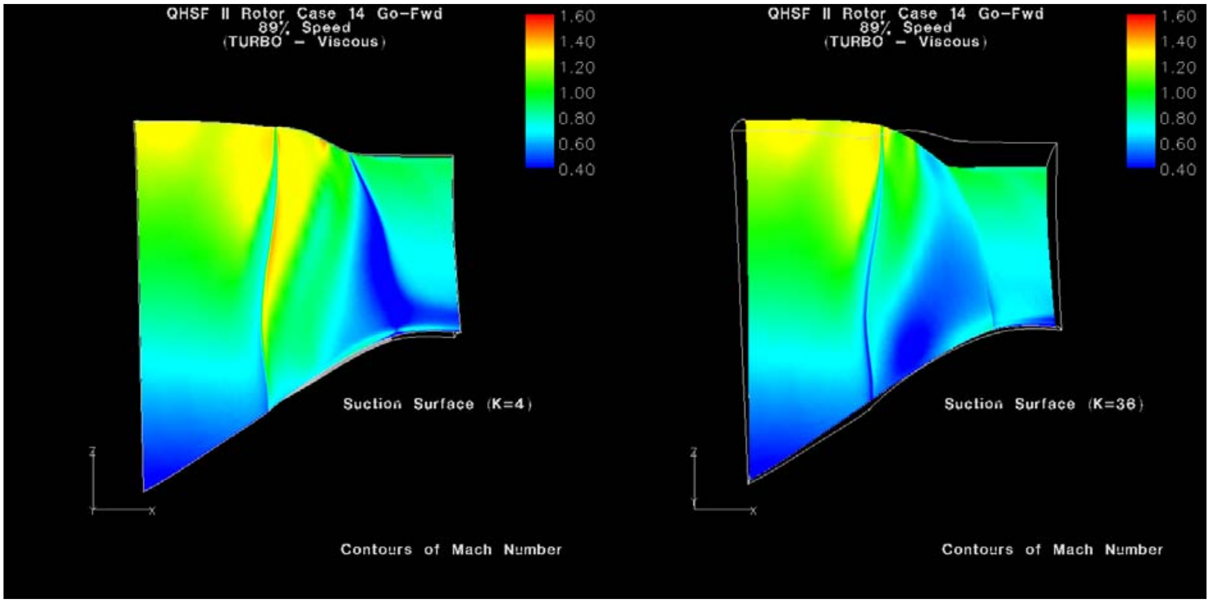

(a) Suction Surface (b) Pressure Surface

Figure 115. Mach Contours From the TURBO Viscous Analysis Show the Shock Positions for the 89% Speed Condition.

5.8.2 Mechanical Performance

A sloped attachment of 4.5 degrees was selected for the QHSF II rotor design as shown in Figure 116. This slope is adequate to put the blade-out loads equal to Baseline II engine levels, meet frequency goals, and provides adequate flutter margin. A state-of-the-art finite element model of the rotor blade and attachment was used for the mechanical analysis. Table 16 is a summary of the mechanical design status.

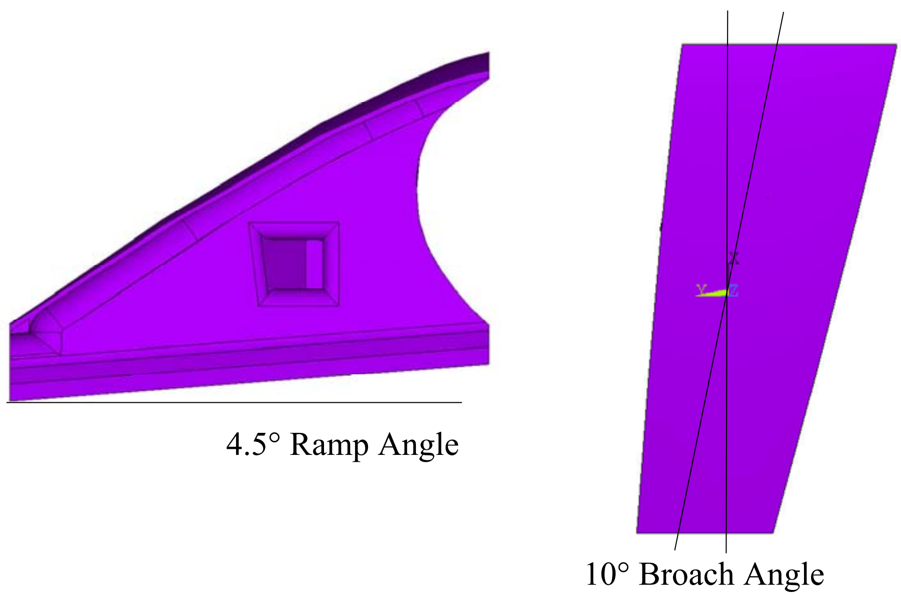

Figure 116. A Sloped Attachment Was Designed for the QHSF II Rotor.

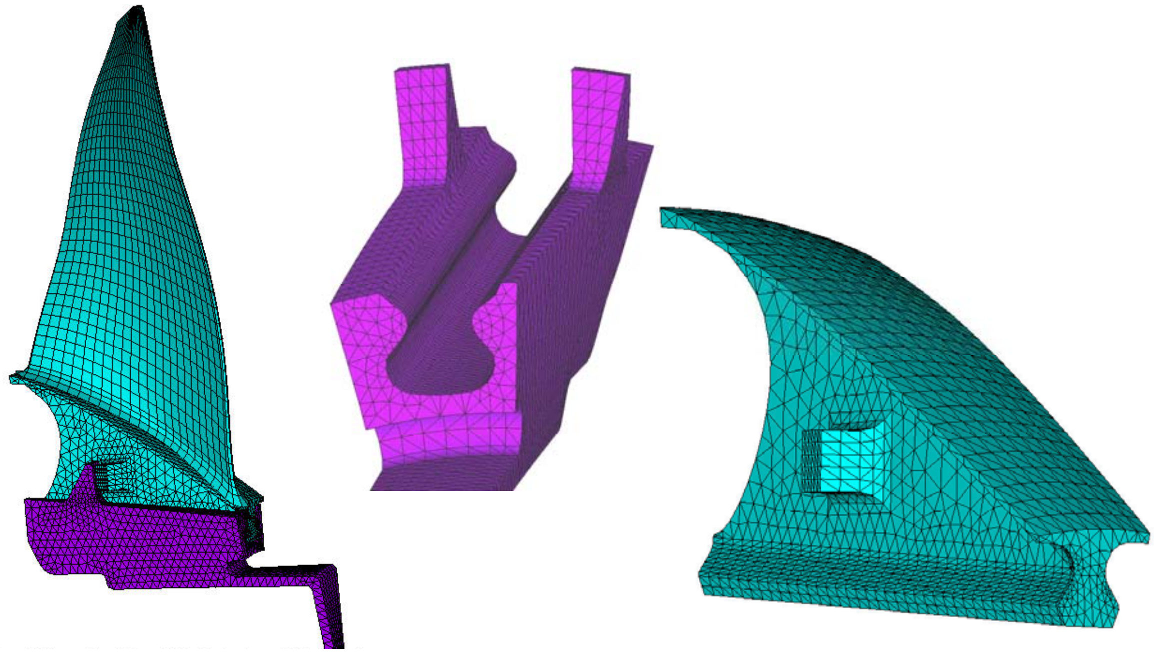

Figure 117. Honeywell Applied State-of-the-Art Finite Element Modeling Techniques in the Mechanical Analysis of the QHSF II Rotor Blade and Attachment.

Table 16. All of the Mechanical Design Requirements Were Met for the QHSF II.

Blade Weight
• Meets target weight requirements (less than Baseline II)
Blade Modal Characteristics
• Adequate frequency margins at 100 percent Speed for 1E to 4E distortion
• Fundamental mode crossing speeds are within Honeywell experience
Medium Bird Ingestion
• Calculated blockage is with in Honeywell experience
Blade Stress
• Results are within Honeywell design experience
Fan Disk Burst Margin
• Relative to NASA criteria, 30 percent above burst margin requirement
• Relative to Honeywell criteria: 53 percent margin, required > 25 percent margin
Fan Stator Vane
• Airfoil-only vibration analysis shows adequate flutter margin

Figure 118 shows blade stress levels at the aerodynamic design point (defined as a tip speed of 1506 ft/s, corresponding to a corrected speed of 15,621 rpm on the 22” rig). All stresses are within Honeywell design experience. Figure 119 shows that stress levels in the sloped blade attachment are well balanced and relatively low in the retention area. The attachment minimum neck stresses redistribute, but are within experience for a frictionless condition. The axial contact stress for the limiting (frictionless) condition is 33.8 Ksi. Figure 120 shows the results of 3-D disk wedge analyses. Results indicate that the disk has adequate burst margin relative to NASA criteria as shown (mechanical design point is defined as physical speed of 15,842 rpm on the 22” rig).

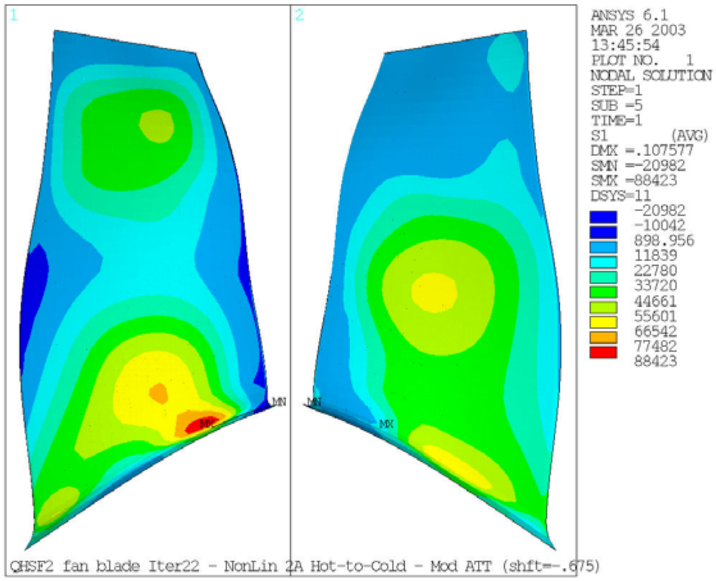

Figure 118. QHSF II Fan Blade Stress Levels at Aerodynamic Design Point Are Within Honeywell Design Experience.

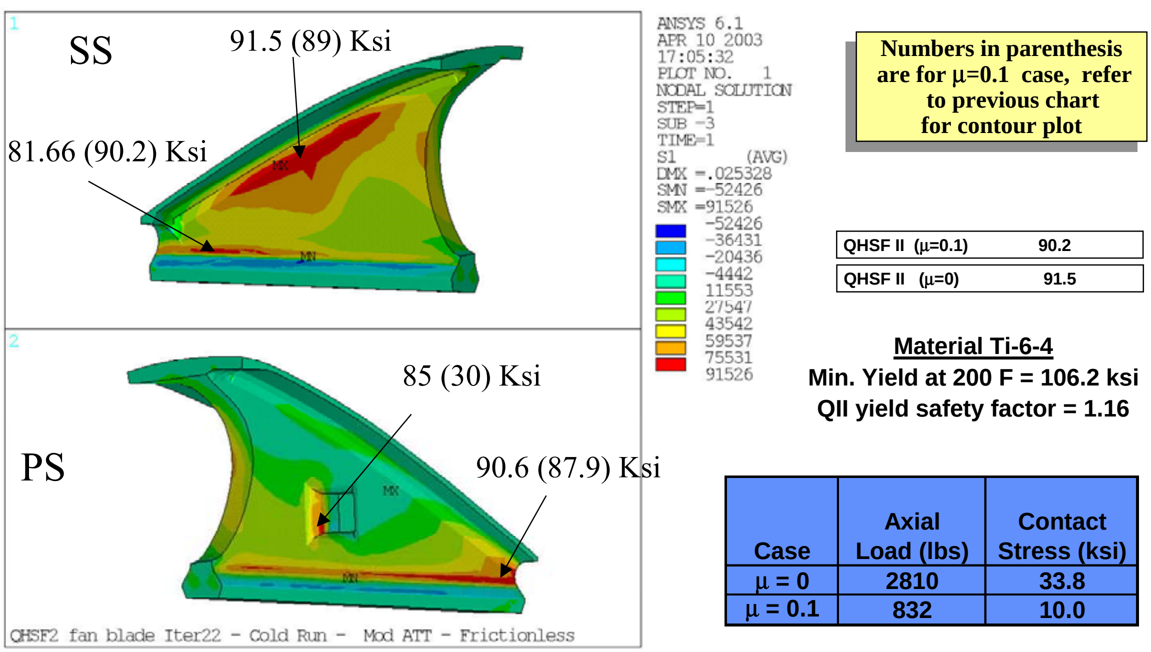

Figure 119. QHSF II Fan Blade Attachment Stress Levels at Aerodynamic Design Point Are Within Honeywell Design Experience.

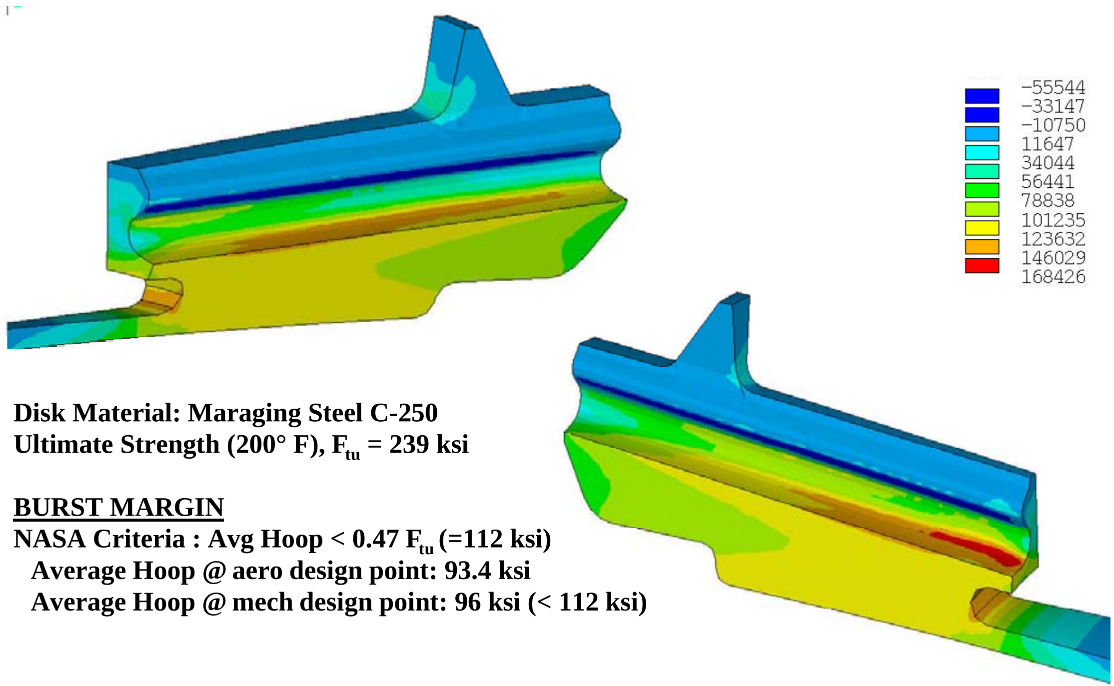

Figure 120. Disk Analysis at Aerodynamic Design Point Show Principal Stress Well Below NASA Burst Margin Criteria.

To support the determination of dynamic loads on the rig and potential blade out loads, the blade weight and center of gravity locations were estimated. Figure 121 shows the calculated values for the airfoil (A/F) only, the release blade (largest portion lost in a blade-out event), and the total blade for the QHSF II.

	Axial CG	Radial CG	Weight, lb
A/F Only	-0.327	7.019	0.55
Release Blade	-0.145	6.166	0.78
Total Blade	-0.127	5.895	0.86

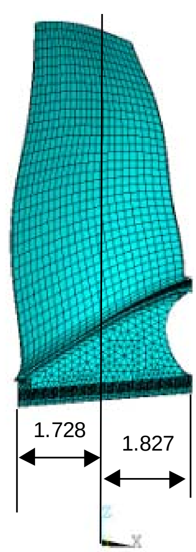

Figure 121. The Blade Weight and Center of Gravity (CG) Location Relative to the Intersection of the Axis of Rotation and the Stacking Axis Are Provided for Rig Structural and Dynamic Analyses.

Modal analysis of the final QHSF II rotor blade design was performed and is summarized by the Campbell Diagram in Figure 122. The characteristics of the first tree mode shapes are shown in Figure 123. The first bending mode is placed between first and second rotational harmonics at the mechanical design point with a 40 percent frequency margin. The second mode is placed between the third and fourth rotational harmonic with a 12.6 percent frequency margin. The third mode was placed between the fourth and fifth rotational harmonic with an 8 percent frequency margin.

Figure 124 shows the ANSYS® calculation of the maximum deflections of the QHSF II rotor blade at 100 percent Speed. The figure shows that the direction of principal motion is circumferential. Figure 125 shows that the QHSF II rotor blade meets the bird strike criterion.

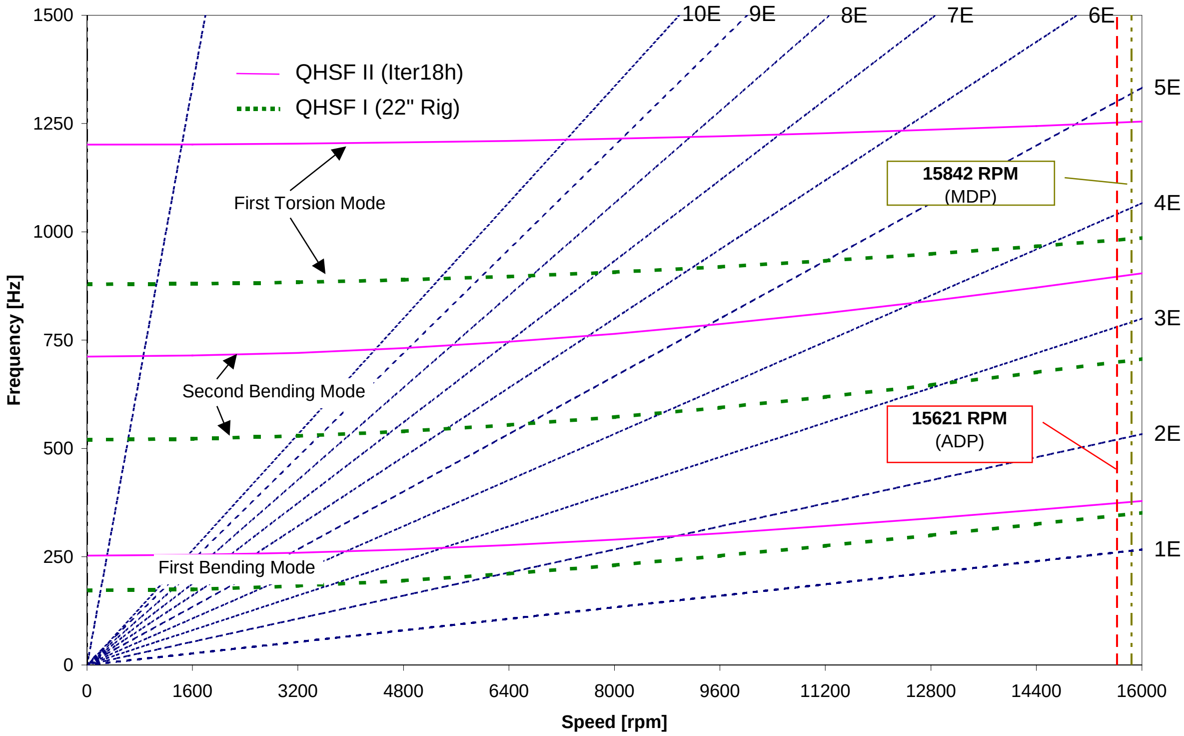

Figure 122. The Campbell Diagram for the QHSF II Rotor Shows Adequate Frequency Margin for the Three Primary Vibration Modes.

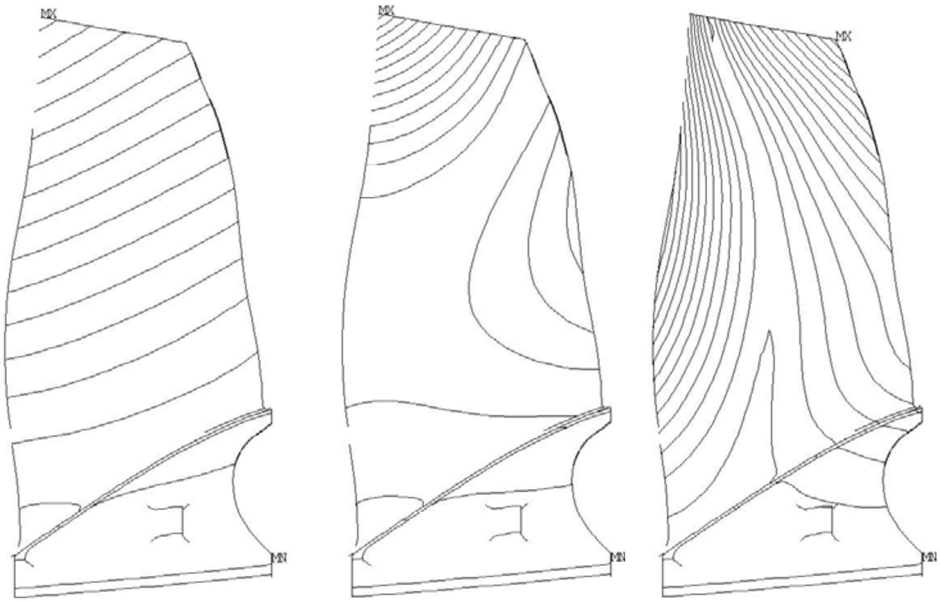

(a) First Bending (b) Second Bending (c) First Torsion

Figure 123. The QHSF II Rotor Blade Has a Complex Vibration Modal Structure.

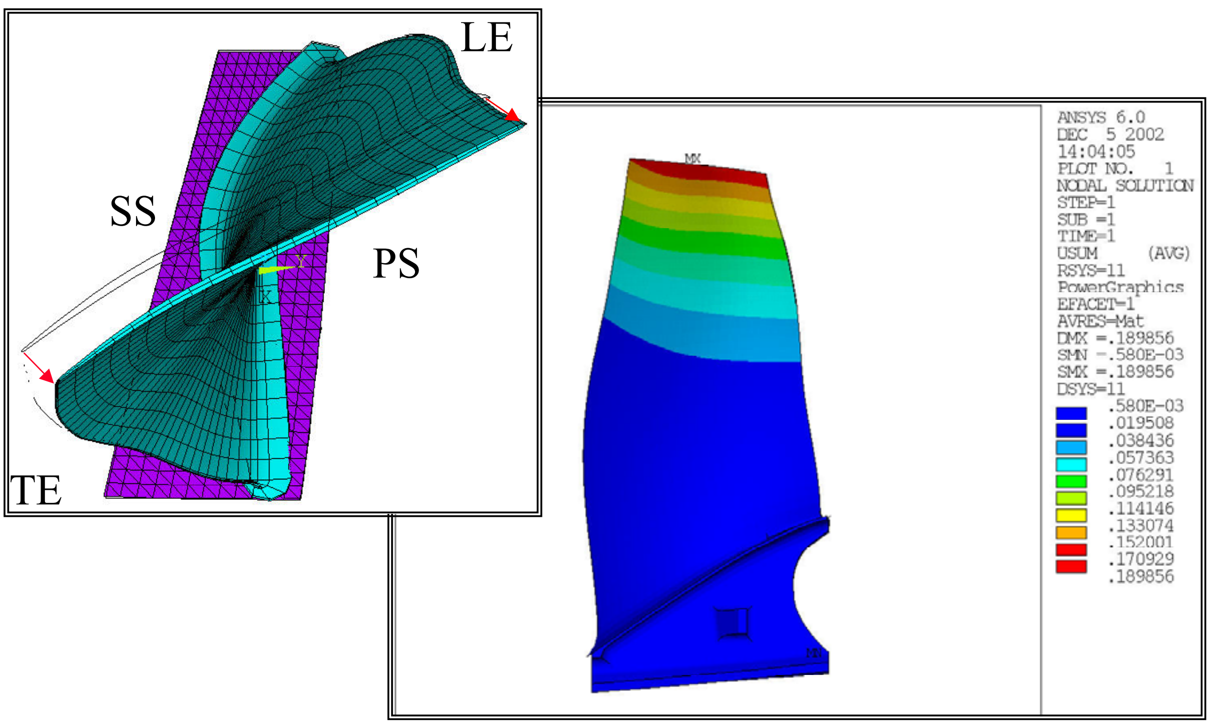

Figure 124. The Direction for the Maximum Deflections of the QHSF II Rotor Is in the Circumferential Direction.

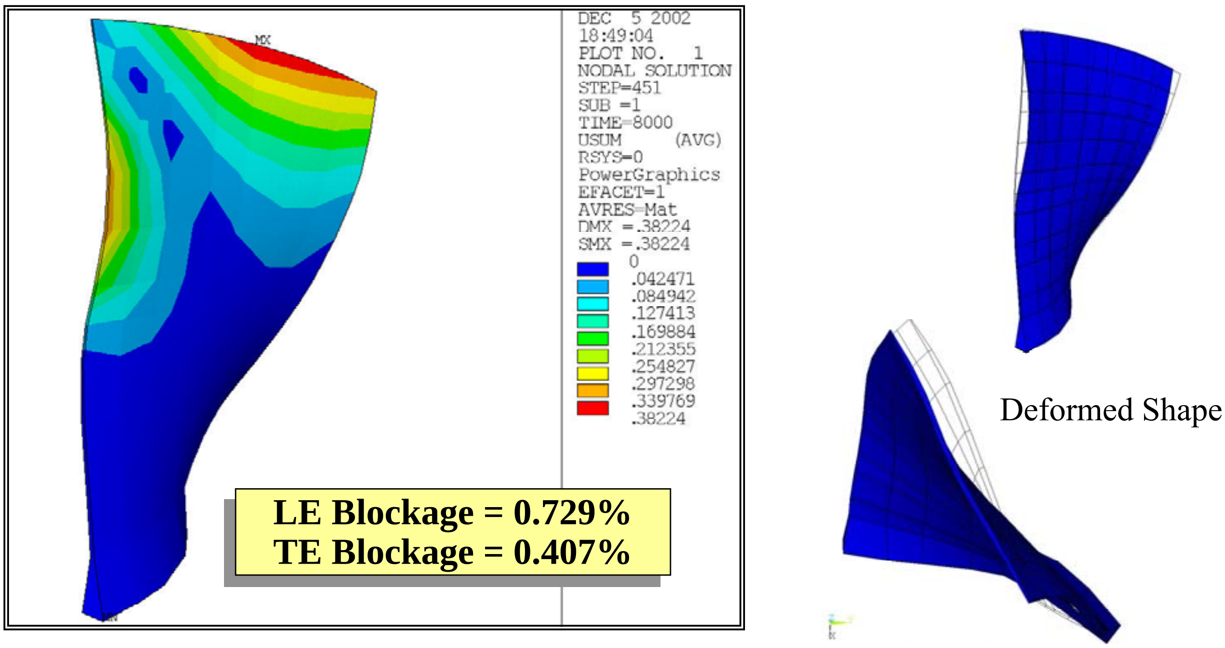

Figure 125. The Analysis of the QHSF II Rotor Blade With NOSAPM Shows That the Blade Will Meet the Bird Strike Criteria.

Figure 126 shows the completed rotor blades being installed in the fan disk. The boundary conditions for the finite element analysis for the QHSF II fan blade assumed the dovetail contact surfaces to be fully fixed in all degrees of freedom. This type of boundary condition was calibrated for fan blades with a beaver tooth, which restrained (in the axial direction) the blade dovetail at the forward end of the dovetail. The QHSF I fan blade has no beaver tooth and thus does not have this additional constraint on the forward side of blade dovetail. The blade is retained axially by the feature added on the pressure side of the shank and the mating tab on the fan disk post. Since the mating retention feature was not incorporated on the broach block, the finite element model boundary conditions were adjusted to match the bench test condition. In the analysis the fan blade was fixed normal to the dovetail contact plane, and a group of nodes were fixed parallel to the contact plane near the dovetail axial center.

A set of 22 QHSF II fan blades were acoustic ring (ARS) tested. The fan blades were mounted on the broach block (P/N R3563132-1) and secured in the slot with the mounting bolts. A bolt torque of 500 in-lb. was applied to ensure the dovetail was securely mounted and the mating surfaces were fully in contact. Results of the test for the first 10 modes are documented in Table 17. There is good agreement with the predicted frequencies of the finite element model.

Figure 126. QHSF II Rotor – Partial Assembly.

Table 17. QHSF II Fan Blade--ARS Bench Test Frequencies.

Blade S/N	Mode 1	Mode 2	Mode 3	Mode 4	Mode 5	Mode 6	Mode 7	Mode 8	Mode 9	Mode 10
Analysis	*234*	*654*	*1158*	*1638*	*2136*	*2463*	*2570*	*2798*	*3455*	*3876*
02	238	664	1154	1634	2132	2407	2549	2783	3428	3727
10	236	662	1168	1650	2138	2465	2610	2828	3495	3603
11	238	665	1171	1655	2141	2453	2587	2825	3482	3714
12	239	668	1174	1659	2141	2459	2601	2829	3484	3724
13	240	670	1164	1652	2131	2426	2580	2812	3452	3703
14	241	674	1168	1662	2144	2460	2579	2842	3475	3747
15	240	669	1165	1654	2134	2438	2576	2828	3466	3724
16	240	670	1166	1654	2133	2424	2574	2820	3461	3706
17	241	670	1168	1656	2137	2434	2572	2825	3468	3696
18	240	670	1166	1655	2136	2437	2572	2826	3463	3738
19	241	672	1168	1662	2141	2444	2584	2828	3470	3710
20	240	671	1166	1658	2134	2436	2575	2828	3463	3741
21	241	672	1167	1657	2135	2424	2579	2821	3459	3746
22	240	668	1167	1654	2138	2459	2582	2835	3464	3736
23	240	670	1168	1659	2141	2462	2573	2830	3469	3741
24	240	668	1166	1651	2138	2432	2573	2822	3466	3739
25	240	669	1163	1658	2135	2428	2579	2829	3466	3742
26	240	670	1165	1657	2137	2444	2574	2825	3469	3735
27	239	667	1165	1660	2134	2453	2576	2833	3470	3742
29	239	668	1168	1660	2138	2452	2584	2841	3479	3603
30	240	669	1163	1651	2127	2432	2582	2821	3458	3745
Min	236	662	1154	1634	2127	2407	2549	2783	3428	3603
Max	241	674	1174	1662	2144	2465	2610	2842	3495	3747
Mean	240	669	1166	1655	2136	2441	2579	2825	3467	3717
Std Dev	1.2	2.7	3.8	6.0	4.0	15.6	11.7	11.8	13.2	41.0

Holography bench testing was conducted on the QHSF II fan blade using the same type of set-up that was used in the ARS bench test. The results are documented in Table 18 where the holography frequencies are compared to the average ARS frequencies of the 21 blades, as well as to the analytically predicted frequencies. The data shows there is good agreement between the bench test and finite element analysis frequencies. Figure 127 shows mode shapes (for modes 1-6, respectively) obtained from holography test and finite element analysis. There is good agreement between the holography bench test and analytically predicted mode shapes. The close agreement of the results indicates the boundary condition used in the finite element analyses is consistent with the conditions of the bench test.

Table 18. QHSF II Fan Blade -- Comparison of Finite Element Analysis, Acoustic Ring Signature, and Holography Test.

Mode	Analysis* (Hz)	ARS** Frequency (Hz) Average	Min	Max	Std Dev	Percent Difference	Holography*** (Hhz)	Percent Difference
1	234	240	236	241	1.2	2.5	236	1.0
2	654	669	662	674	2.7	2.2	659	0.8
3	1158	1166	1154	1174	3.8	0.7	1160	0.2
4	1638	1655	1634	1662	6.0	1.0	1639	0.0
5	2136	2136	2127	2144	4.0	0.0	2137	0.1
6	2463	2441	2407	2465	15.6	-0.9	2428	-1.4
7	2570	2579	2549	2610	11.7	0.4	2562	-0.3
8	2798	2825	2783	2842	11.8	1.0	2798	0.0
9	3455	3467	3428	3495	13.2	0.3	3483	0.8
10	3876	3717	3603	3747	41.0	-4.3	3736	-3.8

* Fixed normal to contact surface + a row of nodes fixed parallel to contact surface at mid-dovetail
**Acoustic ring frequency of a set of 21 fan blades fixed in broach block
***Holography test of a single blade fixed in broach block

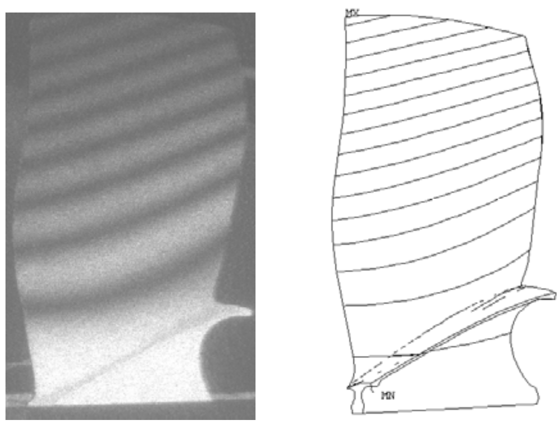

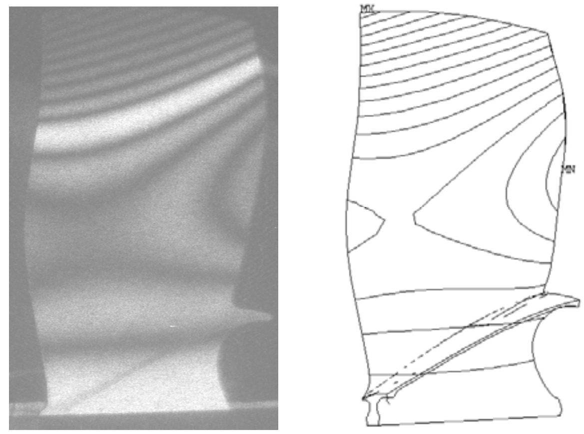

(a) Mode 1 **(b) Mode 2**

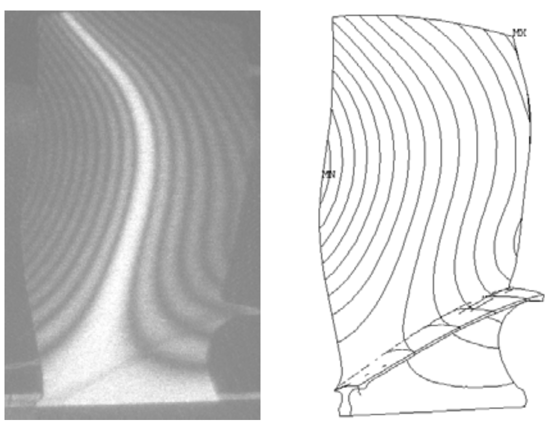

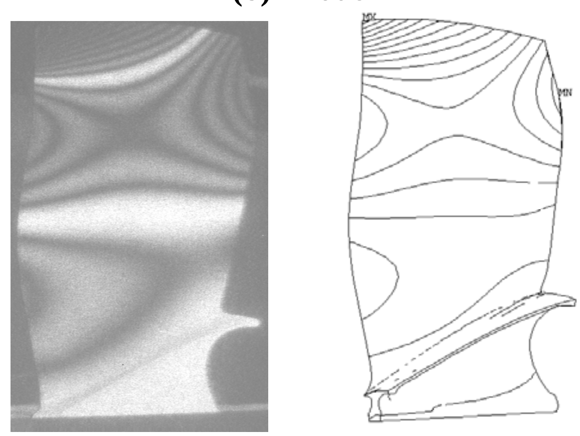

(c) Mode 3 **(d) Mode 4**

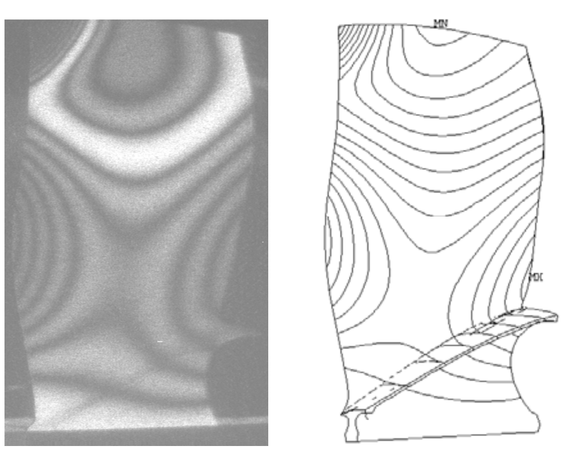

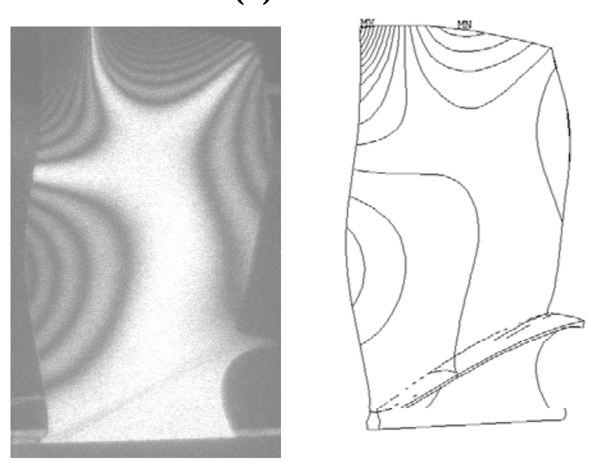

(e) Mode 5 **(f) Mode 6**

Figure 127. QHSF II Fan Blade – Comparison of Holography and Finite Element Analysis.

For the rig configuration, the stator vane is made from SS355 material. The metal vane is brazed to the outer shroud and thus in the finite element model it is fully fixed at the outer shroud. At the hub, the vane is positioned in a pre-cut slot, and constrained in the radial direction by an aluminum ring. The hub shroud itself is on rollers that allow the stator assembly to rotate about the engine axis. In the finite element model, the vane is fixed in radial and axial directions at the hub. The resulting reduced frequencies for the first two modes are above the design criteria. The Campbell Diagram for the stator vane is shown in Figure 128 and the predicted mode shapes are shown in Figure 129. The frequencies for the first 6 vane modes are given below.

Mode	Frequency, Hz
1	807.2
2	3067.2
3	3562.8
4	3755.
5	5132.7
6	5508.7

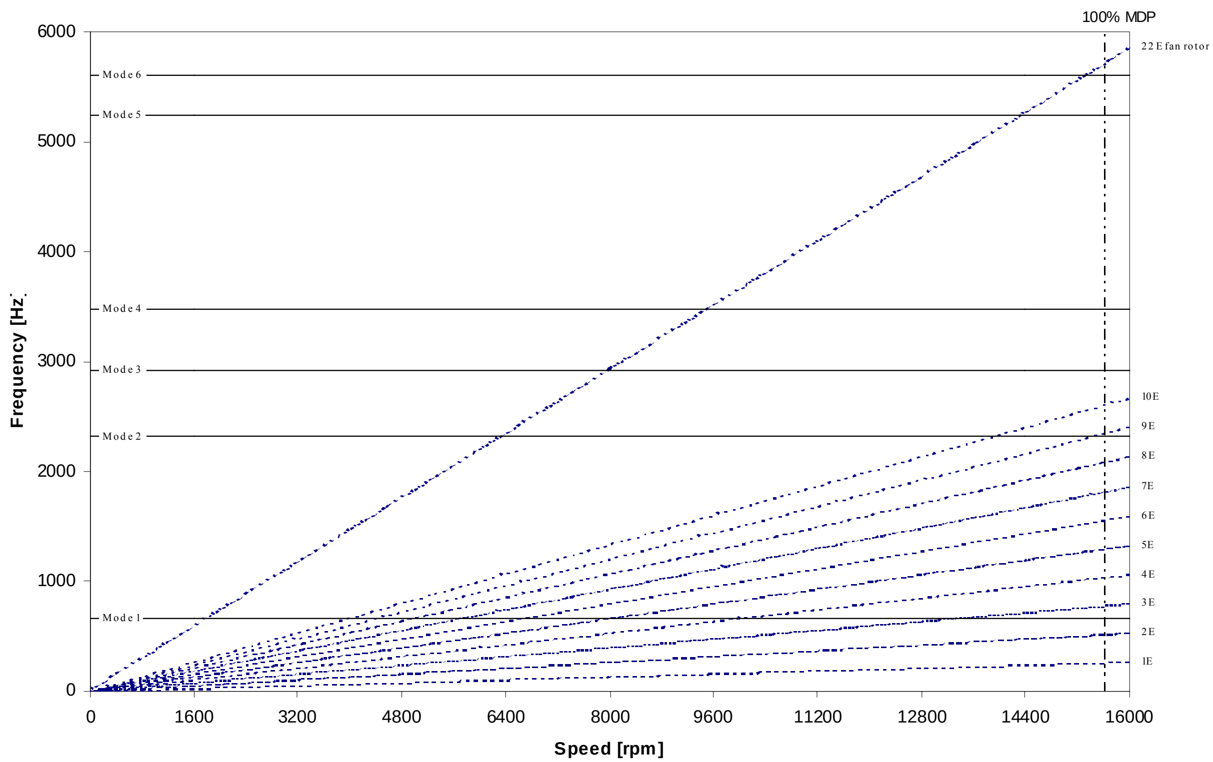

Figure 128. The Campbell Diagram for the QHSF II Vane Shows That No Vibration Issues Are Expected.

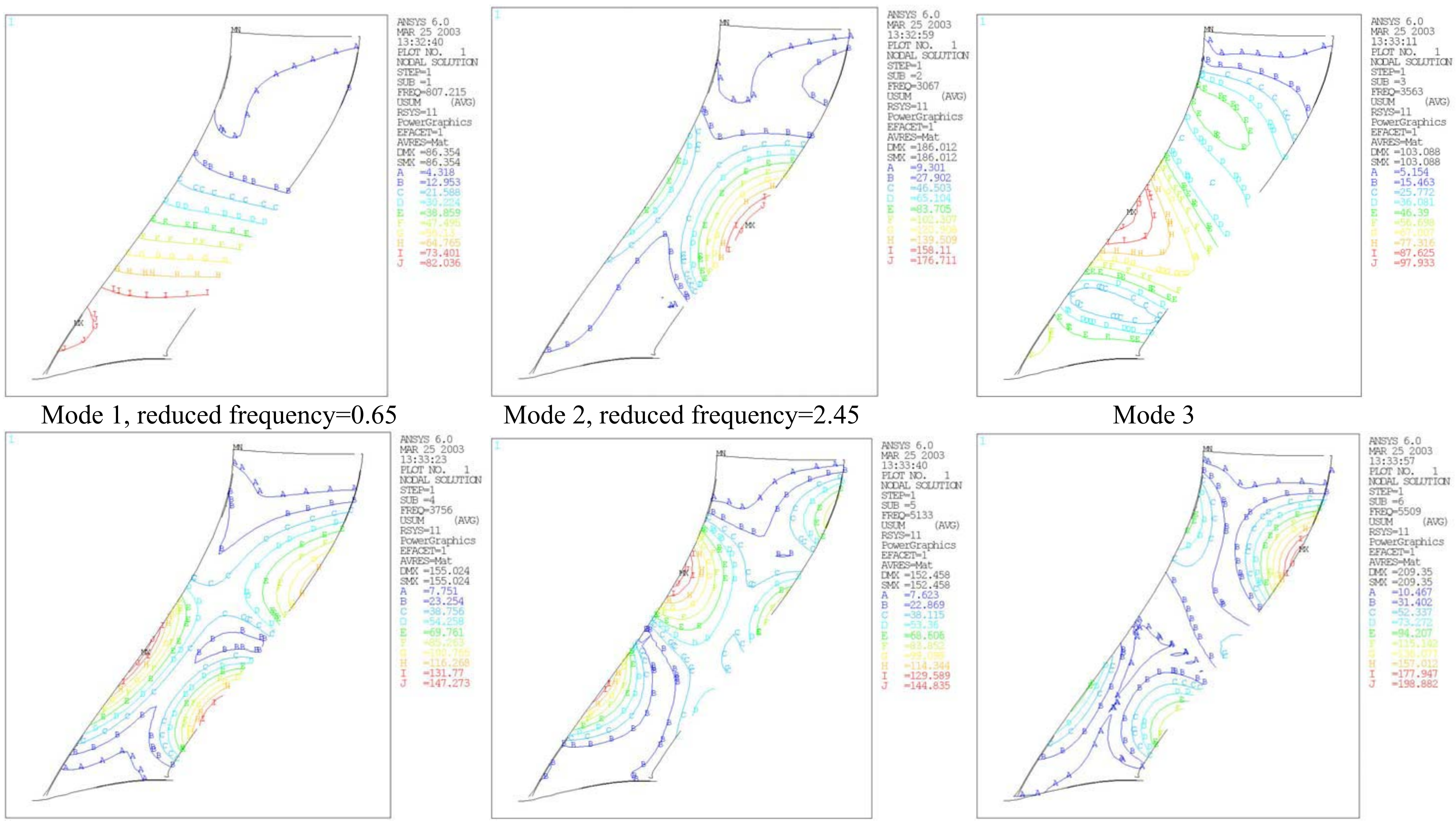

Mode 1, reduced frequency=0.65

Mode 2, reduced frequency=2.45

Mode 3

Mode 4

Mode 5

Mode 6

Figure 129. The First Six Mode Shapes for the QHSF II Rig Vane Were Calculated With ANSYS®.

5.8.3 Aeroelastic Performance

Viscous TURBO-AE analysis of the final design was performed. The predicted flutter boundary is shown in Figure 130 for the various blade attachment concepts. For the current 4.5 degree sloped attachment design, the aeroelastic "pinch point" at 70 percent speed is predicted to be stable based on the viscous results.

5.8.4 Acoustic Performance

Acoustic analysis was performed to verify the performance of the Case 18h design. In summary, noise reduction on QHSF II is anticipated to be similar to that demonstrated on the QHSF I. Noise is reduced primarily by decreased rotor-stator and rotor-strut interactions that are obtained by the geometric features of the rotor and stator.

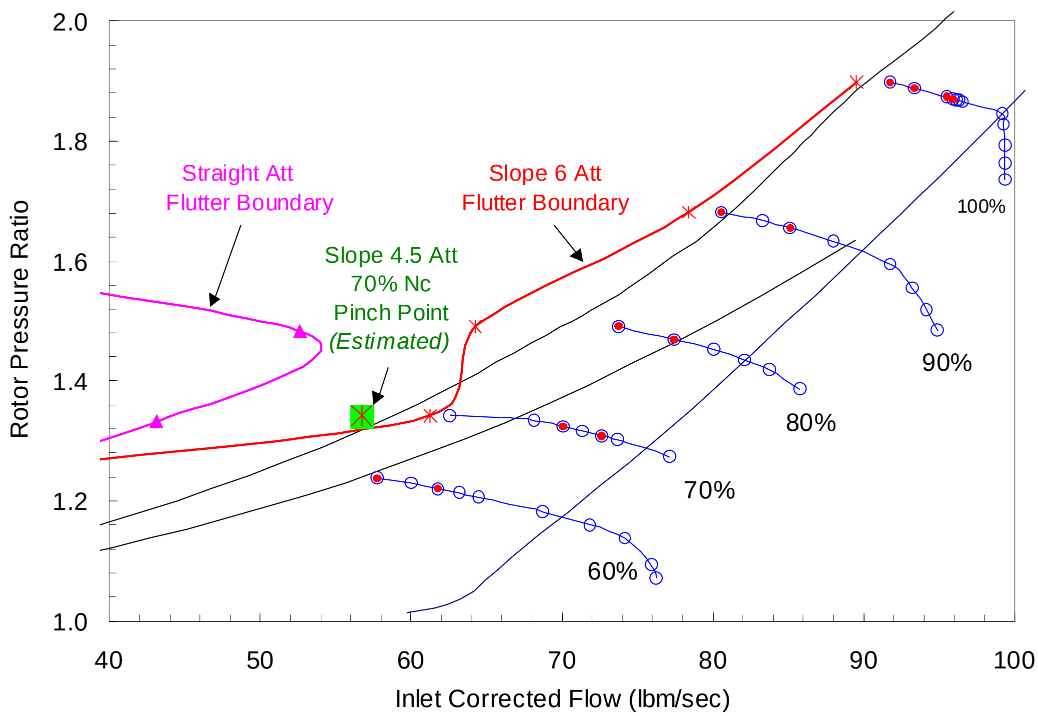

Figure 130. Viscous TURBO Results Show Reduced Risk for 4.5 Degree Sloped Attachment.

5.9 Further Revisions to the Stator Design

Additional aerodynamic design efforts were applied to examine potential solutions to the separation in Case 18h and resulting efficiency loss. Figure 131 shows stator lean and metal angle profiles for the Baseline II, Case 18h, and a new study case for the stator separation elimination, labeled Q2a. A more aggressive lean, with compensating changes to the leading edge metal angle are combined to reduce flow separation and could also offer further noise reduction. Aerodynamic results for QHSF II and "Q2a" are shown in Figure 133 and Figure 134. While the separation has not been completely eliminated, it has been significantly reduced, with an estimated efficiency improvement of 0.3 percent at the peak point, as shown in Figure 135. The improvements to the flow field appear to be significant, indicating that the efficiency improvement may be somewhat under predicted by the CFD results.

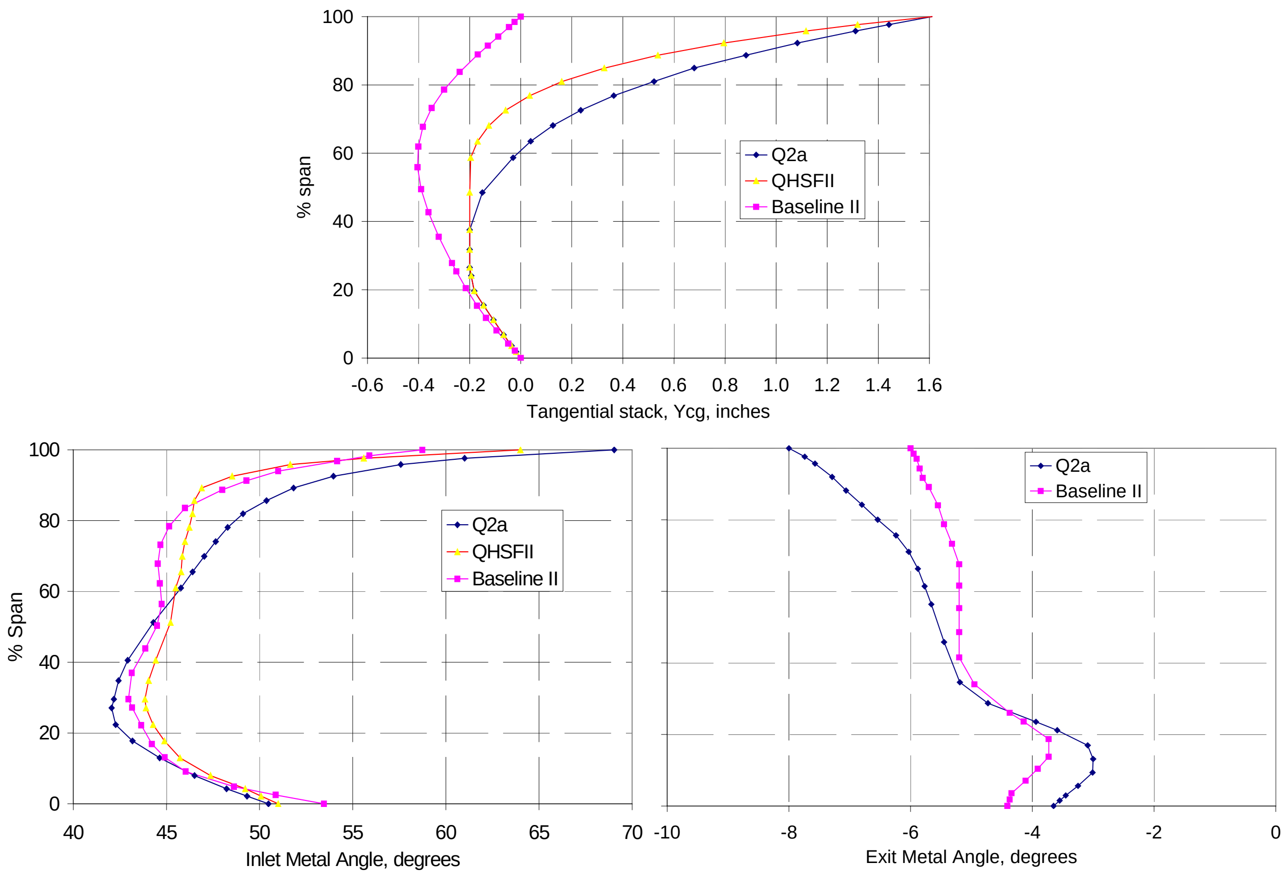

Figure 131. The Stator Separation Was Reduced Through Increased Stator Lean and Metal Angle Changes.

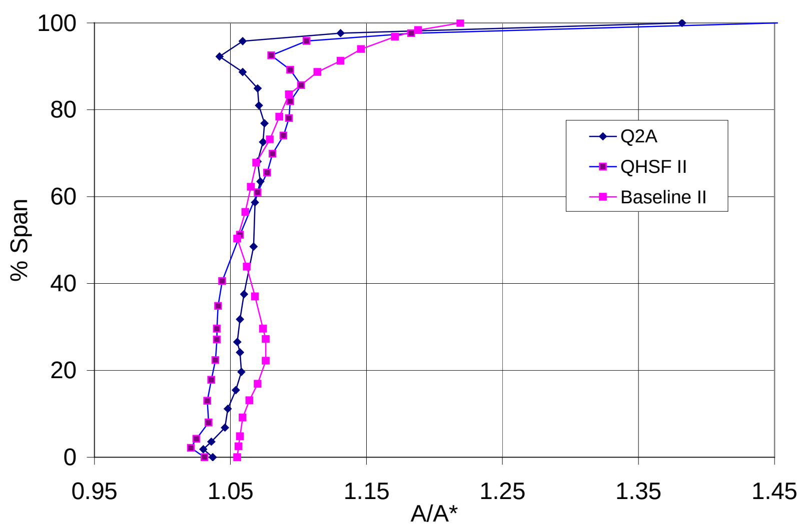

Figure 132. The QHSF II Stator Redesign Maintained Good Throat Area Margin.

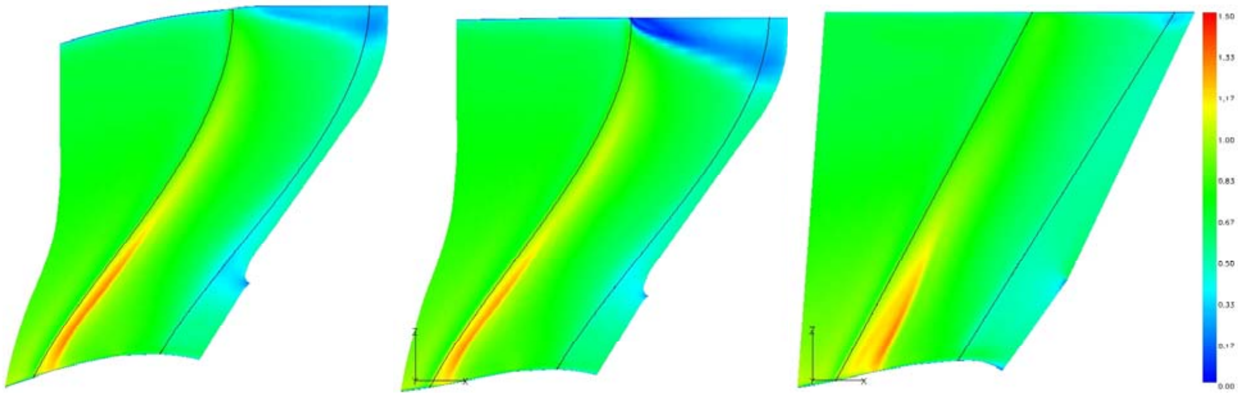

(a) QHSF II – Q2a (b) QHSF II – Case 18h (c) Baseline II

Figure 133. Mach Number Contours on the Vane Suction Surface Show the Reduction of the Flow Separation Near the Shroud.

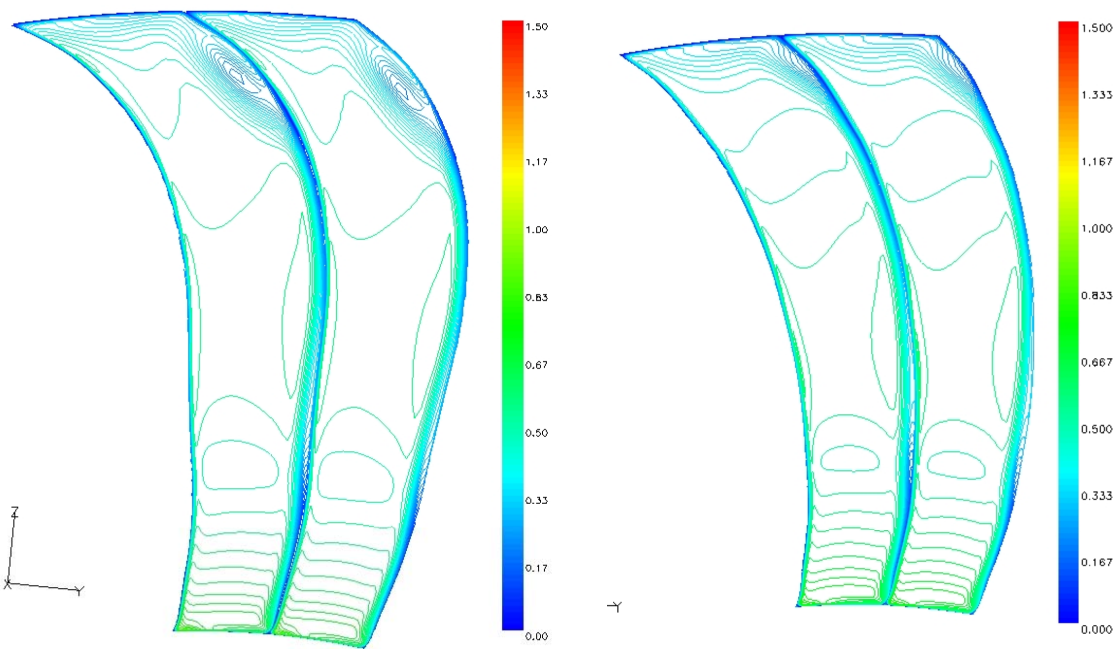

QHSFII_old QHSFII_new

Figure 134. Trailing Edge Mach Contours Show Reduced Stator Separation for the Q2a Design.

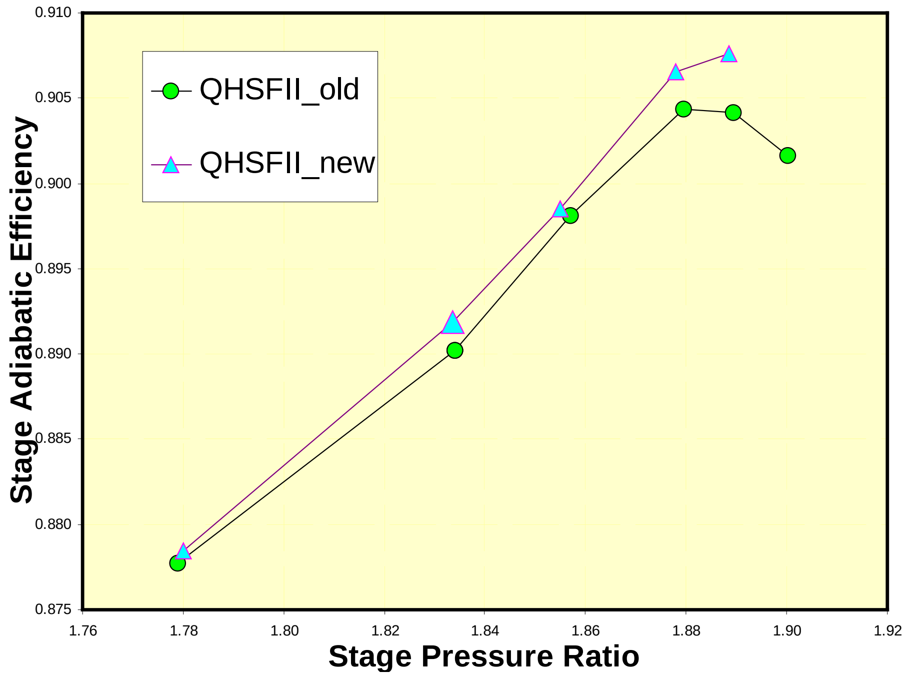

Figure 135. The Results of the CFD Analysis Indicate an Improvement of 0.3% in Peak Efficiency.

5.10 Modifications to the Baseline II Stators

A program augmentation was received on August 11, 2003 to make hardware for a set of Baseline II stators. The aerodynamic design of the Baseline II vane needed to be modified to run effectively behind the QHSF II rotor.

Figure 136 shows a solid model comparison of the QHSF II stator design to the modified Baseline II stator. The new stator has geometry similar to the Baseline II stator, with nearly identical performance to the QHSF II design as indicated by the Mach No. Profile in Figure 137, the pressure ratio comparison in Figure 138, and the adiabatic stage efficiency comparison in Figure 139.

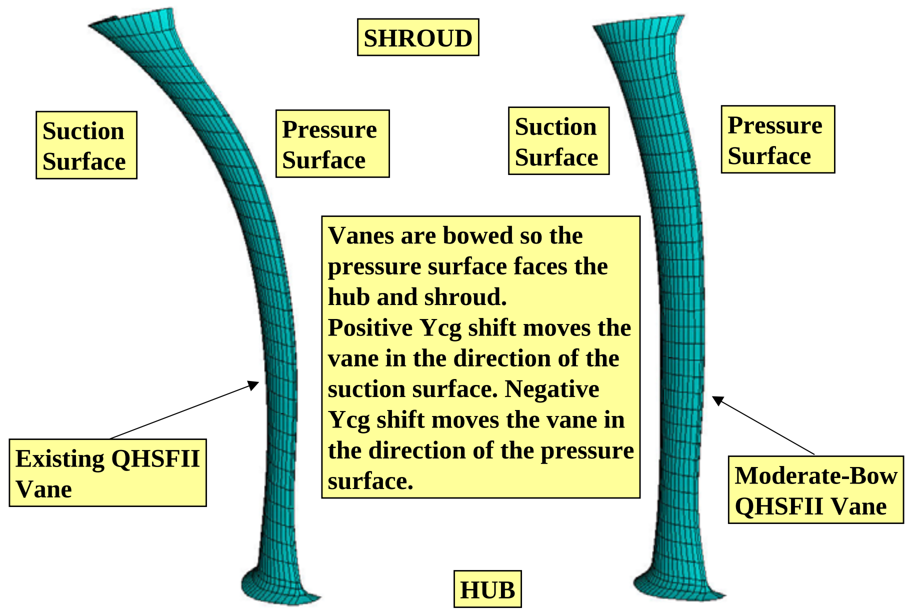

Figure 136. The Baseline II Vane Has Less Circumferential Lean Than the QHSF II Vane.

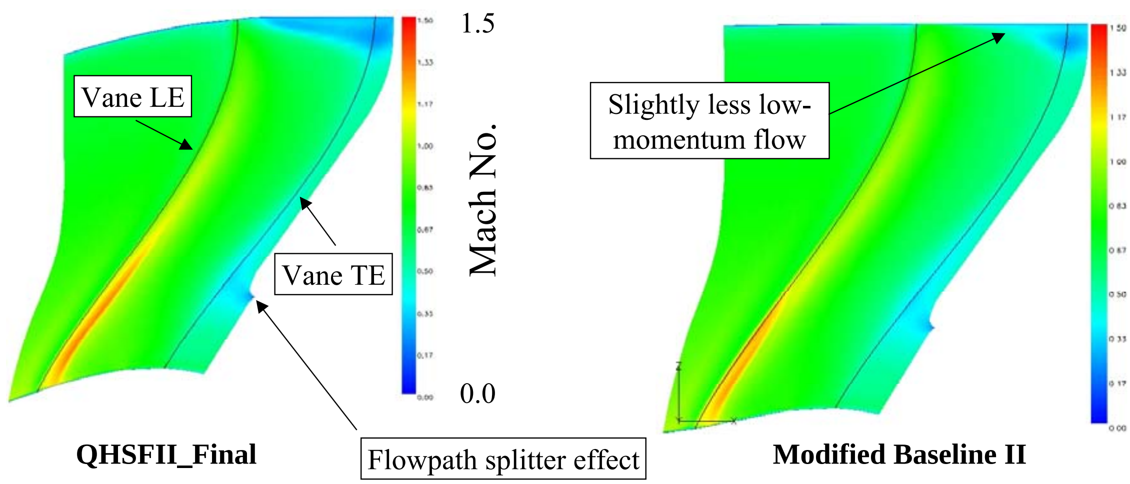

Figure 137. The Baseline II Vane Has a Very Similar Loading Distribution as the QHSF II Vane at the Design Point.

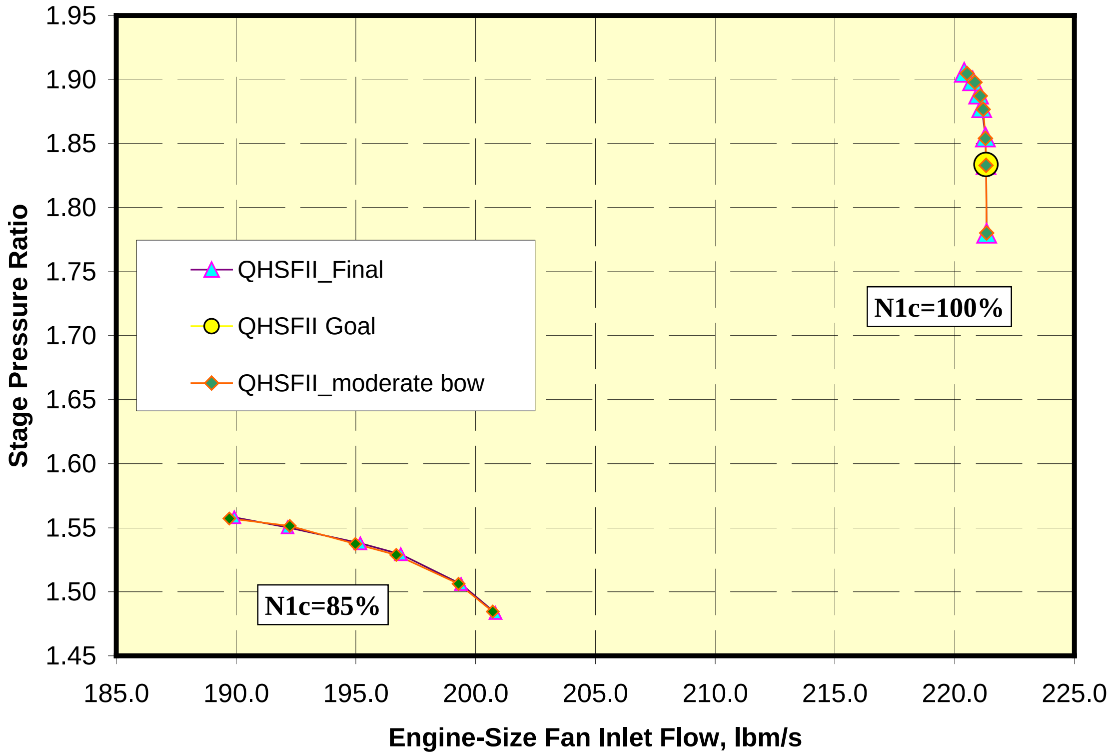

Figure 138. QHSF II Stator and Baseline II Stator Have Nearly Identical Pressure Ratio.

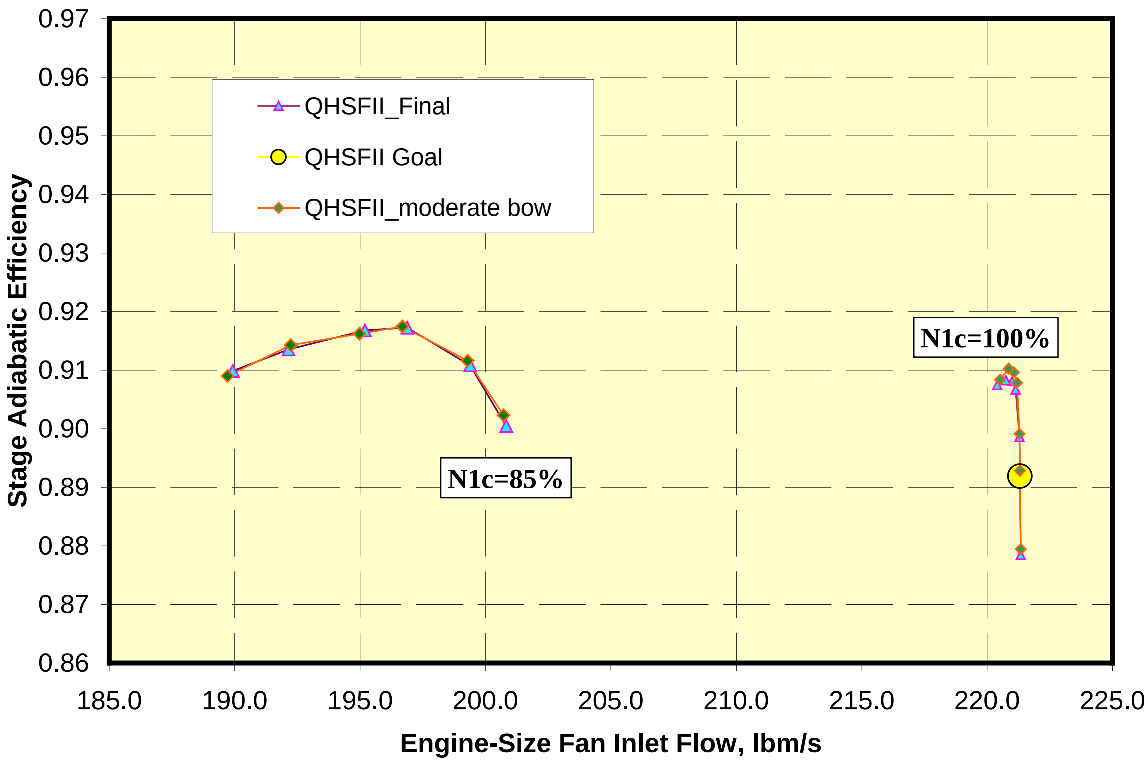

Figure 139. QHSF II Stator and Baseline II Stator Have Nearly Identical Efficiency.

Figure 140 shows the final Baseline II stator fabricated for the 22" QHSF II Rig.

Figure 140. A Baseline II Stator Set Was Designed and Fabricated to Match the QHSF II Rotor for Study of Rotor/Strut Interaction Effects.

5.11 Analysis of the Rotor-Strut Interaction With the Baseline II and QHSF II Stators

The purpose of the Rotor-Strut Interaction Analysis was to further understand the role of the stator in that interaction. In particular, the study focused on the impact on flow behavior of the stator shape (lean and bow) and the pitchwise alignment (or circumferential clocking) of the stators relative to the struts.

Stator/strut flow predictions were performed for 8 flowpath configurations, including 4 different stator/strut clocking positions, for both the Baseline II and QHSF II stators. For purposes of the analyses, the struts were clocked relative to the stators, with clocking angles of 0.0, 1.8, 3.6, and 5.4 degrees. The 4 stator/strut clocking positions are illustrated in Figure 141, for both the Baseline II and QHSF II stators. The strut geometry was identical for both stators. Inlet flow conditions for the stator/strut analyses were taken from an axisymmetric flow analysis prediction of QHSF II rotor exit conditions at the 85 percent corrected speed, SLS operating line point.

The stator/strut flow predictions were performed using the Fluent® CFD analysis program. Each of the flowpath models contained an annular periodic sector composed of 5 stators and 1 strut, as shown in Figure 142. The computational mesh consisted of an unstructured tetrahedral volume mesh constructed from a triangular surface mesh. The triangular surface mesh on the strut is shown in Figure 143. The computational meshes for the Baseline II cases had approximately 3.8 million cells; the meshes for the QHSF II cases totaled approximately 4.2 million cells. These meshes were considerably more dense than those used in the QHSF I rotor-strut interaction analyses. The solutions were performed using Version 6.1.23 of Fluent®, and employed the segregated, implicit solver, with the realizable k-epsilon turbulence model using non-equilibrium wall functions.

Evaluation of the flow analyses focused on the predicted static pressure fields upstream of the stators. Static pressure data were processed at various axial and radial locations in the upstream flowfield, as illustrated in Figure 144.

Figure 145 - Figure 148 present the circumferential distributions of static pressure at selected locations resulting from the flow analyses of all 8 stator/strut configurations. Based on a review of these figures, the following observations may be made:

- At all sampling locations upstream of the stator, a strut-induced static pressure disturbance or pulse is evident. The pulses decay with increasing distance upstream from the strut.
- Lean and bow of the QHSF II stator appear to affect the strut pressure pulses at outer span radial locations. The pulse amplitude appears higher for the unbowed Baseline II stator cases. In addition, as seen in Figure 148, the unbowed Baseline II stator cases show evidence of the stator pressure pulses superposed over the strut pulse; in contrast, the QHSF II cases show very little evidence of stator pressure pulses.
- Clocking effects appear to be evident with both stators. Differences in pulse amplitude and peak shape appear to correlate with stator/strut clocking.

It may be concluded from the Rotor/Strut Interaction Study that the stator shape and pitchwise alignment relative to the struts does have an impact on the static pressure distribution upstream of the stators.

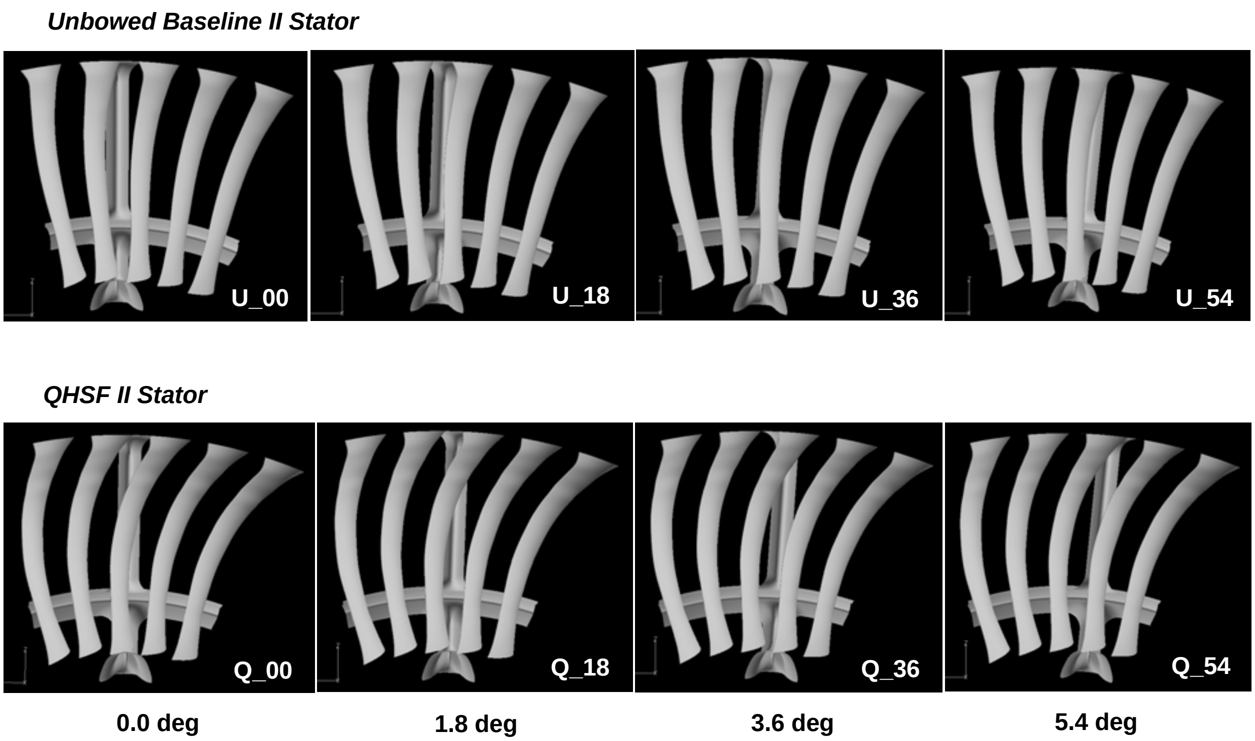

Figure 141. Four Stator/Strut Clocking Positions Were Analyzed for Both the Baseline II and QHSF II Stators.

Figure 142. The Flow Path Model for Rotor/Strut Interaction Analyses Consisted of a Periodic Sector of 5 Stators and 1 Strut.

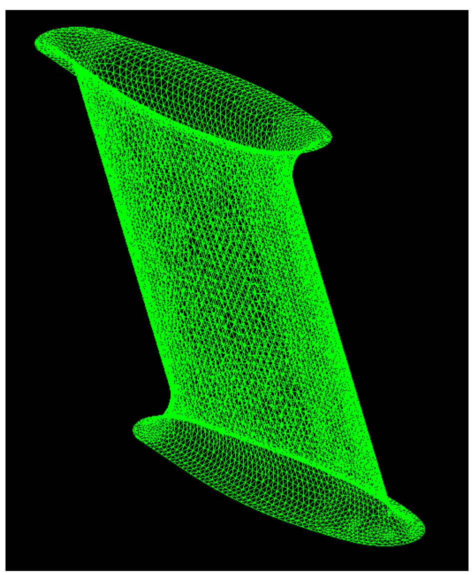

Figure 143. The Unstructured Triangular Surface Mesh, Shown Here Applied to the Bypass Strut, Formed the Basis for the Tetrahedral Volume Mesh.

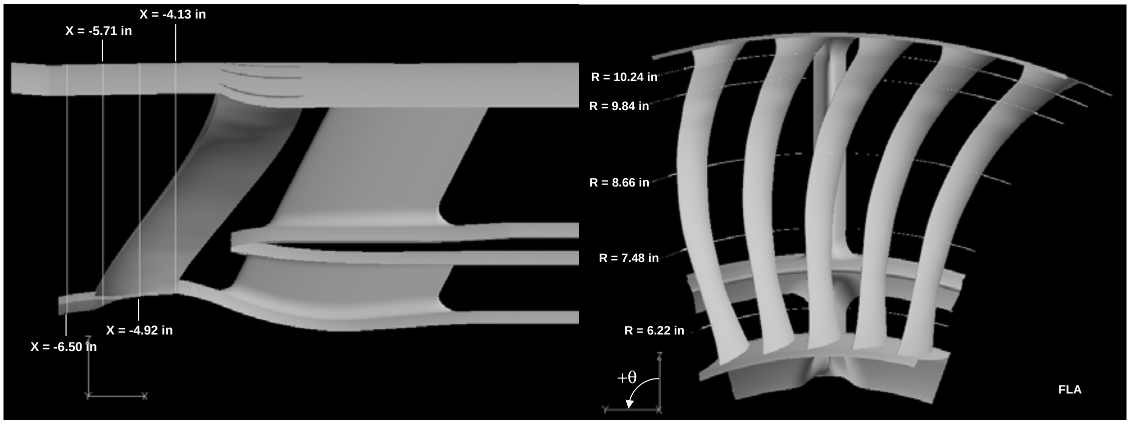

Figure 144. Axial and Radial Locations at Which Static Pressure Data Were Processed in the Region Upstream of the Stators.

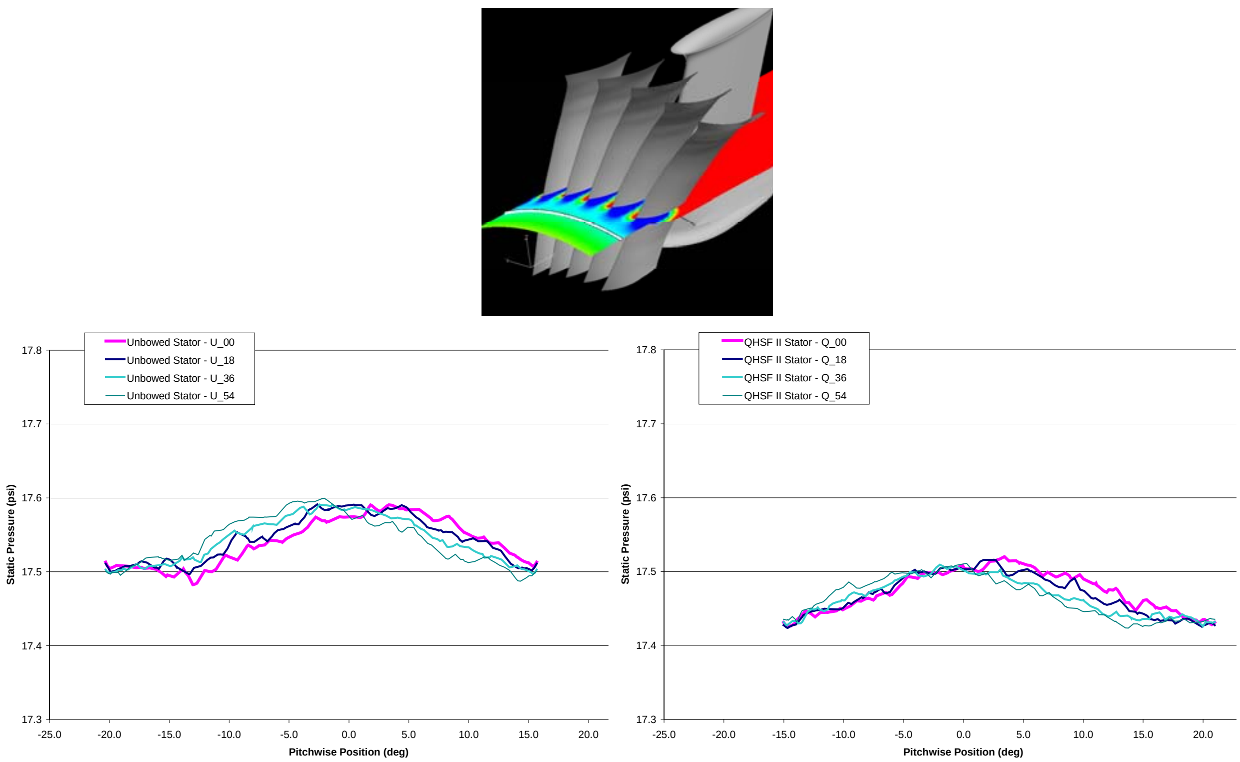

Figure 145. Circumferential Static Pressure Distributions at R = 7.48 Inches and X = -5.71 Inches Show Differences in Pulse Amplitude and Shape With Strut Clocking. Unbowed Baseline II Stator Case Is Shown on the Left; QHSF II Stator Case Is on the Right.

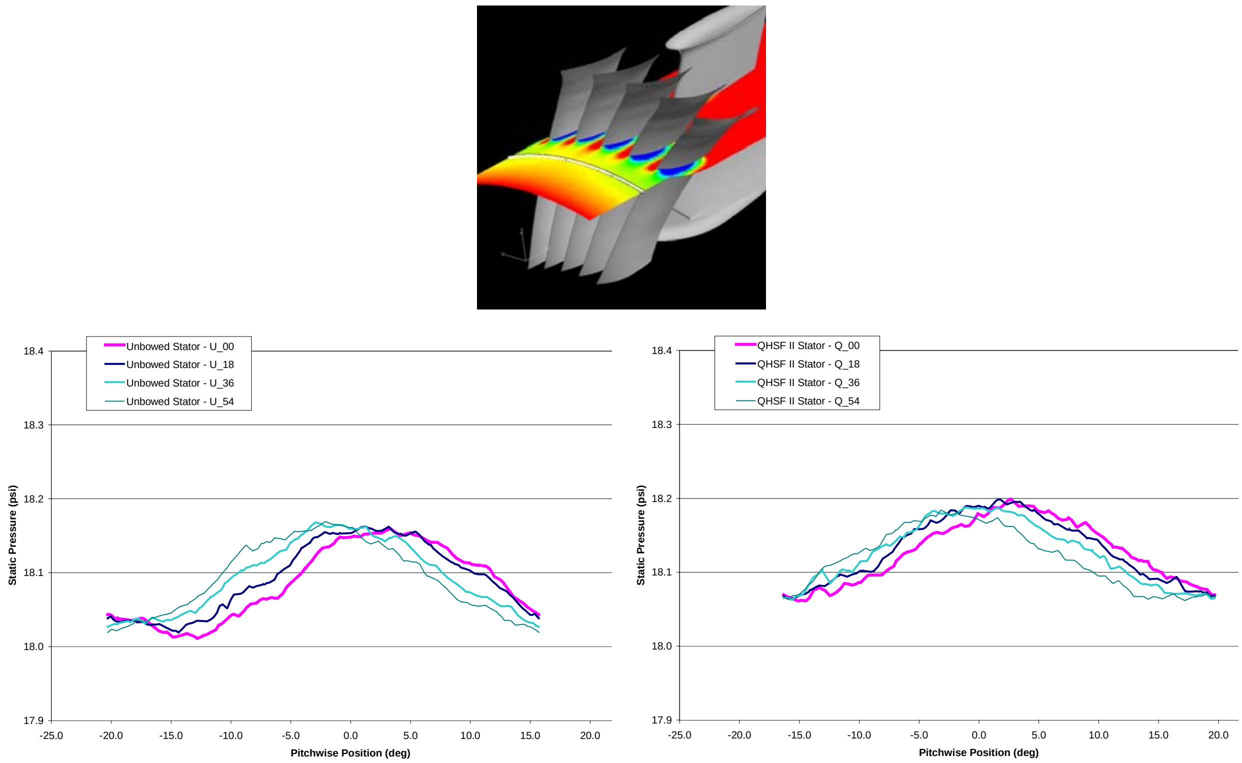

Figure 146. Circumferential Static Pressure Distributions at R = 8.66 Inches and X = -4.92 Inches Show Pulse Amplitude Is Higher for the Unbowed Baseline II Stator Case. Also, Differences Are Seen in Pulse Amplitude and Shape With Strut Clocking. Unbowed Baseline II Stator Case Is Shown on the Left; QHSF II Stator Case Is on the Right.

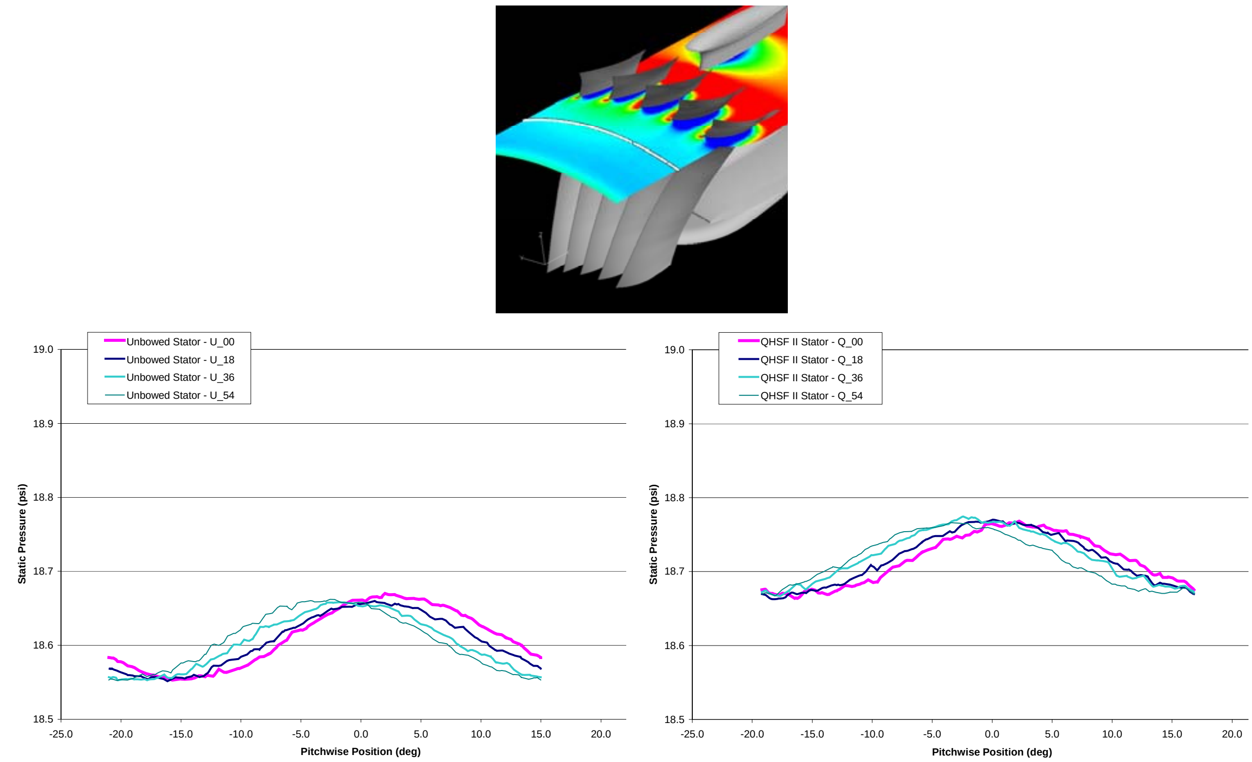

Figure 147. Circumferential Static Pressure Distributions at R = 9.84 Inches and X = -4.92 Inches Show Pulse Amplitude Is Higher for the Unbowed Baseline II Stator Case. Also, Differences Are Seen in Pulse Amplitude and Shape With Strut Clocking. Unbowed Baseline II Stator Case Is Shown on the Left; QHSF II Stator Case Is on the Right.

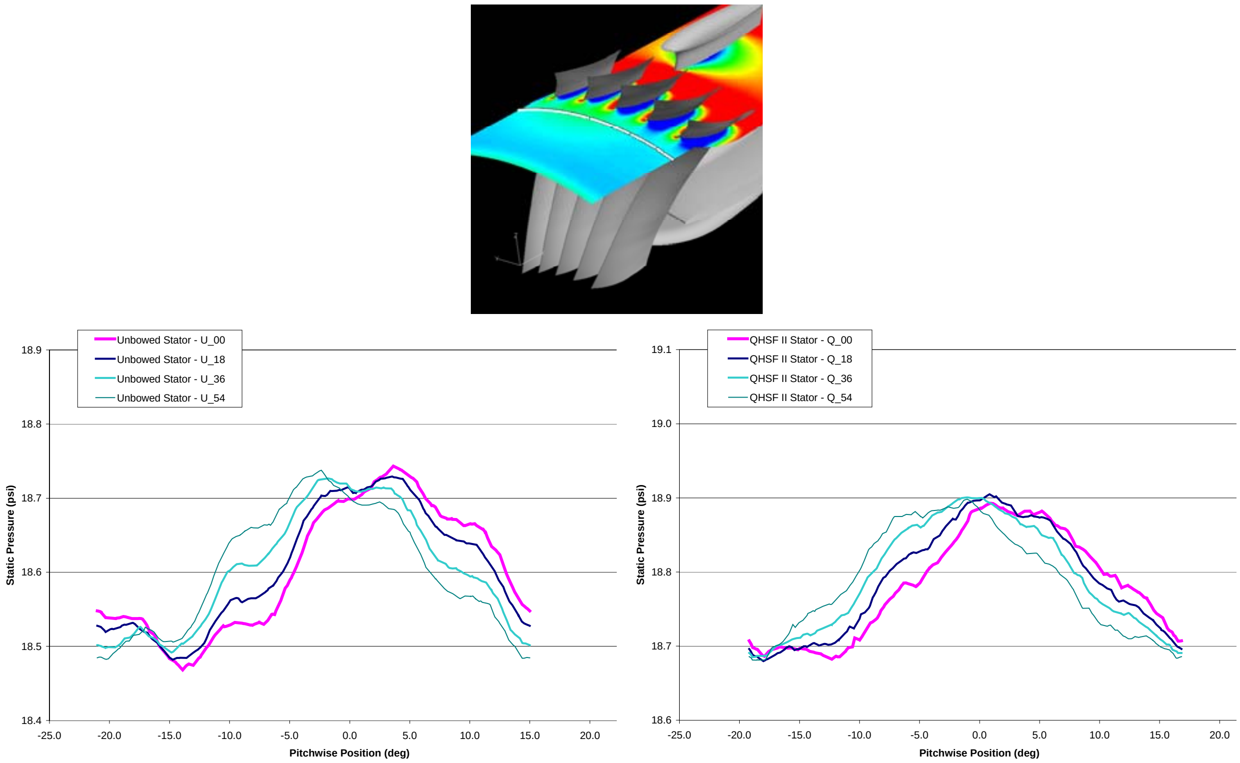

Figure 148. Circumferential Static Pressure Distributions at R = 9.84 Inches and X = -4.13 Inches Show Pulse Amplitude Is Higher for the Unbowed Baseline II Stator Case. Also, Pressure Pulse Shapes for the Baseline II Stators Show the Influence of the Stator Pressure Pulses More Than QHSF II Stators, at the Same Axial Position. Unbowed Baseline II Stator Case Is Shown on the Left; QHSF II Stator Case Is on the Right.

6. RIG MODIFICATIONS

6.1 Overview

Several modifications to the existing QHSF rig were required to accommodate the QHSF II design. Key mechanical differences include a reduced hub/tip ratio, the addition of a rotating stator set & actuation system, and fan frame modifications to accommodate additional instrumentation. An overlay of the QHSF I and QHSF II rigs is shown in Figure 149. Figure 150 is a schematic diagram of the rig installed in the wind tunnel.

A set of distortion screens and a screen rotator device were provided to complete additional mechanical and operability testing of the QHSF II rig in the NASA wind tunnel. Figure 151 shows the inlet distortion screen rotator that has been proven in prior rig testing at Honeywell. Figure 152 shows the rig in the performance test configuration, which has been modified for rotation of stator set during rig operation. Figure 153 shows the rig in the acoustic configuration. Changes to acoustic configuration are minimal. The inlet liner has been changed by NASA from fiberglass to aluminum. During far-field acoustic testing of the QHSF II, the rotating stator actuation system was removed, eliminating the need for any modifications to the nacelle.

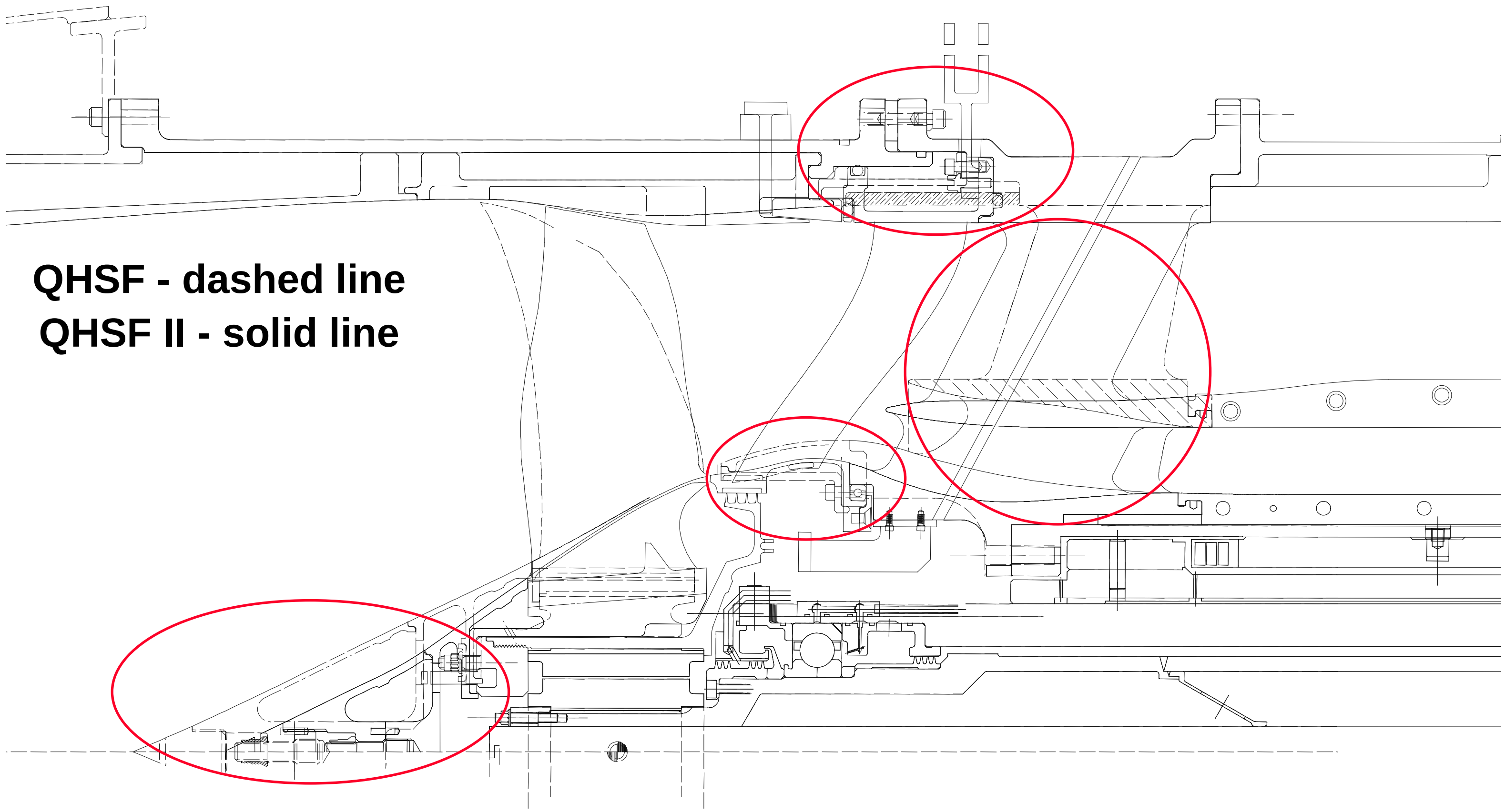

Figure 149. The Major Differences Between the QHSF I and QHSF II Rigs Are the Hub-to-Tip Ratio, Rotating Stator Set, and Frame Modifications.

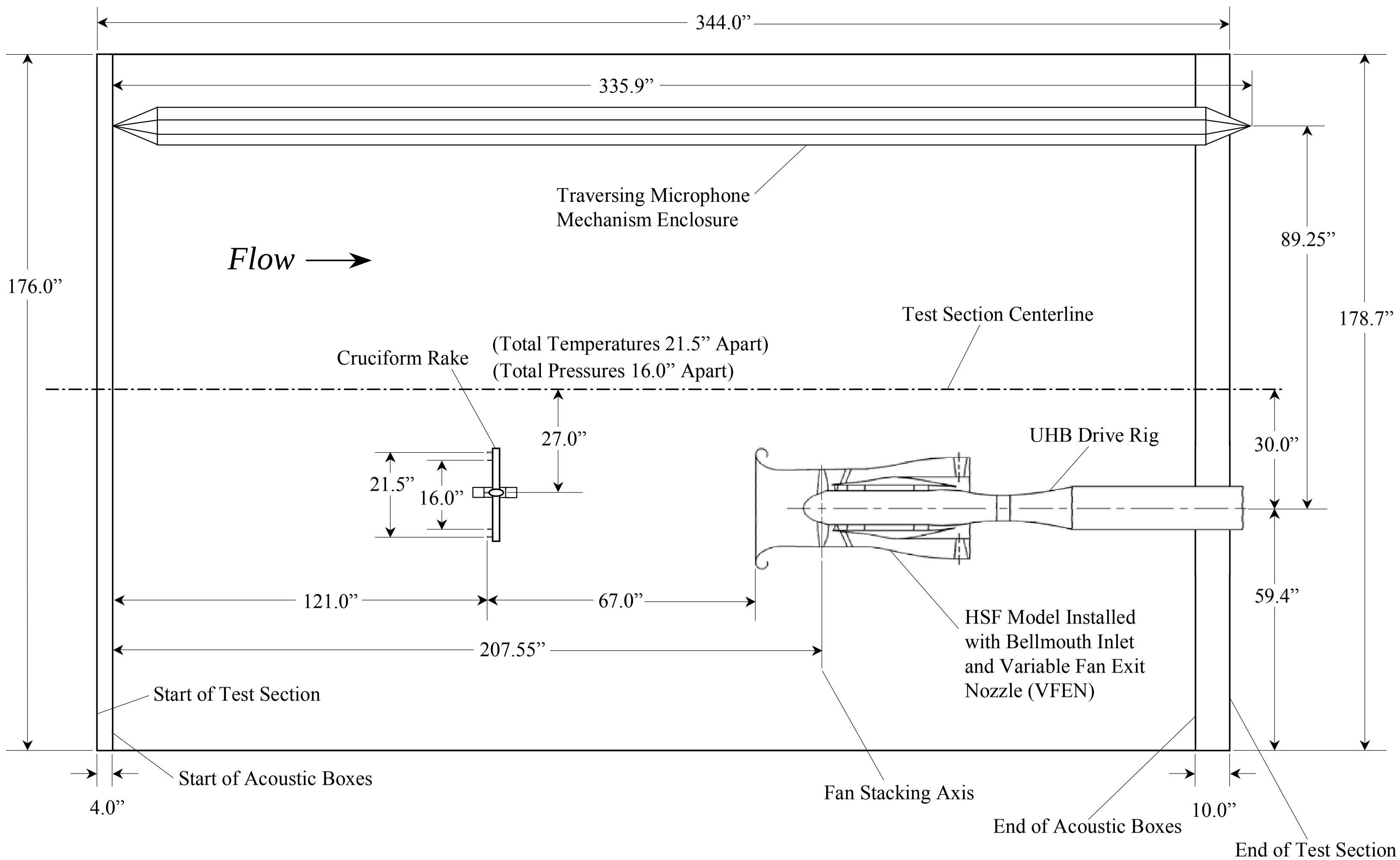

Figure 150. Schematic Diagram of the Rig Installed in the 9x15 Wind Tunnel.

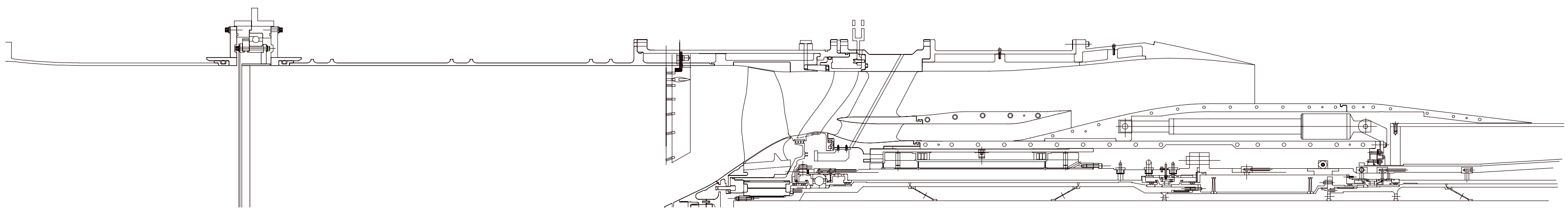

Figure 151. The Fan Distortion Measurement Configuration Is Shown for the 22" QHSF II Rig.

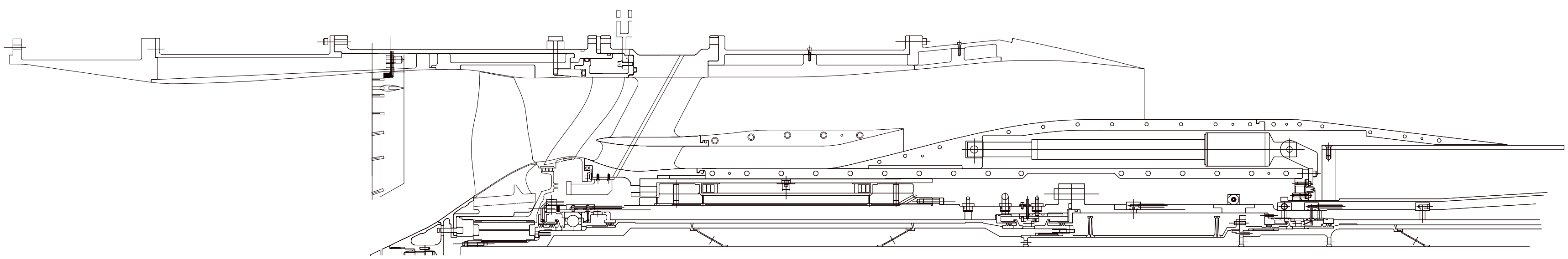

Figure 152. The Performance Configuration Is Shown for the 22" QHSF II Rig.

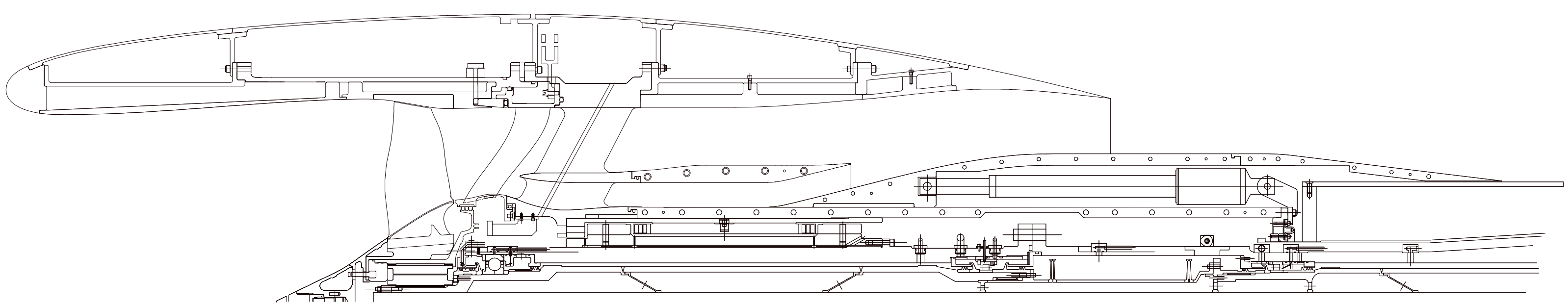

Figure 153. The Acoustic Configuration Is Shown for the 22" QHSF II Rig.

6.2 Front Frame

Figure 154 shows the modifications to the front frame design for the QHSF II rig and Figure 155 shows the new QHSF II aluminum frame mounted on the 22” dummy drive rig.

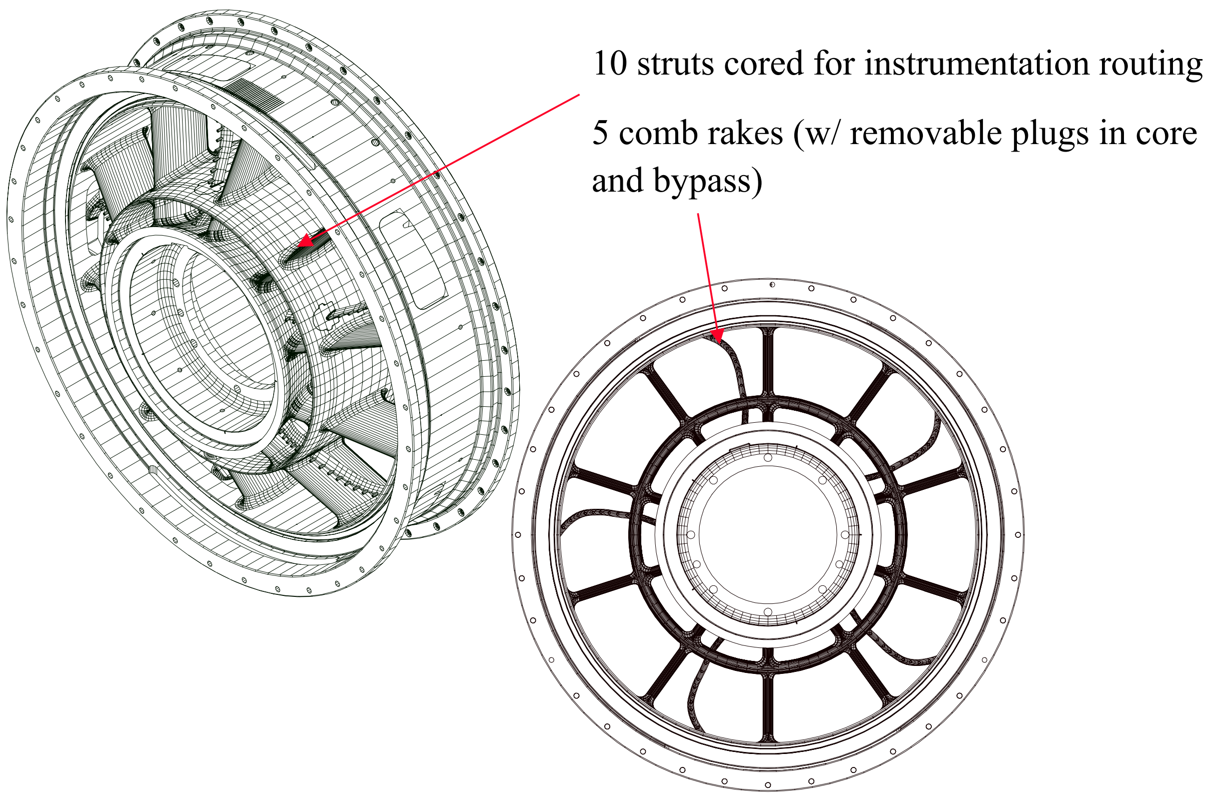

Figure 154. The Front Frame Design for QHSF II Was Modified to Incorporate 5 Comb Rakes for Stage Performance Measurements.

Figure 155. QHSF II Fan Frame on the NASA 22” Dummy Drive Rig.

6.3 Rotating Group

Figure 156 shows the modifications that were made to accommodate the new fan design. The torque sleeve was modified to accommodate the new flow path that was introduced due to the lower hub-to-tip ratio of the QHSF II. The spinner was re-designed to match the new flowpath and to match a more current engine design. The design of the disk was modified to implement the new blades with the sloped attachment. The mechanical design of the disk is presented in Section 5. Figure 157 shows the results of the stress analysis of the aft spinner modification. The maximum stress level was well below acceptable limits established by Honeywell design practice.

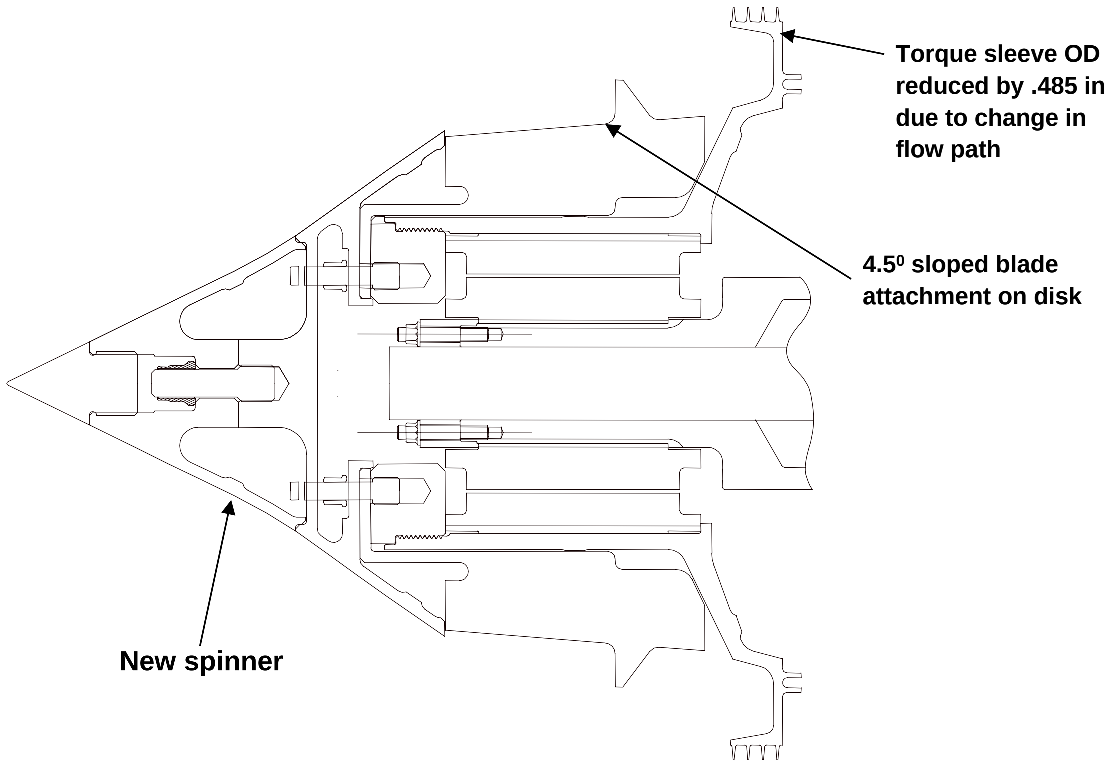

Figure 156. Changes to the Rotor System Design for QHSF II Include a New Disk, Torque Sleeve, and Spinner.

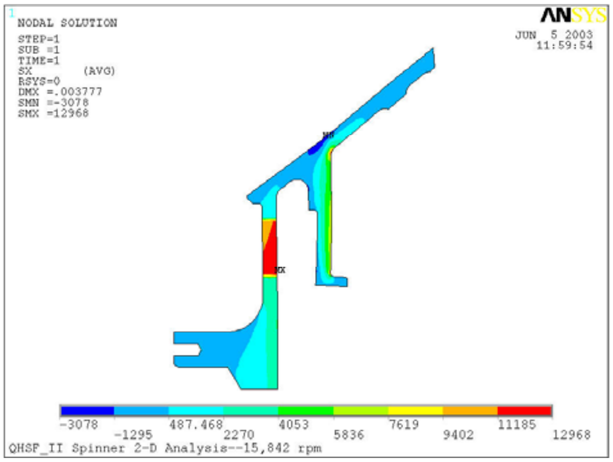

(a) axial

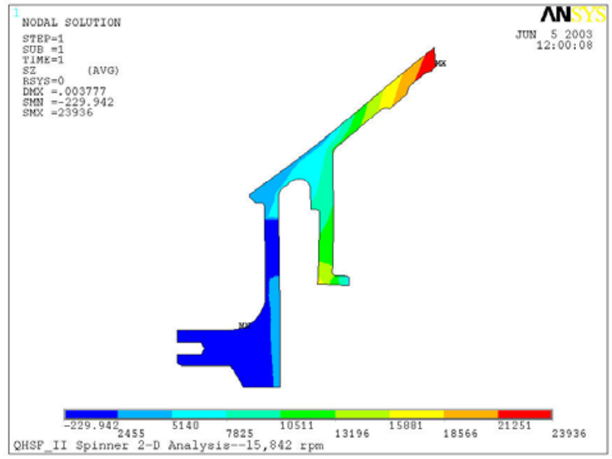

(b) circumferential

Figure 157. The Maximum Stress Level in the Spinner Was Computed to Be 13 ksi.

6.4 Rotating Stator Assembly

A rotating stator concept was proposed to allow detailed flow measurements behind the stator and to allow the stator positions to be clocked relative to the strut positions. A drawing of the dual-actuator system is shown in Figure 158. This concept allows for mechanical rotation of the stators in both the acoustic and performance configurations of the 22” rig.

Figure 158 shows the original design concept for the rotating stator assembly with 2 actuators and 2 horizontal rods. The design load capability for each actuator is 1000 lb. The expected maximum total aerodynamic and mechanical load is expected to be 650 lb. During assembly, it was determined that the opposing actuators, as designed, could potentially bind each other. It was decided that since one actuator had enough authority to rotate the stators, only one actuator and horizontal rod would be used. Figure 159 shows a photograph of the final configuration.

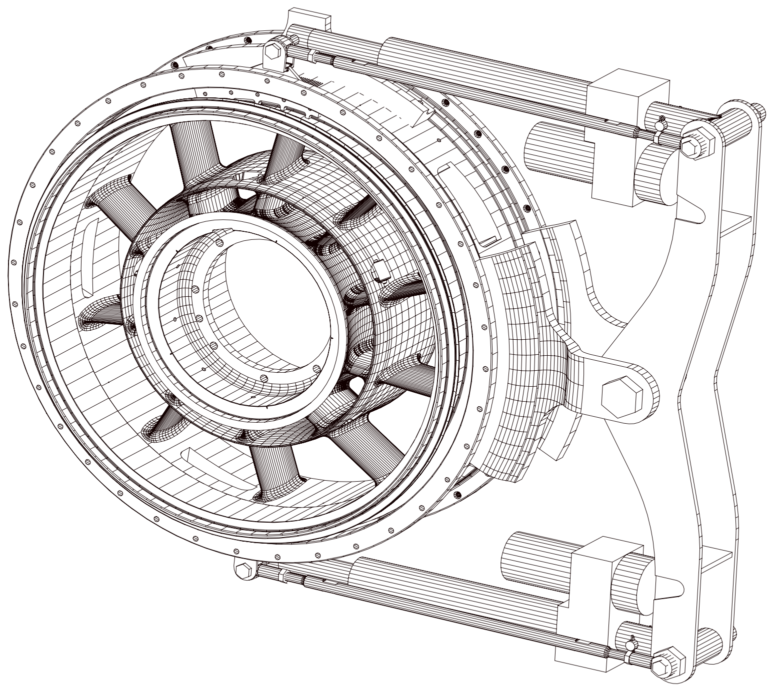

Figure 158. The Rotating Stator Concept Allows for Variable Positioning of the Stator Relative to the Struts in the 22" QHSF II Rig, as Well as Facilitate Stage Performance Measurements.

Figure 159. The Final Rotating Stator Actuation System Uses One Actuator and Horizontal Bar.

6.5 Safety Review

Honeywell's safety analyses for the QHSF II rig are supplemental to those performed on the entire QHSF rig structure (Reference 1), and are focussed only on the previously described mechanical differences in the QHSF II rig. In general, all changes to the QHSF II mechanical structure resulted in either identical or better margins of safety relative to the previous design.

Stress levels of the QHSFII fan disk meet Honeywell design requirements. Table 19 shows the calculated LCF life for the QHSF II fan disk with maraging steel C-250 properties using Honeywell's Browse material database. The maximum test speed analyzed represents the highest speed the rig is expected to achieve as part of the planned testing, and is equivalent to 105 percent of the aerodynamic design speed of the QHSF II.

Table 20 and Figure 160 show the results of the QHSF II airfoil stress calculations at the maximum test speed of 16,402 rpm.

Factor of Safety margins for the new rotating QHSF II hardware are summarized in Table 21, and satisfy the NASA requirements as shown. Details of the calculations are summarized in Table 21.

Table 19. LCF Life for C-250 Fan Disk.

Condition	Max Test Speed	Trip Speed
Speed (RPM)	16402	16700
LCF Life with Min Material Properties (cycles)	9071	7553
LCF Life with Average Fatigue Properties (cycles)	22177	18456
Temperature (Deg F)	200	200
Stress Ratio	0	0
Stress Range (KSI)	186	193

Component	CF Radial Load (lb)	Section Area (in^2)	Average Stress (ksi)
Blade root	38844	1.003	39
Airfoil root	29288	0.774	38

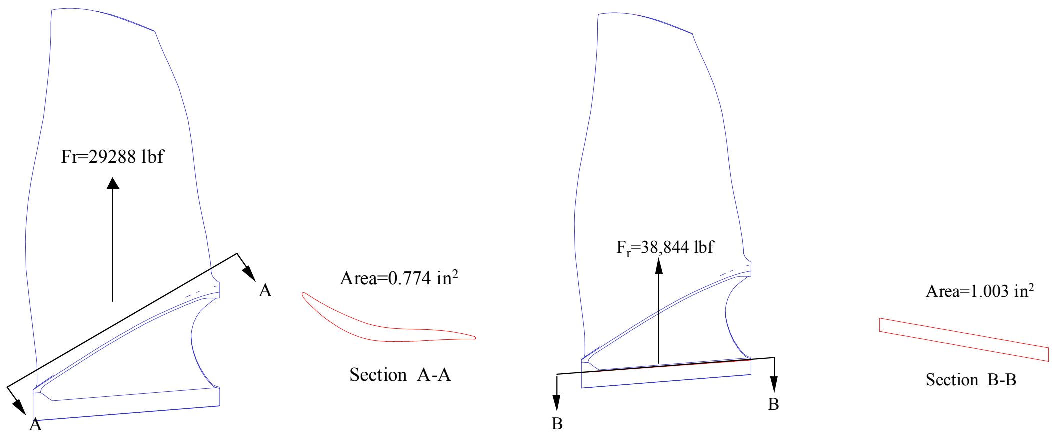

Figure 160. Average Blade Root and Airfoil Root Section Stress Calculation at 16402 RPM.

Table 20. New QHSF II Hardware Satisfies NASA Factor of Safety Requirements.

	QHSF	**QHSF II at 15621 rpm**	**QHSF II at 16402 rpm**	**NASA Req**
Yield Margin for Blade Airfoil	1.2	1.2	1.1	1.1
Yield Margin for Blade Attachment	n/a	1.2	1.1	1.1
Burst Margin (NASA Criterion)	1.5 (ultimate)	1.2	1.1	1.1(1.5 Ultimate)
Yield Margin for Spinner	1.9 (ultimate) (fwd spinner)	3.9	3.7	1.1 (1.5 Ultimate)

Table 21. QHSF II Fan Rotor Margin of Safety Calculation.

											Factor of Safety Met?			
Component	Qty	Material	Fty Yield (ksi)	Ftu Ult. (ksi)	Fsu Ult. Shear (ksi)	Max Stress (ksi)	Avg. Stress (ksi)	FS Yield	FS Ult.	FS Shear	1.1y 1.5u	1.5y 3.0u	3.0y 5.0u	Comments and Source
Disk/Hub	1	Maraging Steel C-250	230 @200°F	239 @200°F		186	103	1.2	1.6		Yes			@16402 rpm, avg tangentail stress
Blade Root	22	Ti-6-4	106.2 @200°F	117 @200°F		99	39	1.1	2.1		Yes			@16402 rpm, Avg section stress
Blade Root	22	Ti-6-4	106.2 @200°F	117 @200°F		90	35	1.2	2.3		Yes			@15621 rpm Avg section stress
Blade airfoil	22	Ti-6-4	106.2 @200°F	117 @200°F		97	38	1.1	2.2		Yes			@16402 rpm Avg section stress
Blade airfoil	22	Ti-6-4	106.2 @200°F	117 @200°F		88	34	1.2	2.4		Yes			@15621 rpm Avg section stress

6.6 Rig Speeds

Table 22 defines key physical operating speeds and their relationship to the corrected aerodynamic design speed of the QHSF II fan.

Table 22. QHSF II Physical and Corrected Design Speed for Key Operating Points.

	Physical Speed*	%N1 re QHSF II
QHSF II Aero Design Point (1485 ft/s corrected tip speed req)	15621	100%
QHSF II Mechanical Design Point (from 1506 ft/s mech tip speed req.)	15842	101%
Max Speed in **QHSF II** Test Plan	16402	105%
22" Rig Mechanical Speed Limit	16850	108%

* Mech. Speed calculations are applicable to 59 deg. Std. Day

6.7 Nozzle Sizing

The predicted exit flow (Wc) for the QHSF II matches the QHSF along most of the operating line (including Approach and Cutback acoustic conditions), but is slightly lower near the Sideline condition (~90% fan speed, Nc). The nozzle may be slightly large for the QHSF II; but the small differences shown in Figure 161 are not critical to the acoustic measurements.

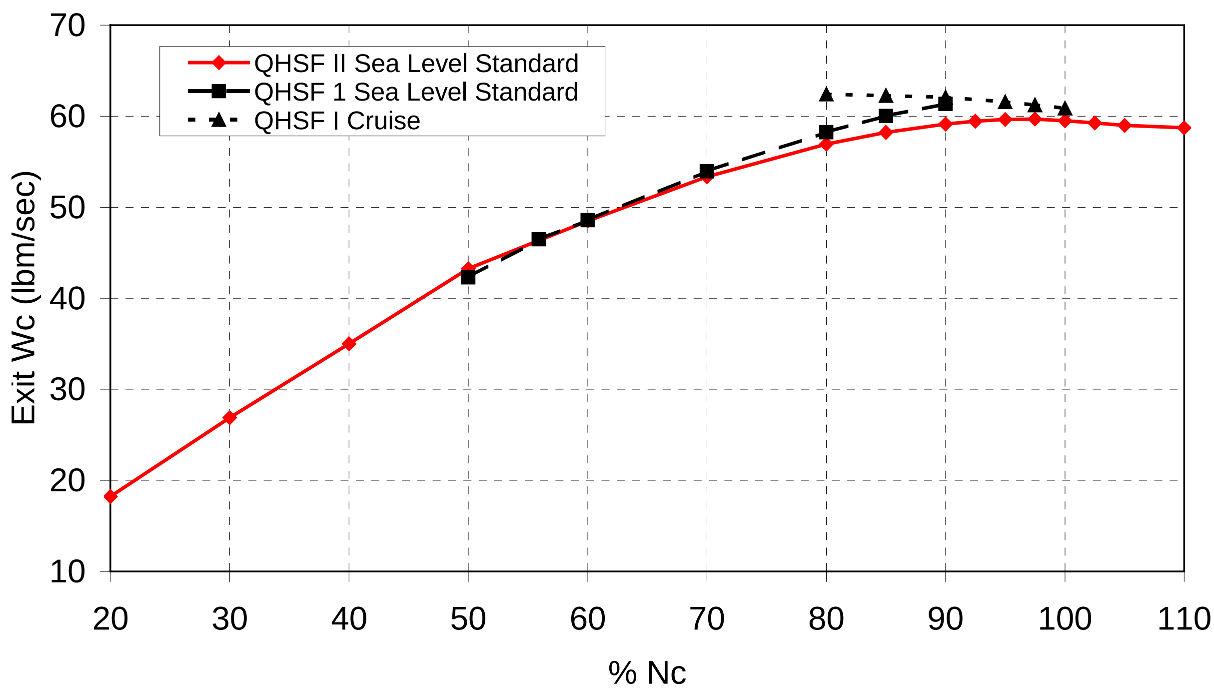

Figure 161. The Predicted QHSF II Operating Line Shows That the Existing QHSF I Nozzle Will Accommodate the QHSF II Fan.

6.8 Instrumentation

The complete instrumentation list for the QHSF II rig is presented in Appendix I. A general description of the rig instrumentation by Honeywell appears below. NASA-provided instrumentation not described in this section (but included in Appendix I) include rig speed & all rig mechanical integrity, instrumented performance bellmouth, rotor exit radial survey probes, light probes, core flow rakes, and the LDV measurement system. Also included in Appendix I are detailed descriptions and figures of the fan case plug instrumentation.

6.8.1 Accelerometers

Three accelerometers mounted at top dead center on the fan frame will provide continuous vibration data (in the vertical, axial, and horizontal directions).

6.8.2 Boundary Layer Rakes

Five rakes with 10 pressure elements each are used to determine the magnitude of the inlet boundary layer (these rakes are identical to the rakes used in QHSF I testing, as described in Reference 1 and Appendix I). The boundary layer rake is pictured in Figure 162.

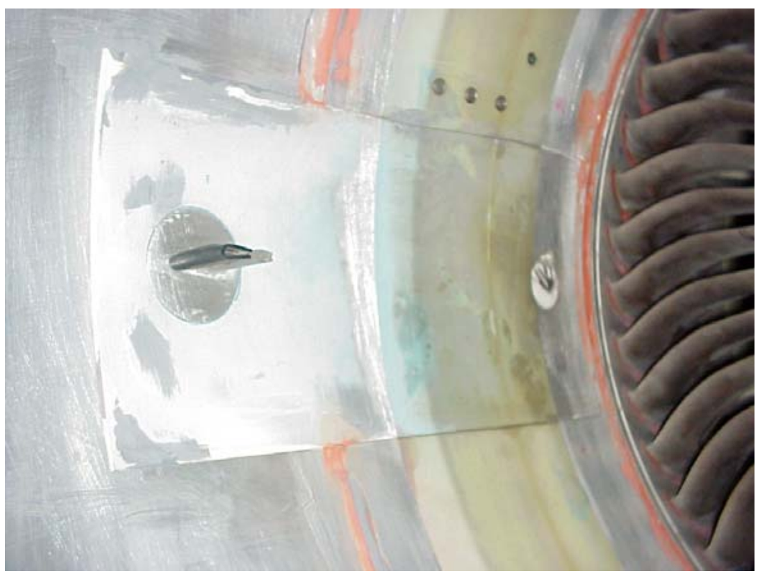

Figure 162. Boundary Layer Rake Shown in QHSF II Fan Case Plug (18 Degree Location).

6.8.3 Capacitance Probes

Four capacitance probes spaced equally spaced around the fan at rotor leading edge, mid-span, and trailing edge are used to measure rotor clearance.

6.8.4 Comb Rakes

Five rakes consisting of 14 pressure and temperature elements each (9 bypass and 5 core) will be used to measure stage performance at traversing positions across the vane passage (accomplished by clocking of the stator set). The comb rakes mimic the trailing edge stator geometry as shown in Figure 163.

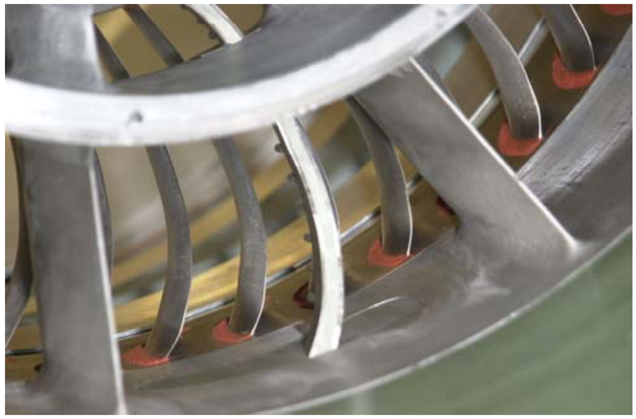

Figure 163. Aft Looking Forward View of Fan Frame and QHSF II Stator, With One Comb Rake Shown.

6.8.5 Distortion Rakes

Ten rakes with six total pressure elements will be used to measure radial inlet distortion effects, forward of the fan rotor (Figure 164).

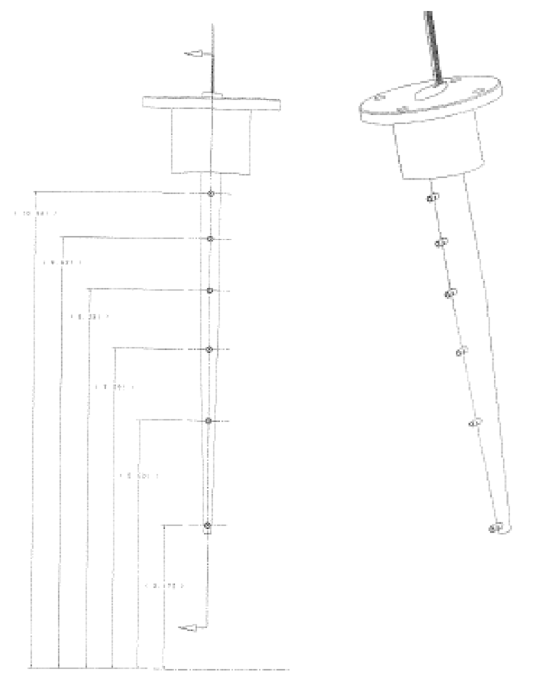

Figure 164. Inlet Distortion Rake Design for QHSF II.

6.8.6 Kulites

Four kulites in a fan case plug and an additional kulite in the fan case spanning 1 strut passage will be used to evaluate strut potential field at the rotor. An additional 10 kulites placed diagonally across the plug will be used to evaluate rotor shock position. Figure 165 shows the kulite locations in the fan case plug.

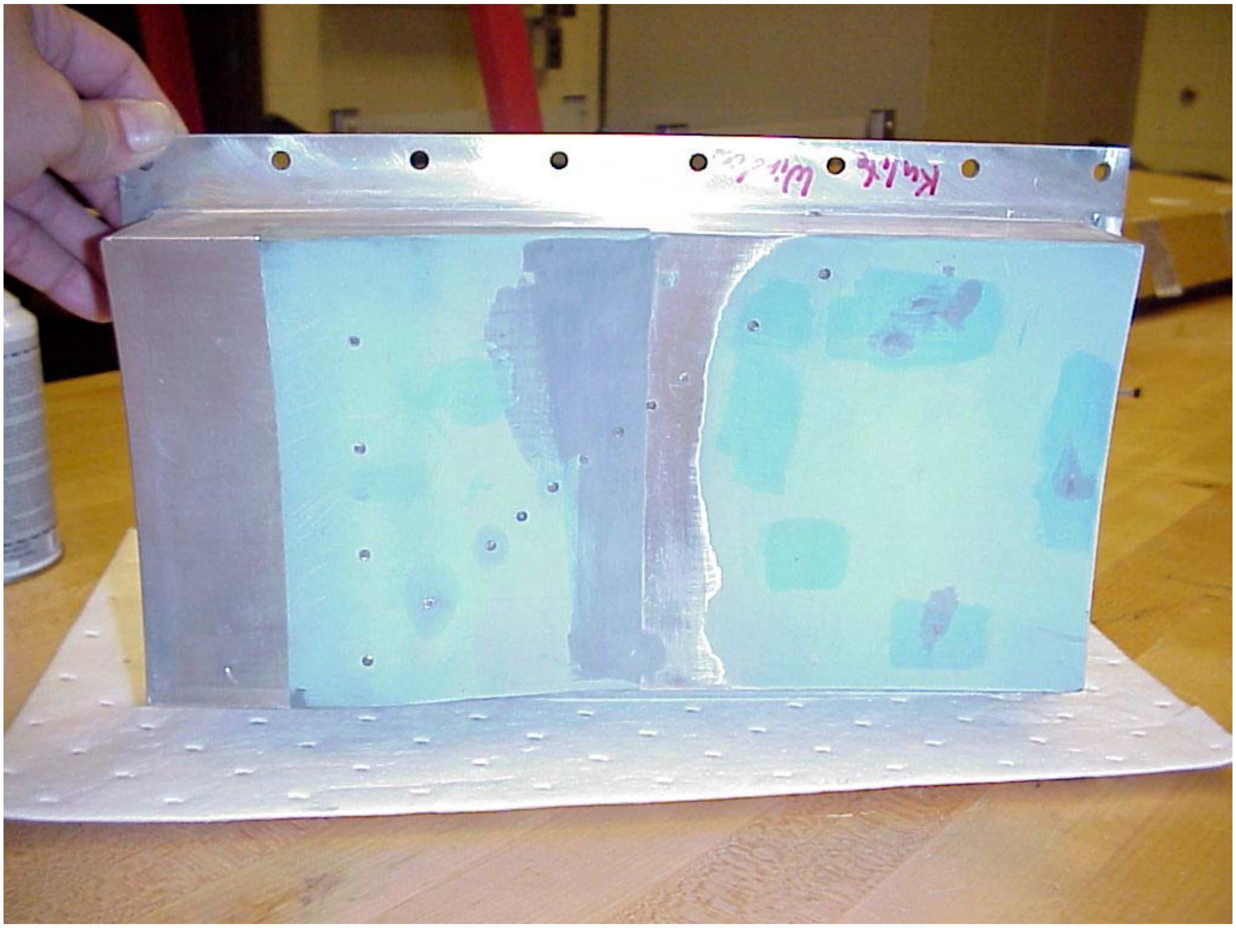

Figure 165. QHSF II Fan Case Plug Kulites.

6.8.7 Static Pressures

Numerous statics (as defined in Appendix I) are located throughout the rig at critical locations on the hub and shroud, including core, bypass, and vane leading edge measurement planes. Figure 166 depicts locations of the static pressure measurements (PS) acquired during aerodynamic performance mapping. (Total temperature (TT) and total pressure (PT) measurement points also shown.)

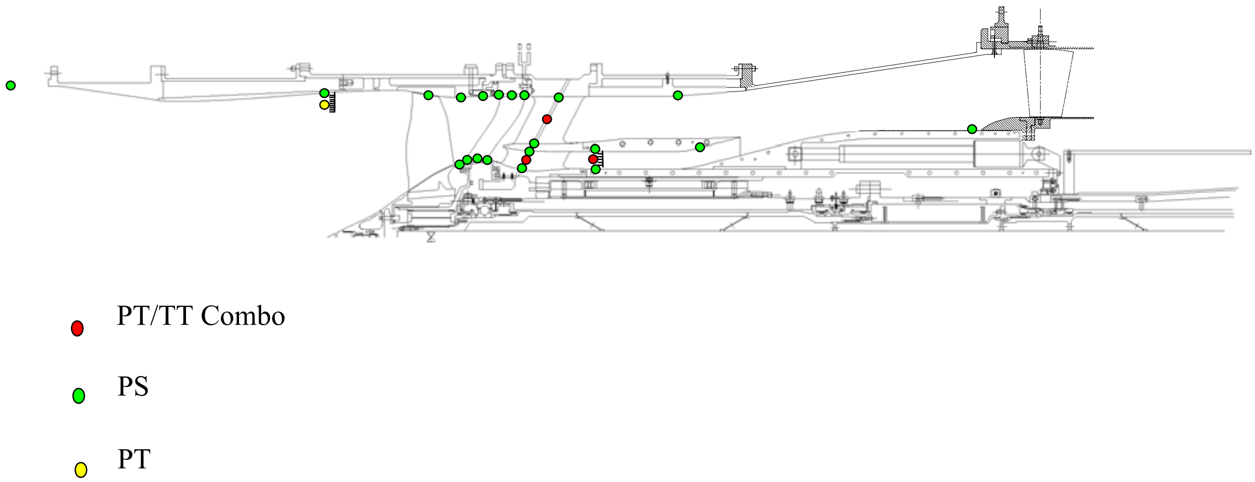

Figure 166. Aerodynamic Performance Measurements on QHSF II Fan Rig.

6.8.8 Strain Gages

A total of twenty strain gages were mounted on critical stress areas of 4 rotor blades (5 per blade), as shown below in Table 23, Table 24, and Figures 167-170. Two strain gages were placed on the fan disk, as shown in Figure 171. Two strain gages were placed on each of two QHSF II stator vanes as shown in Figure 172.

Table 23. The Strain Gages Are Described for the QHSF II Rotor Blade.

GAGE RATIOS	90	75	80	90	90	90	90	90	80	90	GAGE LOCATIONS		
Freq(Hz) ->	370	886	1256	1872	2309	2418	2709	3032	3619	3798	Axial (in)	Radial (in)	Angle (deg)
Mode #-->	1	2	3	4	5	6	7	8	9	10			
Gage #													
1 PS	96	79	2	41	5	17	6	6	3	2	-1.604	-0.586	3.820
2 SS	29	65	89	6	11	7	10	1	30	3	1.603	0.519	6.130
3 SS	3	41	29	100	93	81	8	92	7	39	-1.392	-1.534	9.792
4 SS	1	15	32	63	7	20	97	26	58	58	-0.462	0.009	9.849

Gage Size = 3.2E-2

Table 24. Strain Gage Locations Are Identified for the QHSF II Rotor Blade.

	Global Cartesian			Origin at Ref. Pt (TE Tip) x-along engine axis			Origin at Ref. Point (TE Tip) x-along dovetail		
S/G Loc	**X**	**Y**	**Z**	**X**	**Y**	**Z**	**X**	**Y**	**Z**
1	-1.604	-0.586	3.820	2.202	-2.561	-6.495	-2.608	-2.150	6.495
2	1.603	0.519	6.130	-1.004	-1.456	-4.185	0.741	-1.619	4.185
3	-1.392	-1.534	9.792	1.990	-3.509	-0.523	-2.564	-3.120	0.523
4	-0.462	0.009	9.849	1.060	-1.966	-0.466	-1.950	-2.367	-0.434
Ref. Pt (TE Tip)	0.599	1.975	10.315	0.000	0.000	0.000	0.000	0.000	0.000

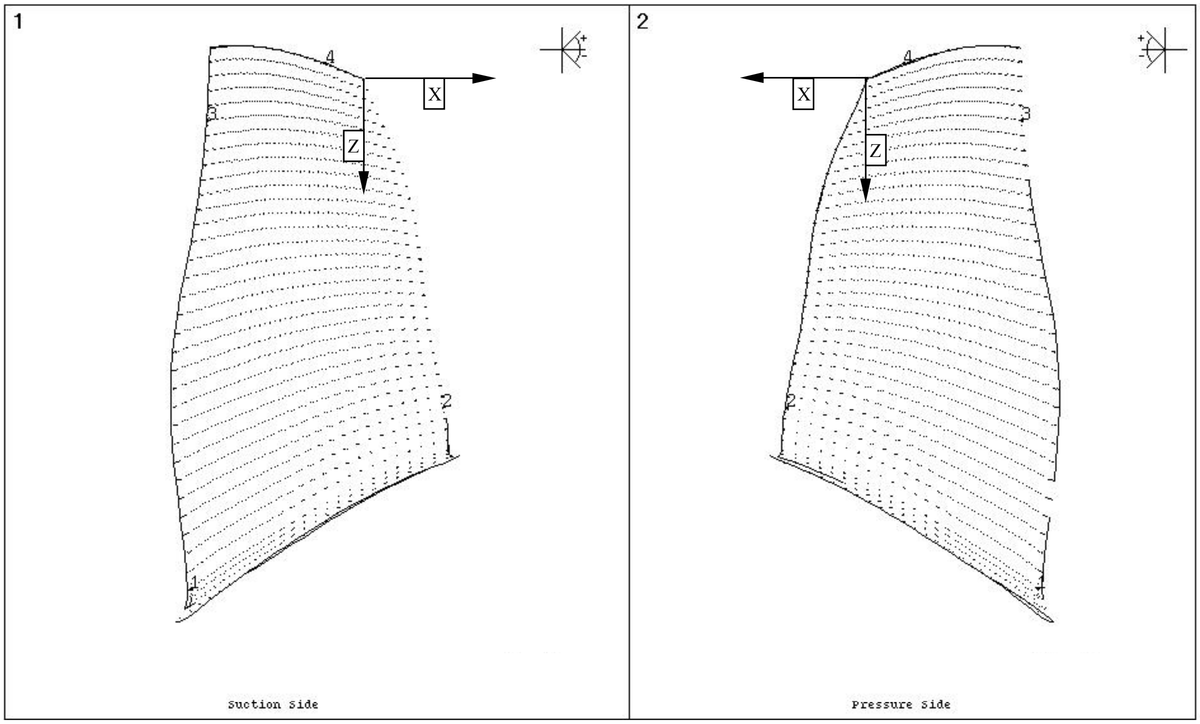

Figure 167. Strain Gage Locations Were Defined to Measure 7 Major Vibrational Modes.

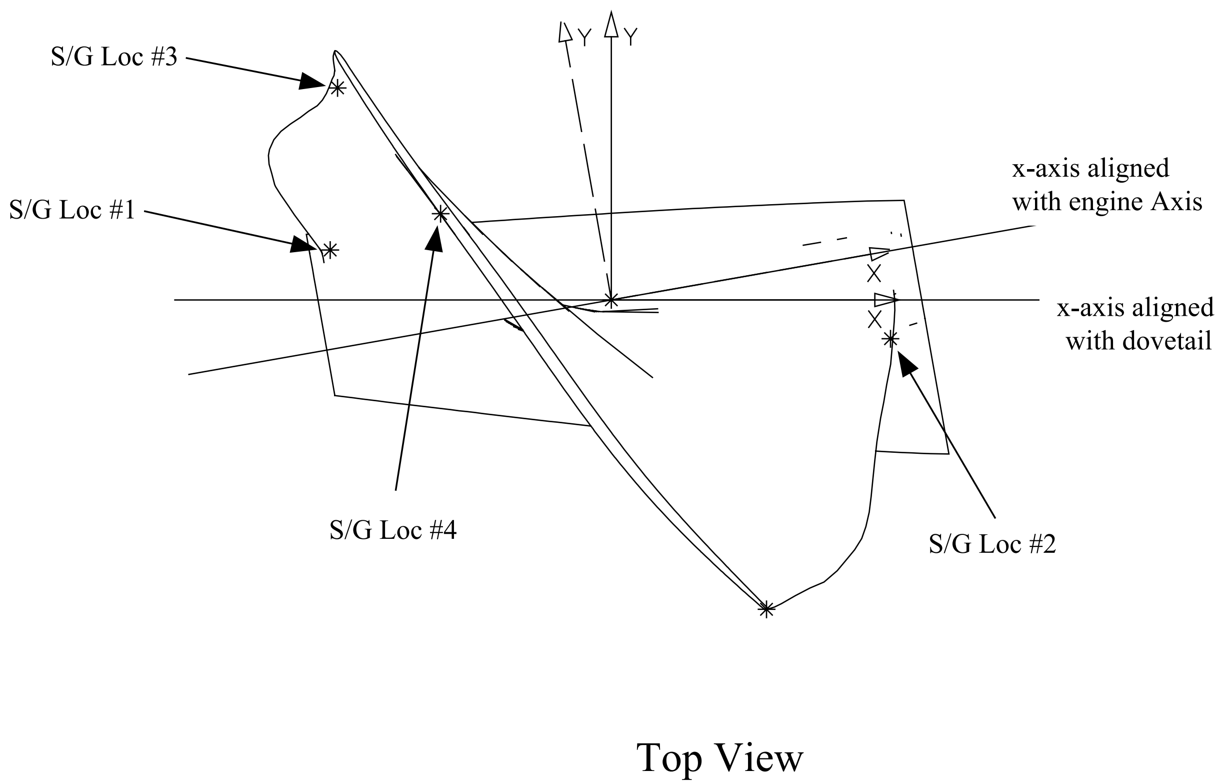

Figure 168. The Top View of Blade Shows the Strain Gage Locations and the Relative Positions of the Engine and Dovetail Axes.

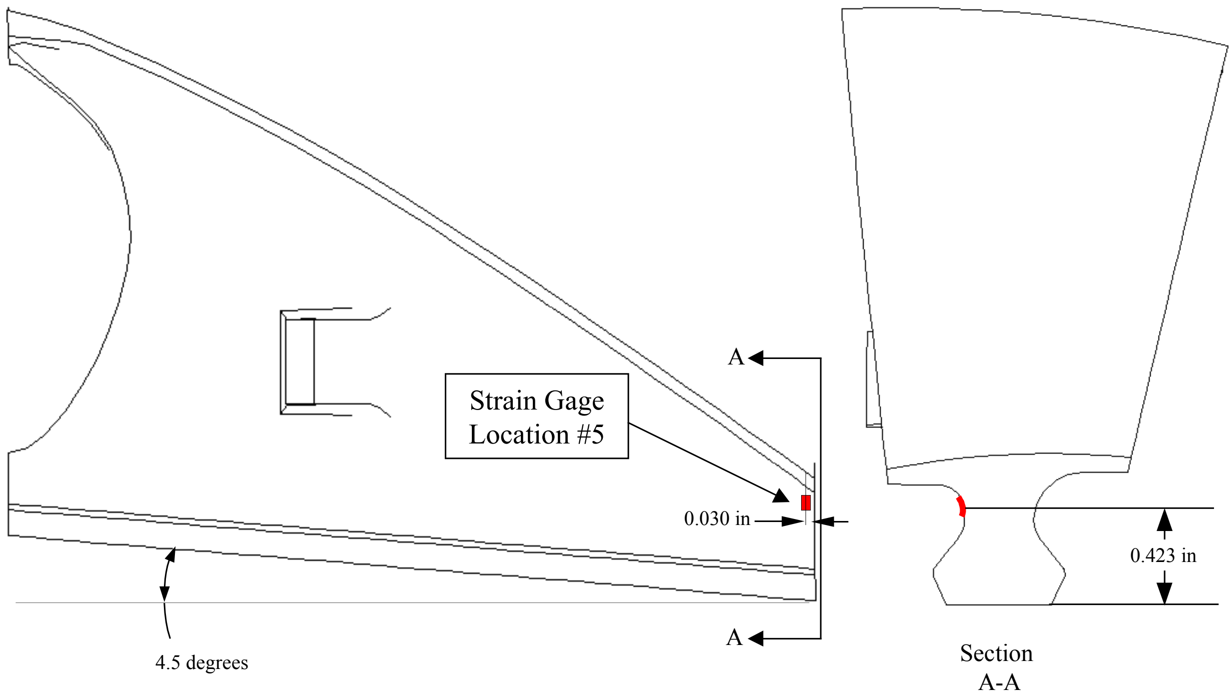

Figure 169. The Fifth Strain Gage Is Located on the Blade Dovetail.

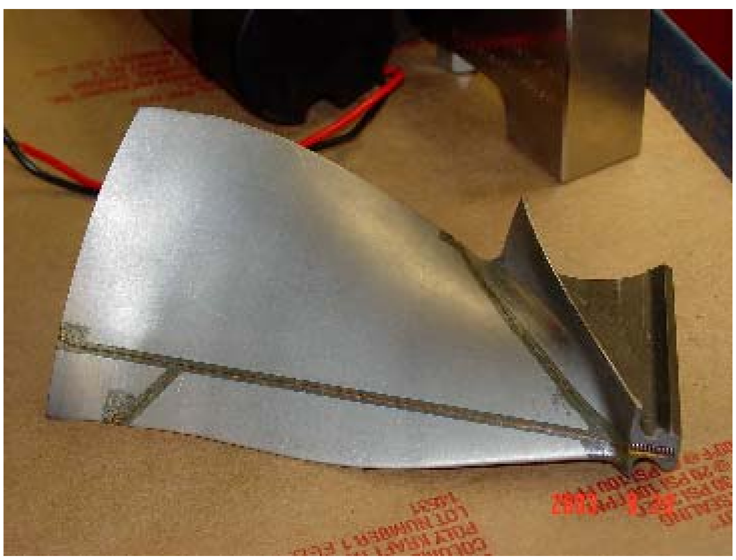

Figure 170. QHSF II Fan Blade – Strain Gages.

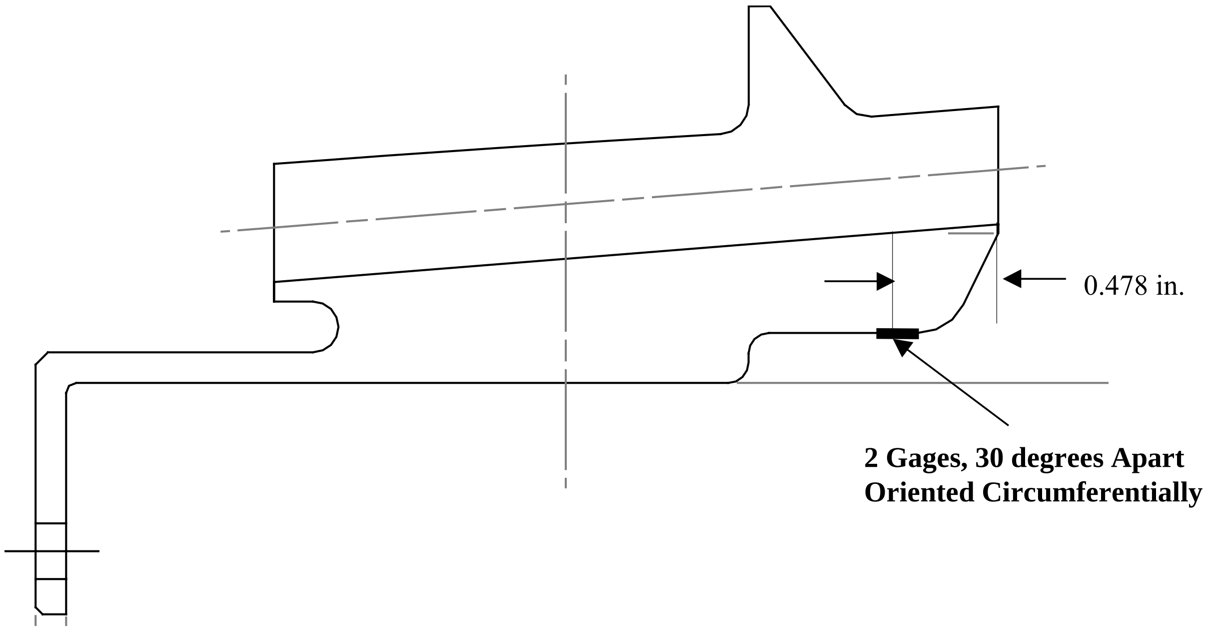

Figure 171. A Strain Gage Was Also Mounted on the Fan Disk to Monitor the Mechanical Behavior.

Strain gage strain limits are set based on Goodman diagram data for Ti-6-4 MA at 190°F. The maximum allowable strain on each gage is summarized below in Table 25. Tables 26 – 30 describe in detail the allowable strain levels at each gage location, for various critical vibration modes.

Table 25. Summary of Maximum Allowable Strains.

Gage Location	Max Allowable Strain (p-p)
1	4500
2	5780
3	5000
4	6440
5	4500
Disk	1000

Table 26. Allowable Strains for Modes 5 and 6, Gage Location #5.

Engine Order	Mode	RPM	Freq (hz)	Mean Stress (ksi)	Gage Loc 5 Allowable		
					Gage Ratio	Sig-Alt (ksi)	Strain (p-p)
4	1	3100	244	3.13	0.98	53.19	6240
3	1	5400	252	9.49	0.98	50.76	5955
2	1	8200	272	21.88	0.98	46.02	5399
	1	16634	352	90.02	0.98	8.68	1018
6	2	7000	702	15.94	0.99	48.79	5723
5	2	8800	724	25.20	0.99	45.21	5304
4	2	11500	766	43.03	0.99	38.32	4495
	2	16634	895	90.02	0.99	8.77	1029

Table 27. Allowable Strains for Modes 1 and 2, Gage Location #1.

Engine Order	Mode	RPM	Freq (hz)	Mean Stress(ksi)	Gage Loc 1 Allowable		
					Gage Ratio	Sig-Alt (ksi)	Strain (p-p)
4	1	3100	244	1.30	0.96	52.79	6193
3	1	5400	252	3.94	0.96	51.80	6077
2	1	8200	272	9.09	0.96	49.88	5851
	1	16634	352	37.40	0.96	39.27	4606
6	2	7000	702	6.62	0.79	41.80	4904
5	2	8800	724	10.47	0.79	40.62	4765
4	2	11500	766	17.88	0.79	38.33	4497
	2	16634	895	37.40	0.79	32.31	3791

Table 28. Allowable Strains for Modes 1, 2, and 3, Gage Location #2.

Engine Order	Mode	RPM	Freq (hz)	Mean Stress(ksi)	Gage Loc 2 Allowable		
					Gage Ratio	Sig-Alt (ksi)	Strain (p-p)
4	1	3100	244	0.01	0.29	16.09	1888
3	1	5400	252	0.03	0.29	16.09	1888
2	1	8200	272	0.06	0.29	16.09	1887
	1	16634	352	0.25	0.29	16.07	1885
6	2	7000	702	0.04	0.65	36.06	4231
5	2	8800	724	0.07	0.65	36.06	4230
4	2	11500	766	0.12	0.65	36.04	4228
3	2	17800	895	0.29	0.65	36.00	4223
10	3	7000	1167	0.04	0.89	49.38	5793
9	3	7800	1170	0.06	0.89	49.38	5792
8	3	8800	1173	0.07	0.89	49.37	5792
7	3	10100	1178	0.09	0.89	49.36	5791
6	3	11950	1195	0.13	0.89	49.35	5789
5	3	14450	1204	0.19	0.89	49.33	5787
4	3	18475	1232	0.31	0.89	49.29	5782

Table 29. Allowable Strains for Modes 4, 5, and 6, Gage Location #3.

Engine Order	Mode	RPM	Freq (hz)	Mean Stress(ksi)	Gage Loc 3 Allowable		
					Gage Ratio	Sig-Alt (ksi)	Strain (p-p)
10	4	10300	1717	2.26	1.0	54.62	6407
9	4	11650	1748	2.90	1.0	54.37	6378
8	4	13300	1773	3.77	1.0	54.03	6338
7	4	15650	1826	5.23	1.0	53.46	6271
14	5	9050	2112	1.75	0.93	50.98	5981
13	5	9770	2117	2.04	0.93	50.88	5968
12	5	10600	2120	2.40	0.93	50.75	5953
11	5	11575	2122	2.86	0.93	50.58	5933
10	5	12730	2122	3.46	0.93	50.36	5908
9	5	14180	2127	4.29	0.93	50.06	5872
8	5	16000	2133	5.46	0.93	49.63	5822
14	6	10500	2450	2.35	0.81	44.21	5186
13	6	11300	2448	2.72	0.81	44.09	5173
12	6	12200	2440	3.18	0.81	43.95	5156
11	6	13280	2435	3.76	0.81	43.77	5134
10	6	14575	2429	4.53	0.81	43.52	5106
9	6	16100	2415	5.53	0.81	43.21	5069
8	6	18000	2400	6.91	0.81	42.77	5017

Table 30. Allowable Strains for Modes 5 and 6, Gage Location #4.

Engine Order	Mode	RPM	Freq (hz)	Mean Stress(ksi)	Gage Loc 4 Allowable		
					Gage Ratio	Sig-Alt (ksi)	Strain (p-p)
14	5	9050	2112	0.40	1.00	55.34	6492
13	5	9770	2117	0.47	1.00	55.32	6489
12	5	10600	2120	0.55	1.00	55.29	6485
11	5	11575	2122	0.66	1.00	55.24	6481
10	5	12730	2122	0.80	1.00	55.19	6474
9	5	14180	2127	0.99	1.00	55.11	6465
8	5	16000	2133	1.26	1.00	55.01	6453
14	6	10500	2450	0.54	1.00	55.29	6486
13	6	11300	2448	0.63	1.00	55.26	6482
12	6	12200	2440	0.73	1.00	55.22	6477
11	6	13280	2435	0.87	1.00	55.16	6471
10	6	14575	2429	1.04	1.00	55.09	6463
9	6	16100	2415	1.27	1.00	55.00	6452
8	6	18000	2400	1.59	1.00	54.88	6438

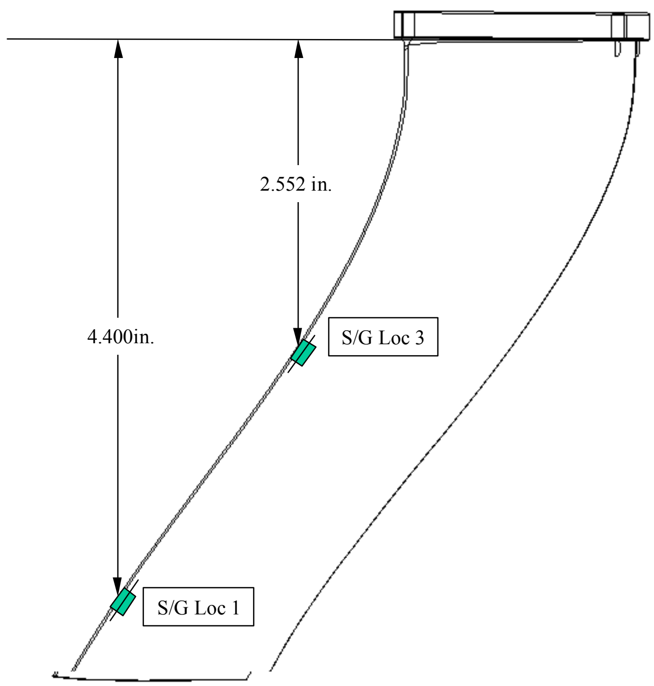

- All gages on the concave side with the gage center 0.100 in. from the edge.

Figure 172. The Side View of Vane Shows the Strain Gage Locations Relative to the Shroud.

Fan stator vane strain gage strain limits are set based on Goodman diagram data for S355 Stainless Steel at 75°F, as shown in Table 31.

Table 31. QHSF II Stator Strain Gage Limits.

Gage Location	Max Allowable Strain (p-p)
1	3520
3	3520

6.9 Distortion Screens

A set of classical, tip radial, and complex distortion screens (described in Table 32) are recommended distortion screens for testing on the QHSF II rig. The screen selections were made after considering the unique design of the QHSF II and reviewing the Honeywell's 18" rig test data of the Baseline II distortion screens. Honeywell has tested all the recommended distortion screens previously on the Baseline II fan rig, with the exception of the tip radial distortion screens. Given the unique nature of the fan tip design of the QHSF II, the tip radial distortion screens were included in this test.

Table 32. Recommended Distortion Screens for the QHSF II Rig Test.

Screen #	MPR	Description	Wire Dia.	Grid Size	Porosity	Dist. Level
1	0	Backer	0.080	1.016	84.8%	
104	1	1E Classical	0.079	1.017	85.1%	4%
112	1	1E Classical	0.054	0.334	70.1%	12%
115	1	1E Classical	0.018	0.085	62.9%	15%
204	2	2E Classical	0.079	1.017	85.1%	4%
212	2	2E Classical	0.054	0.334	70.1%	12%
304	3	3E Classical	0.079	1.017	85.1%	4%
312	3	3E Classical	0.054	0.334	70.1%	12%
404	4	4E Classical	0.079	1.017	85.1%	4%
412	4	4E Classical	0.054	0.334	70.1%	12%
503	0	Tip Radial	0.062	0.606	80.5%	3%
506	0	Tip Radial	0.055	0.314	68.0%	6%
901	Complex	Left Eng. 30 Kt x-wind	See Figure 3			
902	Complex	Right Eng. 30 Kt x-wind	See Figure 4			

Table 32 also indicates what screen material was used to build the distortion screens and the resulting screen porosity. Sample circumferential distortion screens are shown in Figure 173. Figure 174 shows a tip radial distortion screen. Figure 175 and Figure 176 show the complex crosswind distortion screens for the left and right engines, respectively. The OD and ID values quoted in Figure 173 and Figure 174 reflect the diameter of the QHSF II rig test screen holder.

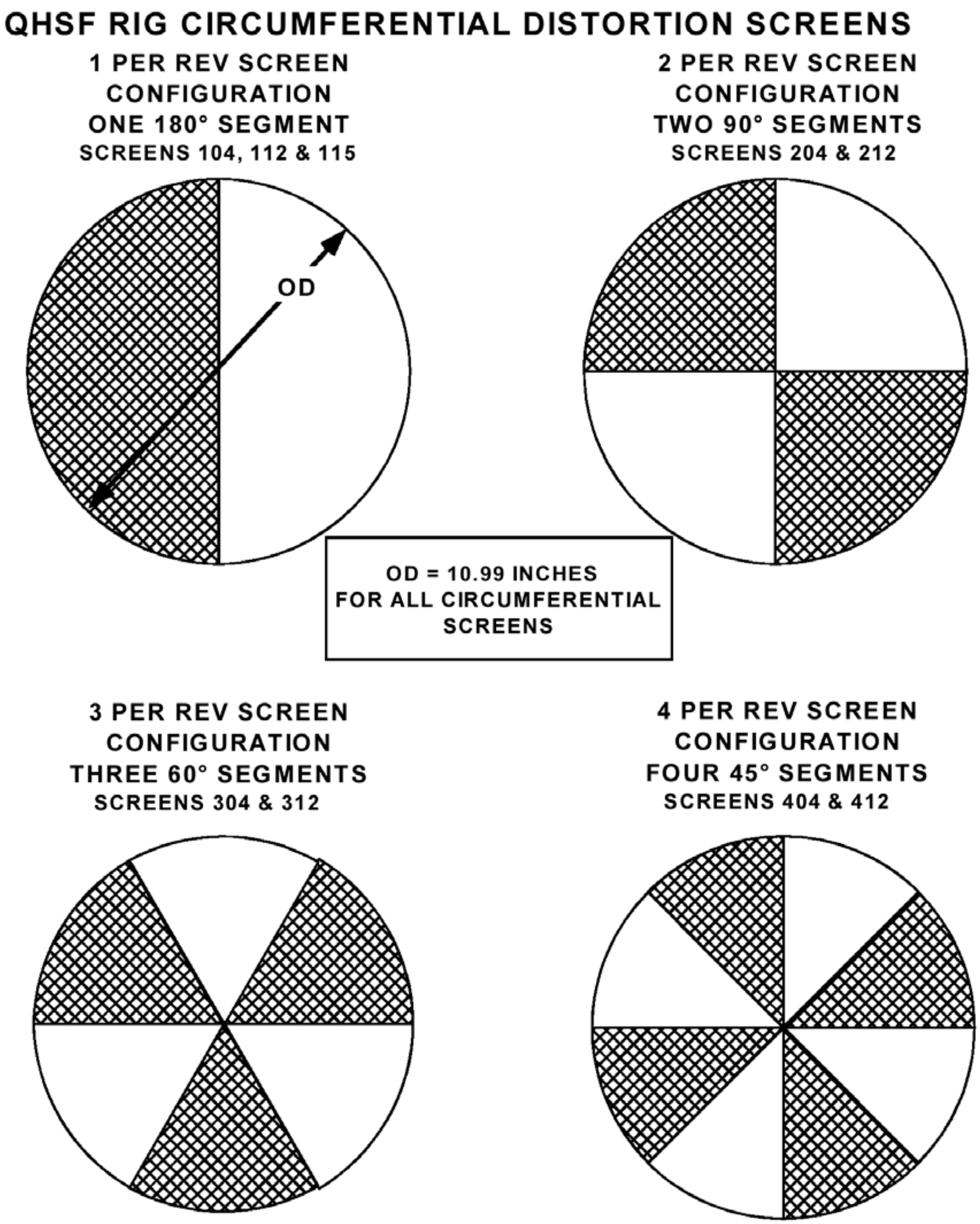

Figure 173. QHSF Rig Circumferential Distortion Screens.

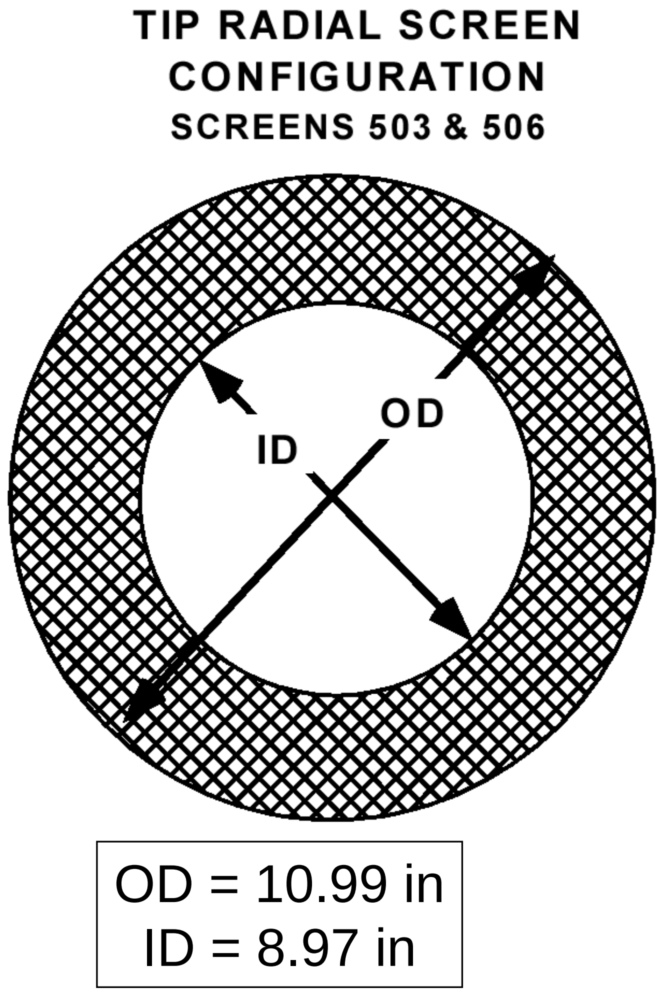

Figure 174. QHSF Rig Tip Radial Distortion Screen.

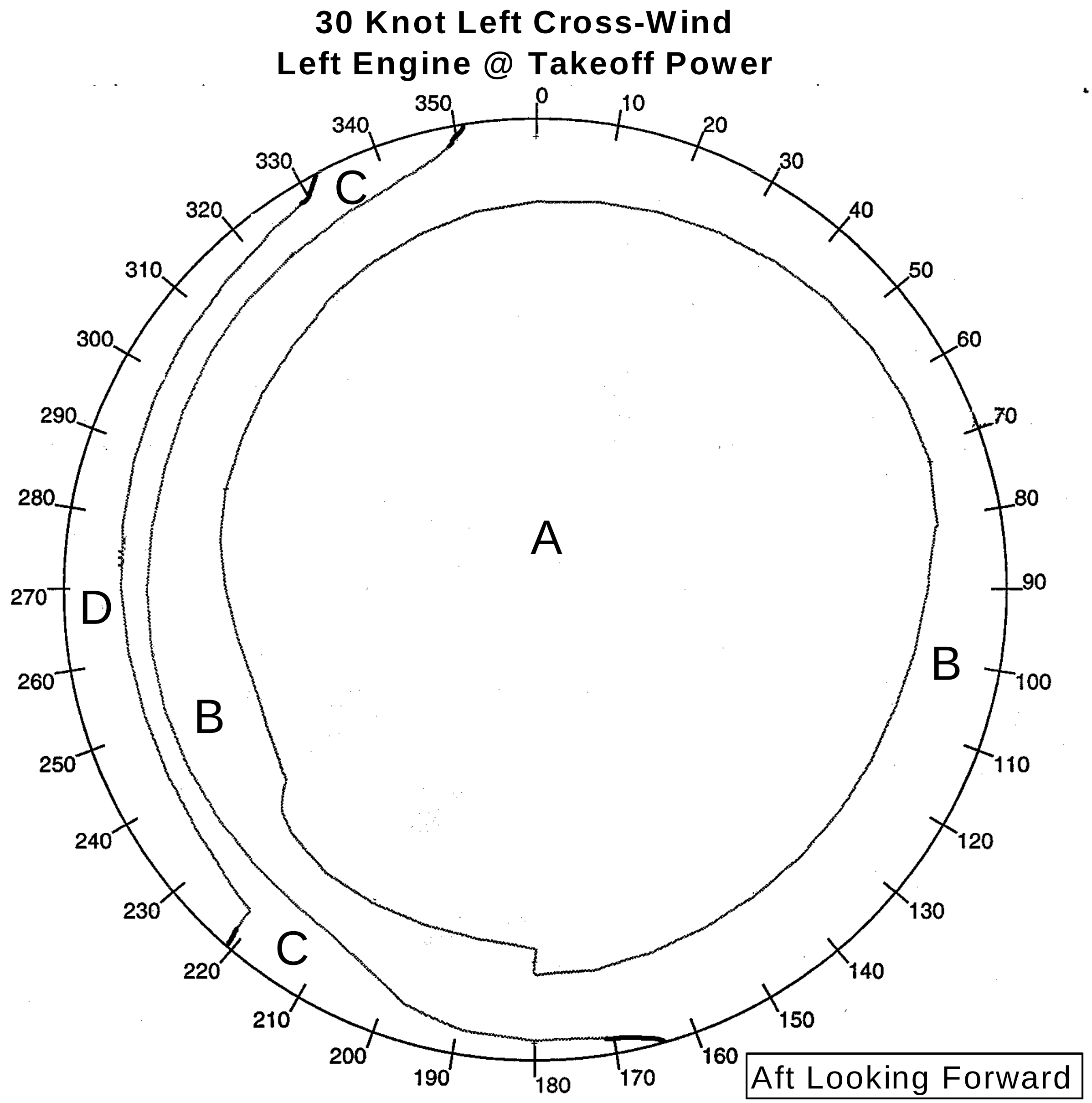

	Squares/Inch	Porosity	Wire Dia. (in)	Notes
Region A	--	84.6	--	*Backer Screen
Region B	4.0	78.9	0.028	
Region C	10.0	56.3	0.025	
Region D	12.0	33.2	0.035	

Figure 175. Left Engine 30-Knot Crosswind Distortion Screen.

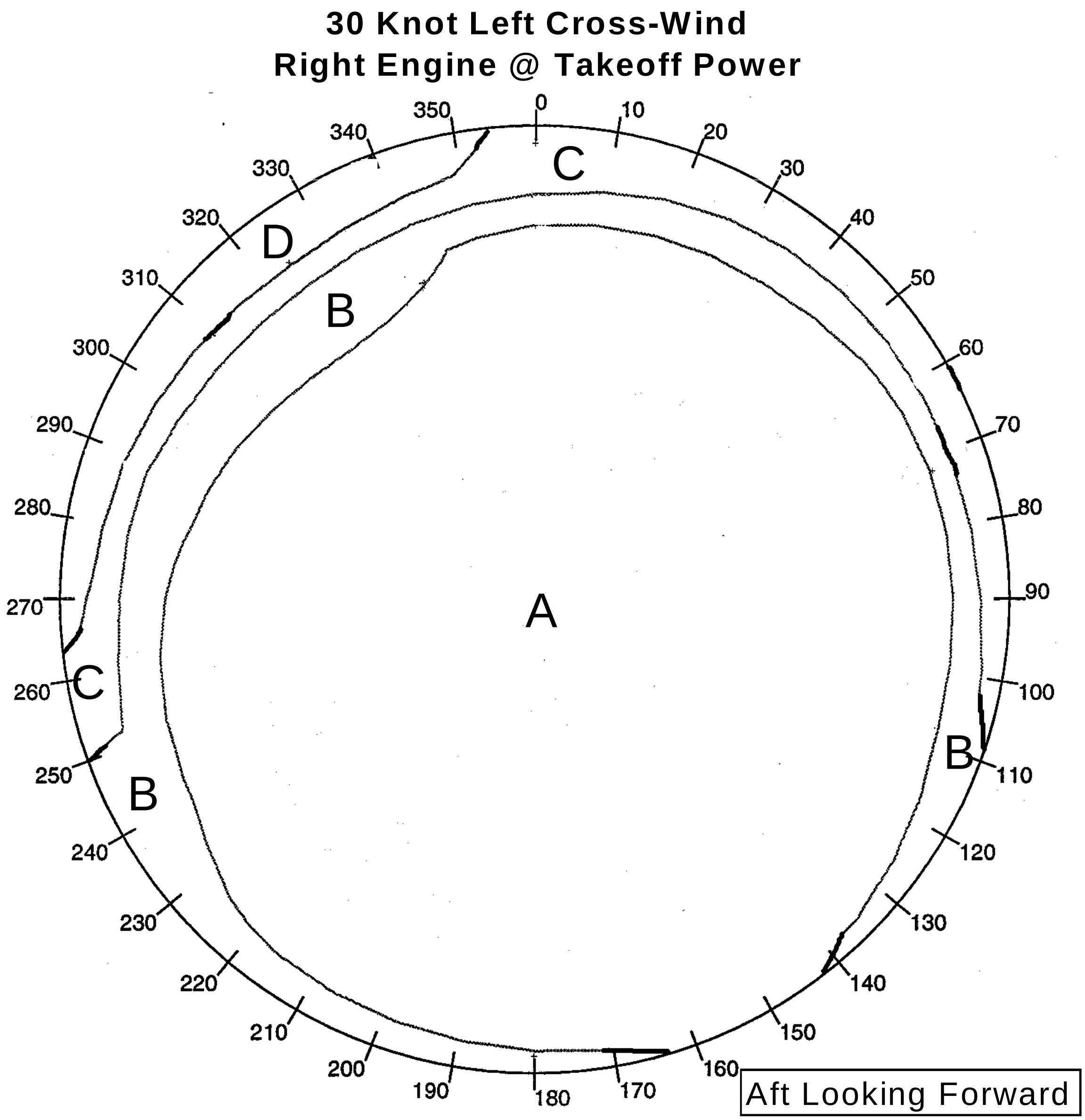

	Squares/Inch	Porosity	Wire Dia. (in)	Notes
Region A	--	84.6	--	*Backer Screen
Region B	4.0	81.0	0.025	
Region C	12.0	60.8	0.018	
Region D	12.0	33.2	0.035	

Figure 176. Right Engine 30-Knot Crosswind Distortion Screen.

6.10 Model Assembly

Overall assembly of the QHSF II rig is as described in Reference 1. Figures 179 – 184 depict phases of the QHSF II rig assembly and wind tunnel installation as described below.

Figure 177. QHSF II Fan Frame on the NASA 22" Dummy Drive Rig.

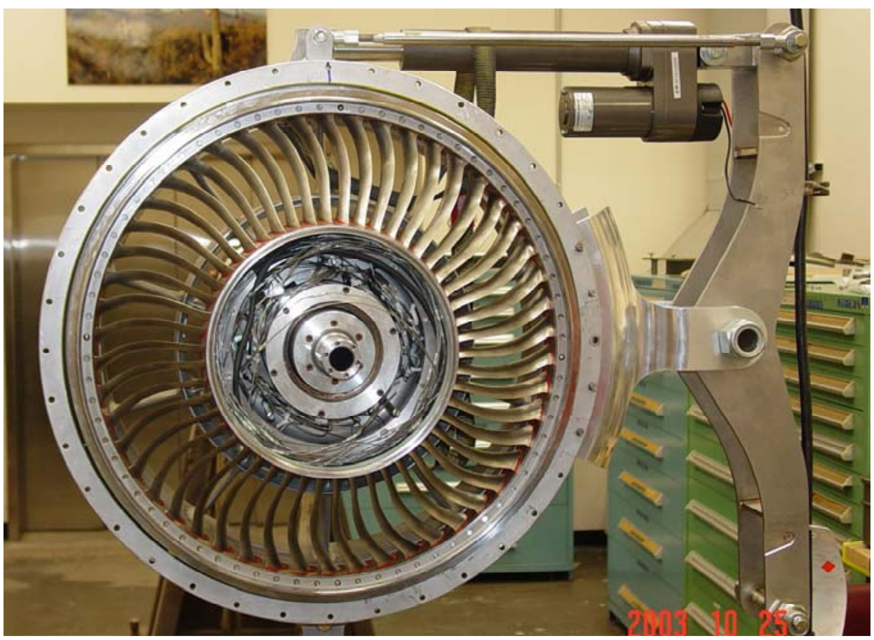

Figure 178. QHSF II Fan Stator and Rotating Stator Actuation Assembly on the NASA 22" Dummy Drive Rig.

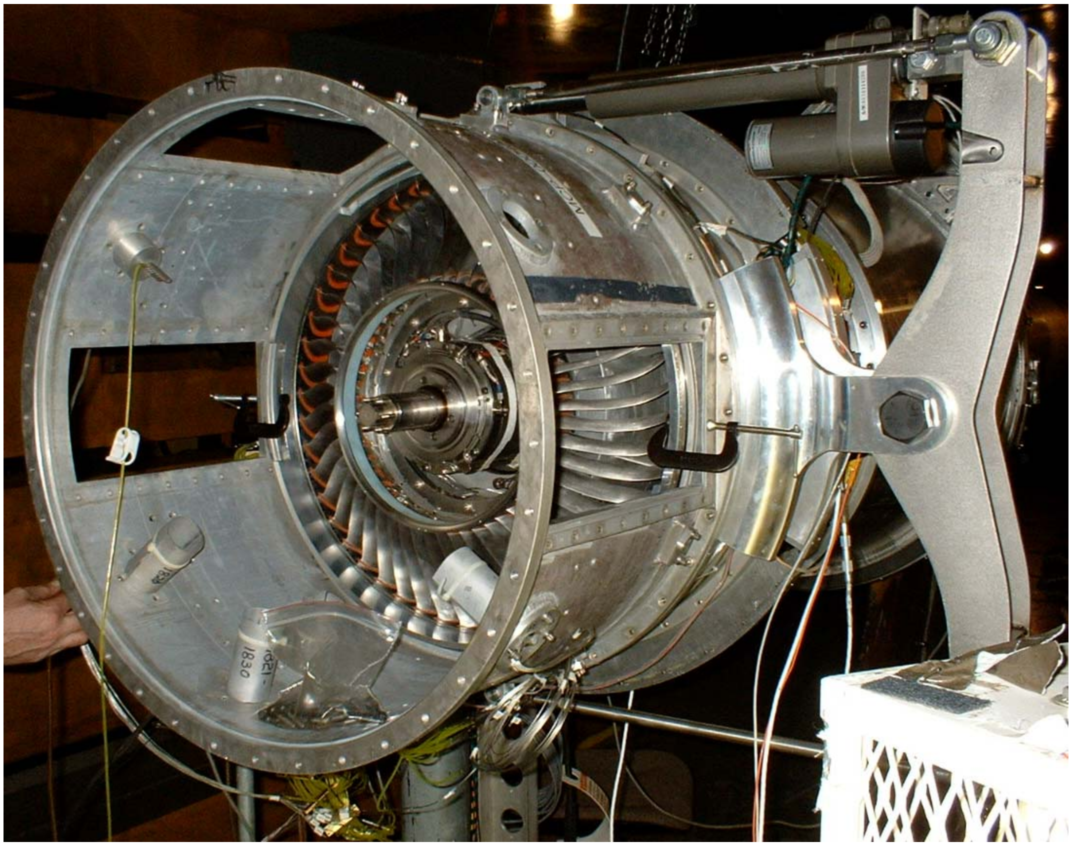

Figure 179. NASA Wind Tunnel Installation of QHSF II Stator Assembly, Shown With Outer Fan Case.

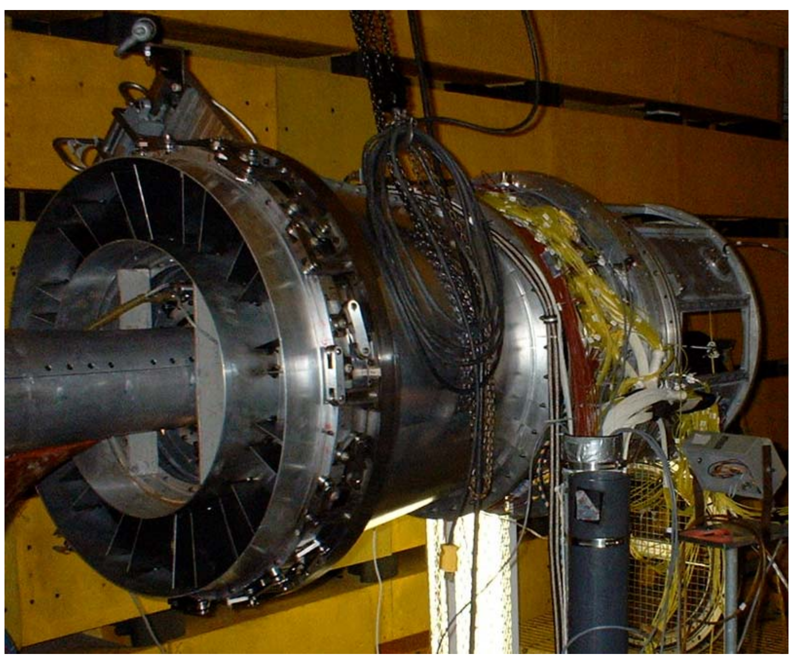

Figure 180. Aft View of NASA USB Drive Rig/QHSF II During Wind Tunnel Installation.

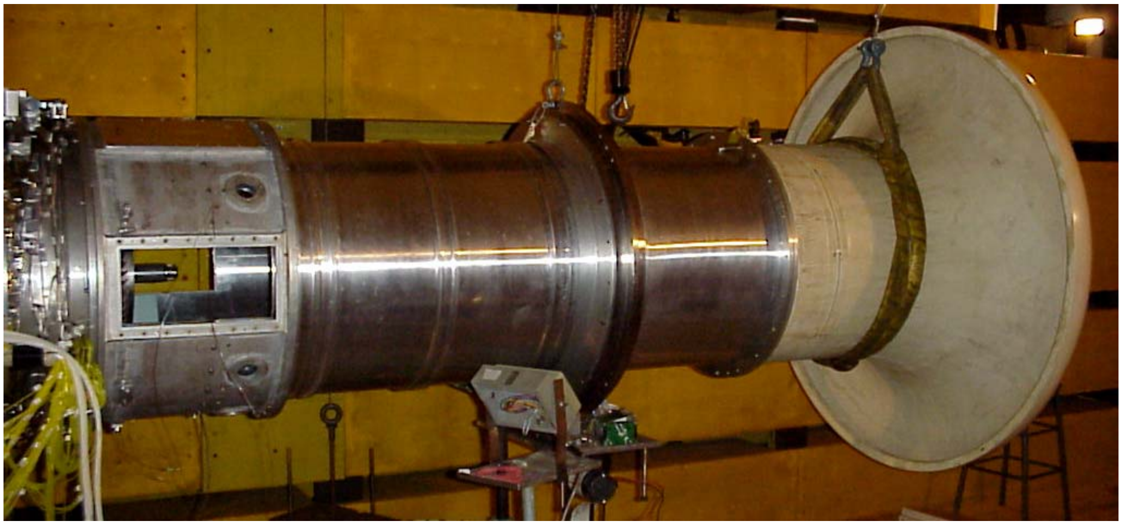

Figure 181. Configuration for Operability Testing Includes Screen Rotator Assembly and Long "Tomato Can" Inlet.

Figure 182. QHSF II Tunnel Installation, in Aerodynamic Performance Measurement Configuration.

Figure 183. QHSF II (a) in Far-Field Acoustic Measurement Configuration (b).

6.11 Modification of Rotating Group After Initial Assembly

NASA discovered an issue with rotor bore size and the “top hat” of the dynamic balance. The top hat was not a feature that had been included in Honeywell’s QHSF drawings that were used as the basis of the QHSF II design. Three parts were identified that would require modification for a larger bore diameter to accommodate the top hat are: 1) fan disk, 2) aft spinner, and 3) torque sleeve nut.

Mechanical design evaluation of the modified hardware was completed. Figure 184 and Figure 185 show the drawings of the modified fan disk and new aft spinner. The modification of the disk has no impact on the hoop strength of disk bore or the peak static stress at the fan disk dovetail slot. Therefore, there will be no change to the previously calculated factors of safety for the fan disk.

Stress analysis results of the new aft spinner are shown in Figure 186. Shifting the inner segment forward (instead of radial on the original design) attenuated the radial stress through the slot hole. The overall peak stress of the modified design (55.3 ksi) is higher than the previously calculated value of 43 ksi. Nevertheless, the redesigned aft spinner has adequate margin of safety. The recalculated values are shown in the table.

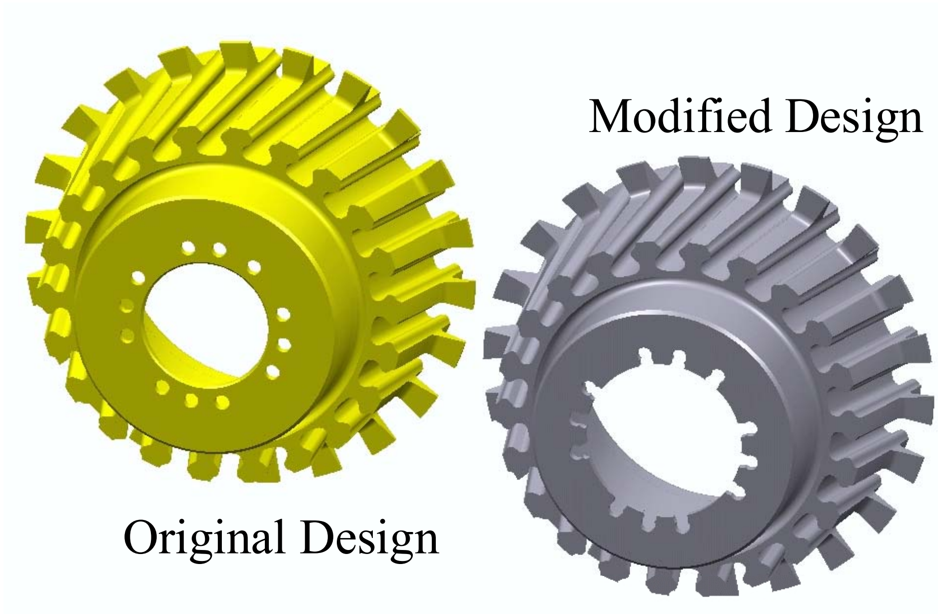

Figure 184. QHSF II Fan Disk Modified for Larger Bore Diameter to Allow Clearance for the Top Hat.

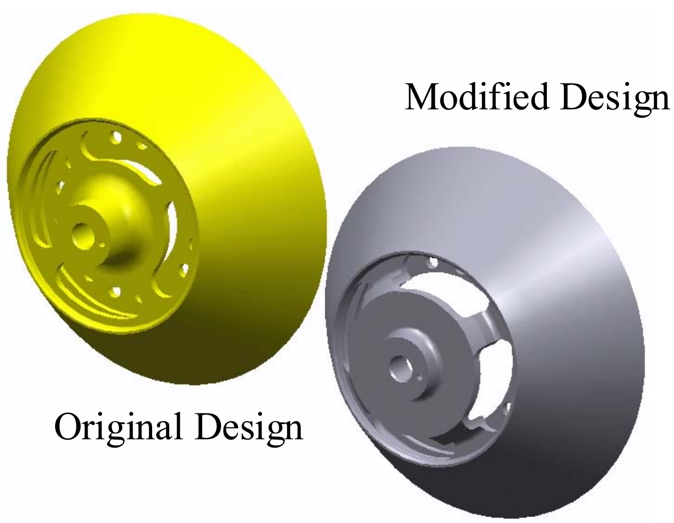

Figure 185. QHSF II Aft Spinner Modification Was Made to Allow Clearance for the Dynamic Balance Top Hat.

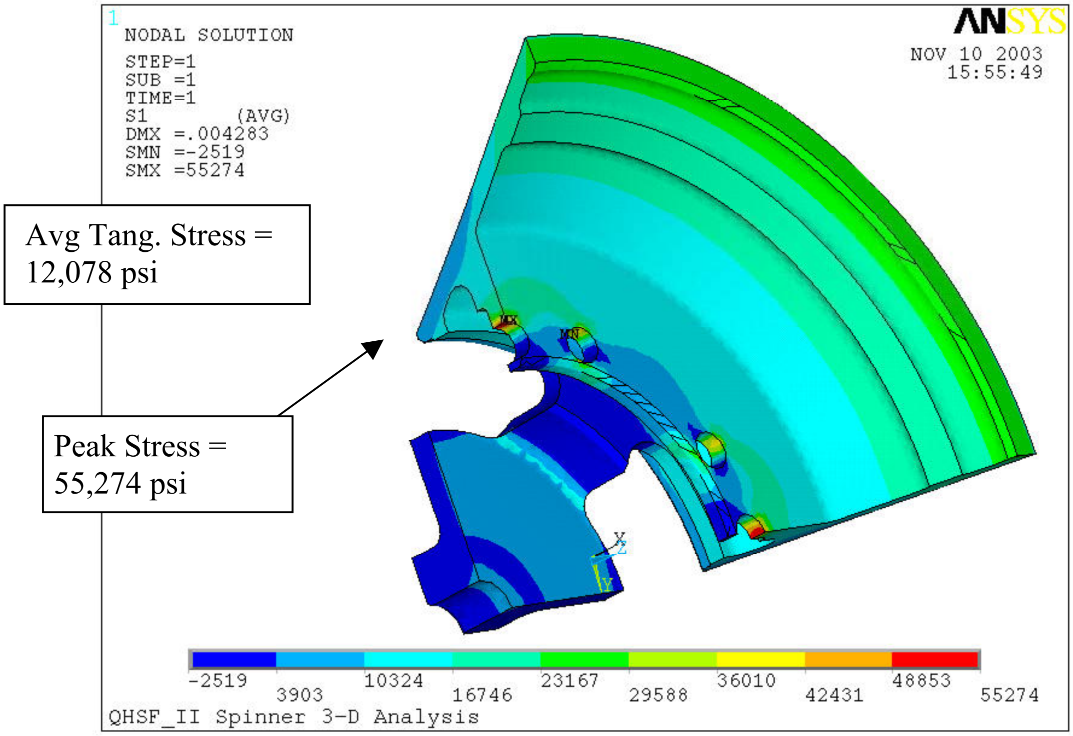

Figure 186. QHSF II New Aft Spinner Maximum Principal Stress -- New Design Maintains Adequate Margin of Safety.

											Factor of Safety Met?		
Component	**Qty**	**Material**	**Fty Yield (ksi)**	**Ftu Ult. (ksi)**	**Fsu Ult. Shear (ksi)**	**Peak Stress (ksi)**	**Avg. Stress * (ksi)**	**FS** Yield**	**FS*** Ult.**	**FS Shear**	**1.1y 1.5u**	**1.5y 3.0u**	**3.0y 5.0u**
Aft Spinner	1	Stainless Steel 17-4	154 @75F	172 @75F		55.3	12.7	2.8	9.5		Yes	Yes	

*Avg stress = average tangential stress
** FS Yield = (PeakStress)/(FtyYield)
** FS Ult = [Avg Stress/(0.7*FtuUlt)]

7. NEW TECHNOLOGY

This final report has identified all nonpatentable discoveries, innovations, and computer code improvements, and all patentable inventions that were developed or discovered during the performance of the contract. In summary, there have been a number of innovations throughout the design, hardware, and test phases of the QHSF II program. Such innovations include the TURBO-AE aeroelastic tool improvement, the multi-disciplinary analytical design of experiments approach to the QHSFII fan design, and the rotating stator capability added to the NASA 22" rig. To date, two innovations have been identified as being patentable: the advanced swept stator and the sloped disk attachment feature. Table 31 summarizes each innovation and references the applicable section of this report. Possible secondary applications of the reported new technology are also identified.

Table 33. Summary of Each Innovation and Applicable Section of This Report.

QHSF II 22" Rig Project	Section	Innovation	Benefit	Secondary Application	Patentable
Design	3.0	Aeroelastic Tool Calibration	Improved design accuracy/higher risk design trades possible	Future Fans	no
Design	5.1	Multi-disciplinary DOE design approach	Optimized design that meets all acoustic, aero, & mechanical requirements	Future Fans	no
Design	5.6	Optimized Non-Linear Stator	Elimination of rotor-strut interaction noise	Future Fans	yes
Design	5.8.2	Sloped fan disk attachment	Uniform stress balance, reduced weight	Future Fans	yes
Hardware/ Instrumentation/ Test	6	All aero measurements (including operability, inlet distortion, synchronous vibration) on NASA 22" Rig	Eliminate need for 2nd rig, reduces test time, hardware fab cost, improves data quality	Future Fans in NASA 9X15 facility	no
Hardware	6.4	Rotating Stator System for NASA 22" Rig	Variable stator position allows investigation of fan source noise evaluation, and investigation of aero/acoustic optimum stator positions	Future Fans in NASA 9X15 facility	no
Test	6.8.4	Stage exit rakes with stator TE geometry	Improved measurement quality required for advanced stator	Future fans with advanced swept stator	no

It has been shown that the shank configuration (such as the buttress and/or the dovetail slope) significantly affects the fan blade mode shape, which in turn is a key driver for flutter behavior. The dovetail slope provides the means to get the desired flutter margin (by controlling the mode shape) while meeting other constraints. This approach is very different from the prior approaches used at Honeywell and other companies, which eliminated flutter problems by increasing the frequency, changing the loading distribution, or clipping the geometry.

TURBO-AE would be applicable to any system that flutters, such as LPT blades and isolated wings. This approach could also be used to reduce the vibration level in a more-typical (Campbell Diagram type) forced response.

8. SUMMARY AND CONCLUSIONS

8.1 Aeroelastic Tool Evaluation

Results from a detailed study of flutter encountered on a forward-swept fan were summarized and compared to experimental data. Overall, the correlation of the computational results is in good agreement with experimental observations. The blade was correctly predicted to be free of flutter up to the stall line at 100 percent speed. At 85 percent and 75 percent speeds, flutter was predicted just above the operating line, and well before stall was encountered. This is again consistent with the rig test, and the predicted and measured flutter boundaries in terms of the fan map are in good agreement. The correct critical nodal diameter was also predicted.

Inviscid analyses were shown to provide predictions of damping in remarkably good agreement with the viscous results. The key benefit of utilizing an inviscid assumption is that the computations require only 2-5 percent of the computational time required for full viscous analyses. Potential uses include identification of the critical nodal diameter, trade studies, and sensitivity assessments. The conclusions from the results provided here are that the primary drivers for fan flutter are dominated by shock structures and are inviscid in nature, and the damping change along the speed line is tied principally to the change in shock position.

Several additional studies were conducted to further investigate the flutter behavior, and to better understand sensitivities. Changes in the aerodynamic damping predictions due to variations in blade shape due to speed changes, inlet and exit pressure profiles, tip clearance, and mode shapes were all evaluated. Surprisingly, none of these changes had a very significant effect on the damping prediction. The position on the fan map gave a consistently good indication of the stability for these effects.

One shortcoming in this correlation effort is that the flutter boundary had to be extrapolated for the viscous analyses at part-speed conditions because “numerical” stall was en-countered. This is a limitation of the “steady” solver, i.e., not related to the blade motion, and is a common limitation of CFD codes. Note that TURBO was able to reach the measured stall boundary at 100 percent speed, and this is very encouraging. However, the ability to reach the actual stall line would provide much more confidence in the ability of the unsteady analysis to accurately predict the flutter boundary.

8.2 QHSF I Data Evaluation

A study was completed to identify and explain any differences between the QHSF I 18-inch and 22-inch measured aerodynamic and aeroelastic performance. This study concludes that the differences in performance would be consistent if the two blade sets differed in hot shape. This difference would have altered blade incidence, thereby explaining differences in both aeroelastic behavior and aerodynamic performance. The possibility that the two blade sets, identical in design except for scale, differed in cold shape was considered unlikely and not further investigated in this study.

Acoustic data from the QHSF I 22” rig test was conducted. The primary noise reduction was achieved by the significant reductions in both rotor-stator and rotor-strut interaction, and is responsible for up to 6 EPNdB noise reduction at higher tip speeds. Less acoustic benefit was achieved at lower tip speeds, and is attributable to a flow separation on the QHSF I rotor blades that occurred only at the lower fan speeds. Comparisons of acoustic results with CFD analyses and LDV measurements are in good agreement, and show the reduced strength of the QHSF I rotor wake relative to the Baseline I. The forward swept blade increases the distance between the rotor trailing edge and stator leading edge, which contributes to the reduction of rotor-stator interaction noise. The rotor wake structure displays a tangential lean due to forward swept geometry, this effect is enhanced by addition lean and sweep of the stator leading edge. As a result, the QHSF I rotor wake traverses the stator leading edge more slowly than the Baseline I stator, and serves to further reduce the rotor-stator interaction tone noise.

Additional noise reduction was achieved by the virtual elimination of rotor-strut interaction tones at some speeds. A rotor-strut interaction CFD study was conducted to assess any differences between pressure distributions upstream of the Baseline I and QHSF I stators. Significant differences in the stator geometry occur near the tip, and results show that the Baseline I fan has more static pressure variation than the QHSF I, suggesting that the cause of rotor-strut interaction tones is the rotor responding to the variation in potential pressure field of the struts.

8.3 QHSF II Design

The QHSF II design was developed based on the experience of the QHSF as well as other recent Honeywell product fan design experience. The design process relied heavily upon use of analytical Design of Experiments (DOEs) to define the optimum rotor and stator system to achieve all acoustic, aerodynamic, aeroelastic, and mechanical performance goals. This series of analyses included the selection of blade forward sweep, blade tangential lean, blade thickness distribution, rotor incidence, and stator sweep and lean optimization. The DOE process allowed the rapid assessment of these key design features relative to all of the interdisciplinary design goals, as well as an understanding of the interaction and sensitivity of key design parameters. Design tool inputs to the DOEs included ADPAC for aerodynamics, ANSYS for stress, V072 and SOURCE3D for acoustics, and TURBOAE for aeroelastics.

The final design selection of the QHSF II includes a forward-swept blade with reduced sweep at the tip and additional sweep at lower spans relative to the QHSF I, and a full span stator with an optimized, non-linear sweep and lean. These features analytically demonstrate the simultaneous achievement of all the NASA program and internal Honeywell goals.

Subsequent to completion of the QHSF II design, a program augmentation was received to fabricate a set of Baseline II stators. The “moderate bow” stators were modified to run effectively behind the QHSF II rotor. The Baseline II stators are expected to have identical aerodynamic performance (pressure ratio and efficiency) as the QHSF II design. Relative to noise, a rotor-strut interaction study concludes that the stator shape and pitchwise alignment relative to the struts does have an impact on the static pressure distribution upstream of the stators, and therefore will impact the noise signature.

8.4 Rig Modifications

Several modifications to the existing QHSF rig were required to accommodate the QHSF II design. Key mechanical differences include a reduced hub/tip ratio, fan frame modifications to accommodate additional instrumentation, and a stator actuation system that allows rotation of the entire stator set during rig operation. The actuation system facilitates aerodynamic stage performance measurements, as well as the investigation of rotor-strut and rotor-stator interaction noise mechanisms. External hardware for the actuation system can be removed, and the system can be manually actuated, allowing the external nacelle to remain intact for far-field noise measurements.

All aerodynamic, mechanical, and acoustic measurements on the QHSF II design will be accomplished on the 22” rig, in the NASA-Glenn 9x15 Wind Tunnel facility, eliminating the possibility for data discrepancies experienced between the 18” and 22” scale fans on the QHSF I program. In order to accomplish all aerodynamic and mechanical testing at NASA, additional hardware was provided for test purposes that included distortion screens and a screen rotator mechanism for additional rotor mechanical and fan operability measurements. Additional instrumentation (relative to the QHSF I 22” fan) included stage performance rakes and CAP probes provided by Honeywell. NASA provided a rotor exit survey probe system.

9. REFERENCES

1. Weir, D., “NAS3-27752, NASA AST – AOI 14, Design and Test of Fan and Nacelle Models for Quiet High Speed Fan – Final Report,” CR-2003-212370, July 2003.
2. Lieber, L., Repp, R., and Weir, D., “Quiet High Speed Fan,” NASA CR-198518, November 1996.
3. Chen, J.P., and Whitfield, D.L., “Navier-Stokes Calculations for the Unsteady Flowfield of Turbomachinery,” AIAA Paper 93-0676, Reno, NV, January 1993.
4. Chen, J.P., Celestina, M., and Adamczyk, J.J., “A New Procedure for Simulating Unsteady Flows Through Turbomachinery Blade Passage,” ASME Paper 94-GT-151, The Hague, The Netherlands, June 1994.
5. Bakhle, M.A., Srivastava, R., Stefko, G.L., and Janus, J.M., “Development of an Aero-elastic Code Based on an Euler / Navier-Stokes Aerodynamic Solver,” ASME Paper 96-GT-311, 1996.
6. Bakhle, M.A., Srivastava, R., Keith, T.G., Jr., and Stefko, G.L., “Aeroelastic Calculations Based on Three-Dimensional Euler Analysis,” AIAA Paper 98-3295, 1998.
7. ANSYS Analysis Guides, SAS IP Inc., 2001.
8. Adamczyk, J.J., “Model Equation for Simulating Flows in Multistage Turbomachinery,” ASME Paper 85-GT-226, 1985.
9. Chen, J.P., and Barter, J., “Comparison of Time-Accurate Calculations for the Unsteady Interaction in Turbomachinery Stage,” AIAA Paper AIAA-98-3292, 1998.
10. Sanders, A., “Stall Flutter Assessment of an Advanced Design Transonic Fan Using TURBO-AE,” 6th National Turbine Engine High Cycle Fatigue Conference, Jacksonville, FL, 2001.
11. Fite, E.B., private correspondence.
12. Dittmar, J.H., Elliott, D.M., and Fite, E.B., “The Noise of a Forward Swept Fan,” NASA TM-2003-212208, November 2003.
13. Heidelberg, L.J., “Comparison of Tone Mode Measurements for a Forward Swept and Baseline Rotor Fan,” 9th AIAA/CEAS Aeroacoustics Conference and Exhibit, Hilton Head, SC, May 12–14, 2003.

APPENDIX I

INSTRUMENTATION

(17 Pages)

QHSF II 22" Rig Instrumentation

No.	Measurement	NASA or Honeywell	Part Number	Instrumentation	Identification Tag/Escort Name	Units	M/N	NASA Word No.	NASA Channel No.	NASA Model No.	Theta Loc. (CW FLA)	Radial Loc.	Axial Loc.	Comments	Range	Steady Pressures	Temperatures	Dynamic Channels
		HON			PT20(3)	psia	1603	1238	9485	1605	18	7.091						
		HON			PT20(4)	psia	1604	1239	9486	1606	18	8.391						
		HON			PT20(5)	psia	1605	1240	9487	1607	18	9.521						
		HON			PT20(6)	psia	1606	1241	9488	1608	18	10.521						
		HON			PT20(7)	psia	1701	1242	9489	1609	54	3.17	Sta 155.09			6		
		HON			PT20(8)	psia	1702	1243	9490	1610	54	5.501						
		HON			PT20(9)	psia	1703	1244	9491	1611	54	7.091						
		HON			PT20(10)	psia	1704	1245	9492	1612	54	8.391						
		HON			PT20(11)	psia	1705	1246	9493	1613	54	9.521						
		HON			PT20(12)	psia	1706	1247	9494	1614	54	10.521						
		HON			PT20(13)	psia	1801	1248	9495	1615	90	3.17	Sta 155.09			6		
		HON			PT20(14)	psia	1802	1249	9496	1616	90	5.501						
		HON			PT20(15)	psia	1803	1250	9497	1617	90	7.091						
		HON			PT20(16)	psia	1804	1251	9498	1618	90	8.391						
		HON			PT20(17)	psia	1805	1252	9499	1619	90	9.521						
		HON			PT20(18)	psia	1806	1253	9500	1620	90	10.521						
		HON			PT20(19)	psia	1901	1254	9501	1621	126	3.17	Sta 155.09			6		
		HON			PT20(20)	psia	1902	1255	9502	1622	126	5.501						
		HON			PT20(21)	psia	1903	1256	9503	1623	126	7.091						
		HON			PT20(22)	psia	1904	1257	9504	1624	126	8.391						
		HON			PT20(23)	psia	1905	1258	9505	1625	126	9.521						
		HON			PT20(24)	psia	1906	1259	9506	1626	126	10.521						
		HON			PT20(25)	psia	2001	1260	9507	1627	162	3.17	Sta 155.09			6		
		HON			PT20(26)	psia	2002	1261	9508	1628	162	5.501						
		HON			PT20(27)	psia	2003	1262	9509	1629	162	7.091						
		HON			PT20(28)	psia	2004	1263	9510	1630	162	8.391						
		HON			PT20(29)	psia	2005	1264	9511	1631	162	9.521						
		HON			PT20(30)	psia	2006	1265	9512	1632	162	10.521						
		HON			PT20(31)	psia	2101	1266	9514	1702	198	3.17	Sta 155.09			6		
		HON			PT20(32)	psia	2102	1267	9515	1703	198	5.501						
		HON			PT20(33)	psia	2103	1268	9516	1704	198	7.091						
		HON			PT20(34)	psia	2104	1269	9517	1705	198	8.391						
		HON			PT20(35)	psia	2105	1270	9518	1706	198	9.521						
		HON			PT20(36)	psia	2106	1271	9519	1707	198	10.521						
		HON			PT20(37)	psia	2201	1272	9520	1708	234	3.17	Sta 155.09			6		
		HON			PT20(38)	psia	2202	1273	9521	1709	234	5.501						
		HON			PT20(39)	psia	2203	1274	9522	1710	234	7.091						
		HON			PT20(40)	psia	2204	1275	9523	1711	234	8.391						
		HON			PT20(41)	psia	2205	1276	9524	1712	234	9.521						
		HON			PT20(42)	psia	2206	1277	9525	1713	234	10.521						
		HON			PT20(43)	psia	2301	1278	9526	1714	270	3.17	Sta 155.09			6		
		HON			PT20(44)	psia	2302	1279	9527	1715	270	5.501						
		HON			PT20(45)	psia	2303	1280	9528	1716	270	7.091						
		HON			PT20(46)	psia	2304	1281	9529	1717	270	8.391						
		HON			PT20(47)	psia	2305	1282	9530	1718	270	9.521						
		HON			PT20(48)	psia	2306	1283	9531	1719	270	10.521						
		HON			PT20(49)	psia	2401	1284	9532	1720	306	3.17	Sta 155.09			6		
		HON			PT20(50)	psia	2402	1285	9533	1721	306	5.501						
		HON			PT20(51)	psia	2403	1286	9534	1722	306	7.091						
		HON			PT20(52)	psia	2404	1287	9535	1723	306	8.391						
		HON			PT20(53)	psia	2405	1288	9536	1724	306	9.521						
		HON			PT20(54)	psia	2406	1289	9537	1725	306	10.521						
		HON			PT20(55)	psia	2501	1290	9538	1726	342	3.17	Sta 155.09			6		
		HON			PT20(56)	psia	2502	1291	9539	1727	342	5.501						
		HON			PT20(57)	psia	2503	1292	9549	1728	342	7.091						
		HON			PT20(58)	psia	2504	1293	9541	1729	342	8.391						
		HON			PT20(59)	psia	2505	1294	9542	1730	342	9.521						
		HON			PT20(60)	psia	2506	1295	9543	1731	342	10.521						
4.0	Bellmouth Pt	NASA	N/A	Tunnel Bellmouth Total Pressure	PTBM(1)	psia	1020	426	9003	103	N/A	N/A	N/A		(-2.5)-0 psig	Standard Tunnel Hook-up		
					PTBM(2)	psia	1021	427	9004	104								
					PTBM(3)	psia	1022	428	9005	105								
					PTBM(4)	psia	1023	429	9006	106								
4.1	Bellmouth Ps			Tunnel Bellmouth Static Pressure	PSBM(1)	psia	1032	430	9007	107								
					PSBM(2)	psia	1033	431	9008	108								
					PSBM(3)	psia	1034	432	9009	109								
					PSBM(4)	psia	1035	433	9010	110								
4.2	Tunnel Pt	NASA	N/A	Tunnel Test Rig Total Pressure	PTTR(1)	psia	1024	434	9011	111								

QHSF II 22" Rig Instrumentation

Instrumentation for QHSFII 22" Rig

M/N Not Applicable

No.	Measurement	NASA or Honeywell	Part Number	Instrumentation	Identification Tag/Escort Name	Units	M/N	NASA Word No.	NASA Channel No.	NASA Model No.	Theta Loc. (CW FLA)	Radial Loc.	Axial Loc.	Comments	Range	Steady Pressures	Temperatures	Dynamic Channels
1.0	Inlet Ps (10)	HON	MCP-0004003	Sta 2.0 Statics	PS20(1)	psia	1001	590	9172	612	9	N/A	2.118	1/2 way between each pair of distortion rake plugs	(-5)-0 psig	10	N/A	
		HON			PS20(2)	psia	1002	591	9173	613	36	N/A	2.118					
		HON			PS20(3)	psia	1003	592	9174	614	72	N/A	2.118					
		HON			PS20(4)	psia	1004	593	9175	615	108	N/A	2.118					
		HON			PS20(5)	psia	1005	594	9176	616	144	N/A	2.118					
		HON			PS20(6)	psia	1006	595	9177	617	180	N/A	2.118					
		HON			PS20(7)	psia	1007	596	9178	618	216	N/A	2.118					
		HON			PS20(8)	psia	1008	597	9179	619	252	N/A	2.118					
		HON			PS20(9)	psia	1009	598	9180	620	288	N/A	2.118					
		HON			PS20(10)	psia	1010	599	9181	621	324	N/A	2.118					
2.0	Inlet Boundary Layer Pt (5x10)	HON	Lab	Station 2.0 Inlet Boundary Layer Rakes	PB20(10)	psia	1101	1326	9555	1811	18	9.814	Sta 155.09	every other distortion rake plug	(-5)-0 psig	50		
		HON			PB20(9)	psia	1102	1325	9554	1810	18	9.779						
		HON			PB20(8)	psia	1103	1324	9553	1809	18	9.725						
		HON			PB20(7)	psia	1104	1323	9552	1808	18	9.617						
		HON			PB20(6)	psia	1105	1322	9551	1807	18	9.474						
		HON			PB20(5)	psia	1106	1321	9550	1806	18	9.331						
		HON			PB20(4)	psia	1107	1320	9549	1805	18	9.187						
		HON			PB20(3)	psia	1108	1319	9548	1804	18	9.044						
		HON			PB20(2)	psia	1109	1318	9547	1803	18	8.901						
		HON			PB20(1)	psia	1110	1317	9546	1802	18	8.757						
		HON			PB20(20)	psia	1201	1336	9565	1821	90	9.814	Sta 155.09					
		HON			PB20(19)	psia	1202	1335	9564	1820	90	9.779						
		HON			PB20(18)	psia	1203	1334	9563	1819	90	9.725						
		HON			PB20(17)	psia	1204	1333	9562	1818	90	9.617						
		HON			PB20(16)	psia	1205	1332	9561	1817	90	9.474						
		HON			PB20(15)	psia	1206	1331	9560	1816	90	9.331						
		HON			PB20(14)	psia	1207	1330	9559	1815	90	9.187						
		HON			PB20(13)	psia	1208	1329	9558	1814	90	9.044						
		HON			PB20(12)	psia	1209	1328	9557	1813	90	8.901						
		HON			PB20(11)	psia	1210	1327	9556	1812	90	8.757						
		HON			PB20(30)	psia	1301	1346	9575	1831	162	9.814	Sta 155.09					
		HON			PB20(29)	psia	1302	1345	9574	1830	162	9.779						
		HON			PB20(28)	psia	1303	1344	9573	1829	162	9.725						
		HON			PB20(27)	psia	1304	1343	9572	1828	162	9.617						
		HON			PB20(26)	psia	1305	1342	9571	1827	162	9.474						
		HON			PB20(25)	psia	1306	1341	9570	1826	162	9.331						
		HON			PB20(24)	psia	1307	1340	9569	1825	162	9.187						
		HON			PB20(23)	psia	1308	1339	9568	1824	162	9.044						
		HON			PB20(22)	psia	1309	1338	9567	1823	162	8.901						
		HON			PB20(21)	psia	1310	1337	9566	1822	162	8.757						
		HON			PB20(40)	psia	1401	1356	9586	1910	234	9.814	Sta 155.09					
		HON			PB20(39)	psia	1402	1355	9585	1909	234	9.779						
		HON			PB20(38)	psia	1403	1354	9584	1908	234	9.725						
		HON			PB20(37)	psia	1404	1353	9583	1907	234	9.617						
		HON			PB20(36)	psia	1405	1352	9582	1906	234	9.474						
		HON			PB20(35)	psia	1406	1351	9581	1905	234	9.331						
		HON			PB20(34)	psia	1407	1350	9580	1904	234	9.187						
		HON			PB20(33)	psia	1408	1349	9579	1903	234	9.044						
		HON			PB20(32)	psia	1409	1348	9578	1902	234	8.901						
		HON			PB20(31)	psia	1410	1347	9576	1832	234	8.757						
		HON			PB20(50)	psia	1501	1366	9596	1920	306	9.814	Sta 155.09					
		HON			PB20(49)	psia	1502	1365	9595	1919	306	9.779						
		HON			PB20(48)	psia	1503	1364	9594	1918	306	9.725						
		HON			PB20(47)	psia	1504	1363	9593	1917	306	9.617						
		HON			PB20(46)	psia	1505	1362	9592	1916	306	9.474						
		HON			PB20(45)	psia	1506	1361	9591	1915	306	9.331						
		HON			PB20(44)	psia	1507	1360	9590	1914	306	9.187						
		HON			PB20(43)	psia	1508	1359	9589	1913	306	9.044						
		HON			PB20(42)	psia	1509	1358	9588	1912	306	8.901						
		HON			PB20(41)	psia	1510	1357	9587	1911	306	8.757						
3.0	Inlet Pt Distortion Rakes (10x6)	HON		Station 2.0 Inlet Distortion Rakes	PT20(1)	psia	1601	1236	9483	1603	18	3.17	Sta 155.09	6 immersions		6		
		HON			PT20(2)	psia	1602	1237	9484	1604	18	5.501						

QHSF II 22" Rig Instrumentation

No.	Measurement	NASA or Honeywell	Part Number	Instrumentation	Identification Tag/Escort Name	Units	M/N	NASA Word No.	NASA Channel No.	NASA Model No.	Theta Loc. (CW FLA)	Radial Loc.	Axial Loc.	Comments	Range	Steady Pressures	Temperatures	Dynamic Channels
					PTTR(2)	psia	1025	435	9012	112								
					PTTR(3)	psia	1026	436	9013	113								
					PTTR(4)	psia	1027	437	9014	114								
4.1	Tunnel Ps			Tunnel Test Rig Static Pressure	PSTR(1)	psia	1036	438	9015	115								
					PSTR(2)	psia	1037	439	9016	116								
					PSTR(3)	psia	1038	440	9017	117								
					PSTR(4)	psia	1039	441	9018	118								
4.2	Cruciform Pt	NASA	N/A	Reference Freestream Total Pressure	PTRO(1)	psia	1028	442	9019	119	0	8	Sta. 83.54					
					PTRO(2)	psia	1029	443	9020	120	90	8	Sta. 83.54					
					PTRO(3)	psia	1030	444	9021	121	180	8	Sta. 83.54					
					PTRO(4)	psia	1031	445	9022	122	270	8	Sta. 83.54					
4.5	Barometric Pressure	NASA	N/A	Barometric Pressure	PBAR	psia	545	425	9002	102								
4.6	Humidity			Dewpoint	TDEW1	degF	401	31	8031	x								
					TDEW2	degF	402	32	8032	x								
					TDEW3	degF	403	33	8033	x								
5.0	Inlet Temperature	NASA	N/A	Ref freestream RTD	TRRO(1)	degF	500	104	8104	5106	0	N/A	N/A		60-120 deg. F	Standard Tunnel Hook-up		
					TRRO(2)	degF	501	105	8105	5107	90							
					TRRO(3)	degF	502	106	8106	5108	180							
					TRRO(4)	degF	503	107	8107	5109	270							
	Inlet Temperature	NASA	N/A	Tunnel Bellmouth T-Temp	TTBM(1)	degF	504	163	8656	5301	N/A							
					TTBM(2)	degF	505	164	8657	5302								
					TTBM(3)	degF	506	165	8658	5303								
					TTBM(4)	degF	507	166	8659	5304								
	Inlet Temperature	NASA	N/A	Tunnel Test Rig T-Temp	TTTR(1)	degR	508	167	8660	5305								
					TTTR(2)	degR	509	168	8661	5306								
					TTTR(3)	degR	510	169	8662	5307								
					TTTR(4)	degR	511	170	8663	5308								
	Inlet Temperature	NASA	N/A	Reference Freestream Total Temperatures (MV)	ETTRO(1)	Volt	512	171	8512	6101	0	11.875	Sta. 83.54					
				Cruciform Rake?	ETTRO(2)	Volt	513	172	8513	6102	90	11.875	Sta. 83.54					
					ETTRO(3)	Volt	514	173	8514	6103	180	11.875	Sta. 83.54					
					ETTRO(4)	Volt	515	174	8515	6104	270	11.875	Sta. 83.54					
					ETTRO(5)	Volt	516	175	8516	6105	0	0	Sta. 83.54					
6.0	Stage Exit Pressure & Temperature	HON		Core Inet Total Pressure	PT025(1)	psia	10101	1619	9674	2202	54	5.466	Front Frame	Core and bypass comb rake. 5 rakes, 9+5 immersions		14		
		HON			PT025(2)	psia	10102	1620	9675	2203	54	5.733						
		HON			PT025(3)	psia	10103	1621	9676	2204	54	5.987						
		HON			PT025(4)	psia	10104	1622	9677	2205	54	6.232						
		HON			PT025(5)	psia	10105	1623	9678	2206	54	6.467						
		HON		Sta 17.0 Total Pressure	PT17(1)	psia	10106	1498	9610	2002	54	7.23						
		HON			PT17(2)	psia	10107	1499	9611	2003	54	7.693						
		HON			PT17(3)	psia	10108	1500	9612	2004	54	8.13						
		HON			PT17(4)	psia	10109	1501	9613	2005	54	8.544						
		HON			PT17(5)	psia	10110	1502	9614	2006	54	8.939						
		HON			PT17(6)	psia	10111	1503	9615	2007	54	9.318						
		HON			PT17(7)	psia	10112	1504	9616	2008	54	9.682						
		HON			PT17(8)	psia	10113	1505	9617	2009	54	10.032						
		HON			PT17(9)	psia	10114	1506	9618	2010	54	10.371						
		HON		Core Inet Total Pressure	PT025(6)	psia	10201	1624	9679	2207	126	5.466				14		
		HON			PT025(7)	psia	10202	1625	9680	2208	126	5.733						
		HON			PT025(8)	psia	10203	1626	9681	2209	126	5.987						
		HON			PT025(9)	psia	10204	1627	9682	2210	126	6.232						
		HON			PT025(10)	psia	10205	1628	9683	2211	126	6.467						
		HON		Sta 17.0 Total Pressure	PT17(10)	psia	10206	1507	9619	2011	126	7.23						
		HON			PT17(11)	psia	10207	1508	9620	2012	126	7.693						
		HON			PT17(12)	psia	10208	1509	9621	2013	126	8.13						
		HON			PT17(13)	psia	10209	1510	9622	2014	126	8.544						
		HON			PT17(14)	psia	10210	1511	9623	2015	126	8.939						

QHSF II 22" Rig Instrumentation

No.	Measurement	NASA or Honeywell	Part Number	Instrumentation	Identification Tag/Escort Name	Units	M/N	NASA Word No.	NASA Channel No.	NASA Model No.	Theta Loc. (CW FLA)	Radial Loc.	Axial Loc.	Comments	Range	Steady Pressures	Temperatures	Dynamic Channels
		HON			PT17(15)	psia	10211	1512	9624	2016	126	9.318						
		HON			PT17(16)	psia	10212	1513	9625	2017	126	9.682						
		HON			PT17(17)	psia	10213	1514	9626	2018	126	10.032						
		HON			PT17(18)	psia	10214	1515	9627	2019	126	10.371						
		HON		Core Inet Total Pressure	PT025(11)	psia	10301	1629	9684	2212	198	5.466				14		
		HON			PT025(12)	psia	10302	1630	9685	2213	198	5.733						
		HON			PT025(13)	psia	10303	1631	9686	2214	198	5.987						
		HON			PT025(14)	psia	10304	1632	9687	2215	198	6.232						
		HON			PT025(15)	psia	10305	1633	9688	2216	198	6.467						
		HON		Sta 17.0 Total Pressure	PT17(19)	psia	10306	1516	9628	2020	198	7.23						
		HON			PT17(20)	psia	10307	1517	9629	2021	198	7.693						
		HON			PT17(21)	psia	10308	1518	9630	2022	198	8.13						
		HON			PT17(22)	psia	10309	1519	9631	2023	198	8.544						
		HON			PT17(23)	psia	10310	1520	9632	2024	198	8.939						
		HON			PT17(24)	psia	10311	1521	9633	2025	198	9.318						
		HON			PT17(25)	psia	10312	1522	9634	2026	198	9.682						
		HON			PT17(26)	psia	10313	1523	9635	2027	198	10.032						
		HON			PT17(27)	psia	10314	1524	9636	2028	198	10.371						
		HON		Core Inet Total Pressure	PT025(16)	psia	10401	1634	9689	2217	270	5.466				14		
		HON			PT025(17)	psia	10402	1635	9690	2218	270	5.733						
		HON			PT025(18)	psia	10403	1636	9691	2219	270	5.987						
		HON			PT025(19)	psia	10404	1637	9692	2220	270	6.232						
		HON			PT025(20)	psia	10405	1638	9693	2221	270	6.467						
		HON		Sta 17.0 Total Pressure	PT17(28)	psia	10406	1525	9637	2029	270	7.23						
		HON			PT17(29)	psia	10407	1526	9638	2030	270	7.693						
		HON			PT17(30)	psia	10408	1527	9639	2031	270	8.13						
		HON			PT17(31)	psia	10409	1528	9640	2032	270	8.544						
		HON			PT17(32)	psia	10410	1529	9642	2102	270	8.939						
		HON			PT17(33)	psia	10411	1530	9643	2103	270	9.318						
		HON			PT17(34)	psia	10412	1531	9644	2104	270	9.682						
		HON			PT17(35)	psia	10413	1532	9645	2105	270	10.032						
		HON			PT17(36)	psia	10414	1533	9646	2106	270	10.371						
		HON		Core Inet Total Pressure	PT025(21)	psia	10501	1639	9694	2222	342	5.466				14		
		HON			PT025(22)	psia	10502	1640	9695	2223	342	5.733						
		HON			PT025(23)	psia	10503	1641	9696	2224	342	5.987						
		HON			PT025(24)	psia	10504	1642	9697	2225	342	6.232						
		HON			PT025(25)	psia	10505	1643	9698	2226	342	6.467						
		HON		Sta 17.0 Total Pressure	PT17(37)	psia	10506	1534	9647	2107	342	7.23						
		HON			PT17(38)	psia	10507	1535	9648	2108	342	7.693						
		HON			PT17(39)	psia	10508	1536	9649	2109	342	8.13						
		HON			PT17(40)	psia	10509	1537	9650	2110	342	8.544						
		HON			PT17(41)	psia	10510	1538	9651	2111	342	8.939						
		HON			PT17(42)	psia	10511	1539	9652	2112	342	9.318						
		HON			PT17(43)	psia	10512	1540	9653	2113	342	9.682						
		HON			PT17(44)	psia	10513	1541	9654	2114	342	10.032						
		HON			PT17(45)	psia	10514	1542	9655	2115	342	10.371						
7.1	Stage Exit Ps	HON	MCP-0004042	Core Inlet (I/D) Static Pressure	PSCII(1)	psia	3101	1094	9423	1407	18	Core duct hub	Rake measurement	In front Frame, **in plane of comb rakes**	(-2)-10 psig	5		
		HON			PSCII(2)	psia	3102	1095	9424	1408	90							
		HON			PSCII(3)	psia	3103	1096	9425	1409	162							
		HON			PSCII(4)	psia	3104	1097	9426	1410	234							
		HON			PSCII(5)	psia	3105	1098	9427	1411	306							
7.2		HON		Core Inlet (O/D) Static Pressure	PSCIO(1)	psia	3106	1084	9418	1402	18	Core duct shroud	Rake measurement plane	In front Frame, **in plane of comb rakes**		5		
		HON			PSCIO(2)	psia	3107	1085	9419	1403	90							
		HON			PSCIO(3)	psia	3108	1086	9420	1404	162							
		HON			PSCIO(4)	psia	3109	1087	9421	1405	234							
		HON			PSCIO(5)	psia	3110	1088	9422	1406	306							
7.3		HON		Sta 17.0 (I/D) Static Pressure	PS17I(1)	psia	3111	1014	9386	1302	18	Bypass duct hub	Rake measurement plane	In front Frame, **in plane of comb rakes**		5		
		HON			PS17I(2)	psia	3112	1015	9387	1303	90							
		HON			PS17I(3)	psia	3113	1016	9388	1304	162							

QHSF II 22" Rig Instrumentation

No.	Measurement	NASA or Honeywell	Part Number	Instrumentation	Identification Tag/Escort Name	Units	M/N	NASA Word No.	NASA Channel No.	NASA Model No.	Theta Loc. (CW FLA)	Radial Loc.	Axial Loc.	Comments	Range	Steady Pressures	Temperatures	Dynamic Channels
		HON			PS17I(4)	psia	3114	1017	9389	1305	234							
		HON			PS17I(5)	psia	3115	1018	9390	1306	306							
7.4		HON		Sta 17.0 (O/D) Static Pressure	PS17O(1)	psia	3116	1004	9375	1223	18	Bypass duct shroud	Rake measurement plane	In front Frame, **in plane of comb rakes**		5		
		HON			PS17O(2)	psia	3117	1005	9376	1224	90							
		HON			PS17O(3)	psia	3118	1006	9377	1225	162							
		HON			PS17O(4)	psia	3119	1007	9378	1226	234							
		HON			PS17O(5)	psia	3120	1008	9379	1227	306							
8.0	Stage Exit Temperature	HON		Core Inlet Total Temperatures (MV)	ETT025(1)	Volt	20101	353	8569	6210	54	5.466		Core and bypass comb rake. 5 rakes, 9+5 immersions			14	
		HON			ETT025(2)	Volt	20102	354	8570	6211	54	5.733						
		HON			ETT025(3)	Volt	20103	355	8571	6212	54	5.987						
		HON			ETT025(4)	Volt	20104	356	8572	6213	54	6.232						
		HON			ETT025(5)	Volt	20105	357	8573	6214	54	6.467						
		HON		Sta 17.0 Total Temperatures (MV)	ETT17(1)	Volt	20106	301	8521	6110	54	7.23						
		HON			ETT17(2)	Volt	20107	302	8522	6111	54	7.693						
		HON			ETT17(3)	Volt	20108	303	8523	6112	54	8.13						
		HON			ETT17(4)	Volt	20109	304	8524	6113	54	8.544						
		HON			ETT17(5)	Volt	20110	305	8525	6114	54	8.939						
		HON			ETT17(6)	Volt	20111	306	8526	6115	54	9.318						
		HON			ETT17(7)	Volt	20112	307	8527	6116	54	9.682						
		HON			ETT17(8)	Volt	20113	308	8528	6117	54	10.032						
		HON			ETT17(9)	Volt	20114	309	8529	6118	54	10.371						
		HON		Core Inlet Total Temperatures (MV)	ETT025(6)	Volt	20201	358	8574	6215	126	5.466					14	
		HON			ETT025(7)	Volt	20202	359	8575	6216	126	5.733						
		HON			ETT025(8)	Volt	20203	360	8576	6217	126	5.987						
		HON			ETT025(9)	Volt	20204	361	8577	6218	126	6.232						
		HON			ETT025(10)	Volt	20205	362	8578	6219	126	6.467						
		HON		Sta 17.0 Total Temperatures (MV)	ETT17(10)	Volt	20206	310	8530	6119	126	7.23						
		HON			ETT17(11)	Volt	20207	311	8531	6120	126	7.693						
		HON			ETT17(12)	Volt	20208	312	8532	6121	126	8.13						
		HON			ETT17(13)	Volt	20209	313	8533	6122	126	8.544						
		HON			ETT17(14)	Volt	20210	314	8534	6123	126	8.939						
		HON			ETT17(15)	Volt	20211	315	8535	6124	126	9.318						
		HON			ETT17(16)	Volt	20212	316	8536	6125	126	9.682						
		HON			ETT17(17)	Volt	20213	317	8537	6126	126	10.032						
		HON			ETT17(18)	Volt	20214	318	8538	6127	126	10.371						
		HON		Core Inlet Total Temperatures (MV)	ETT025(11)	Volt	20301	363	8579	6220	198	5.466					14	
		HON			ETT025(12)	Volt	20302	364	8580	6221	198	5.733						
		HON			ETT025(13)	Volt	20303	365	8581	6222	198	5.987						
		HON			ETT025(14)	Volt	20304	366	8582	6223	198	6.232						
		HON			ETT025(15)	Volt	20305	367	8583	6224	198	6.467						
		HON		Sta 17.0 Total Temperatures (MV)	ETT17(19)	Volt	20306	319	8539	6128	198	7.23						
		HON			ETT17(20)	Volt	20307	320	8540	6129	198	7.693						
		HON			ETT17(21)	Volt	20308	321	8541	6130	198	8.13						
		HON			ETT17(22)	Volt	20309	322	8542	6131	198	8.544						
		HON			ETT17(23)	Volt	20310	323	8543	6132	198	8.939						
		HON			ETT17(24)	Volt	20311	324	8544	6133	198	9.318						
		HON			ETT17(25)	Volt	20312	325	8545	6134	198	9.682						
		HON			ETT17(26)	Volt	20313	326	8546	6135	198	10.032						
		HON			ETT17(27)	Volt	20314	327	8547	6136	198	10.371						
		HON		Core Inlet Total Temperatures (MV)	ETT025(16)	Volt	20401	368	8584	6225	270	5.466					14	
		HON			ETT025(17)	Volt	20402	369	8585	6226	270	5.733						
		HON			ETT025(18)	Volt	20403	370	8586	6227	270	5.987						
		HON			ETT025(19)	Volt	20404	371	8587	6228	270	6.232						
		HON			ETT025(20)	Volt	20405	372	8588	6229	270	6.467						
		HON		Sta 17.0 Total Temperatures (MV)	ETT17(28)	Volt	20406	328	8548	6137	270	7.23						
		HON			ETT17(29)	Volt	20407	329	8549	6138	270	7.693						
		HON			ETT17(30)	Volt	20408	330	8550	6139	270	8.13						
		HON			ETT17(31)	Volt	20409	331	8551	6140	270	8.544						
		HON			ETT17(32)	Volt	20410	332	8552	6141	270	8.939						
		HON			ETT17(33)	Volt	20411	333	8553	6142	270	9.318						

QHSF II 22" Rig Instrumentation

No.	Measurement	NASA or Honeywell	Part Number	Instrumentation	Identification Tag/Escort Name	Units	M/N	NASA Word No.	NASA Channel No.	NASA Model No.	Theta Loc. (CW FLA)	Radial Loc.	Axial Loc.	Comments	Range	Steady Pressures	Temperatures	Dynamic Channels
		HON			ETT17(34)	Volt	20412	334	8554	6143	270	9.682						
		HON			ETT17(35)	Volt	20413	335	8555	6144	270	10.032						
		HON			ETT17(36)	Volt	20414	336	8556	6145	270	10.371						
		HON		Core Inlet Total Temperatures (MV)	ETT025(21)	Volt	20501	373	8589	6230	342	5.466					14	
		HON			ETT025(22)	Volt	20502	374	8590	6231	342	5.733						
		HON			ETT025(23)	Volt	20503	375	8591	6232	342	5.987						
		HON			ETT025(24)	Volt	20504	376	8592	6233	342	6.232						
		HON			ETT025(25)	Volt	20505	377	8593	6234	342	6.467						
		HON		Sta 17.0 Total Temperatures (MV)	ETT17(37)	Volt	20506	337	8560	6201	342	7.23						
		HON			ETT17(38)	Volt	20507	338	8561	6202	342	7.693						
		HON			ETT17(39)	Volt	20508	339	8562	6203	342	8.13						
		HON			ETT17(40)	Volt	20509	340	8563	6204	342	8.544						
		HON			ETT17(41)	Volt	20510	341	8564	6205	342	8.939						
		HON			ETT17(42)	Volt	20511	342	8565	6206	342	9.318						
		HON			ETT17(43)	Volt	20512	343	8566	6207	342	9.682						
		HON			ETT17(44)	Volt	20513	344	8567	6208	342	10.032						
		HON			ETT17(45)	Volt	20514	345	8568	6209	342	10.371						
9.0	Rotor Exit Velocities	NASA/HON	N/A	Rotor Exit Survey - LDV	1 Window						270			Honeywell makes window frames/ NASA makes glass and provides LDV system				
10.0	Total Mass Flow	NASA	N/A	Bellmouth Weight Flow Static Pressure	PSBMW(1)	psia	901	549	9130	502	0	N/A	N/A	NASA Bellmouth				
		NASA			PSBMW(2)	psia	902	550	9131	503	45							
		NASA			PSBMW(3)	psia	903	551	9132	504	90							
		NASA			PSBMW(4)	psia	904	552	9133	505	135							
		NASA			PSBMW(5)	psia	905	553	9134	506	180							
		NASA			PSBMW(6)	psia	906	554	9135	507	225							
		NASA			PSBMW(7)	psia	907	555	9136	508	270							
		NASA			PSBMW(8)	psia	908	556	9137	509	315							
12.0	Core Flow Inner Statics	HON/NASA		Core Weight Flow (I/D) Static Pressure	PSCWI(1)	psia	910	1115	9433	1417	18	Core duct hub	N/A	NASA will fabricate rakes and send to Honeywell. Honeywell will modify R3563000-1 and R3562732-1 to install				
		HON/NASA			PSCWI(2)	psia	911	1116	9434	1418	90	Core duct hub	N/A					
		HON/NASA			PSCWI(3)	psia	912	1117	9435	1419	198	Core duct hub	N/A					
		HON/NASA			PSCWI(4)	psia	913	1118	9436	1420	270	Core duct hub	N/A					
12.1	Core Flow Outer Statics	HON/NASA		Core Weight Flow (O/D) Static Pressure	PSCWO(1)	psia	914	1105	9428	1412	18	Core duct shroud	N/A					
		HON/NASA			PSCWO(2)	psia	915	1106	9429	1413	90	Core duct hub	N/A					
		HON/NASA			PSCWO(3)	psia	916	1107	9430	1414	198	Core duct shroud	N/A					
		HON/NASA			PSCWO(4)	psia	917	1108	9431	1415	270	Core duct shroud	N/A					
13.0	Rotor Shock Positions	HON	MCP-0004020	15 kulites at rotor tip							TBD	N/A	TBD	High Response - Sample rate of no less than 220/rev. Honeywell to provide/install	0-2 psig			15
		HON									TBD	N/A	TBD					
		HON									TBD	N/A	TBD					
		HON									TBD	N/A	TBD					
		HON									TBD	N/A	TBD					
		HON									TBD	N/A	TBD					
		HON									TBD	N/A	TBD					
		HON									TBD	N/A	TBD					
		HON									TBD	N/A	TBD					
		HON									TBD	N/A	TBD					
		HON									TBD	N/A	TBD					
		HON									TBD	N/A	TBD					
		HON									TBD	N/A	TBD					
		HON									TBD	N/A	TBD					
		HON									TBD	N/A	TBD					
14.0	Rotor Shock Position	NASA/HON	N/A	Interblade shock position - LDV	n/a									Honeywell makes window frames/ NASA makes glass and provides LDV system				
15.0	Shock Position	NASA	N/A	Pressure Sensitive Paint							N/A	N/A	N/A	CFD Validation				

QHSF II 22" Rig Instrumentation

No.	Measurement	NASA or Honeywell	Part Number	Instrumentation	Identification Tag/Escort Name	Units	M/N	NASA Word No.	NASA Channel No.	NASA Model No.	Theta Loc. (CW FLA)	Radial Loc.	Axial Loc.	Comments	Range	Steady Pressures	Temperatures	Dynamic Channels
16.0	RPM	NASA	N/A	Rotor RPM	RPM	rpm	50	1736	15005	15005	N/A	N/A	N/A	1/rec and 128/rev				1
				Rotor RPM backup	RPMX	rpm	51	1737	15006	15006								
17.0	Noise	NASA	N/A	Far field microphones	n/a						N/A	N/A	N/A	standard tunnel array	0-1 psia			5
18.0	Noise	NASA	N/A	Mode measurement system	n/a						N/A	N/A	N/A	rotating rake	0-1 psia			16
19.0	Vibration	HON	MCP-0004042	Accelerometers							0	TBD	TBD	Honweywell's std. engine FFV and FFH Positions + Axial				2
		HON									90	TBD	TBD					
		HON									90	TBD	TBD					
20.0	Fan Tip Clearance	NASA	MCP-0004020	Capacitance probe		in	101				0	Fan rotor shroud	LE	Leading Edge, Mid, Trailing Edge.				
						in	111				0		Midchord					
						in	121				0		TE					
						in	102				90		LE					
						in	112				90		Midchord					
						in	122				90		TE					
21.0	Fan Tip Displacement	NASA	N/A	Optical Probe - Light Probe							N/A	N/A	N/A					
22.0	Rotor blade/attachment strain	HON	R3562758-1	Strain gauges							TBD	rad 1	TBD	16 total -- 4 blades, 3 locations on blade & 1 on attachment	(-2)-10 psig			20
		HON									TBD	rad 2	TBD					
		HON									TBD	rad 3	TBD					
		HON									TBD	rad 4	TBD					
		HON									TBD	rad 1	TBD					
		HON									TBD	rad 2	TBD					
		HON									TBD	rad 3	TBD					
		HON									TBD	rad 4	TBD					
		HON									TBD	rad 1	TBD					
		HON									TBD	rad 2	TBD					
		HON									TBD	rad 3	TBD					
		HON									TBD	rad 4	TBD					
		HON									TBD	rad 1	TBD					
		HON									TBD	rad 2	TBD					
		HON									TBD	rad 3	TBD					
		HON									TBD	rad 4	TBD					
23.0	Static Pressures in core A/B	HON	MCP-0004044	Core Afterbody Static Pressure	PSCAB(1)	psia	918	1166	9450	1502	30	8.029	Sta 215.108	Diagnose core flow, taps are in line at one theta, varying axial location		10		
		HON		(sliding core noz plug)	PSCAB(2)	psia	919	1167	9451	1503		8.029	Sta 216.108					
		HON			PSCAB(3)	psia	920	1168	9452	1504		8.029	Sta 217.108					
		HON			PSCAB(4)	psia	921	1169	9453	1505		8.029	Sta 218.108					
		HON			PSCAB(5)	psia	922	1170	9454	1506		8.029	Sta 219.108					
		HON			PSCAB(6)	psia	923	1171	9455	1507		8.029	Sta 220.108					
		HON			PSCAB(7)	psia	924	1172	9456	1508		8.029	Sta 221.108					
		HON			PSCAB(8)	psia	925	1173	9457	1509		8.029	Sta 222.108					
		HON			PSCAB(9)	psia	926	1174	9458	1510		8.029	Sta 223.108					
		HON			PSCAB(10)	psia	927	1175	9459	1511		8.013	Sta 224.108					
23.5	Rotor shroud merid Ps	HON		Fan Rubstrip Static Pressure	PSVR(1)	psia	811	1220	9471	1523	Passage 1	Shroud	Rotor LE	Chordwise line		5		
		HON			PSVR(2)	psia	812	1221	9472	1524			25%					
		HON			PSVR(3)	psia	813	1222	9473	1525			50%					
		HON			PSVR(4)	psia	814	1223	9474	1526			75%					
		HON			PSVR(5)	psia	815	1224	9475	1527			Rotor TE					
	Rotor shroud merid Ps	HON		Fan Rubstrip Static Pressure	PSVR(6)	psia	821	1225	9476	1528	Passage 2	Shroud	Rotor LE	Chordwise line				
		HON			PSVR(7)	psia	822	1226	9477	1529			25%					
		HON			PSVR(8)	psia	823	1227	9478	1530			50%					
		HON			PSVR(9)	psia	824	1228	9479	1531			75%					
		HON			PSVR(10)	psia	825	1229	9480	1532			Rotor TE			5		
24.0	Pressure/ Area Measurements	HON		Wall static taps	20 locations on shroud						TBD	TBD	TBD	20 locations on shroud. Determine thrust corrections		20		
25.0	Rotor Exit Pt/Tt survey	HON		Perf probe Pt	PT125(1)	psia	700	1378	9605	1929	18	Var.	Sta 172.0337			1		
25.1		HON		Perf probe Tt	ETT125(1)	Volt	704	218	8517	6106	18	Var.	Sta 172.0337				1	
25.2		HON		Perf Probe R	RADPOS1	in	705	1727	13001	x	18	Var.	Sta 172.0337					
25.3		HON		Perf Probe Alpha	ANG1	deg	706	1728	13002	x	18	Var.	Sta 172.0337					

QHSF II 22" Rig Instrumentation

No.	Measurement	NASA or Honeywell	Part Number	Instrumentation	Identification Tag/Escort Name	Units	M/N	NASA Word No.	NASA Channel No.	NASA Model No.	Theta Loc. (CW FLA)	Radial Loc.	Axial Loc.	Comments	Range	Steady Pressures	Temperatures	Dynamic Channels
25.4	Rotor Exit swirl survey	HON		wedge probe PL	PSWP2	psia	701	1669	9725	2321	90	Var.	Sta 172.0337			1		
25.5		HON		wedge probe PC	PTWP	psia	702	1668	9724	2320	90	Var.	Sta 172.0337			1		
25.6		HON		wedge probe PR	PSWP3	psia	703	1670	9726	2322	90	Var.	Sta 172.0337			1		
25.6		HON		wedge Probe Temp	ETTCP	Volt	30060	394	8613	6306	90	Var.	Sta 172.0337					
25.7		HON		wedge probe R	RADPOS2	in	707	1729	13003	x		Var.	Sta 172.0337					
25.8		HON		wedge probe alpha	ANG2	deg	708	1730	13004	x		Var.	Sta 172.0337					
25.9	Rotor Exit Survey Ps	HON		DELETED-REDUNDANT W/ MN 3151,3171-3173,3156,3174-3178	PS125I		3131				TBD	Hub	Survey Plane			5		
		HON			PS125I		3132				TBD							
		HON			PS125I		3133				TBD							
		HON			PS125I		3134				TBD							
		HON			PS125I		3135				TBD							
26.0	Rotor Exit Survey Ps	HON		Station 12.5 (O/D) Static Pressure	PS125O(1)	psia	3141	983	9354	1202	0	Shroud	172.0337	survey plane		5		
		HON			PS125O(2)	psia	3142	984	9355	1203	36							
		HON			PS125O(3)	psia	3143	985	9356	1204	72							
		HON			PS125O(4)	psia	3144	986	9357	1205	108							
		HON			PS125O(5)	psia	3145	987	9358	1206	144							
		HON			PS125O(6)	psia	3146	988	9359	1207	180							
		HON			PS125O(7)	psia	3147	989	9360	1208	216							
		HON			PS125O(8)	psia	3148	990	9361	1209	252							
		HON			PS125O(9)	psia	3149	991	9362		288							
		HON			PS125O(10)	psia	3150	992	9363		324							
		HON			PS125O(11)	psia	3136							survey plane in plugs				
		HON			PS125O(12)	psia	3137											
		HON			PS125O(13)	psia	3138											
		HON			PS125O(14)	psia	3139											
26.0	Stator Hub Merid Ps	HON		Fan Duct (I/D) Vane Passage Static Pressure Statics, Inner	PSFDI(1)	psia	3151	876	9322	1102	8.59	Stator Hub	LE	Stator hub chordwise line of 5 Ps, 2 vane passages				
		HON			PSFDI(2)	psia	3152	877	9323	1103	4.6		25%					
		HON			PSFDI(3)	psia	3153	878	9324	1104	2.97		50%					
		HON			PSFDI(4)	psia	3154	879	9325	1105	2.64		75%					
		HON			PSFDI(5)	psia	3155	880	9326	1106	2.8		TE					
		HON		Fan Duct (I/D) Vane Passage Static Pressure Statics, Inner	PSFDI(6)	psia	3156	881	9327	1107	152.59	Stator Hub	LE	Stator hub chordwise line of 5 Ps, 2 vane passages				
		HON			PSFDI(7)	psia	3157	882	9328	1108	148.6		25%					
		HON			PSFDI(8)	psia	3158	883	9329	1109	146.97		50%					
		HON			PSFDI(9)	psia	3159	884	9330	1110	146.64		75%					
		HON			PSFDI(10)	psia	3160	885	9331	1111	146.8		TE					
27.0	Stator Shroud Merid Ps	HON		Fan Duct (O/D) Vane Passage Static Pressure Statics, Outer	PSFDO(1)	psia	3161	795	9306	1018	1.99	Stator Shroud	LE	Stator shroud chordwise line of 5 Ps, 2 vane passages				
		HON			PSFDO(2)	psia	3162	796	9307	1019	359.86		25%					
		HON			PSFDO(3)	psia	3163	797	9308	1020	357.84		50%					
		HON			PSFDO(4)	psia	3164	798	9309	1021	356.88		75%					
		HON			PSFDO(5)	psia	3165	799	9310	1022	0		TE					
		HON		Fan Duct (O/D) Vane Passage Static Pressure Statics, Outer	PSFDO(6)	psia	3166	800	9311	1023	145.99	Stator Shroud	LE	Stator shroud chordwise line of 5 Ps, 2 vane passages				
		HON			PSFDO(7)	psia	3167	801	9312	1024	143.86		25%					
		HON			PSFDO(8)	psia	3168	802	9313	1025	141.84		50%					
		HON			PSFDO(9)	psia	3169	803	9314	1026	140.88		75%					
		HON			PSFDO(10)	psia	3170	804	9315	1027	144		TE					
28.0	Stator LE Hub Ps Ring	HON		Sta. 12.5 (I/D) Static Pressure Vane Leading Edge Statics, Inner	PS125I(1)	psia	3171	993	9364	1212	44.59	Stator Hub	LE	Stator LE Hub ring of 10 Ps (2 are the LE Ps from the chordwise Ps lines). Rotor exit radial survey plane Hub Ps.				
		HON			PS125I(2)	psia	3172	994	9365	1213	80.59	Stator Hub	LE					
		HON			PS125I(3)	psia	3173	995	9366	1214	116.59	Stator Hub	LE					

QHSF II 22" Rig Instrumentation

No.	Measurement	NASA or Honeywell	Part Number	Instrumentation	Identification Tag/Escort Name	Units	M/N	NASA Word No.	NASA Channel No.	NASA Model No.	Theta Loc. (CW FLA)	Radial Loc.	Axial Loc.	Comments	Range	Steady Pressures	Temperatures	Dynamic Channels
		HON			PS125I(4)	psia	3174	996	9367	1215	188.59	Stator Hub	LE					
		HON			PS125I(5)	psia	3175	997	9368	1216	224.59	Stator Hub	LE					
		HON			PS125I(6)	psia	3176	998	9369	1217	260.59	Stator Hub	LE					
		HON			PS125I(7)	psia	3177	999	9370	1218	296.59	Stator Hub	LE					
		HON			PS125I(8)	psia	3178	1000	9371	1219	332.59	Stator Hub	LE					
29.0	Stator TE Hub Ps Ring	HON		Vane Passage Static Pressure (Vane Trailing Edge Statics)	PSVP(1)	psia	3181	1176	9460	1512	38.8	Stator Hub	TE	Stator TE Hub ring of 10 Ps (2 are the TE Ps from the chordwise Ps lines)				
		HON			PSVP(2)	psia	3182	1177	9461	1513	74.8	Stator Hub	TE					
		HON			PSVP(3)	psia	3183	1178	9462	1514	110.8	Stator Hub	TE					
		HON			PSVP(4)	psia	3184	1179	9463	1515	182.8	Stator Hub	TE					
		HON			PSVP(5)	psia	3185	1180	9464	1516	218.8	Stator Hub	TE					
		HON			PSVP(6)	psia	3186	1181	9465	1517	254.8	Stator Hub	TE					
		HON			PSVP(7)	psia	3187	1182	9466	1518	290.8	Stator Hub	TE					
		HON			PSVP(8)	psia	3188	1183	9467	1519	326.8	Stator Hub	TE					
30.0	Stator LE Shroud Ps Ring	HON		Fan Leading Edge Static Pressure (Vane Leading Edge Statics Outer)	PSFLE(1)	psia	3191	962	9332	1112	37.99	Stator Shroud	LE	Stator LE Shroud ring of 10 Ps (2 are the LE Ps from the chordwise Ps lines)				
		HON			PSFLE(2)	psia	3192	963	9333	1113	73.99	Stator Shroud	LE					
		HON			PSFLE(3)	psia	3193	964	9334	1114	109.99	Stator Shroud	LE					
		HON			PSFLE(4)	psia	3194	965	9335	1115	181.99	Stator Shroud	LE					
		HON			PSFLE(5)	psia	3195	966	9336	1116	217.99	Stator Shroud	LE					
		HON			PSFLE(6)	psia	3196	967	9337	1117	253.99	Stator Shroud	LE					
		HON			PSFLE(7)	psia	3197	968	9338	1118	289.99	Stator Shroud	LE					
		HON			PSFLE(8)	psia	3198	969	9339	1119	325.99	Stator Shroud	LE					
31.0	Stator TE Shroud Ps Ring	HON		Fan Trailing Edge Static Pressure (Vane Trailing Edge Statics Outer)	PSFTE(1)	psia	3201	972	9342	1122	36	Stator Shroud	TE	Stator TE Shroud ring of 10 Ps (2 are the TE Ps from the chordwise Ps lines)				
		HON			PSFTE(2)	psia	3202	973	9343	1123	72	Stator Shroud	TE					
		HON			PSFTE(3)	psia	3203	974	9344	1124	108	Stator Shroud	TE					
		HON			PSFTE(4)	psia	3204	975	9345	1125	180	Stator Shroud	TE					
		HON			PSFTE(5)	psia	3205	976	9346	1126	216	Stator Shroud	TE					
		HON			PSFTE(6)	psia	3206	977	9347	1127	252	Stator Shroud	TE					
		HON			PSFTE(7)	psia	3207	978	9348	1128	288	Stator Shroud	TE					
		HON			PSFTE(8)	psia	3208	979	9349	1129	324	Stator Shroud	TE					
31.5	Strut Ps Field	HON		Strut Ps Field		psia	3211				41.59	Stator Shroud	LE					
	Strut Ps Field	HON		Strut Ps Field		psia	3212				45.19	Stator Shroud	LE					
	Strut Ps Field	HON		Strut Ps Field		psia	3213				48.79	Stator Shroud	LE					
	Strut Ps Field	HON		Strut Ps Field		psia	3214				52.39	Stator Shroud	LE					
	Strut Ps Field	HON		Strut Ps Field		psia	3215				55.99	Stator Shroud	LE					
	Strut Ps Field	HON		Strut Ps Field		psia	3216				59.59	Stator Shroud	LE					
	Strut Ps Field	HON		Strut Ps Field		psia	3217				63.19	Stator Shroud	LE					
	Strut Ps Field	HON		Strut Ps Field		psia	3218				66.79	Stator Shroud	LE					
	Strut Ps Field	HON		Strut Ps Field		psia	3219				70.39	Stator Shroud	LE					
	Strut Ps Field	HON		Strut Ps Field		psia	3221				77.59	Stator Shroud	LE					
	Strut Ps Field	HON		Strut Ps Field		psia	3222				81.19	Stator Shroud	LE					
	Strut Ps Field	HON		Strut Ps Field		psia	3223				84.79	Stator Shroud	LE					
	Strut Ps Field	HON		Strut Ps Field		psia	3224				88.39	Stator Shroud	LE					
	Strut Ps Field	HON		Strut Ps Field		psia	3225				91.99	Stator Shroud	LE					
	Strut Ps Field	HON		Strut Ps Field		psia	3226				95.59	Stator Shroud	LE					
	Strut Ps Field	HON		Strut Ps Field		psia	3227				99.19	Stator Shroud	LE					
	Strut Ps Field	HON		Strut Ps Field		psia	3228				102.79	Stator Shroud	LE					
	Strut Ps Field	HON		Strut Ps Field		psia	3229				106.39	Stator Shroud	LE					
	Strut Ps Field	HON		Strut Ps Field		psia	3230				109.99	Stator Shroud	LE					
32.0	Distortion rake strain gauges (2x2)	HON									18	on rake	N/A					
		HON									18	on rake	N/A					
		HON									90	on rake	N/A					
		HON									90	on rake	N/A					
33.0	Stator Vane strain gauges (2x1)	HON									TBD	TBD	TBD	2 vanes, one in front of strut, one mid-passage				
		HON									TBD	TBD	TBD					
34.0	Rotor Seal Statics (4)	NASA		Rotor Seal Static Pressure	PSRS(1)	psia	321	482	9060	228	45		Sta 172.062					
		NASA			PSRS(2)	psia	322	483	9061	229	135							
		NASA			PSRS(3)	psia	323	484	9062	230	225							

QHSF II 22" Rig Instrumentation

No.	Measurement	NASA or Honeywell	Part Number	Instrumentation	Identification Tag/Escort Name	Units	M/N	NASA Word No.	NASA Channel No.	NASA Model No.	Theta Loc. (CW FLA)	Radial Loc.	Axial Loc.	Comments	Range	Steady Pressures	Temperatures	Dynamic Channels
		NASA			PSRS(4)	psia	324	485	9063	231	315							
36.0	Fan Duct Ring Statics Shroud (8)	NASA	R3562734-1	Fan Duct Ring (O/D) Static Pressure	PSFDRO(1)	psia	331	1024	9396	1312				Bypass duct shroud Ps near nozzle				
		NASA			PSFDRO(2)	psia	332	1025	9397	1313								
		NASA			PSFDRO(3)	psia	333	1026	9398	1314								
		NASA			PSFDRO(4)	psia	334	1027	9399	1315								
		NASA			PSFDRO(5)	psia	335	1028	9400	1316								
		NASA			PSFDRO(6)	psia	336	1029	9401	1317								
		NASA			PSFDRO(7)	psia	337	1030	9402	1318								
		NASA			PSFDRO(8)	psia	338	1031	9403	1319								
37.0	Nozzle Outer Ring Statics (8)	NASA		Ps	deleted													
		NASA			deleted													
		NASA			deleted													
		NASA			deleted													
		NASA			deleted													
		NASA			deleted													
		NASA			deleted													
		NASA			deleted													
38.0	Core afterbody Ps	NASA		**REDUNDANT W/ MN 918-927**	PSCAB						N/A	Hub	Merid. Line of 10					
		NASA			PSCAB													
		NASA			PSCAB													
		NASA			PSCAB													
		NASA			PSCAB													
		NASA			PSCAB													
		NASA			PSCAB													
		NASA			PSCAB													
		NASA			PSCAB													
		NASA			PSCAB													
39.0	Core flow Pt	NASA		Core Weight Flow Total Pressure	PT025(26)	psia	11101	1644	9699	2227	45	5.272	Plane of PSCWI and PSCWO	3 rakes, 5 immersions				
		NASA			PT025(27)	psia	11102	1645	9700	2228		5.58						
		NASA			PT025(28)	psia	11103	1646	9701	2229		5.83						
		NASA			PT025(29)	psia	11104	1647	9702	2230		6.089						
		NASA			PT025(30)	psia	11105	1648	9703	2231		6.338						
		NASA			PT025(31)	psia	11201	1649	9704	2232	252	5.272						
		NASA			PT025(32)	psia	11202	1650	9706	2302		5.58						
		NASA			PT025(33)	psia	11203	1651	9707	2303		5.83						
		NASA			PT025(34)	psia	11204	1652	9708	2304		6.089						
		NASA			PT025(35)	psia	11205	1653	9709	2305		6.338						
		NASA			PT025(36)	psia	11301	1654	9710	2306	315	5.272						
		NASA			PT025(37)	psia	11302	1655	9711	2307		5.58						
		NASA			PT025(38)	psia	11303	1656	9712	2308		5.83						
		NASA			PT025(39)	psia	11304	1657	9713	2309		6.089						
		NASA			PT025(40)	psia	11305	1658	9714	2310		6.338						
40.0	Core flow Tt	NASA		Core Weight Flow Total Temperature (MV)	ETT025(26)	Volt	21101	378	8594	6235	45	5.272	Plane of PSCWI and PSCWO	3 rakes, 5 immersions				
		NASA			ETT025(27)	Volt	21102	379	8595	6236		5.58						
		NASA			ETT025(28)	Volt	21103	380	8596	6237		5.83						
		NASA			ETT025(29)	Volt	21104	381	8597	6238		6.089						
		NASA			ETT025(30)	Volt	21105	382	8598	6239		6.338						
		NASA			ETT025(31)	Volt	21201	383	8599	6240	252	5.272						
		NASA			ETT025(32)	Volt	21202	384	8600	6241		5.58						
		NASA			ETT025(33)	Volt	21203	385	8601	6242		5.83						
		NASA			ETT025(34)	Volt	21204	386	8602	6243		6.089						
		NASA			ETT025(35)	Volt	21205	387	8603	6244		6.338						
		NASA			ETT025(36)	Volt	21301	388	8608	6301	315	5.272						
		NASA			ETT025(37)	Volt	21302	389	8609	6302		5.58						
		NASA			ETT025(38)	Volt	21303	390	8610	6303		5.83						
		NASA			ETT025(39)	Volt	21304	391	8611	6304		6.089						
		NASA			ETT025(40)	Volt	21305	392	8612	6305		6.338						
41.0	Rotor disk strain	HON	R3562757-1	Strain gauges	Critical modes/ 2 gauges						TBD	TBD	TBD		(-2)-10 psig			2
42.0	Stator angular position	HON		Vane rotation position sensor	ROTVANE	deg	40	25	8025	x								

QHSF II 22" Rig Instrumentation

No.	Measurement	NASA or Honeywell	Part Number	Instrumentation	Identification Tag/Escort Name	Units	M/N	NASA Word No.	NASA Channel No.	NASA Model No.	Theta Loc. (CW FLA)	Radial Loc.	Axial Loc.	Comments	Range	Steady Pressures	Temperatures	Dynamic Channels
43.0	Distortion Screen angular position	HON		Distortion screen rotation position sensor	ROTDIST	deg	45	26	8026	x								
44.0	Core plug position	NASA		Core Plug Position	CLPLUGPOS	in	46	15	8015	x								
45.0	Vfen blade angle	NASA		Vfen Blade Angle	ANVFEN	deg	47	27	8027	5193								
46.0		NASA		Vfen blade angle backup	ANVFENX	deg	48	28	8028	5194								
47.0	Vfen vane position sensor	NASA		Vfen vane position sensor	VFENPOS	?	49	29	8029	x								
48.0	TC Refs.	NASA		TC Ref Oven 1	TCREF(1)	degF	52	40	8040	x								
		NASA		TC Ref Oven 2	TCREF(2)	degF	53	41	8041	x								
		NASA		TC Ref Oven Cald 11	TCREF(3)	degF	54	42	8042	x								
		NASA		TC Ref Oven Cald 12	TCREF(4)	degF	55	43	8043	x								
		NASA		TC Ref Oven Cald 13	TCREF(5)	degF	56	44	8044	x								
		NASA		TC Ref Oven Cald 14	TCREF(6)	degF	57	45	8045	x								
		NASA		TC RefA Oven Cald 11	REF11A	degF	58	47	8047	x								
		NASA		TC RefB Oven Cald 11	REF11B	degF	59	48	8048	x								
		NASA		TC RefA Oven Cald 12	REF12A	degF	60	49	8049	x								
		NASA		TC RefB Oven Cald 12	REF12B	degF	61	50	8050	x								
		NASA		TC RefA Oven Cald 13	REF13A	degF	62	51	8051	x								
		NASA		TC RefB Oven Cald 13	REF13B	degF	63	52	8052	x								
		NASA		TC RefA Oven Cald 14	REF14A	degF	64	53	8053	x								
		NASA		TC RefB Oven Cald 14	REF14B	degF	65	54	8054	x								
49.0	Drive Turbine exit Temps	NASA		Turbine Exit Total Temperatures	TT5(1)	degF	71	134	8134	5343	36	3.001	Sta 269.13	TTETCE(859)				
		NASA			TT5(2)	degF	72	135	8135	5344		3.775	Sta 269.71	TTETCD(861)				
		NASA			TT5(3)	degF	73	136	8136	5345		4.412	Sta 270.14	TTETCC(863)				
		NASA			TT5(4)	degF	74	137	8137	5346		4.966	Sta 270.52	TTETCB(865)				
		NASA			TT5(5)	degF	75	138	8138	5347		5.462	Sta 270.81	TTETCA(867)				
		NASA			TT5(6)	degF	81	139	8139	5348	252	3.001	Sta 269.13	TTETSE(5048)				
		NASA			TT5(7)	degF	82	140	8140	5349		3.775	Sta 269.71	TTETSD(5049)				
		NASA			TT5(8)	degF	83	141	8141	5350		4.412	Sta 270.14	TTETSC(5050)				
		NASA			TT5(9)	degF	84	142	8142	5351		4.966	Sta 270.52	TTETSB(5051)				
		NASA			TT5(10)	degF	85	143	8143	5352		5.462	Sta 270.81	TTETSA(5052)				
50.0	Drive Turbine inlet Temps	NASA		Turbine Inlet Temperatures	TT4(1)	degF	90	160	8160	5001								
		NASA			TT4(2)	degF	91	161	8161	5002								
		NASA			TT4(3)	degF	92	162	8162	5003								
51.0	Cal Signals	NASA		T/D Ref 11 Cal Signal	ETTCAL11	Volt	93	300	8559	x								
		NASA		T/D Ref 12 Cal Signal	ETTCAL12	Volt	94	351	8607	x								
		NASA		T/D Ref 13 Cal Signal	ETTCAL13	Volt	95	399	8655	x								
		NASA		T/D Ref 14 Cal Signal	ETTCAL14	Volt	96	400	8703	x								
52.0	Core Duct Shroud Merid Ps	NASA		Core Duct (O/D) Static Pressure	PSCDO(1)	psia	131	1126	9439	1423	342	6.46	Sta 182.994					
		NASA			PSCDO(2)	psia	132	1127	9440	1424		6.46	Sta 184.134					
		NASA			PSCDO(3)	psia	133	1128	9441	1425		6.46	Sta 185.274					
		NASA			PSCDO(4)	psia	134	1129	9442	1426		6.46	Sta 186.414					
		NASA			PSCDO(5)	psia	135	1130	9443	1427		6.46	Sta 187.554					
		NASA			PSCDO(6)	psia	136	1131	9444	1428		6.466	Sta 188.694					
		NASA			PSCDO(7)	psia	137	1132	9445	1429		6.637	Sta 189.834					
		NASA			PSCDO(8)	psia	138	1133	9446	1430		6.924	Sta 190.974					
		NASA			PSCDO(9)	psia	139	1134	9447	1431		7.206	Sta 192.114					
		NASA			PSCDO(10)	psia	140	1135	9448	1432		7.485	Sta 193.254					
53.0	Turbine Inlet Pt	NASA		Turbine Inlet Total Pressure	PT4(1)	psia	141	1690	9738	2402	60	4.175	Sta 258.2					
		NASA			PT4(2)	psia	142	1691	9739	2403	120							
		NASA			PT4(3)	psia	143	1692	9740	2404	160							
		NASA			PT4(4)	psia	144	1693	9741	2405	240							

QHSF II 22" Rig Instrumentation

No.	Measurement	NASA or Honeywell	Part Number	Instrumentation	Identification Tag/Escort Name	Units	M/N	NASA Word No.	NASA Channel No.	NASA Model No.	Theta Loc. (CW FLA)	Radial Loc.	Axial Loc.	Comments	Range	Steady Pressures	Temperatures	Dynamic Channels
		NASA			PT4(5)	psia	145	1694	9742	2406	270							
		NASA			PT4(6)	psia	146	1695	9743	2407	320							
54.0	Turbine Ps	NASA		Turbine Wheel Well Static Pressure	PSTW(1)	psia	151	1699	9747	2411	1	4.816	Sta 259.4					
		NASA			PSTW(2)	psia	152	1700	9748	2412	2	4.831	260.44					
		NASA			PSTW(3)	psia	153	1701	9749	2413	1	4.7	260.49					
		NASA			PSTW(4)	psia	154	1702	9750	2414	1	5.025	261.61					
		NASA			PSTW(5)	psia	155	1703	9751	2415	1	5.211	262.61					
		NASA			PSTW(6)	psia	156	1704	9752	2416	4	5.5	263.93					
		NASA			PSTW(7)	psia	157	1705	9753	2417	2	5.7	264.95					
		NASA			PSTW(8)	psia	158	1706	9754	2418	4	5.745	266.495					
		NASA			PSTW(9)	psia	159	1707	9755	2419	181	4.816	259.4					
		NASA			PSTW(10)	psia	160	1708	9756	2420	182	4.831	260.44					
		NASA			PSTW(11)	psia	161	1709	9757	2421	181	4.7	260.49					
		NASA			PSTW(12)	psia	162	1710	9758	2422	181	5.025	261.61					
		NASA			PSTW(13)	psia	163	1711	9759	2423	181	5.211	262.61					
		NASA			PSTW(14)	psia	164	1712	9760	2424	184	5.5	263.93					
		NASA			PSTW(15)	psia	165	1713	9761	2425	182	5.7	264.95					
		NASA			PSTW(16)	psia	166	1714	9762	2426	184	5.745	266.495					
55.0	450 Piping Pressures	NASA		V1 CONTROL PRESSURE	PTV1CON	psia	171	1715	9763	2427								
		NASA		DRIVE STRUT	PTDRST	psia	172	1716	9764	2428								
		NASA		D/S OF V3	PTV3CON	psia	173	1717	9765	2429								
		NASA		VENTURI THROAT	PS450V	psia	174	1718	9766	2430								
		NASA		VENTURI UPSTREAM	PT450V	psia	175	1719	9767	2431								
		NASA		U/S OF V3	PT450SP	psia	176	1720	9768	2432								
56.0		NASA		USED AS ESPREF	WESP1	psia	181	1721	12201	x								
		NASA		TUNNEL BELLMOUTH DELTA PRESSURE (WESP2)	DQBM	psid	182	7122	12202	x								
		NASA		TUNNEL TEST RIG DELTA PRESSURE (WESP3)	DQTR	psid	183	1723	12203	x								
		NASA		USED AS ESPCK	WESP4	psia	184	1724	12204	x								
		NASA		USED AS ESPCK	WESP5	psia	185	1725	12205	x								
		NASA		USED AS ESPCK	WESP6	psia	186	1726	12206	x								
57.0		NASA		Tunnel Bellmouth T-Pres	PTBME	psia	191	1733	14013	14013								
		NASA		Tunnel Test Rig T-Pres	PTTRE	psia	192	1734	14015	14015								
58.0	Rotor Balance Ps	NASA		Rotor Balance D/S Static Pressure	PSRBD(1)	psia	201	456	9034	202	10	2	Sta 172					
		NASA			PSRBD(2)	psia	202	457	9035	203	100							
		NASA			PSRBD(3)	psia	203	458	9036	204	190							
		NASA			PSRBD(4)	psia	204	459	9037	205	280							
		NASA			PSRBD(5)	psia	205	460	9038	206	10	2.8	Sta 172.34					
		NASA			PSRBD(6)	psia	206	461	9039	207	100							
		NASA			PSRBD(7)	psia	207	462	9040	208	190							
		NASA			PSRBD(8)	psia	208	463	9041	209	280							
59.0	Cowl Balance Upstream Ps	NASA		Cowl Balance U/S Static Pressure	PSCBU(1)	psia	211	464	9042	210	20	3	Sta 177.85					
		NASA			PSCBU(2)	psia	212	465	9043	211	170							
		NASA			PSCBU(3)	psia	213	466	9044	212	190							
		NASA			PSCBU(4)	psia	214	467	9045	213	355							
60.0	Cowl Balance Internal Ps	NASA		Cowl Balance Internal Static Pressure	PSCBI(1)	psia	221	468	9046	214	90	3.425	Sta 179.75					
		NASA			PSCBI(2)	psia	222	469	9047	215	270							
		NASA			PSCBI(3)	psia	223	470	9048	216	90	3.425	Sta 182.25					
		NASA			PSCBI(4)	psia	224	471	9049	217	270							
		NASA			PSCBI(5)	psia	225	472	9050	218	90	3.425	Sta 190.45					
		NASA			PSCBI(6)	psia	226	473	9051	219	270							
61.0	Cowl Balance Downstream Ps	NASA		Cowl Balance D/S Static Pressure	PSCBD(1)	psia	231	474	9052	220	10	3	Sta 200					
		NASA			PSCBD(2)	psia	232	475	9053	221	100							
		NASA			PSCBD(3)	psia	233	476	9054	222	190							
		NASA			PSCBD(4)	psia	234	477	9055	223	280							

QHSF II 22" Rig Instrumentation

No.	Measurement	NASA or Honeywell	Part Number	Instrumentation	Identification Tag/Escort Name	Units	M/N	NASA Word No.	NASA Channel No.	NASA Model No.	Theta Loc. (CW FLA)	Radial Loc.	Axial Loc.	Comments	Range	Steady Pressures	Temperatures	Dynamic Channels
62.0	Afterbody Cavity Ps	NASA		Afterbody Cavity Static Pressure	PSAC(1)	psia	241	478	9056	224	50	3	Sta 215					
		NASA			PSAC(2)	psia	242	479	9057	225	140							
		NASA			PSAC(3)	psia	243	480	9058	226	230	3	Sta 215					
		NASA			PSAC(4)	psia	244	481	9059	227	320							
63.0	Turbine Exit Pt	NASA		Turbine Exit Total Pressure	PT5(1)	psia	251	518	9098	402	36	3.001	Sta 269.13					
		NASA			PT5(2)	psia	252	519	9099	403		3.775	269.71					
		NASA			PT5(3)	psia	253	520	9100	404		4.412	270.14					
		NASA			PT5(4)	psia	254	521	9101	405		4.966	270.52					
		NASA			PT5(5)	psia	255	522	9102	406		5.462	270.81					
		NASA			PT5(6)	psia	256	523	9103	407	252	3.001	Sta 269.13					
		NASA			PT5(7)	psia	257	524	9104	408		3.775	269.71					
		NASA			PT5(8)	psia	258	525	9105	409		4.412	270.14					
		NASA			PT5(9)	psia	259	526	9106	410		4.966	270.52					
		NASA			PT5(10)	psia	260	527	9107	411		5.462	270.81					
64.0	Turbine Exit Ps	NASA		Turbine Exit Static Pressure	PS5(1)	psia	261	528	9108	412	0	5.745	Sta 267.85					
		NASA			PS5(2)	psia	262	529	9109	413	180	5.745	Sta 267.85					
		NASA			PS5(3)	psia	263	530	9110	414	30	5.675	Sta 270.14					
		NASA			PS5(4)	psia	264	531	9111	415	247	5.675	Sta 270.14					
		NASA			PS5(5)	psia	265	532	9112	416	36	2.58	Sta 268.056					
		NASA			PS5(6)	psia	266	533	9113	417	252	2.58	Sta 268.056					
65.0	Turbine Discharge Ps	NASA		Turbine Discharge Static Pressure	PS7(1)	psia	271	534	9114	418	0	5.64	Sta 277.5					
		NASA			PS7(2)	psia	272	535	9115	419	216							
66.0	Cavity pressures	NASA		Cavity Pressures	PSCAV(1)	psia	273	537	9117	421	10	2.5	Sta 213.75					
		NASA			PSCAV(2)	psia	274	538	9118	422	0	4.75	Sta 251.3					
67.0	Aft Coupling Cavity Ps	NASA		Aft Coupling Cavity Pressure	PSACC	psia	275	539	9119	423								
68.0	Windscreen Ps	NASA		Windscreen Static Pressure	PSWS(1)	psia	281	540	9120	424	0	3.25	Sta 220					
		NASA			PSWS(2)	psia	282	541	9121	425		3.275	225					
		NASA			PSWS(3)	psia	283	542	9122	426		3.61	230					
		NASA			PSWS(4)	psia	284	543	9123	427		4.21	235					
		NASA			PSWS(5)	psia	285	544	9124	428	90	3.25	Sta 220					
		NASA			PSWS(6)	psia	286	545	9125	429		3.275	225					
		NASA			PSWS(7)	psia	287	546	9126	430		3.61	230					
		NASA			PSWS(8)	psia	288	547	9127	431		4.21	235					
69.0	Check Pressures	NASA			ESPMC(1)	psia	291	401	9001	101								
		NASA			ESPMC(2)	psia	292	402	9033	201								
		NASA			ESPMC(3)	psia	293	403	9065	301								
		NASA			ESPMC(4)	psia	294	404	9097	401								
		NASA			ESPMC(5)	psia	295	405	9129	501								
		NASA			ESPMC(6)	psia	296	406	9161	601								
		NASA			ESPMC(7)	psia	297	407	9193	701								
		NASA			ESPMC(8)	psia	298	408	9225	801								
		NASA			ESPMC(9)	psia	299	409	9257	901								
		NASA			ESPMC(10)	psia	300	410	9289	1001								
		NASA			ESPMC(11)	psia	301	411	9321	1101								
		NASA			ESPMC(12)	psia	302	412	9353	1201								
		NASA			ESPMC(13)	psia	303	413	9385	1301								
		NASA			ESPMC(14)	psia	304	414	9417	1401								
		NASA			ESPMC(15)	psia	305	415	9449	1501								
		NASA			ESPMC(16)	psia	306	416	9481	1601								
		NASA			ESPMC(17)	psia	307	417	9513	1701								
		NASA			ESPMC(18)	psia	308	418	9545	1801								
		NASA			ESPMC(19)	psia	309	419	9577	1901								
		NASA			ESPMC(20)	psia	310	420	9609	2001								
		NASA			ESPMC(21)	psia	311	421	9641	2101								
		NASA			ESPMC(22)	psia	312	422	9673	2201								
		NASA			ESPMC(23)	psia	313	423	9705	2301								
		NASA			ESPMC(24)	psia	314	424	9737	2401								
70.0	TURNTABLE POT	NASA		ANGLE-OF-ATTACK (+ LEFT)	ALPHA	deg	30001	1	8001	5031		1.475	Sta 170					
	ROLL	NASA		ROTOR BAL. FORCE	SRBFC(1)	?	30002	2	8002	5056			Sta 170					
	AXIAL	NASA			SRBFC(2)	?	30003	3	8003	5057			Sta168.375					

Circumferential Placement of Plugs

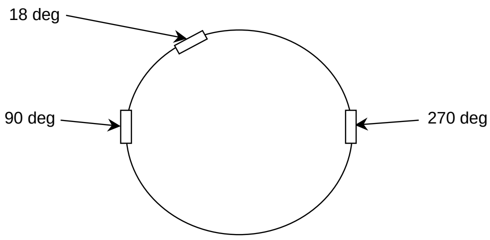

Forward Looking Aft

Detailed Plug Configuations

Plug 1

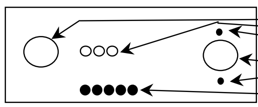

Instrumentation	Test Config	Placement	Responsibility
Inlet Boundary Layer/Inlet Distortion	Aero/Dist	90 deg	NASA
CAP probes (LE, Mid, TE)	Aero	90 deg	Honeywell
PS125O Static Pressures	Aero	90 deg	NASA
Rotor Exit Survey (Wedge Probe)	Aero	90 deg	NASA
Fan Rubstrip static pressure, Passage 1	Aero	90 deg	Honeywell

Plug 2

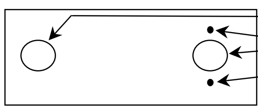

Inlet Boundary Layer/Inlet Distortion	Aero/Dist	18 deg	NASA
Rotor Exit Survey (Combo PT/TT Probe)	Aero	18 deg	NASA
PS125O Static Pressures	Aero	18 deg	NASA

Plug 3

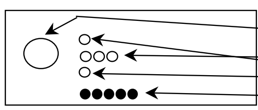

Inlet Boundary Layer/Inlet Distortion	Aero/Dist	270 deg	NASA
CAP probes (LE, Mid, TE)	Aero	270 deg	Honeywell
Optical light probes for flutter	Aero	270 deg	NASA
Fan Rubstrip static pressure, Passage 2	Aero	270 deg	Honeywell

Plug 4

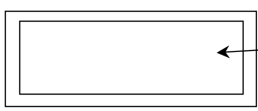

LDV Window	Aero	90 deg	NASA

Plug 5

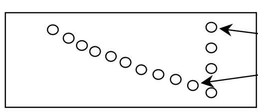

Shock Position & Strut Potential kulites (15 total, 14+ one in fan case)	Aero	18 deg	NASA

Plug 6

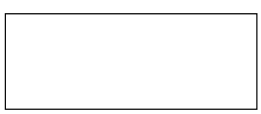

Blank			(NASA)

Plug 7

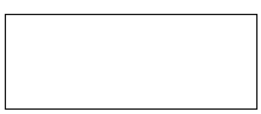

Blank			(NASA)

Plug 8

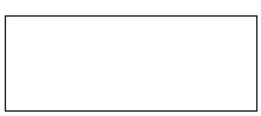

Blank			(NASA)

Fan Case Liner with Plugs

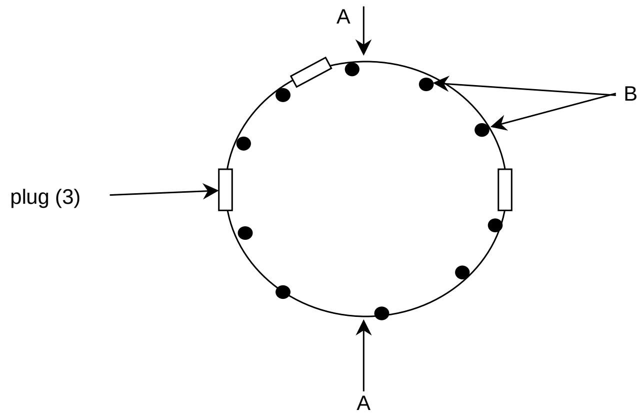

	Instrumentation to Modify Part	Config	Location	Comment
A	CAP probes (LE, Mid, TE)	Aero	0 deg, 180 deg	2 in fan case, 2 in plugs for total of 4(x3)
B	Rotor Exit Survey Ps, 10 total	Aero	in survey plane	all 10 in case when no plugs 6 in case when plugs installed, (2 in two plugs for a total of 4): 10 total

18 deg
window

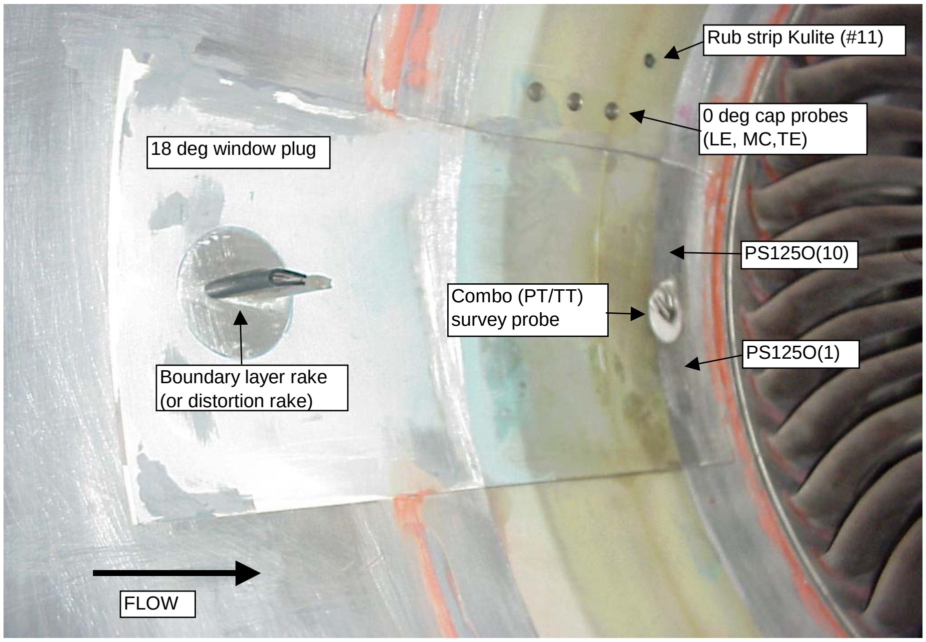

90 deg
window

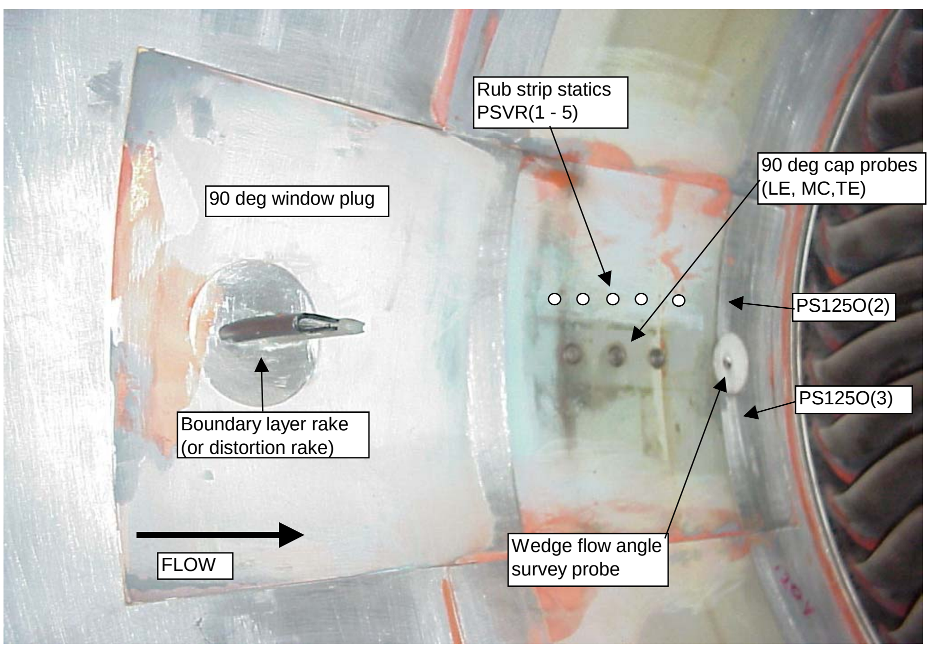

270 deg window

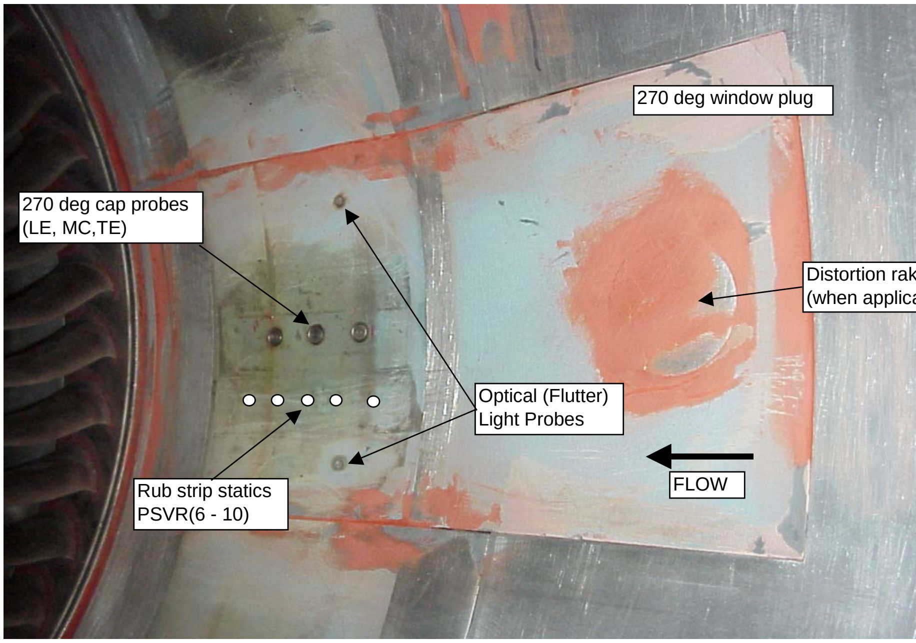

18 deg Kulite window

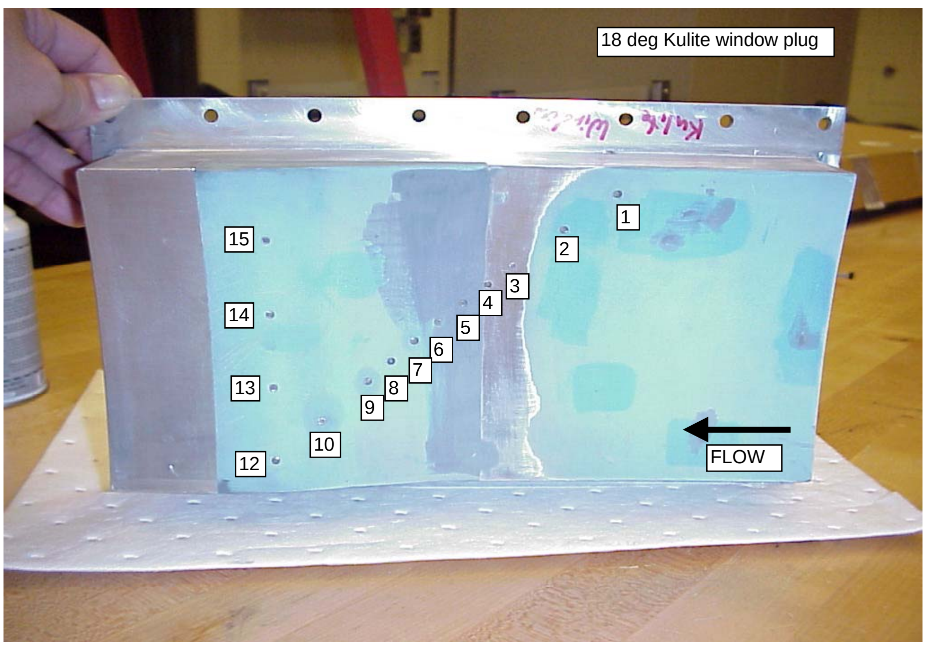

REPORT DOCUMENTATION PAGE	*Form Approved* *OMB No. 0704-0188*

1. REPORT DATE *(DD-MM-YYYY)*	**2. REPORT TYPE**	**3. DATES COVERED** *(From - To)*
01-08-2012	Final Contractor Report	

4. TITLE AND SUBTITLE
Quiet High Speed Fan II (QHSF II): Final Report

5a. CONTRACT NUMBER
NAS3-01136

5b. GRANT NUMBER

5c. PROGRAM ELEMENT NUMBER

6. AUTHOR(S)
Kontos, Karen; Weir, Don; Ross, Dave

5d. PROJECT NUMBER

5e. TASK NUMBER
2

5f. WORK UNIT NUMBER
WBS 561581.02.08.03.45.04

7. PERFORMING ORGANIZATION NAME(S) AND ADDRESS(ES)
Honeywell
P.O. Box 52181
Phoenix, Arizona 85072

8. PERFORMING ORGANIZATION REPORT NUMBER
E-18181

9. SPONSORING/MONITORING AGENCY NAME(S) AND ADDRESS(ES)
National Aeronautics and Space Administration
Washington, DC 20546-0001

10. SPONSORING/MONITOR'S ACRONYM(S)
NASA

11. SPONSORING/MONITORING REPORT NUMBER
NASA/CR-2012-217451

12. DISTRIBUTION/AVAILABILITY STATEMENT
Unclassified-Unlimited
Subject Category: 71
Available electronically at http://www.sti.nasa.gov
This publication is available from the NASA Center for AeroSpace Information, 443-757-5802

13. SUPPLEMENTARY NOTES

14. ABSTRACT
This report details the aerodynamic, mechanical, structural design and fabrication of a Honey Engines Quiet High Speed Fan II (lower hub/tip ratio and higher specific flow than the Baseline I fan). This fan/nacelle system incorporates features such as advanced forward sweep and an advanced integrated fan/fan exit guide vane design that provides for the following characteristics: (1) Reduced noise at supersonic tip speeds, in comparison to current state-of-the-art fan technology; (2) Improved aeroelastic stability within the anticipated operating envelope; and (3) Aerodynamic performance consistent with current state-of-the-art fan technology. This fan was fabricated by Honeywell and tested in the NASA Glenn 9- by 15-Ft Low Speed Wind Tunnel for aerodynamic, aeromechanical, and acoustic performance.

15. SUBJECT TERMS
Low noise; Models; Scale models; Turbofan; Acoustic measurements; Aerodynamic characteristics

16. SECURITY CLASSIFICATION OF: a. REPORT	b. ABSTRACT	c. THIS PAGE	**17. LIMITATION OF ABSTRACT**	**18. NUMBER OF PAGES**	**19a. NAME OF RESPONSIBLE PERSON** / **19b. TELEPHONE NUMBER** *(include area code)*
U	U	U	UU	202	STI Help Desk (email:help@sti.nasa.gov) 443-757-5802

Standard Form 298 (Rev. 8-98)
Prescribed by ANSI Std. Z39-18